

Perovskite/c-Si TandemSolar Cells with High Temperature Carrier-Selective Passivating Contacts

Singh, M.

DOI

[10.4233/uuid:e68141db-e816-46fd-8293-798e7e9e1542](https://doi.org/10.4233/uuid:e68141db-e816-46fd-8293-798e7e9e1542)

Publication date

2025

Document Version

Final published version

Citation (APA)

Singh, M. (2025). *Perovskite/c-Si TandemSolar Cells with High Temperature Carrier-Selective Passivating Contacts*. [Dissertation (TU Delft), Delft University of Technology]. <https://doi.org/10.4233/uuid:e68141db-e816-46fd-8293-798e7e9e1542>

Important note

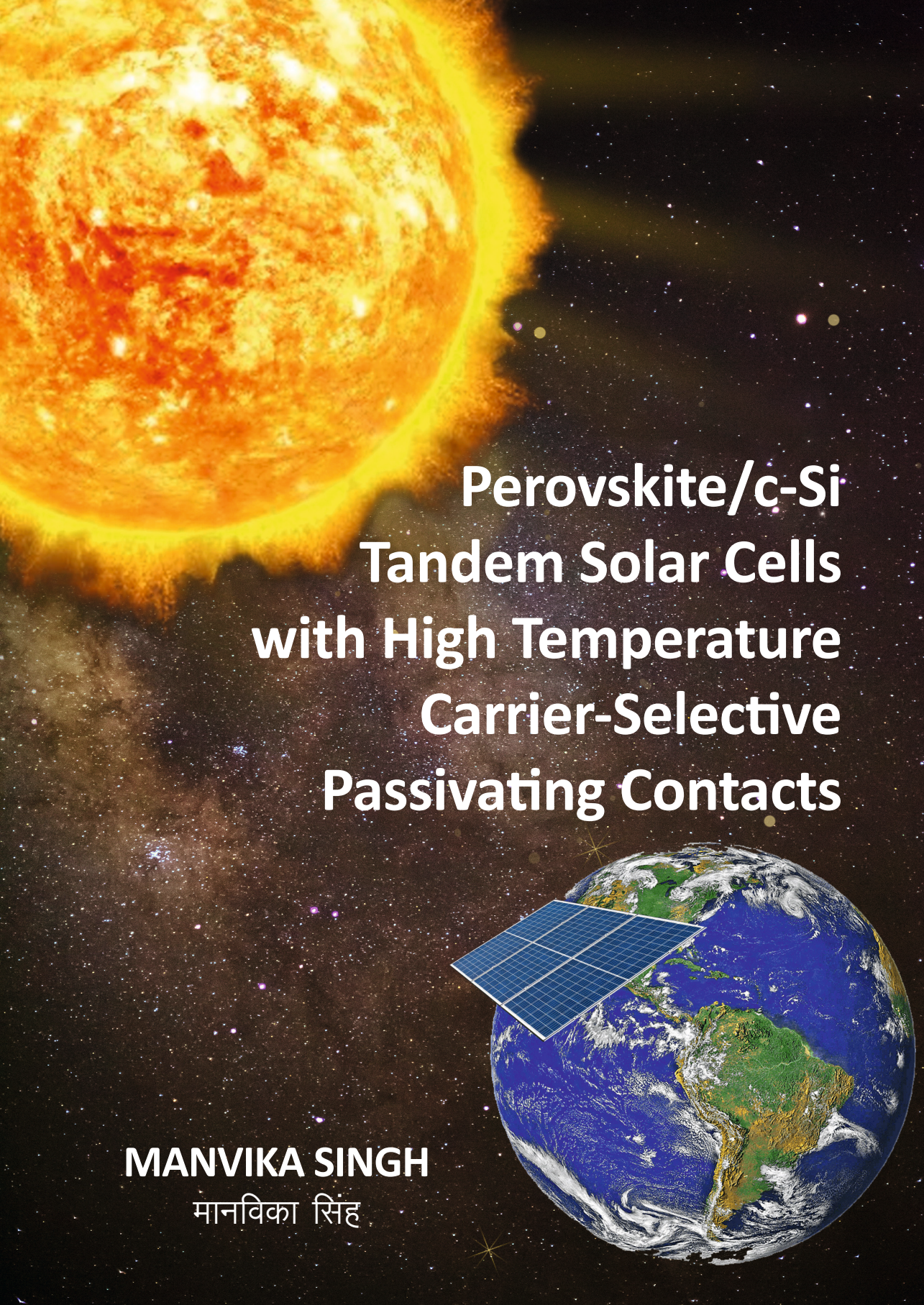
To cite this publication, please use the final published version (if applicable). Please check the document version above.

Copyright

Other than for strictly personal use, it is not permitted to download, forward or distribute the text or part of it, without the consent of the author(s) and/or copyright holder(s), unless the work is under an open content license such as Creative Commons.

Takedown policy

Please contact us and provide details if you believe this document breaches copyrights. We will remove access to the work immediately and investigate your claim.



**Perovskite/c-Si
Tandem Solar Cells
with High Temperature
Carrier-Selective
Passivating Contacts**

MANVIKA SINGH

मानविका सिंह

Perovskite/c-Si Tandem Solar Cells with High Temperature Carrier-Selective Passivating Contacts

Manvika SINGH

मानविका सिंह

Propositions

accompanying the dissertation

Perovskite/c-Si Tandem Solar Cells with High Temperature Carrier-Selective Passivating Contacts

by

Manvika SINGH

1. Alloying a material with another material can change its properties. The resulting new material can open doors to new inventions. (This thesis)
2. Modelling and experiments go hand in hand for optimization. Simulations help predict reality, while experiments bring it to life. (This thesis)
3. As the saying goes "Two heads are better than one." A tandem solar cell has a higher efficiency and yield than a single junction solar cell. (This thesis)
4. As the optimal thickness of perovskite in a tandem varies with conditions, similarly each person should find their own path in life, there is no universal solution, only what fits one's unique circumstances. (This thesis)
5. Love relations are seldom based on logic.
6. Karma suggests that actions (whether good or bad) have consequences that eventually come back to the individual either in this life or future lives. Newton's third law says that every action has an equal and opposite reaction. Karma theory in the spiritual world has similarities to Newton's third law in the scientific world.
7. Freedom is one of the most prized possession of any living being, while existence itself remains life's greatest marvel.
8. Time has the potential to change everything. It holds the power to heal, to transform wounds into wisdom and struggles into strength. Time is divine.
9. Accepting life as it unfolds, especially when it deviates from our expectations, is one of the most difficult challenges. It is in these moments that our true strength is revealed.
10. The inevitability of making choices without knowing the outcomes can make life both thrilling and daunting.

These propositions are regarded as opposable and defensible, and have been approved as such by the promotor Em. prof.dr. M. Zeman, and the promotor

Prof.dr.ir. O. Isabella.

Perovskite/c-Si Tandem Solar Cells with High Temperature Carrier-Selective Passivating Contacts

Proefschrift

ter verkrijging van de graad van doctor
aan de Technische Universiteit Delft,
op gezag van de Rector Magnificus Prof.dr.ir. T.H.J.J. van der Hagen,
voorzitter van het College voor Promoties,
in het openbaar te verdedigen op
donderdag 17 april om 10.00 uur

door

Manvika SINGH

Master of Science in Electrical Engineering,
Delft University of Technology, the Netherlands
geboren te Jabalpur, Madhya Pradesh, India

Dit proefschrift is goedgekeurd door de promotoren.

Samenstelling promotiecommissie bestaat uit:

Rector Magnificus	voorzitter
Em. prof.dr. M. Zeman	Technische Universiteit Delft, promotor
Prof.dr.ir. O. Isabella	Technische Universiteit Delft, promotor
Dr.ir. R. Santbergen	Technische Universiteit Delft, co-promotor

Onafhankelijke leden:

Prof.dr. A.W. Weeber	Technische Universiteit Delft
Prof.dr. P. Roca i Cabarrocas	École Polytechnique, France
Prof.dr. I.M.F. Gordon	IMEC, Genk, Belgium / Technische Universiteit Delft
Prof.dr. B. Stannowski	Berliner Hochschule für Technik / Helmholtz Zentrum Berlin
Prof.dr.ir. A.H.M. Smets	Technische Universiteit Delft, reservelid



Keywords: Perovskite/c-Si tandem solar cells, High temperature carrier-selective passivating contacts, Poly-SiO_x

Copyright © 2025 by M. Singh

No part of this material may be reproduced, stored in a retrieval system, nor transmitted in any form or by any means without the prior written permission of the copyright owner.

ISBN 978-94-6384-753-7

An electronic version of this dissertation is available at

<http://repository.tudelft.nl/>.

"I choose not to limit myself, embracing every challenge as an opportunity to grow, broaden my horizons, and venture beyond the conventional boundaries."

*To my beloved parents
father (Manoj Singh), mother (Rekha Singh)*

Contents

Summary	xi
Samenvatting	xiii
1 Introduction	1
1.1 Renewable Energy	1
1.1.1 Solar Energy.	3
1.2 PV fundamentals	4
1.2.1 Working of a solar cell	4
1.2.2 Recombination and surface passivation mechanisms.	7
1.2.3 Carrier-selective passivating contacts.	9
1.3 PV cell technologies	11
1.3.1 Crystalline silicon solar cells.	12
1.3.2 Perovskite solar cells	15
1.3.3 Tandem solar cells	16
1.4 Solar cell characteristics	20
1.4.1 IV and EQE	20
1.4.2 Losses in solar cell	22
1.5 Aim of the thesis	23
1.6 Outline of the thesis	23
1.7 Main contributions to the field	25
2 Modelling Approaches and Experimental Methods	27
2.1 Cell level modelling	27
2.1.1 Optical model.	27
2.1.2 Electrical model	28
2.2 Module level modelling	29
2.3 Fabrication of Poly-Si alloys passivated solar cells.	31
2.3.1 Cleaning and Texturing	31
2.3.2 Thermal Oxidation	32
2.3.3 Low Pressure Chemical Vapour Deposition (LPCVD)	33
2.3.4 Plasma Enhanced Chemical Vapour Deposition (PECVD).	33
2.3.5 RF Magnetron Sputtering	34
2.3.6 Screen Printing and Thermal Evaporation	34

2.4	Electrical Characterization methods	35
2.4.1	J-V curves	35
2.4.2	EQE	35
2.4.3	Minority carriers lifetime measurement	36
2.5	Optical characterization methods.	37
2.5.1	Photothermal Deflection Spectroscopy (PDS)	37
2.5.2	Raman Spectroscopy	38
2.5.3	Reflection-Transmission (RT) measurements	38
2.5.4	Ellipsometer	40
2.5.5	Electrochemical Capacitance Voltage (ECV) profiling	40
3	Optical characterization of poly-SiO_x and poly-SiC_x carrier-selective passivating contacts	41
3.1	Introduction	42
3.2	Experiments and methods.	44
3.2.1	Sample preparation	44
3.2.2	Characterization methods	45
3.2.3	Optical modelling.	47
3.2.4	Flowchart for extracting absorption coefficients	50
3.3	Results.	51
3.3.1	Characterization on quartz substrates	51
3.3.2	RT measurements on c-Si substrate.	54
3.4	Discussion	56
3.4.1	Absorption coefficients.	56
3.4.2	Effect of R _{CO₂} , R _{CH₄} , R _{PH₃} , and R _{B₂H₆} on Optical Properties	58
3.4.3	Effect of thickness on absorption coefficients extracted by IM	60
3.5	Conclusions.	61
4	Comparing optical performance of perovskite/silicon tandem architectures under real-world conditions	63
4.1	Introduction	64
4.2	Evaluation of optical potential of device architectures	66
4.2.1	2T perovskite/c-Si tandem solar cells	67
4.2.2	3T perovskite/c-Si tandem solar cell	69
4.2.3	4T perovskite/c-Si tandem solar cell	71
4.3	Real world conditions	72
4.3.1	Air mass	73
4.3.2	Angle of incidence	74
4.3.3	Effect of location on mono-facial tandem modules	74
4.3.4	Effect of albedo and perovskite band gap on bifacial tandem modules	77

4.3.5	Effect of location on bi-facial tandem modules	78
4.4	Discussion	78
4.4.1	Overall comparison between different perovskite/c-Si tandem architectures and CSPCs	78
4.4.2	Comparison of real-world conditions with standard test conditions	80
4.4.3	Comparison of mono-facial and bi-facial tandem solar cells .	81
4.5	Conclusions.	82
5	Poly-SiO_x passivated c-Si solar cells for perovskite/c-Si tandems	85
5.1	Introduction	86
5.2	Experimental details	87
5.2.1	Crystalline silicon (c-Si) solar cells	87
5.2.2	Perovskite/c-Si tandem solar cells.	89
5.3	Results and discussion.	90
5.3.1	Passivation properties of poly-SiO _x CSPCs	90
5.3.2	Solar cell results.	94
5.3.3	Application in four terminal (4T) perovskite/c-Si tandem solar cells	96
5.3.4	Application in two terminal (2T) perovskite/c-Si tandem solar cells	97
5.4	Conclusions.	99
6	On the annual energy yield of perovskite/silicon tandem modules with different bottom cell technologies	101
6.1	Introduction	102
6.2	Experimental	103
6.3	Simulation approach.	104
6.4	Validation	106
6.5	Input parameters and structures	108
6.6	Results and Discussion.	111
6.6.1	Energy yield at Standard Test Conditions (STC)	111
6.6.2	Energy yield in outdoor conditions	113
6.6.3	Comparison of SJ and tandem modules based on poly-SiO _x and SHJ bottom cells	118
6.7	Conclusions.	124
7	Conclusions and Outlook	127
7.1	Conclusions.	127
7.2	Outlook	129

Appendices:	130
A Comparing optical performance of perovskite/silicon tandem architectures under real-world conditions	131
A.1 Modelling approach	131
A.1.1 Cell level optical model	131
A.1.2 Module level optical model	132
A.2 Simulation input and validation	133
B Poly-SiO_x passivated c-Si solar cells for perovskite/c-Si tandems	139
References	141
Acknowledgements	177
List of Publications, Conference Contributions and Awards	179
Curriculum Vitae	183

Summary

Due to increasing population growth and industrialization, the energy demand is soaring around the world. In order to meet this energy demand and continuing with business as usual, there is an increased need for fossil fuels. Burning of fossil fuels such as coal, gas and oil lead to emission of carbon dioxide in atmosphere. Emission of carbon dioxide rises the earth's surface temperature and is leading to global warming. In order to tackle this crisis, an alternative to fossil fuels need to be investigated. In this regard, renewable energy sources are key as they can be replenished. Solar energy is one of the fastest growing and promising renewable energy sources.

Photovoltaics (PV) modules or solar panels have been installed across the world, converting solar energy into electrical energy. The PV market is dominated by single junction crystalline silicon (c-Si) solar cells. In order to improve the efficiency of single junction solar cells beyond their efficiency limit, tandem solar cells, which stack one solar cell on top of another, are being actively explored by researchers. In this work, we have focused on perovskite/c-Si tandem solar cells.

Since direct contact of metal with semiconductor leads to recombination, the concept of carrier-selective passivating contacts (CSPCs), which separates the absorber from the metal by a thin passivating layer, becomes important. The most common type of CSPCs are doped hydrogenated amorphous silicon (a-Si:H) on intrinsic amorphous silicon, as in the case of silicon heterojunction (SHJ) solar cells. The other type of CSPCs are polycrystalline silicon (poly-Si) on ultrathin silicon oxide (SiO_x) as in the case of poly-Si solar cells. Depending on the fabrication temperature of CSPCs, the former comes under low temperature CSPCs while the latter is a type of high temperature CSPCs. While low temperature CSPCs have been successfully integrated in perovskite/c-Si tandem solar cells, research involving high temperature CSPCs is less developed. In this work, high temperature CSPCs are studied, optimized and integrated in perovskite/c-Si tandem solar cells. In addition, the performance of tandem solar cells is evaluated not only in terms of efficiency but also energy yield which is more relevant for outdoor environment. In addition to poly-Si, this work explores novel materials such as polycrystalline silicon oxide (poly- SiO_x) and polycrystalline silicon carbide (poly- SiC_x) as high temperature CSPCs. This work has been divided into chapters which are described briefly below.

Chapter 1 gives the introduction to this work. It details the basic concepts

used in the work and the motivation behind using perovskite/c-Si tandem solar cells with high temperature carrier-selective passivating contacts. **Chapter 2** gives the details about the optical model used in this work to study and optimize the perovskite/c-Si tandem solar cells and modules. It also gives fabrication details of poly-Si alloys passivated c-Si solar cells in single junction and tandem applications. It also explains the various optical and electrical characterization methods used in the work.

Chapter 3 presents an optical model to extract the absorption coefficients of poly-SiO_x and poly-SiC_x CSPCs. Since these materials have mixed phase nature and weak free carrier absorption in infra-red region, their absorption coefficient cannot be measured accurately by conventional measurements setups, such as ellipsometer. In this work, a more accurate *Inverse modelling based Reflection Transmission (RT) method*, is used to extract absorption coefficients of such CSPCs. These absorption coefficients are subsequently used in the optical simulations of solar cells endowed with such CSPCs. In addition, it is shown that free carrier absorption increases with increasing the doping concentration in such CSPCs.

Chapter 4 reports an implied photo-current density of 20 mA/cm² in perovskite /c-Si tandem solar cells with poly-Si, poly-SiO_x and poly-SiC_x CSPCs along with being compatible with high temperature fabrication process. The thickness of perovskite in two terminal (2T) tandem solar cells with high temperature CSPCs are optimized for different locations. It is shown that for bi-facial tandem solar cells, a thicker or lower bandgap perovskite absorber is required to current match in 2T case. In addition, the effect of albedo is evaluated for bi-facial tandems. The optical performance of mono-facial and bi-facial 2T, three terminal (3T) and four terminal (4T) tandem architectures, has been evaluated for tandem solar cells with high temperature CSPCs.

Chapter 5 elaborates on the fabrication of 2T and 4T perovskite/c-Si tandem solar cells with poly-SiO_x CSPCs with an efficiency of 23.2% and 28.1% respectively. The passivation of p-type poly-SiO_x CSPCs on textured interfaces has been improved to 687 mV via two-step annealing process.

Chapter 6 introduces the *hybrid modelling* approach to predict the annual energy yield of 2T/4T, mono-facial/bi-facial perovskite/c-Si tandem solar modules with novel poly-SiO_x passivated c-Si solar bottom cells. Additionally, overall performance is optimized in different locations by varying the perovskite thickness and bandgap.

Chapter 7 concludes this thesis work and presents an outlook for future research directions.

Samenvatting

Door de toenemende bevolkingsgroei en industrialisatie stijgt de wereldwijde vraag naar energie sterk. Om aan deze energievraag te voldoen en bij doorgaan op de manier zoals wij tot nu toe gedaan hebben, is er meer behoefte aan fossiele brandstoffen. Het verbranden van fossiele brandstoffen zoals kolen, gas en olie leidt tot de uitstoot van koolstofdioxide in de atmosfeer. De uitstoot van koolstofdioxide verhoogt de temperatuur aan het aardoppervlak en draagt bij aan de opwarming van de aarde. Om het effect van deze opwarming aan te pakken, moet er een alternatief voor fossiele brandstoffen komen. Hernieuwbare energiebronnen zijn in dit opzicht essentieel. Zonne-energie is een van de snelst groeiende en veelbelovende hernieuwbare energiebron.

Fotovoltaïsche (PV) modules of zonnepanelen worden wereldwijd geïnstalleerd om zonne-energie direct om te zetten in elektrische energie. De PV-markt wordt gedomineerd door enkelvoudige kristallijne silicium (c-Si) zonnecellen. Om de efficiëntie van enkelvoudige zonnecellen verder te verhogen, voorbij hun theoretische efficiëntielimiet, wordt veel onderzoek en ontwikkeling gedaan aan zogenaamde tandemzonnecellen, waarbij één zonnecel bovenop een andere gestapeld wordt. In dit proefschrift richten we ons op perovskiet/c-Si tandemzonnecellen.

Aangezien direct contact tussen metaal en halfgeleider leidt tot recombinatieverliezen, is het concept van ladingsdrager-selectieve passiverende contacten (CSPCs, afkorting van het Engelse carrier-selective passivating contacts), waarbij tussen de absorber en het metaalcontact een dunne passiverende laag aangebracht wordt, van groot belang. Het meest voorkomende type CSPC bestaat uit een gedoteerde gehydrogeneerde amorf silicium (a-Si) laag op een intrinsieke amorf silicium laag, zoals bij silicium heterojunctie (SHJ) zonnecellen. Een ander type CSPC bestaat uit een polykristallijn silicium (poly-Si) laag op ultradun siliciumoxide (SiO_x) laag, zoals bij zogenaamde TOPCon Si zonnecellen. TOPCon staat voor Tunnel Oxide Passivated Contact. Afhankelijk van de fabricagetemperatuur van CSPCs vallen de eerstgenoemde onder lage-temperatuur CSPCs, terwijl de laatstgenoemde een type hoge-temperatuur CSPC is.

Hoewel lage-temperatuur CSPCs succesvol zijn geïntegreerd in perovskiet/c-Si tandemzonnecellen, is de ontwikkeling van hoge-temperatuur CSPCs minder ver. In dit werk worden hoge-temperatuur CSPCs bestudeerd, geoptimaliseerd en

geïntegreerd in perovskiet/c-Si tandemzonnecellen. Daarnaast wordt de prestatie van tandemzonnecellen niet alleen geëvalueerd op basis van efficiëntie, maar ook op basis van energieopbrengst, wat relevanter is voor daadwerkelijk toepassing in een buitenomgeving. Naast onderzoek aan poly-Si voor TOPCon cellen omvat dit proefschrift ook onderzoek aan nieuwe materialen zoals polykristallijn siliciumoxide (poly-SiO_x) en polykristallijn siliciumcarbide (poly-SiC_x) als hoge-temperatuur CSPCs. Deze thesis is opgebouwd uit verschillende hoofdstukken, waarvan de inhoud hieronder kort beschreven wordt.

Hoofdstuk 1 geeft een inleiding op dit werk. Het bespreekt de basisconcepten die in dit onderzoek gebruikt worden en de motivatie achter het gebruik van perovskiet/c-Si tandemzonnecellen met hoge-temperatuur ladingsdragerselectieve passiverende contacten. **Hoofdstuk 2** beschrijft details over het optische model dat in dit werk gebruikt wordt om de perovskiet/c-Si tandemzonnecellen en -modules te bestuderen en te optimaliseren. Het geeft ook fabricagedetails van c-Si-zonnecellen met CSPCs op basis poly-Si en poly-Si-legeringen en dat in enkelvoudige en tandemtoepassingen. Daarnaast worden de verschillende optische en elektrische karakteriseringsmethoden die in het werk gebruikt zijn, toegelicht.

Hoofdstuk 3 presenteert een optisch model om de absorptiecoëfficiënten van poly-SiO_x en poly-SiC_x CSPCs te extraheren. Aangezien deze materialen een gemengde fase hebben en een zwakke absorptie door vrije ladingsdragers in het infraroodgebied vertonen, kunnen hun absorptiecoëfficiënten niet nauwkeurig worden gemeten met conventionele meetopstellingen, zoals een ellipsometer. In dit werk wordt een nauwkeurigere methode, gebaseerd op inverse modellering en reflectie-transmissie (RT), gebruikt om de absorptiecoëfficiënten van dergelijke CSPCs te bepalen. Deze absorptiecoëfficiënten worden vervolgens gebruikt in de optische simulaties van zonnecellen met dergelijke CSPCs. Bovendien wordt aangetoond dat de absorptie door vrije ladingsdragers toeneemt bij een hogere dotering in deze CSPCs.

Hoofdstuk 4 beschrijft bij een impliciete foto-stroomdichtheid van 20 mA/cm² het gedrag van perovskiet/c-Si tandemzonnecellen met poly-Si, poly-SiO_x en poly-SiC_x CSPCs, en die zijn aangebracht met het hoge-temperatuur fabricageproces. De dikte van de perovskietlaag in twee-terminal (2T) tandemzonnecellen met hoge-temperatuur CSPCs is geoptimaliseerd voor toepassing op verschillende locaties. Er is aangetoond dat voor bifaciale tandemzonnecellen een perovskietabsorber met een dikkere laag of lagere bandkloof nodig is om de stroom in de 2T-configuratie te laten overeenkomen. Daarnaast wordt het effect van albedo geëvalueerd voor bifaciale tandemzonnecellen. De optische prestaties van mono-faciale en bi-faciale 2T, drie-terminal (3T) en vier-terminal (4T) tandemarchitecturen zijn geëvalueerd voor tandemzonnecellen met hoge-temperatuur

CSPCs.

Hoofdstuk 5 gaat dieper in op de fabricage van 2T en 4T perovskiet/c-Si tandemzonnecellen met poly-SiO_x CSPCs waarbij efficiënties van respectievelijk 23,2% en 28,1% behaald zijn. De passivering van p-type poly-SiO_x CSPCs op getextureerde oppervlakken is verbeterd en heeft via een twee-staps warmtebehandeling tot 687 mV.

Hoofdstuk 6 introduceert de hybride modelleringsaanpak om de jaarlijkse energieopbrengsten van 2T/4T, mono-faciale/bifaciale perovskiet/c-Si tandemzonnepanelen met nieuwe poly-SiO_x gepassiveerde c-Si zonnecellen aan de onderzijde te voorspellen. Daarnaast wordt de algehele prestatie geoptimaliseerd voor toepassing op verschillende locaties door de dikte en bandkloof van de perovskiet te variëren.

Hoofdstuk 7 concludeert dit proefschrift en biedt een vooruitblik op toekomstige onderzoeksrichtingen.

1

Introduction

1.1. Renewable Energy

Due to the increasing population, industrialization, civilization and economic growth, there has been a rise in demand for energy sources. Currently, most of the energy demand of the world is met by fossil fuels [1]. Fossil fuels such as coal, gas and oil are exhaustible carriers of stored energy and will get depleted in future [2]. Moreover, burning of energy sources based on fossil fuels emits greenhouse gases such as carbon dioxide, methane etc. which trap radiated heat from earth's surface and increase earth's surface temperature [3–5]. Emission of greenhouse gases poses a threat to environment, climate and human beings [6]. Figure 1.1 shows annual world emission of CO₂ from fossil fuels and industry. It clearly shows the increasing trend in CO₂ emission which is a threat to the environment and people of this planet.

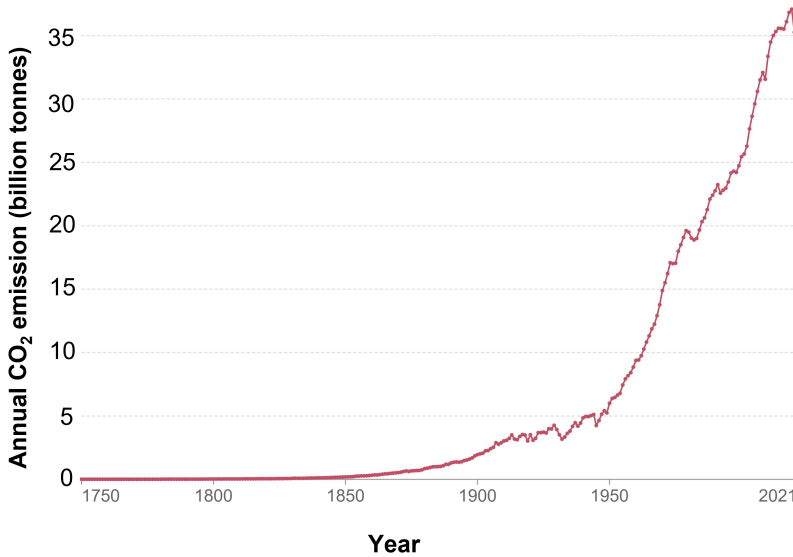
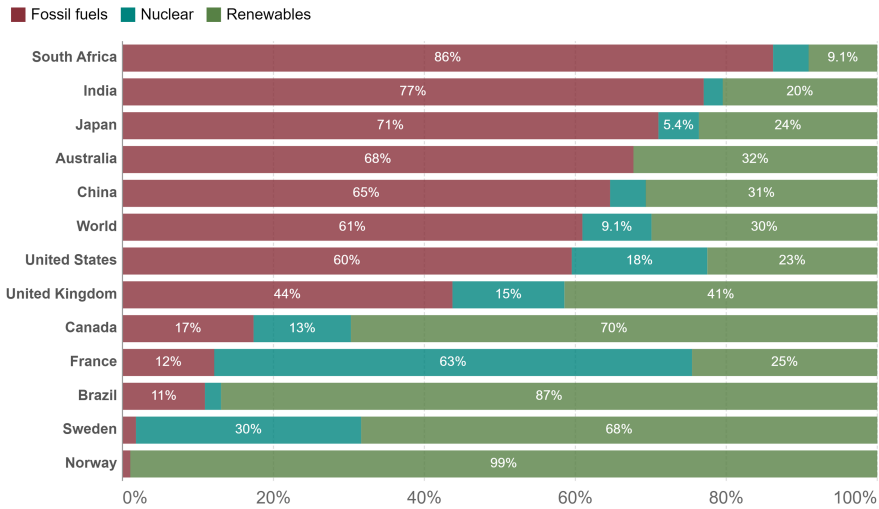


Figure 1.1: Annual world CO₂ emissions from fossil fuels and industry. Taken from [7].

The rising levels of greenhouse gases, leading to global warming and climate change, have been a major environmental, social and economic issue. Global warming is leading to polar ice caps and glaciers melting and rising sea level. In order to tackle these energy and environmental crises, renewable energy sources such as solar, wind, hydro and biomass have been introduced to generate electricity alongside efforts to electrify societal activities as much as possible[3, 4, 8]. Renewable energy sources are environmentally clean as they can generate power with almost no emission of air pollutants and are available in abundance in nature. Renewable energy is important for sustainable and eco-friendly generation of electricity. Figure 1.2 shows the electricity consumption from fossil fuels, nuclear and renewable energy around the world and various different countries in 2022. From Figure 1.2, we find that 30% of the world's electricity consumption is met by renewable energy in 2022, although there are large difference from country to country. In order to increase the use of renewable energy for meeting world's energy demand, the governments, scientists, environmentalists and citizens around the globe need to be aware and put efforts together. In this work, we have focused on one of the promising and reliable renewable energy sources, solar energy.



ELECTRICITY CONSUMPTION FROM FOSSIL FUELS, NUCLEAR AND RENEWABLE ENERGY (%)

Figure 1.2: Electricity consumption from fossil fuels, nuclear and renewable energy, 2022. Taken from [7].

1.1.1. Solar Energy

Solar energy is derived from the sun which is an abundant, everlasting and free source of energy. The annual solar radiation received by earth is 3,400,000 EJ which is much higher than the annual world's total primary energy consumption (620 EJ) [9, 10]. Solar energy is clean, eco-friendly and renewable form of energy which can be beneficial for the environment and society [11]. It is not accompanied by release of greenhouse gases. Solar technologies are more labour intensive as compared to fossil fuels. Hence, solar industry will also help producing more job opportunities in future. Above reasons make solar energy one of the best options for meeting future energy demand [11]. However, solar energy has some limitations such as high system costs and being available only during daytime. Researchers are making the conversion process of usable energy from renewable energy more efficient and overcoming their limitations. There are various solar technologies, such as solar thermal energy, concentrated solar power and PV technology. Among solar technologies, Photovoltaic (PV) technology is one of the fastest growing market and will play an important role in meeting future energy demand of the world [12, 13]. In 2022, investments in photovoltaics increased by 47% to 301.5 billion which accounts for 60% of the renewable energy investment

[14, 15]. Figure 1.3 shows the cumulative world photovoltaic installations from 2010 to 2023. The growth in world photovoltaic installations is exponential which clearly shows enormous potential in this technology and the efforts taken around the world to harvest solar energy. In the following sections, some of these PV technologies are discussed in more detail.

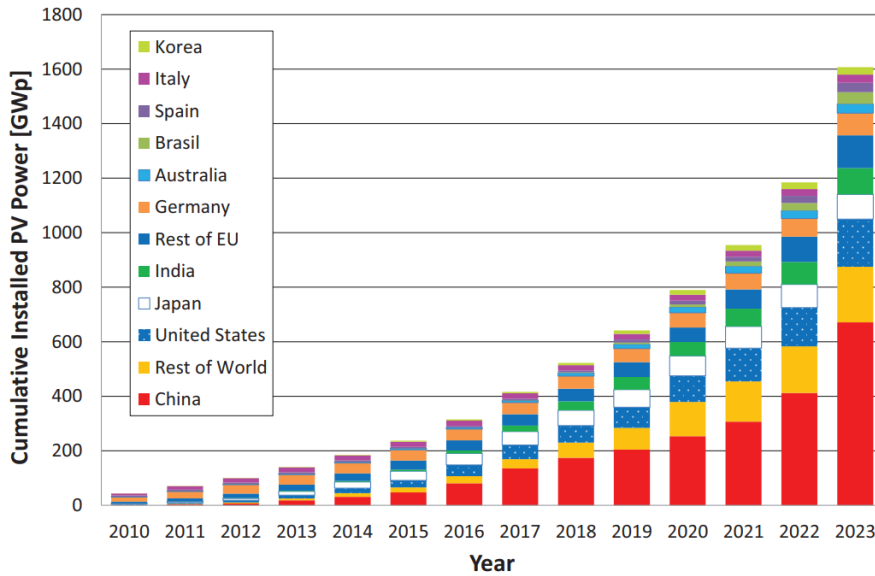


Figure 1.3: Cumulative photovoltaic installations from 2010 to 2023. Taken from [14–16].

1.2. PV fundamentals

1.2.1. Working of a solar cell

In order to understand the working of solar cell, the electronic band theory of a material needs to be studied. According to that theory, a material can be classified into metal, semiconductor and insulator. The energy bands are available energy levels of electrons in a material. The valence band is the energy band of electrons in atomic shell's outermost orbitals. The conduction band is the energy band of free electrons. These free electrons contribute to the electrical conductivity of the material. The difference between the highest occupied energy level in valence band and lowest unoccupied energy level in conduction band is called bandgap of the material. In metals, the valence and conduction band are overlapping and so metals have high electrical conductivity. Whereas in insulators, the bandgap is large and the electrons cannot be excited from the valence band to the conduction band. In semiconductors, the bandgap is relatively small and an external

energy, such as that of photons can excite electrons from the valence band to the conduction band, liberating electrons from localized bonds and making it mobile. In a direct bandgap semiconductor, the highest point of the valence band and the lowest point of conduction band are aligned at the same momentum value in k -space. For the electrons to be excited from the valence to the conduction band in a direct bandgap semiconductor, only the energy of photons is required. That is, no additional momentum transfer from the lattice via phonon to the electron is required to excite that electron from the valence to the conduction band. On the other hand, in an indirect bandgap semiconductor, the highest point of the valence band and the lowest point of the conduction band are not aligned in the k -space. For an electron to get excited from the valence band to the conduction band in an indirect semiconductor, energy provided by the photon and additional momentum provided from vibrations of crystal lattice or phonons are required. Gallium Arsenide (GaAs) is a direct bandgap semiconductor whereas crystalline silicon (c-Si) is an indirect bandgap semiconductor.

A solar cell is basically a p-n junction diode made of semiconductor material or materials. Here, we take crystalline silicon (c-Si) as the semiconductor material. Semiconductors can be doped to form n-type and p-type materials. Doping is achieved by adding impurity atoms to the intrinsic semiconductor. For example, when phosphorus atoms replace some silicon atoms in the crystal lattice, each phosphorus atom has five valence electrons and it bonds with four silicon atoms but the fifth electron is weakly bond and at room temperature, the thermal energy is enough to excite it to the conduction band. Hence, a phosphorus atom is a n-type dopant because it introduces extra electrons when it bonds with silicon atoms, resulting in n-type c-Si, whereas a boron atom is a p-type dopant as it creates excess *holes* when it bonds with silicon atoms, resulting in p-type Si. The p-type and n-type materials, together form the p-n junction which has p-type and n-type regions. There are excess electrons in the n-type region and excess holes in the p-type region. That is, the majority carriers in an n-type region are electrons and the minority charge carriers are holes. The opposite is true for a p-type region.

A solar cell converts solar energy (energy from photons) directly into electrical energy. This process consists of three steps [17]. The first step is the generation of photo-generated charge carriers upon absorbing photons. If the energy of the absorbed photons is greater than the bandgap energy of the semiconductor, the absorbed photons generate mobile charge carriers i.e. liberating electrons from a bond leaving a hole (electron-hole pairs). For a solar cell to have high efficiency, it becomes important to separate these electron-hole pairs in a solar cell to prevent recombination, which would otherwise reduce the cell's performance. The second step in the working of a solar cell is thus the separation of the photo-generated

charge carriers.

In dark condition, there is diffusion of electrons from high concentration (n-type) to lower concentration (p-type) region in a p-n junction, as shown in figure 1.4. Holes move in the opposite direction (from p-type to n-type) due to diffusion. This process leaves positively charged donor atoms near the junction in the n-type region and negatively charged acceptor atoms in the p-type region. These ionized atoms are fixed atoms that have gained or lost electrons resulting in a net electrical charge. Depletion of mobile carriers due to diffusion leads to formation of depletion region or space charge region. The formation of the depletion region gives rise to electric field. Due to this electric field, drift force starts acting on electrons and holes. The electrons move from p-type region to n-type region and holes move from n-type region to p-type region due to drift force. The movement of electrons and holes due to diffusion and drift forces is shown in figure 1.4. This electric field gives rise to built in potential voltage. In dark, the diffusion and drift force balance each other.

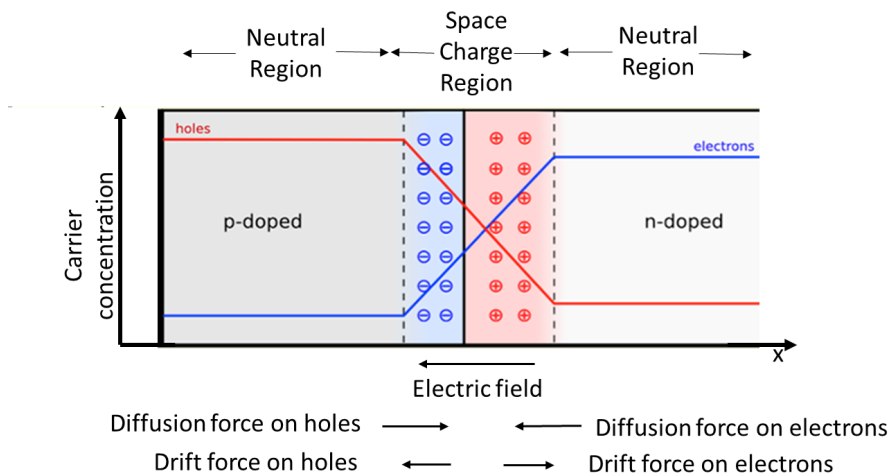


Figure 1.4: A pn junction diode showing the effect of diffusion and drift forces on electrons and holes.

Under illumination condition, when excess electron-hole pairs are created due to absorption of photons, the concentration of minority carriers increases manifolds whereas the majority carriers are also created but their concentration does not change significantly in the p-type and n-type regions. As shown by Wur-fel et al. in Ref. [18], the difference in conductivity of holes and electrons in p-type and n-type regions is the reason for separation of charge carriers in an illuminated

solar cell [19]. The higher conductivity of majority carriers and lower conductivity of minority carriers in the n-type and p-type regions is the decisive factor for selective transport of electrons and holes to their respective terminals [18]. This conductivity difference in a p-n junction is realized by manipulating the concentrations of electrons and holes by doping. For non-homojunction architectures such as the p-i-n heterojunction semiconductor wherein an intrinsic absorber is sandwiched between high bandgap *transport layers*, this conductivity difference is achieved by doping the so-called *transport layers* [18]. Additionally, the large bandgap of transport layers makes them transparent to the incident sunlight which helps them to avoid an increase in the minority carrier concentration by illumination. So, p-i-n heterojunction is able to maintain the lower conductivity for minority carriers even under illumination unlike the p-n homojunction case. More information about such CSPCs can be found in Ref. [18, 20]. Section 1.2.3 explains the important concept of carrier-selective passivating contacts (CSPCs).

The third step in the working of a solar cell is the collection of charge carriers in doped layers. The electrical contacts, such as metal electrodes, connect the solar cell to the external circuit, allowing the flow of current. These solar cells are connected in series or parallel via their contacts to form a module. These modules are placed in outdoor environment to convert solar energy into electrical energy.

Figure 1.5 shows the working of a solar cell. Here, photons are absorbed as much as possible in the absorber, generating electron-hole pairs. The charge carriers are separated by formation of electron and hole selective regions. The electron selective region, due to its higher electron concentration achieved by doping, has much higher conductivity for electrons than holes. Opposite is true for hole selective region.

1.2.2. Recombination and surface passivation mechanisms

There are various recombination mechanisms which deteriorate the performance of a solar cell [17]. The recombination rate in an illuminated solar cell is determined by the recombination of minority charge carriers as illumination increases the concentration of minority charge carriers in a solar cell. Hence, minority carrier lifetime is related to recombination and plays an important role in determining the efficiency of the solar cell. Minority carrier lifetime is the average time a carrier can stay in an excited state before it gets recombined. One of the recombination types is radiative recombination which is mainly seen in direct bandgap semiconductors such as GaAs. In radiative recombination, the electron transitions from an energy level in the conduction band to one in the valence band, emitting a photon and thus instead of occupying an energy level in conduction band, it occupies an energy level in the valence band.

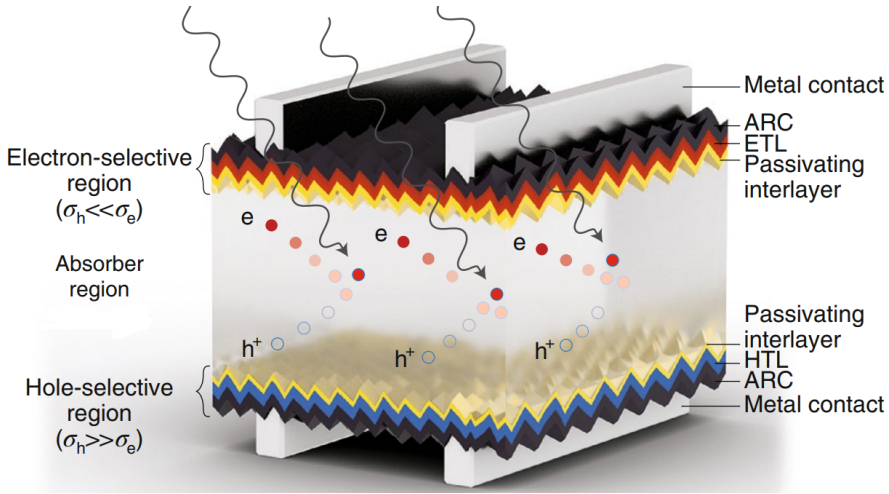


Figure 1.5: Working of a solar cell. Absorbed photons (shown in the form of wavy arrows) in solar cell absorber generate electrons (red) and holes (blue). The electron conductivity (σ_e), is much higher in electron-selective region, due to higher electron concentration achieved by doping, whereas the hole conductivity (σ_h), is much higher in the hole selective region, due to higher holes concentration achieved by doping. Generated electrons and holes move towards their respective contact via formation of charge carrier selective regions. ARC stands for anti reflection coating, ETL stands for electron transport layer and HTL stands for hole transport layer. Taken from [21].

The other type of recombination is non-radiative recombination in which an electron and hole recombine and the excess energy is emitted as heat or lattice vibrations instead of a photon. This type of recombination is more dominant in indirect bandgap semiconductors. There are several types of non-radiative recombination, including Auger recombination and Shockley-Read-Hall Recombination (SRH). In Auger recombination, the electrons and holes recombine giving away the energy and momentum to excite a third particle which could be an electron or hole. This third particle, electron (hole), is excited to a higher (deeper) level in electronic band and then falls back (thermalization) to the valence band giving away phonon modes [17]. Auger recombination is dominant in heavily doped silicon as more particles are present and the probability of three particle process increases. SRH recombination is facilitated by impurity atoms (dopants) or lattice defects. These defects act as recombination centres introducing energy level within the bandgap. In SRH recombination, an electron transitioning via the bandgap gets trapped in these defects and recombines with a hole. This non-radiative recombination releases excess energy in the form of heat in lattice. SRH recombination is also called as trap assisted recombination. It is dominant in moderately doped silicon. Surface recombination is SRH recombination at the surface of silicon. There is a large density of states within the bandgap (defects),

on the surface of silicon which acts as trap. These defects on surface of silicon are created due to disruption in periodicity of crystal lattice of silicon and lead to dangling bonds which are basically unsatisfied valence electrons. The rate at which recombination takes place on surface of silicon is called as surface recombination velocity (SRV).

In order to passivate the defects and dangling bands at the surface of silicon, it is crucial that surface passivation techniques are applied [22, 23]. There are two types of passivation techniques that are used to reduce surface recombination in c-Si solar cells. These are chemical passivation and field effect passivation. Chemical passivation is achieved by growing a dielectric layer which reduces interface defect densities [22, 24]. Silicon dioxide is one of the most common passivation layer grown/deposited on surface of c-Si to passivate defects and dangling bonds [22–24]. Also, hydrogenated intrinsic amorphous silicon (a-Si:H) is commonly used to provide chemical passivation in c-Si solar cells [25, 26]. In field effect passivation, surface carrier concentration is modified to reduce recombination and so it can be called as charge assisted population control [19, 27]. In this context, population refers to the number of charge carriers (electrons or holes) at the surface of the silicon. This modification of surface concentration is achieved by depositing a dielectric layer with fixed charges such as silicon nitride (SiN_x) [28, 29] and aluminium oxide (Al_2O_3) [30]. Since, the above mentioned layers have high number of positive and negative fixed charges respectively. They lead to reduction of one of the charge carriers in the underneath silicon leading to a reduction of SRV [24]. This type of surface passivation has been shown in regions I and II in figure 1.6. The other way to modify the surface carrier concentration is to implement a doping profile at front or rear silicon surface, underneath the metal contacts, to either create a high-low junction (n^+n or p^+p) or p-n junction [23] (See regions III and IV in figure 1.6). As explained in section 1.2.1, creation of such junction helps to repel minority charge carriers from the front or rear surface of silicon.

1.2.3. Carrier-selective passivating contacts

The PV market is dominated by crystalline silicon (c-Si) solar cells and modules [21, 32]. One type, known as Al-BSF (aluminum back surface field) cells, features an entire rear side of the silicon absorber alloyed with aluminum (See figure 1.7 (a)). Due to direct contact of the metal with the absorber in Al-BSF solar cells, there is huge recombination which limits the efficiency. Al-BSF solar cells are not manufactured anymore. The other type of commercially manufactured c-Si solar cells are a group of PER(X) cells, which includes variations like PERC/PERL/PERT (passivated emitter and rear cell/ passivated emitter and rear

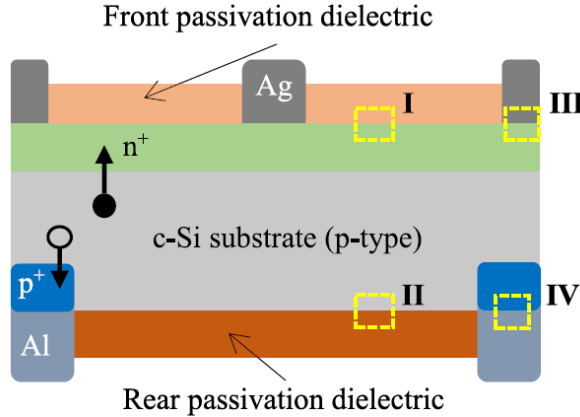


Figure 1.6: Possible interfaces for passivation in a c-Si solar cell. Regions I, II: Front and rear side passivation with a dielectric layer. Regions III, IV: Increasing the doping level under the metal contacts to form a high-low junction. Taken from [31].

locally-diffused/passivated emitter and rear totally-diffused) cells. In all PER(X) cells, there is additional back surface passivation layer of $\text{AlO}_x/\text{SiN}_x$ and the contact area between metal and absorber is reduced. In PERL cells, there is additional high doping at the metal contact which act as localized BSF. In PERT cells, the entire rear side of the absorber is doped instead of localized regions. In PERC cells (See figure 1.7 (b)), rear side openings need to be formed in the passivated contact which could damage the bulk Si [33]. Also, the carriers have to travel longer paths due to localized metal contacts. In order to mitigate recombination due to direct contact between the metal and the absorber, the concept of carrier-selective passivating contacts (CSPCs), where the CSPC is separated from the silicon absorber material, was introduced in solar cells [21].

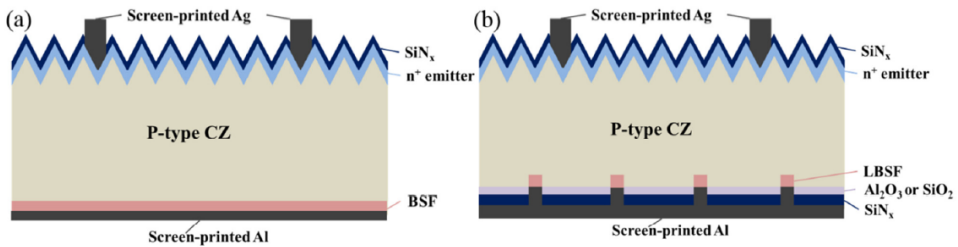


Figure 1.7: (1) Al-BSF (2) PERC. Taken from [33].

A carrier-selective passivating contact, as the name suggests, has the dual purpose of passivating surface defects and allowing one type of charge carrier to pass through while blocking the other type of charge carrier [34]. This type of

carrier-selectivity is achieved by difference in conductivity for holes and electrons, i.e. higher conductivity towards one type of charge carrier than other type of charge carrier [18]. The difference in conductivity for electrons and holes in CSPCs ensures that one type of charge carrier (majority carrier) can move easily, while the other type (minority carrier) is suppressed. This phenomenon is typically achieved by doping the material to create regions with different carrier concentrations, which facilitates the selective transport. More details about such CSPCs can be found in Ref. [18, 20]. The CSPC physically separates the c-Si absorber from the metal along with passivating defects. A good CSPC has low contact resistivity, high selectivity and high passivation [34]. It should also follow optical guidelines such as optical transparency which is affected by thickness. Also, doping affects the free carrier absorption (FCA) in such CSPCs.

A good CSPC should maximize the flow of majority carriers and suppress the flow of minority carriers to the contact [21]. The contact resistance, ρ_{contact} , affects the majority carrier collection at the contact. The flow of minority carriers to the majority contact would lead to recombination. This recombination can be measured by the recombination current density, J_0 . Thus, a good CSPC should have a low ρ_{contact} and a low J_0 . If a CSPC is only passivating and not selective, as shown in figure 1.8 (a), (band diagram of n-type Si with wide bandgap Al_2O_3) it will have a low conductivity even towards the majority carriers. Direct contact between a metal and semiconductor leads to recombination, as shown in figure 1.8 (b). The band diagram of a passivating and selective contact is shown in figure 1.8 (c). Here, the conduction band of the two materials are aligning but the valence bands of the two materials are not aligning. The valence band offset is induced by the reduced hole concentration at the interface of the two materials. This valence offset causes selectivity of electrons [35].

In order to avoid direct contact of metal and silicon, commonly used passivating thin films are silicon oxide (SiO_x) or hydrogenated amorphous silicon (a-Si:H). However, some of the problems associated with a-Si:H are the optical absorption losses, thermal instability and defect formation when annealing for longer time [20]. Since, a-Si:H is fabricated at low temperature ($< 200^\circ\text{C}$), it can be classified as a low temperature CSPC. Poly-Si, poly- SiO_x and poly- SiC_x are high temperature CSPCs as they require higher annealing temperature (800°C - 1000°C). The above mentioned CSPC have sufficiently low J_0 and ρ_{contact} and provide excellent passivation [21, 36–39] and selectivity.

1.3. PV cell technologies

There are various types of PV cell technologies for terrestrial applications. One major category includes the wafer based c-Si solar cells such as mono and multi

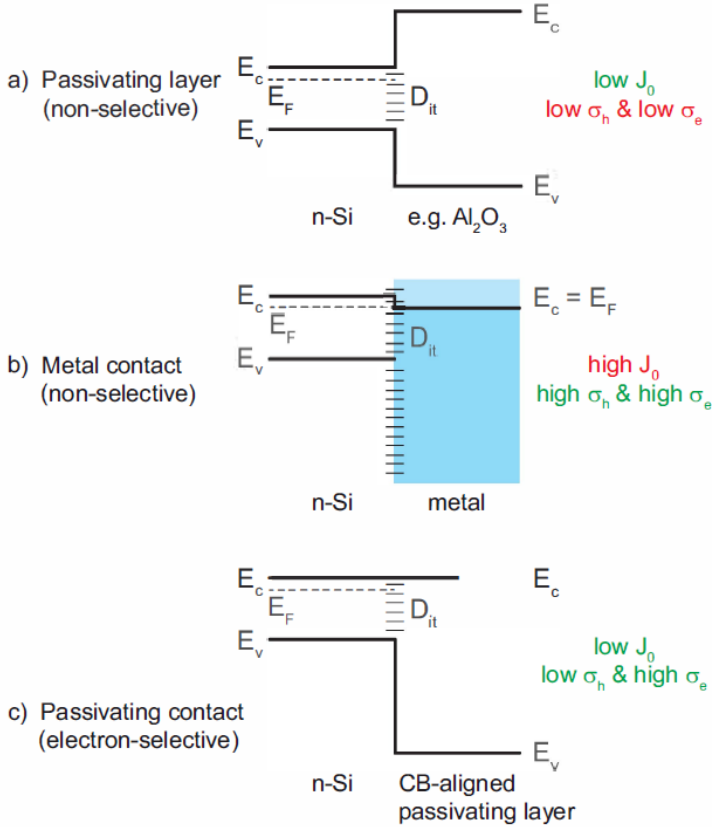


Figure 1.8: Idealized equilibrium band diagrams of (a) n-type Si with passivating layer, Al_2O_3 (b) n-type Si with metal (Unoccupied/occupied states indicated in light/dark blue) (c) n-type Si with electron selective layer. D_{it} denotes the interface defect density at the Si surface. Taken from [35].

c-Si. Thin film solar cells such as hydrogenated amorphous silicon (a-Si:H), Cadmium Telluride (CdTe) and copper indium gallium selenide (CIGS) are another category. There are other PV cell technologies such as organic PV and perovskite solar cells. In the following section, PV cell technologies such as c-Si, perovskite solar cells and tandems are introduced.

1.3.1. Crystalline silicon solar cells

Various c-Si solar cells have reported efficiencies greater than 25% [40–45]. These cells have CSPCs which provide them excellent passivation and carrier selectivity. One such type of solar cell is Silicon Heterojunction (SHJ) which incorporates intrinsic hydrogenated amorphous silicon (a-Si:H(i)) to passivate the surface

defects and n and p-type doped hydrogenated amorphous silicon ((a-Si:H(n)), (a-Si:H(p))) for carrier-selectivity. Various architectures exist in c-Si solar cells according to contacting schemes. Different architectures of SHJ solar cells are shown in figure 1.9. If the CSPCs are on the front and rear side of the solar cell, it is called as front back contacted (FBC) solar cell. FBC solar cells can be further categorized as front or rear junction solar cells. When the minority carrier-collecting contact is on the front side of the wafer, it is called as front junction. In a n-type c-Si solar cell, holes are the minority carriers and front junction has a-Si:H(p) layer on the front side of the cell as shown in figure 1.9(a). Similarly, in a rear junction solar cell, the minority carrier-collecting contact is on the rear side of the solar cell as shown in figure 1.9(c). The front CSPCs absorb light before it reaches the c-Si absorber which leads to reduction in the current of the solar cell. Also, the metal contacts on the front side reflect light leading to shading losses. In order to reduce this parasitic absorption and shading losses, both the front CSPCs and metal contacts are moved to the rear side in an Interdigitated back contacted (IBC) solar cell (See figure 1.9(d)). Solar cells can also be classified as mono-facial and bi-facial solar cells. In a mono-facial solar cell, the metal fully covers the rear side of the solar cell. In order to collect light from both surfaces in the solar cell, the full area coverage of the rear side metal can be reduced such that the light can also be incoming from rear side after being reflected from the ground surface. Such cells are called bi-facial solar cells (See figure 1.9(b),(c) and (d)).

The other approach of using CSPCs in c-Si solar cells is by replacing a-Si with polycrystalline (poly-Si) and inserting a thin layer of silicon oxide in between c-Si and poly-Si. These poly-Si passivating contacts with ultra-thin silicon oxide layer are called tunnel oxide passivating contacts (TOPCon). TOPCon solar cell architecture, along with its band diagram is shown in figure 1.10. Similar to SHJ solar cells, TOPCon solar cells can also be categorized into front junction FBC, rear junction FBC, IBC, mono-facial and bi-facial solar cells. Poly-Si passivating contacts have higher temperature stability and are compatible with current high temperature industrial processes [47, 48]. Since, their fabrication process is similar to PERC processing, it is easier to transfer from PERC to TOPCon [49]. For SHJ, completely different equipment is needed.

Phosphorus-doped poly-Si passivating contacts have less contact resistivity [52–56] and are more conductive than a-Si passivating contacts. However, the drawback is parasitic absorption and free carrier absorption in these poly-Si passivating contacts [57, 58]. The high FCA is due to the high doping in these contacts which is necessary to achieve good carrier-selectivity [38, 59]. One way to reduce this absorption is to use thin poly-Si [60]. The tunneling oxide underneath poly-Si can be damaged during the deposition of additional layers (transparent conductive oxide (TCO) or metal contact). Especially for a thin poly-Si layer, the

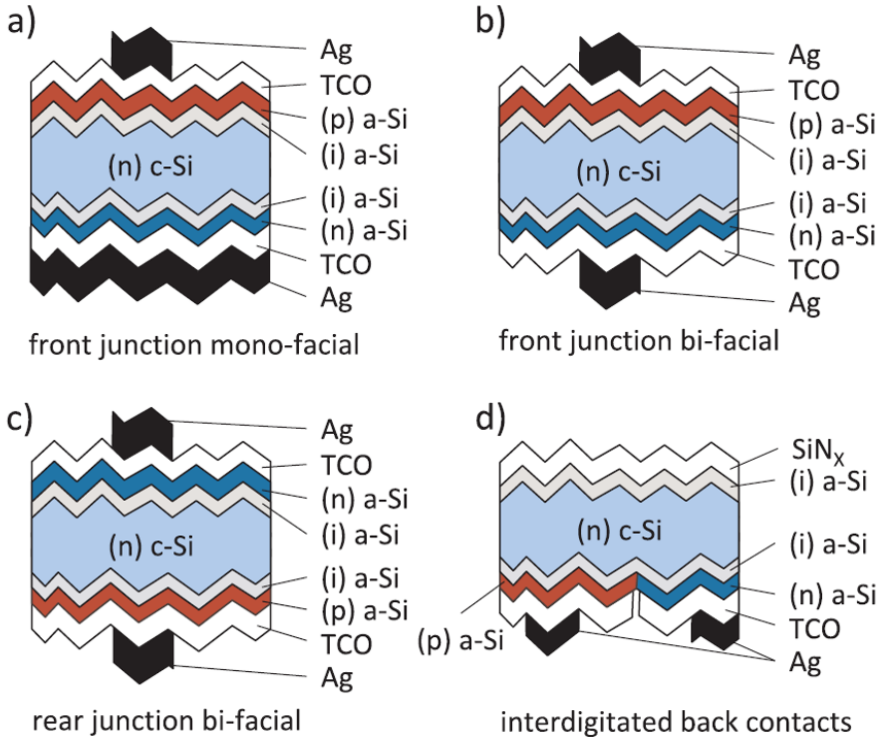


Figure 1.9: Device architectures of SHJ solar cells (a) Front junction mono-facial (b) front junction bi-facial (c) rear junction bi-facial (d) interdigitated back contacts (IBC). Taken from [46].

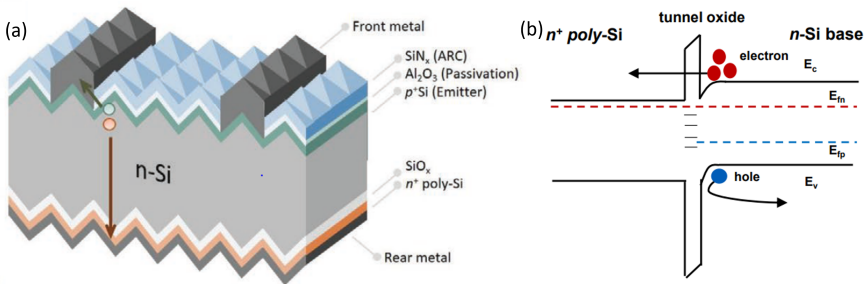


Figure 1.10: (a) TOPCon architecture (b) Band diagram of n-type poly-Si based carrier-selective passivating contact. Taken from [50, 51].

damage of the oxide can occur during TCO and metal deposition as well. In case of a thicker polySi layer, potential damage during TCO (or metal) deposition will be less. Also, thin poly-Si can be easily damaged by screen printed metallization [60]. An alternative is to alloy the poly-Si with oxygen and carbon to form poly-SiO_x

and poly-SiC_x [60]. By changing the oxygen and carbon content in these CSPCs, its bandgap can be tuned. This can help increasing its' bandgap and making it more transparent which can help more light to reach the c-Si absorber. Research shows that using poly-SiO_x CSPCs can also help improving band bending and carrier-selectivity [38, 61]. Various high efficiency solar cells have been fabricated with the poly-Si based high temperature CSPCs [38, 62–68].

Figure 1.11 shows the world market share of different PV cell technologies. Al-BSF cells have been largely phased out in commercial production in favor of more efficient technologies, particularly PERC and TOPCon cells. However, market share of PERC cells show a declining trend as they are getting replaced by TOPCon cells which offer higher efficiency [69, 70]. The rear side contacted cell forms a small percentage in the world market share which shows the supremacy of front back contacted solar cell technologies in terms of market share. Although SHJ shows an increasing trend (from 8% in 2024 to 20% in 2034), it does not play a primary role in the world market share due to slightly higher CapEx than TOPCon production lines. Complex processing steps, high cost, requirement of major change in current cell processing are some of the factors that are responsible for a lower market share of IBC solar cells [69]. According to ITRPV 2024 data, TOPCon technologies are currently dominating the market and will continue to do so in the upcoming years. The tandem technology is expected to play a role in the market share in the upcoming years. Hence, it becomes important to study and investigate high temperature CSPCs that can be incorporated into tandem solar cells, which is also the focus of this work.

1.3.2. Perovskite solar cells

Generally, perovskites have the formula ABX₃, where 'A' and 'B' are cations and 'X' is anion. In solar cells, two types (i) alkali and (ii) organic-inorganic based halide perovskites are generally used. In alkali based halide perovskites, 'A' could be cesium, rubidium, potassium, sodium or lithium. In organic-inorganic based perovskites, 'A' is an organic cation, generally methylammonium, ethyl ammonium or formamidinium or a mixed cation. 'B' is a divalent cation such as lead, tin or germanium. 'X' is a halogen anion i.e. bromine, chlorine, iodine or fluorine. Methyl ammonium lead iodide is one of the commonly used perovskite solar cell. Some of the advantages of perovskite solar cells are the high absorption coefficient [72] of perovskite material, wide tunable bandgap [73], long diffusion length [74], high charge carrier mobility, ease of fabrication, low cost [75] etc. The wide tunability of perovskite bandgap makes it useful for multijunction solar cells. Perovskite solar cells have poorer stability as compared to silicon which is a hindrance in commercialization of perovskites. Most of the reported perovskite

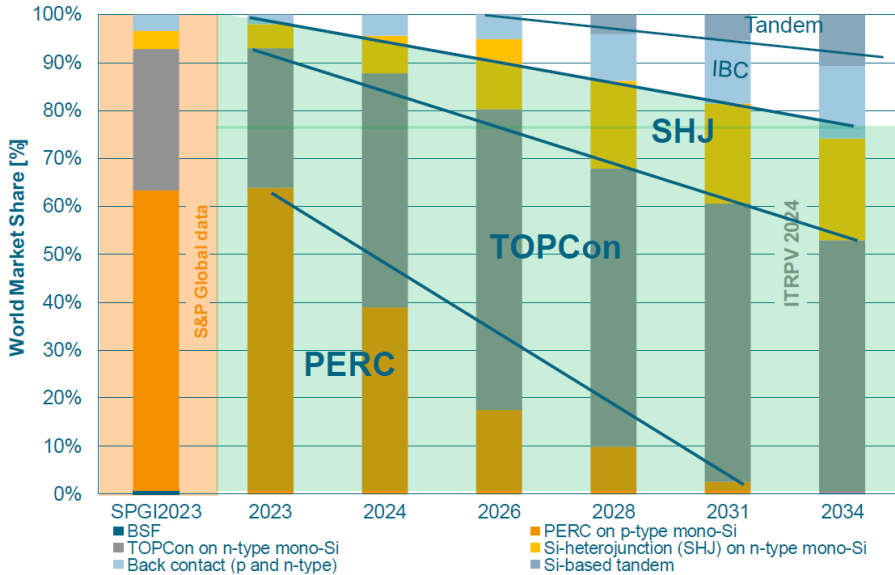


Figure 1.11: Global market share of different PV cell technologies [71].

solar cells have average lifetimes of less than 0.5 year [76] whereas silicon solar cells have a lifetime of at least 25 years. Some of the factors affecting perovskite solar cells are degradation in presence of oxygen or moisture, temperature, additives, thermal stress etc. [77]. Perovskite absorber layers can be deposited via one-step or two-step solution processing method or vapor deposition methods. According to the sequence of depositing electron transport layer (ETL), perovskite absorber and hole transport layer (HTL), perovskite solar cells can be n-i-p (normal structure) or p-i-n (inverted structure). ETL could be organic such as PCBM or inorganic such as TiO_2 or SnO_2 . HTL could be organic (SpiroOMeTAD), inorganic (NiO_x) or a polymer (PTAA). Single junction perovskite solar cell efficiency has seen an increase from 3.8% to 26.7% [78] in few years.

1.3.3. Tandem solar cells

As single junction c-Si solar cells are reaching their theoretical efficiency limit [80], researchers started looking into ways to further increase the efficiency of solar cells. One such concept is of tandem solar cells which is stacking one cell on top of the other cell. Tandem solar cells are useful as they can help reduce thermalization losses as compared to single junction solar cells. When a solar cell with a wider bandgap is stacked on top of a solar cell with a narrower bandgap, better utilization of the spectrum is aimed for. The top sub-cell in a tandem solar cell absorbs higher energy photons and transmits lower energy photons

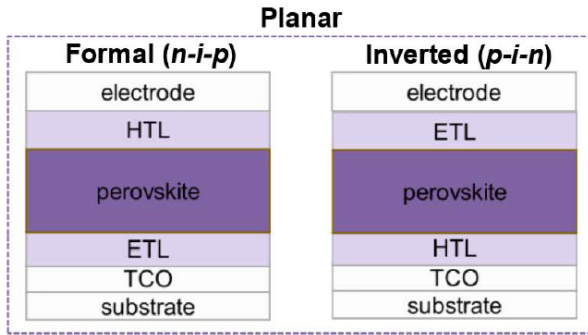


Figure 1.12: *n-i-p* and *p-i-n* architecture of perovskite solar cells. Light enters from the bottom of devices. Taken from [79].

which are absorbed by the bottom sub-cell. In a tandem solar cell, electron-hole pairs are generated in both the top and bottom sub-cells separately. There are various types of tandem solar cells such as III- V tandems, III- V/c-Si tandems, perovskite/perovskite tandems, perovskite/CIGS tandems and perovskite/c-Si tandem solar cells. The various types of perovskite tandems have been explained in various literature sources [81–84]. Perovskite/c-Si tandem solar cell is the focus of this work. Perovskite solar cells are used as top cell in the tandem solar cell owing to their bandgap in the range (1.55 eV - 1.7 eV), sharp optical edge and lower material cost. Crystalline silicon solar cells with a bandgap of 1.12 eV are used as bottom cell in tandem solar cells.

There are different types of tandem architectures depending on their interconnection, such as four terminal (4T), two terminal (2T) and three terminal (3T) tandem solar cells. The interconnection of the 4T, 2T and 3T tandem architectures are given in figure 1.13. 4T perovskite/c-Si tandem is the mechanical stacking of top and bottom sub-cells, as shown in figure 1.13 (a). As the top and bottom cells are fabricated separately in this case, they have their own transport layers for lateral collection of current that leads to more parasitic absorption losses and higher fabrication costs. In tandem solar cells, current matching is the concept of ensuring that both the top and bottom sub-cells generate similar amounts of electrical current to maximize the device's efficiency. This requirement typically applies when the sub-cells are electrically connected in series connection and they share the same current flow. The advantage of a 4T tandem configuration is that it does not have the current matching requirement between the top and bottom sub-cells. So, there is no strict bandgap or thickness selection for the perovskite absorber needed in the 4T case.

The most common tandem architecture is the monolithic integrated 2T tandem solar cell which is a straightforward integration of the two sub-cells (See

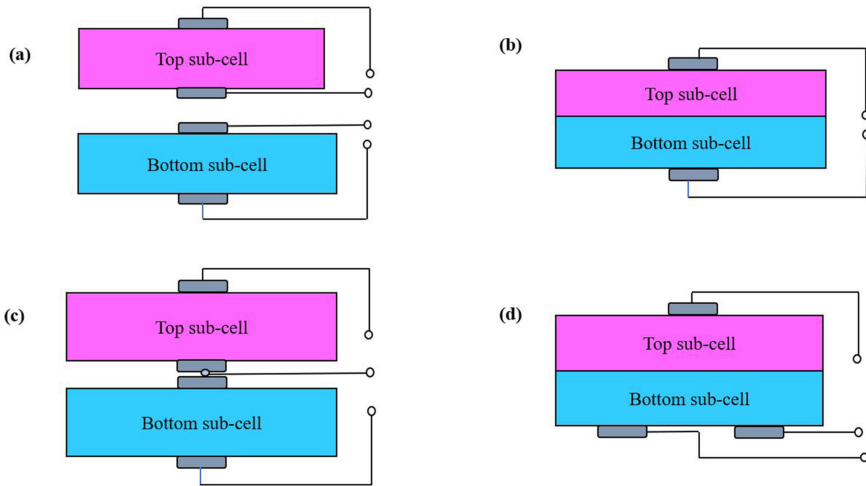


Figure 1.13: Electrical connection of (a) four terminal (4T), (b) two terminal (2T), (c) three terminal (3T) middle and (d) three terminal (3T) IBC tandem devices. Taken from [77].

figure 1.13 (b)). Here, the top cell is directly integrated on the bottom cell. In 2T tandems, the top and bottom sub-cells are electrically connected to each other via tunnel recombination junction (TRJ). As an example, 2T tandem case has been shown in figure 1.14 where the electrons are collected from the top sub-cell and the holes are collected from the bottom sub-cell. The holes from the top sub-cell and the electrons from the bottom sub-cell recombine in the tunnel recombination junction. A 2T tandem has only two electrodes, like a single-junction cell, resulting in fewer transport layers which means lesser number of deposition steps, less material usage and lower parasitic absorption in non-active layers. In a 2T configuration, the current between the top and bottom sub-cells of the tandem needs to be matched in order to achieve high/optimum efficiency otherwise the current of the limiting sub-cell will reduce the overall current of the tandem. This makes 2T tandem sensitive to spectral variations as the spectrum changes throughout the day and location affecting the current-matching conditions. This change in the spectrum means that the sub-cells need to be optimized for different locations and weather conditions in order to be current matched. Similar to bi-facial single junction solar cells, tandem solar cells could also be fabricated without full area metal on rear side making it bi-facial. Since extra light is absorbed in the bottom cell of the 2T bi-facial perovskite/c-Si tandem solar cell, the perovskite absorber needs to be either thicker or with a lower bandgap in order to absorb more photo-current for current matching. High sensitivity to

spectral variations leads to stringent bandgap selection of perovskite absorber in bi-facial 2T tandems. Various literature sources give details about bi-facial perovskite/c-Si tandem solar cells [85–87].

The advantages of both 2T and 4T tandem are combined into a 3T tandem solar cell. In addition to the front and back electrode, a 3T tandem has a third electrode for current extraction. This third electrode is added as a middle contact between top and bottom sub-cells (See figure 1.13 (c)) or as an Interdigitated back contacted (IBC) added in bottom sub-cell (See figure 1.13 (d)). Unlike the 2T tandem case, a 3T tandem device does not require current matching and yet has a monolithic device architecture. However, the interconnection for 3T tandems in a module circuit is more complex than 2T and 4T tandem cases. 3T tandems are not the focus of this thesis and will not be discussed further.

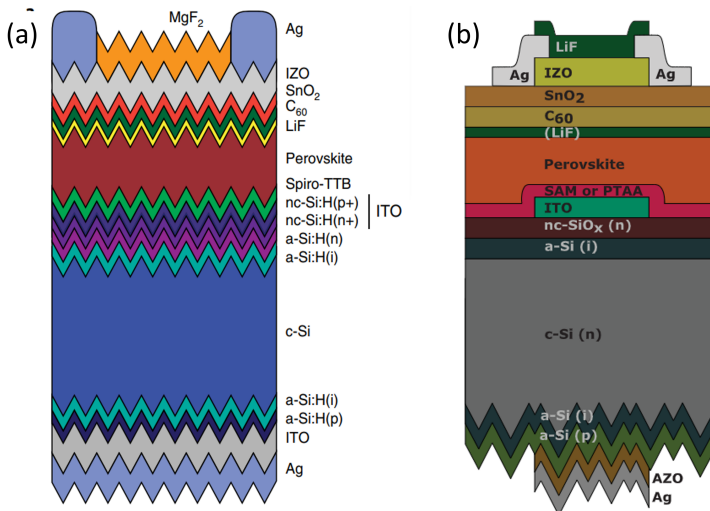


Figure 1.14: (a) Fully textured perovskite/c-Si tandem solar cell with 25.2% efficiency. Taken from [88]. (b) Perovskite/c-Si tandem solar cell with SAM with greater than 29% efficiency. Taken from [89].

First, perovskite/c-Si tandem solar cells with flat interfaces were fabricated [90, 91]. Then textured interfaces were incorporated in perovskite/c-Si tandem solar cell to improve the optics. The first fully textured monolithic perovskite/c-Si tandem solar cell was developed by E. Sahli et al. [88] (See figure 1.14 (a)). This fully textured tandem architecture has also been used later in this work for optical optimization of perovskite/c-Si tandem solar cells (See chapter 4). Perovskite/c-Si tandem solar cells have shown tremendous growth in terms of efficiency. The 2T perovskite/c-Si tandem solar cells have shown an increase from 13.7% [92] to 33.9% [93] and 34.6% [94]. After achieving 33.9% and 34.6% efficiency,

perovskite/c-Si tandem solar cells have surpassed the Shockley-Queisser (SQ) limit of single junction c-Si solar cells [95]. This tremendous growth is possible due to extensive research on the top sub-cell, bottom sub-cell and tunnel recombination junction (TRJ). For the perovskite top cell, the research is related to composition and thickness of perovskite absorber, development of suitable process on textured c-Si substrate, introduction of additional passivation layers and additives [88, 89, 91, 96–102]. An example of top cell development in tandem solar cells has been shown by A Al-Ashouri et al. wherein by incorporating self-assembled monolayer (SAM) as hole transporting layer instead of PTAA, the perovskite/c-Si tandem solar cell was shown to have a higher efficiency than 29% efficiency [89] (also shown in figure 1.14) (b).

Most of the perovskite/c-Si tandem solar cells have silicon heterojunction as bottom cell [88–91, 103]. Since lead free perovskite absorbers need annealing temperatures of greater than 200 °C that are exceeding the stability of SHJ bottom cell [104], a temperature stable bottom cell such as poly-Si/poly-SiO_x/poly-SiC_x could be useful for future perovskite/c-Si tandem applications. Also, in comparison to silicon heterojunction based tunnel junction in a 2T tandem, poly-Si based tunnel junction has higher thermal stability [105–107] and is compatible with mainstream PERC technology. Research in the area of perovskite/c-Si tandem solar cells with poly-Si, poly-SiO_x and poly-SiC_x CSPC is ongoing and has shown promising results [47, 106, 108–112]. However, it is not as advanced as perovskite/SHJ tandem technology. In this work, we have studied perovskite/c-Si tandem solar cells with high temperature CSPCs and compared their performance with perovskite/c-Si tandem solar cells with SHJ bottom cell.

1.4. Solar cell characteristics

In this section, we describe how the performance of a solar cell is characterized optically and electrically.

1.4.1. IV and EQE

Performance of a solar cell is characterized by parameters such as short circuit current (I_{sc}), open circuit voltage (V_{oc}), fill factor (FF) and power at maximum power point (P_{mpp}). Efficiency of a solar cell is calculated by output power divided by input power (equation 1.1). The power at maximum power point is calculated by the formula given in equation 1.2 wherein I_{mpp} is the current and V_{mpp} is the voltage at maximum power point condition. The fill factor is defined as the ratio of the power at maximum power point to the product of (I_{sc}) and (V_{oc}).

$$\eta[\%] = \frac{P_{\text{out}}[W]}{P_{\text{in}}[W]} \times 100 = \frac{V_{\text{oc}}[V] \times I_{\text{sc}}[A] \times FF[-]}{P_{\text{in}}[W]} \times 100 \quad (1.1)$$

$$P_{\text{mpp}}[W] = I_{\text{mpp}}[A] \times V_{\text{mpp}}[V] \quad (1.2)$$

A solar cell's efficiency is measured at standard test conditions (STC). The standard test conditions are defined as measuring the solar cell in Air Mass (AM) 1.5 spectrum, at 1000 W/m^2 at 25°C . The illumination is perpendicular to the solar cell in STC. The wavelength-dependent performance of solar cell can be seen from External Quantum Efficiency (EQE) and Internal Quantum Efficiency (IQE). The EQE is the ratio of number of electrons extracted from the solar cell to the number of incident photons. The IQE is the ratio of number of electrons given out by the solar cell to the number of absorbed photons. Figure 1.15 (a) shows the EQE, IQE and Reflectance spectra of a typical c-Si solar cell and figure 1.15 (b) shows the J-V curves of a typical solar cell.

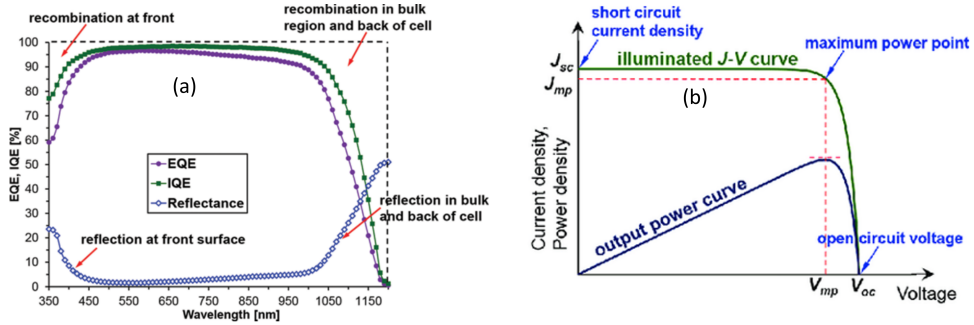


Figure 1.15: (a) EQE, IQE and Reflectance of a solar cell (b) J-V curves of a solar cell. J_{sc} , J_{mp} , V_{oc} , V_{mpp} stand for short circuit current density, current density at maximum power point, open circuit voltage, open circuit voltage at maximum power point respectively. Taken from [113].

Since the position of the sun, angle of incidence, irradiance intensity and temperature change during the day and across the globe, efficiency at STC is not the best way to assess PV modules performance in outdoor conditions. In this regard, the energy yield which is the accumulated electrical energy harvested from a solar module, is a more realistic approach to evaluate the performance of modules in outdoor conditions. Annual energy yield takes into account these spectrum and weather variations throughout the year for a specific location. In this work, we have optically optimized the PV module performance in real world conditions (See chapter 4). The energy yield analysis has been explained in more detail in chapter 2 and the results are given in chapter 6.

1.4.2. Losses in solar cell

Various losses play a role in reducing the efficiency of a solar cell [17]. These losses can be divided into optical and electrical losses. Largest optical losses in a solar cell occur due to spectral mismatch. Non-absorption and thermalization losses are types of spectral mismatch losses. Photons with energy lower than the absorber bandgap cannot be used by a solar cell. These losses are categorized as non-absorption losses. High-energy photons incident on a solar cell can be used if their energy is greater than the absorber's bandgap energy. However, only a fraction of energy of these high energy photons is converted into useful energy as the remaining energy is lost as heat. These losses are termed as thermalization losses. The other significant optical losses in a solar cell are due to reflection, transmission and absorption of light by the solar cell stack. Reflection of light from the solar cell's front surface and other interfaces lead to reflection losses. Light that is neither reflected, nor absorbed is transmitted through the solar cell and constitute the transmission losses. The light that is absorbed in the non-absorber layers of solar cell does not contribute to its current and is lost as parasitic absorption in a solar cell. The photons that are absorbed in semiconductor absorber of a solar cell contribute to its current. The other optical losses in solar cell occur due to shading from nearby objects. Wavelength-dependent refractive index (n) and extinction coefficient (k) are used to optically characterize solar cells' stack layers. Absorption coefficient is calculated from the extinction coefficient using the equation 1.3.

$$\alpha[cm^{-1}] = \frac{4 \times \pi \times k[-]}{\lambda[cm]} \quad (1.3)$$

The refractive index is the ratio of speed of light in vacuum to the speed of light in medium. It denotes the bending ability of light when light travels from one medium to the other. Absorption coefficient denotes how far the light can travel into the material, before it gets absorbed. Refractive index and absorption coefficient are wavelength dependent properties of the material, which help in determining the reflection, transmission and absorption in a solar cell stack of layers for a given thickness of each layer. Shading of solar cells and modules due to nearby objects also reduces current and contributes to optical losses in a solar cell.

Electrical losses also deteriorate the performance of a solar cell by reducing voltage and fill factor of the solar cell [17]. The voltage is reduced by bulk and surface recombination of minority charge carriers. The recombination mechanisms in solar cells have been explained in more detail in section 1.2.2. Series and shunt resistances in a solar cell lead to a reduction of the fill factor. The bulk resistance of the semiconductor, resistance of metal electrodes and

the contact resistance between semiconductor and metal contribute to series resistance in a solar cell. The series resistance is the resistance of the current path via which the photo-generated carriers reach the external circuit [17]. Shunt resistance is leakage in current due to defects in solar cell. A low shunt resistance in a solar cell causes power losses due to alternating current paths for photo-generated current.

1.5. Aim of the thesis

The aim of this work is to study, optimize, evaluate and integrate high temperature carrier selective passivating contacts such as poly-Si, poly-SiO_x and poly-SiC_x in 2T and 4T perovskite/c-Si tandem solar cells and compare their performance with respect to standard perovskite/c-Si tandem solar cells with SHJ bottom cell. The primary research objectives are:

1. To find accurate optical constants for high temperature CSPCs which are of mixed-phase nature such as poly-SiO_x and poly-SiC_x
2. To study, evaluate and optimize optical performance of mono-facial and bi-facial 2T, 3T and 4T perovskite/c-Si tandem solar cells with poly-Si, poly-SiO_x and poly-SiC_x CSPCs in real world conditions
3. To optimize passivation properties of poly-SiO_x CSPC on ultra-thin thermal tunnelling oxide and fabricate poly-SiO_x passivated c-Si solar cells.
4. To fabricate poly-SiO_x passivated c-Si bottom solar cells for 2T and 4T perovskite/c-Si tandem solar cells. We choose this CSPC because it is a new material whose performance in tandem has not been reported so far.
5. To estimate annual energy yield of 2T/4T, mono/bi-facial perovskite/c-Si tandem modules with poly-SiO_x passivated bottom cell and compare them with perovskite/c-Si tandem modules with standard SHJ bottom cell.

1.6. Outline of the thesis

The outline of the thesis is given below:

Chapter 1: Introduction

This chapter discusses renewable energy with a focus on solar energy, the fundamentals of PV and solar cell characteristics. The concept of carrier-selective passivating contacts have been explained. PV cell technologies with a focus on perovskite/c-Si tandem solar cells with high temperature carrier-selective passivating contacts have also been introduced.

Chapter 2: Modelling approaches and experimental methods

In this chapter, the modeling approaches used in this work to optimize the optical performance of tandem modules are discussed. Both cell and module level modelling approaches are explained. Also, deposition techniques for high temperature c-Si solar cells based poly-SiO_x CSPCs are given. Besides, optical and electrical characterization methods and procedures for both poly-SiO_x based c-Si solar cells and perovskite/c-Si tandem solar cells are explained.

Chapter 3: Optical characterization of high temperature carrier-selective passivating contacts

This chapter focuses on finding the accurate absorption coefficients of high temperature carrier-selective passivating contacts such as poly-SiO_x and poly-SiC_x. Two different techniques, inverse modelling based on reflection-transmission measurements and photo thermal deflection spectroscopy have been explored.

Chapter 4: Comparing optical performance of perovskite/silicon tandem architectures under real world conditions

In this chapter, optical study of 2T, 3T and 4T perovskite/c-Si tandem solar cells with poly-Si, poly-SiO_x and poly-SiC_x carrier-selective passivating contacts with respect to tandems with SHJ bottom cell has been performed. Study on bi-facial tandem solar cells has been included wherein the effect of albedo, perovskite thickness, bandgap as well as geographical location on its optical performance has been included.

Chapter 5: Crystalline silicon solar cells with thin poly-SiO_x carrier-selective passivating contacts for perovskite/c-Si tandem applications

In this chapter, the n-type and p-type doped poly-SiO_x CSPCs have been optimized. Bottom c-Si solar cells with poly-SiO_x CSPCs have been integrated into 2T and 4T perovskite/c-Si tandem solar cells.

Chapter 6: Predicting annual energy yield of perovskite/silicon tandem modules with different bottom cell technologies

This chapter focuses on predicting annual energy yield of perovskite/c-Si tandem modules with different bottom cell technologies such as silicon heterojunction or novel poly-SiO_x passivated c-Si solar bottom cells, using an advanced hybrid modelling framework. Additionally, the output power of novel tandem with poly-SiO_x passivated c-Si solar bottom cells is optimized in different locations with respect to different perovskite thickness and bandgaps.

Chapter 7: Conclusions and outlook

This chapter summarizes the key results of this thesis and gives an outlook on the future research on perovskite/c-Si tandem solar cells with high temperature carrier-selective passivating contacts.

1.7. Main contributions to the field

The work carried out in this thesis has helped filling the research gap in the area of single junction c-Si solar cells and perovskite/c-Si tandem solar cells with high temperature CSPCs.

The main contributions are summarized herewith :

1. **Absorption coefficients of high temperature CSPCs**

Optical modelling of solar cells provides important guidelines that help improving their efficiency. The absorption coefficient of a layer plays an important role in understanding its optical properties. In this work, we have determined the accurate absorption coefficients of poly-SiO_x and poly-SiC_x doped high temperature CSPCs in the wavelength range (300-2000 nm) using a novel inverse modelling approach based on reflection-transmission measurements. This method could be extended to find accurate absorption coefficients of other c-Si based CSPCs.

2. **Optical performance of perovskite/c-Si tandems with high temperature CSPCs**

This part of the work helps gain insight in the optical performance of 2T, 3T and 4T perovskite/c-Si tandems in real world conditions. We have demonstrated that the matched photocurrent density of un-encapsulated perovskite /c-Si tandem solar cells with poly-Si, poly-SiO_x and poly-SiC_x can go higher than 20 mA/cm². Factors affecting optimum perovskite thickness in current matching in 2T perovskite/silicon tandem solar cells have been explored. It also contributed to the field of optically optimizing bi-facial tandems according to albedo, location and perovskite thickness.

3. **Optimizing passivation properties and device fabrication with high temperature CSPCs**

The passivation provided by textured n-type poly-SiO_x CSPC on ultra-thin thermally grown tunneling SiO_x layer has been improved to 710 mV. To improve the passivation provided by textured p-type poly-SiO_x CSPC to 687 mV, a two-step annealing approach was used. Using n and p-type doped CSPCs, single-junction c-Si solar cell with 20.47% efficiency has been fabricated with low temperature screen printing yielding fill factor greater than 80%. This work helps gain insight in the thermal oxide growth conditions, annealing and hydrogenation process in forming high temperature CSPCs and the device study using high temperature CSPCs such as poly-SiO_x.

4. **Integration of high temperature CSPCs in 2T and 4T tandem solar cells**

In this work, we have fabricated 2T and 4T perovskite/c-Si tandem solar

cells with poly-SiO_x passivated c-Si bottom cell. The efficiencies of these 4T and 2T tandems are 28.1% and 23.2% respectively. To our knowledge, it is the first time tandem solar cells with poly-SiO_x CSPCs have been fabricated.

5. **Annual energy yield of tandem modules with high temperature CSPCs**

With the help of our hybrid modelling framework, wherein the experimentally obtained and simulated current-voltage curves are combined, we predicted the annual energy yield of perovskite/c-Si tandem with novel poly-SiO_x passivated c-Si solar bottom cell. This work helps us gain insight on energy yield of tandems with high temperature CSPCs and compare it with the performance of reference tandem with SHJ bottom cell. Additionally, the performance of perovskite/c-Si tandem with novel poly-SiO_x passivated c-Si solar bottom cell is optimized for different locations with respect to different perovskite thickness and bandgap. This hybrid approach can be extended to optimize the performance of other novel tandems.

2

Modelling Approaches and Experimental Methods

Modelling solar cells is an important way to optimize the various parameters of a solar cell. In this work, we have used GenPro4 [114] and PVMD toolbox [115] for optical optimization and energy yield analysis of perovskite/c-Si tandem solar cells and modules respectively. In this chapter, optical and electrical modelling of solar cells and modules has been explained. Additionally, the tools used during fabrication and measurement of poly-SiO_x passivated c-Si solar cells for single junction and tandem applications are explained.

2.1. Cell level modelling

2.1.1. Optical model

In this work, Genpro4 has been used to model solar cell optically [114] (See chapter 3 and chapter 4). GenPro4 is an in-house developed optical modelling software tool where a solar cell is defined as a multi-layer structure [114]. Here, thickness, refractive index and extinction coefficients of each layer of the solar cell stack are given as input.

Light travels in a straight line according to ray optics. Ray optics is applied when the size of the object is large compared to the wavelength of light. When the size of the object is comparable to the wavelength of light, then effects such as diffraction can play a role which cannot be explained by ray optics. Hence, light is considered as an electromagnetic wave in this case. Wave optics is the study of various phenomena of light such as diffraction, interference, polarization etc.

GenPro4 uses net-radiation method on flat interfaces [116]. GenPro4 takes

into account interference in ‘coatings’ (thinner than the coherence length of sunlight (1 μm)) but not in ‘layers’ (thicker than the coherence length of light). For textured interfaces, the light scattering effect of the texture needs to be taken into account. GenPro4 utilizes a 3D Atomic Force Microscopy (AFM) scan of textures for this purpose. For interfaces with textures having feature size smaller than the wavelength of light, wave optics is applied and scalar scattering model is used in GenPro4 [117, 118]. When textures with feature size greater than the wavelength of light are implemented, then the built in ray-optics model is used. Using flat, ray and wave models as described above, GenPro4 calculates the absorption profile in coherent and incoherent layers. GenPro4 gives reflectance, transmittance and absorptance of each layer of the solar cell stack as a function of wavelength.

For a given spectrum (such as AM1.5), the incident spectral power density is given. This can be converted to the incident spectral photon flux ($\Phi_{\text{inc}}(\lambda)$) using equation 2.1. Here, $E_{\text{inc}}(\lambda)$ is the incident spectral power density and the energy of each photon is calculated with the formula $\frac{hc}{\lambda}$ (h = planck’s constant, c = speed of light in vacuum and λ is the wavelength of light). In equation 2.2, the absorbed spectral photon flux ($\Phi_{\text{abs}}(\lambda)$) is obtained by multiplying the incident photon flux with wavelength dependent absorptance (obtained from GenPro4). The photocurrent density is calculated by integrating the absorbed spectral photon flux, according to equation 2.3, where q is the charge of an electron. λ_{min} and λ_{max} are 300 nm and 1200 nm respectively for c-Si based single junction and tandem solar cells.

$$\Phi_{\text{inc}}(\lambda) = E_{\text{inc}}(\lambda) \cdot \frac{1}{\frac{hc}{\lambda}} \quad (2.1)$$

$$\Phi_{\text{abs}}(\lambda) = \Phi_{\text{inc}}(\lambda) \cdot A(\lambda) \quad (2.2)$$

$$J_{\text{ph}} = q \int_{\lambda_{\text{min}}}^{\lambda_{\text{max}}} \Phi_{\text{abs}}(\lambda) d\lambda \quad (2.3)$$

2.1.2. Electrical model

Advanced Semiconductor Analysis (ASA) [119, 120] is a one-dimensional optoelectronic software that solves the poisson equation and the continuity equations for electrons and holes and is based on drift diffusion coupled with tunneling and recombination models. It is used to simulate solar cell structures. In this work, ASA is used to compute the J-V curves of perovskite and c-Si solar cells at different temperatures and irradiance levels.

2.2. Module level modelling

Researchers in the past have focused on finding energy yield of perovskite/c-Si tandem modules with SHJ bottom cell [121–125]. In this work, the PVMD toolbox has been used to do optical and energy yield analysis of perovskite/c-Si tandem solar modules with poly-SiO_x passivated c-Si solar cell [115] (See chapter 4 and 6). In this section, the working principle of the PVMD toolbox for module level modelling has been explained.

Genpro4 computes angle and wavelength dependent absorption in each layer of the solar cell which serves as an input to ray tracing model [126, 127]. For bi-facial solar cells, both front and rear irradiance are calculated. Using ray tracing models [126, 127], the sensitivity map of the PV module is obtained. The sensitivity map contains the sensitivity of the PV module for light coming from each direction (See figure 2.1). It ranges from 0 to 1. The sensitivity map is calculated with the mounting, shading and albedo information given as input such as tilt, size of the cells, the mounting height, the frame, the distance between cells, etc.

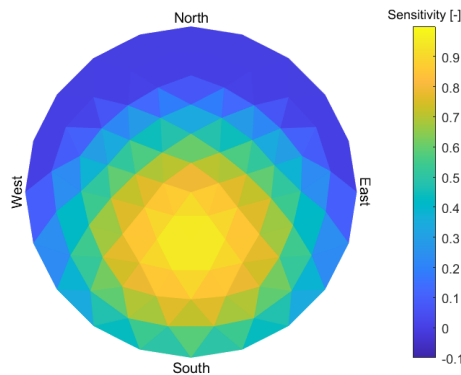


Figure 2.1: Sensitivity map of a perovskite/c-Si tandem module with poly-SiO_x passivated c-Si solar cell in Rome with a tilt of 27 °.

The weather model computes the sky map with the Perez [128] and SMARTS or SBDART [129–131] models. The Perez model determines the intensity of irradiance while SMARTS or SBDART determine the spectral shape of the incoming irradiance. The sky map contains information on how much light comes from each direction (See figure 2.2). The product of the sky map and sensitivity map is integrated over the whole sky to find the total irradiance absorbed by the PV module and its corresponding photo-current density [127]. This photo-current density is simulated for every hour of the year. In chapter 4, we have used the

yearly average photo-current density to compare different tandem architectures and optimize the perovskite thickness in 2T tandems for different locations. Taking the absorbed irradiance, ambient temperature, wind speed, module efficiency at STC as input, the thermal model calculates the temperature of each cell of the module for every hour of the year using the fluid dynamic model [132].

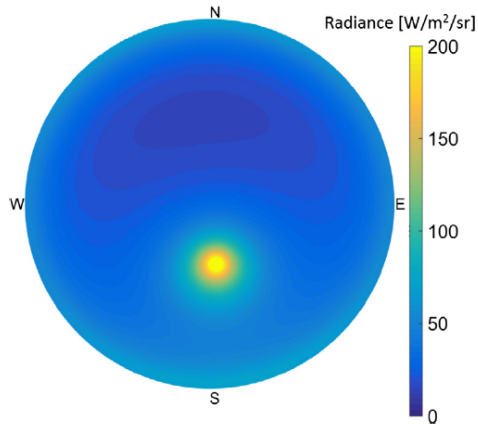


Figure 2.2: Sky map for a sunny instant in time ($\text{DNI} = 905 \text{ W/m}^2$ and $\text{DHI} = 111 \text{ W/m}^2$). Taken from [127]. DNI and DHI stand for direct normal irradiance and diffuse horizontal irradiance respectively.

In addition to the absorptance (see section 2.1.1), GenPro4 also computes the generation profile of the multi-layer solar cell which serves as an input to ASA software. ASA computes the temperature and irradiance dependent J-V curves of the top and bottom cells. Alternatively, temperature and irradiance dependent JV curves obtained from measurements can be given as input. This was done for the poly-SiO_x passivated c-Si solar cell, as shown in chapter 6. These J-V curves are then fitted with a one-diode circuit model (as shown in figure 2.3) to obtain the temperature and irradiance dependent diode parameters for each of the cell. The corresponding equation for the one diode equivalent circuit is given in equation 2.4. Here, I is the output current, V is the output voltage, I_{ph} is the photo-generated current, n is the ideality factor, I_o is the saturation current, R_s is series resistance, R_{sh} is the shunt resistance, k_B Boltzmann constant and T is the temperature of the cell.

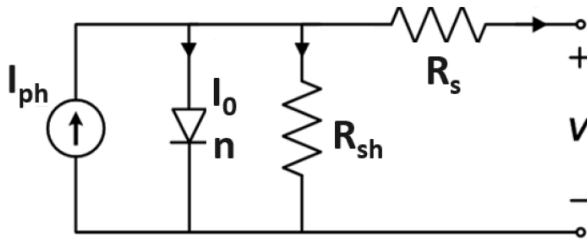


Figure 2.3: One-diode equivalent circuit model. Here, I_{ph} is the photo-generated current, n is the ideality factor, I_0 is the saturation current, R_s is series resistance, R_{sh} is the shunt resistance and V is the output voltage.

$$I = I_{ph} - I_0 \left[\exp \left(\frac{q(V + IR_s)}{nk_bT} \right) - 1 \right] - \frac{V + IR_s}{R_{sh}} \quad (2.4)$$

Using Lumped Element Model [115] and Lambert W function [133], allows the fast calculation of the module level JV curves by series connecting all cells in the module. The input parameters are photo-generated current, temperature of each cell of the module and temperature and irradiance dependent diode parameters. More details about these electrical simulations can be found in Ref. [134]. From these simulated J-V curves for every hour of the year, the output power of the module and, correspondingly, the annual energy yield are obtained. Chapter 6 includes the results of the energy yield of poly-SiO_x passivated perovskite/c-Si tandem modules and its comparison with SHJ tandem modules.

2.3. Fabrication of Poly-Si alloys passivated solar cells

In this section, the tools used during fabrication of poly-SiO_x passivated c-Si solar cells are explained. These tools are used in chapter 5 to fabricate poly-SiO_x passivated c-Si solar cells.

2.3.1. Cleaning and Texturing

Phosphorus doped n-type float-zone (FZ) c-Si wafers from *Topsil* company have been used for fabrication of poly-SiO_x passivated c-Si solar cells. N-type wafers are used over p-type wafers due to higher minority lifetime of n-type bulk wafers [135, 136]. Moreover, the p-type wafers show light induced degradation effect [137]. The boron in p-type wafers forms boron-oxygen complexes which act as recombination centres. The specifications of the wafer are given in table 2.1.

Table 2.1: Wafer Specifications

Parameter	Value
Resistivity (Ω cm)	1-5
Diameter (mm)	100 ± 20
Orientation	<100>
Thickness (μ m)	280 ± 20

These polished wafers are then textured to increase the absorption and reduce reflectance in solar cells. An anisotropic etching is done to form pyramids like structure, showing <111> orientation. For texturing, the wafers are immersed in Tetramethylammonium Hydroxide (TMAH) aqueous solution (TMAH and water in the ratio 1:4 along with 120 ml of ALKA-TEX 8 from GP-Solar-GmbH) maintained at 80 °C for 15 minutes. In this work, single side textured and double side textured wafers are used. For single side texturing, first silicon nitride (SiN_x) is deposited on one side to protect the wafers from texturing. Later, that protective (SiN_x) is etched with Buffered Hydrofluoric (BHF) Acid. After this, the standard procedure of cleaning of wafers is followed. First the wafers are dipped in HNO_3 (99 %) to remove organic contaminants and then rinsed in de-ionised water. This is followed by HNO_3 (69.5 %) and DI water rinsing to remove inorganic contaminants. The formation of native oxide on wafer during cleaning procedure is removed by marangoni cleaning wherein the wafers are dipped in 0.55 % HF and rinsed in DI water and Iso-propanol (IPA).

2.3.2. Thermal Oxidation

Next, thin tunneling oxide layer of 1-2 nm is formed via thermal oxidation on the c-Si wafers in a *Tempress* tube furnace. The c-Si wafers are kept in a quartz boat in the furnace. First, the furnace is flushed with nitrogen gas and then the temperature is ramped up to a desired set-point. In the high temperature environment, oxygen gas is flushed into the furnace to initiate the oxidation process. The oxygen atoms diffuse in the silicon surface to form thin silicon dioxide layer on the surface of c-Si wafer. Thermal oxidation can take place via dry oxidation or wet oxidation method. Dry oxidation uses oxygen as pure gas whereas wet oxidation uses oxygen in the form of water vapour/steam. Dry oxidation is slower and produces a thinner and denser layer. In this work, we have used dry oxidation method to form thin tunneling oxide on c-Si wafers.

2.3.3. Low Pressure Chemical Vapour Deposition (LPCVD)

Amorphous-silicon (a-Si) is deposited by Low Pressure Chemical Vapour Deposition (LPCVD) process. LPCVD is thermally driven wherein the precursor gases introduced in the reaction chamber undergo a chemical reaction on the surface of substrate to deposit thin film. 10 nm of a-Si layer is deposited at 2 nm/min rate at 580 °C at a pressure of 150 mTorr and a silane (SiH_4) gas flow rate of 45 sccm. In LPCVD, the thin films deposited are more uniform, denser and have lower defects as compared to films deposited by Plasma Enhanced Chemical Vapour Deposition (PECVD) process. After intrinsic a-Si deposition, marangoni is used to remove native oxide from LPCVD grown intrinsic a-Si surface.

2.3.4. Plasma Enhanced Chemical Vapour Deposition (PECVD)

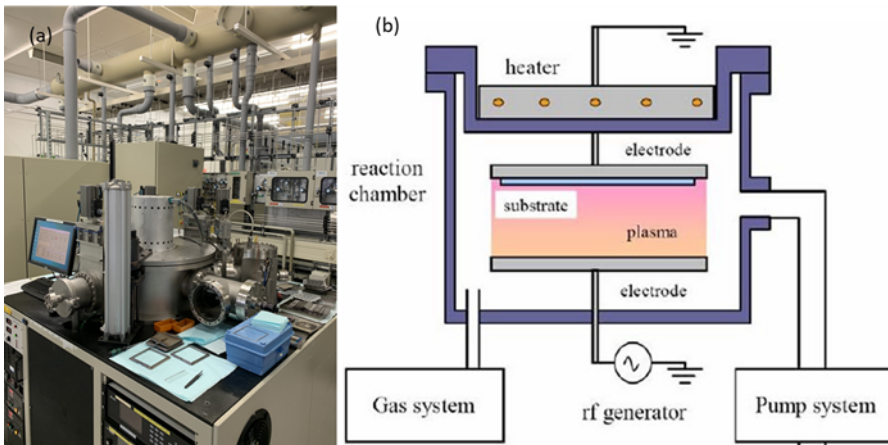


Figure 2.4: (a) PECVD chamber used for deposition of a-SiO_x:H (b) Schematic of a typical PECVD chamber. Taken from [138].

Doped amorphous silicon oxide (a-SiO_x:H) is deposited using plasma enhanced chemical vapour deposition (PECVD) process at a pressure of 1-2 mbar. In PECVD process, plasma enhances the chemical vapour deposition process. The reactant gases are introduced in between the *RF* electrode and the *ground* electrode. Due to the plasma created by an electric field generated from a RF power source (commonly at 13.56 MHz), the reactant gas ionizes and reacts on the surface of the wafer to form thin film. The reactant gases are silane (SiH_4), carbon dioxide (CO_2) and hydrogen (H_2) for poly-SiO_x passivating contacts. For poly-SiC_x passivating contacts, methane (CH_4) is used. Phosphine (PH_3) and diborane (B_2H_6) gases are used as doping sources. The PECVD process takes place at lower temperature (200 °C - 350 °C). The PECVD chamber, used in this

work, is shown in figure 2.4 (a) and its schematic is shown in figure 2.4 (b) .

High temperature annealing (900 °C - 950 °C), in nitrogen atmosphere, is performed on the wafers to crystallize the a-SiO_x:H layer into poly-SiO_x and activate the dopants within. Since hydrogen effuses out of the SiO_x/c-Si interface after such high annealing step leaving dangling bonds, a hydrogentaion step is performed. In our case, SiN_x:H capping is deposited from ammonia and silane gases using PECVD at 400 °C. Thereby, forming gas annealing is done at 400 °C for an hour. Later, SiN_x layer is removed with a BHF dip.

2.3.5. RF Magnetron Sputtering

RF magnetron sputtering is used to sputter Indium tin oxide (ITO) on desired areas of the solar cell stack using a mask. Sputtering is a physical vapor deposition method wherein the target is bombarded by plasma of argon ions to deposit thin films. The plasma is created by RF power source. ITO is 90% indium oxide and 10% tin oxide. ITO helps in lateral transport of charge carriers. Front ITO also acts as anti-reflection coating and can be optimized to minimize reflection. In case ITO is deposited on the rear side, it acts as a back side reflector. Due to the sputtering damage caused by bombardment of ions, the passivation is reduced [139, 140]. Annealing at temperatures between 200-400 °C helps recovering of the passivation [141–143]. In this work, a TCO recovery annealing of 400 °C for 1 hour is done in hydrogen atmosphere.

2.3.6. Screen Printing and Thermal Evaporation

Finally, the metallic contacts are deposited on solar cells. Such contacts collect charge carriers in a solar cell but also affect the optical properties of the solar cell. Their usage needs to be minimized especially at the front side of the solar cell as they prevent some light from being absorbed. For single junction solar cells, screen printing technique is used, whereas for tandem applications, the metal is thermally evaporated over the full area on the rear side. Screen printing is a technique that uses a stencil to transfer ink or paste onto the substrate through a mesh screen, using a squeegee. Samples are then annealed at 170 °C for 30 minutes to ensure contact formation. Thermal evaporation is a vacuum process wherein the metal is heated and it condenses on the substrate as a thin film. In both techniques, silver (Ag) was used as the metal.

For more details about processing perovskite and tandem solar cells, refer to chapter 5.

2.4. Electrical Characterization methods

2.4.1. J-V curves

The J-V curves of single junction c-Si solar cells, shown in this work, are measured with a AAA class Wacom WXS-90S-L2 solar simulator (See figure 2.5). This solar simulator has a xenon and halogen lamp to mimic the AM 1.5 spectrum, 1000 W/m^2 intensity at a temperature of 25°C . In this way, the solar simulator creates sunlight spectrum in an artificial controlled environment and the JV measurements of the cell are done at STC conditions. There is a voltage sweep and the corresponding current is measured for each voltage using four point probe method. For 4T perovskite/c-Si tandem solar cells, the measurement is done as given in Ref. [144]. First, the perovskite cell's J-V and EQE are measured as single junction against a black background to avoid reflection and overestimation of current. The transmitted spectrum is multiplied with the EQE of c-Si solar cell to get the filtered EQE of the c-Si solar cell in 4T tandem configuration. The J_{sc} of the bottom cell is calculated from this filtered EQE. The voltage and fill factor of the bottom c-Si solar cell in 4T tandem configuration is measured at the reduced intensity without affecting the spectral shape.



Figure 2.5: Wacom setup used in this work.

2.4.2. EQE

The External Quantum Efficiency (EQE) setup is used to measure the ratio of output current (charge carriers) of a solar cell with respect to the incoming photons

for each wavelength. In this work, an EQE setup is used to measure the EQE from 300 nm to 1200 nm, as shown in figure 2.6. Short circuit current density (J_{sc}) can be calculated from the EQE curve by integrating the EQE curve with spectral photon flux in the relevant wavelength range, as given in equation 2.5. For a single junction solar cell, the EQE setup has a lamp which is the light source. Light passes through a monochromator that selects the desired wavelength of light and then light passes through the beam splitter which divides the light into two beams. One beam goes to the sample being measured and the other beam of the light goes to the reference photo-diode. By measuring the wavelength dependent current in photo-diode and sample solar cell, EQE of the solar cell is obtained. For 2T perovskite/silicon tandem solar cell, EQE of the target sub-cell is measured by using an additional bias light, which saturates the non-target sub-cell. By doing so, the current of the target sub-cell becomes the limiting current and the EQE of the target sub-cell is measured.

$$J_{sc} = \int_{\lambda_{min}}^{\lambda_{max}} EQE(\lambda) \cdot q \cdot \Phi_{inc}(\lambda) d\lambda \quad (2.5)$$

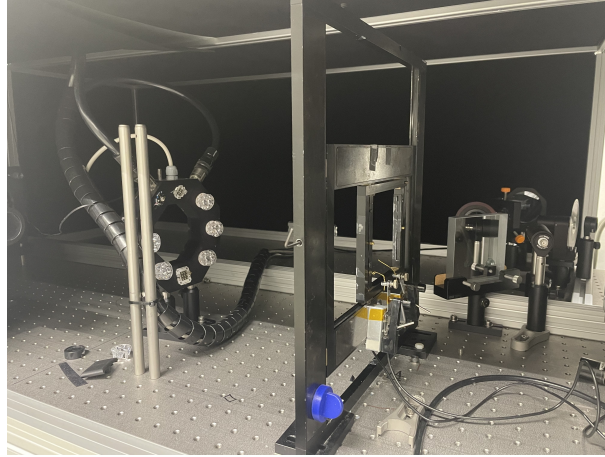


Figure 2.6: EQE setup used in this work.

2.4.3. Minority carriers lifetime measurement

Sinton WCT-120 Lifetime Tester [145] is used for these measurements, as shown in figure 2.7. It uses a flash lamp to generate excess carriers in the silicon wafer which increases the photoconductance. These excess carriers recombine and the photoconductance decay is measured by the lifetime tester. The lifetime of minority carriers is obtained from this photoconductance decay. If the lifetime is

higher than $100 \mu\text{s}$ then it is most accurate to use the transient mode. For smaller than $100 \mu\text{s}$ lifetime, Quasi-Steady-State Photoconductance (QSSPC) mode is used. From these measurements, the implied V_{oc} (iV_{oc}) is obtained.

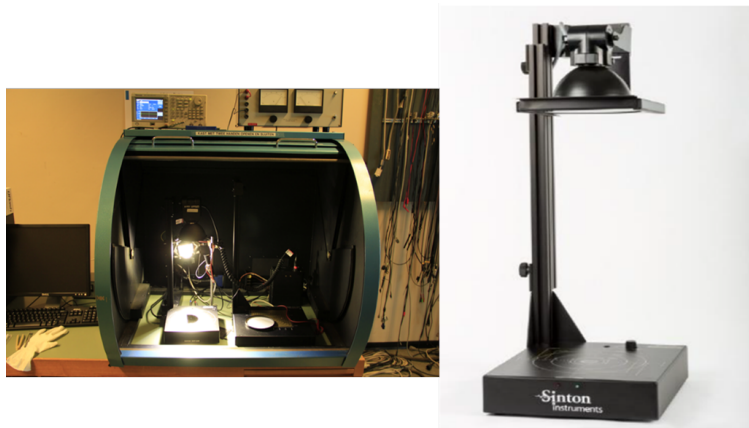


Figure 2.7: Sinton WCT-120 Lifetime Tester measurement system.

2.5. Optical characterization methods

2.5.1. Photothermal Deflection Spectroscopy (PDS)

This technique is used in Chapter 3 to detect weak absorption of n and p-type doped poly-SiO_x and poly-SiC_x layers in the infra-red region. The PDS setup used in this work is shown in figure 2.8.

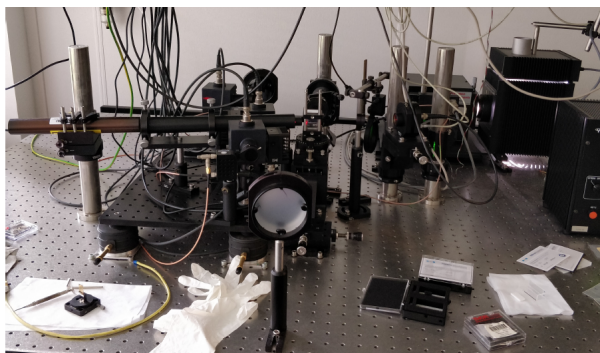


Figure 2.8: Photothermal Deflection Spectroscopy setup used in this work.

The absorptance, reflectance and transmittance are measured at the same spot. For this measurement, the layer is deposited on quartz, immersed in FC-72

liquid. When the incident light falls on the layer to be measured, it increases the temperature of the layer which generates heat. Since quartz is non-absorbing, this heat is transferred to the surround liquid and thermal waves are generated, which changes its index of refraction and deflects the laser beam. The amplitude of the oscillation of the laser beam is read by a position detector and a lock in amplifier and then is converted into absorbance.

2.5.2. Raman Spectroscopy

Raman spectroscopy uses laser beam to identify the vibrational modes in a material. Due to the interaction of laser beam with vibrations of molecules in a material, the energy of photon is shifted which is used to determine vibrational modes of the material. For these measurements, Renishaw's inVia Raman microscope is used, as shown in figure 2.9. These measurements are performed on poly-SiO_x layers with increasing oxygen content (See chapter 3) to determine the amorphous and crystalline phase. In Raman spectroscopy, 532 nm (green) and 633 nm (red) laser beams are commonly used to measure phase of silicon semiconductor. These wavelengths are effective because they excite the phonon vibrations in silicon, providing clear and strong Raman signals that reveal information about the material's crystalline structure.

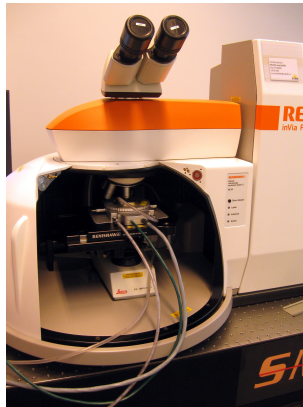


Figure 2.9: Raman measurement setup used in this work.

2.5.3. Reflection-Transmission (RT) measurements

The wavelength dependent Reflection-Transmission (RT) measurements are performed on double side textured wafers with poly-SiO_x and poly-SiC_x CSPCs in chapter 3. PerkinElmer Lambda 950 spectrophotometer, shown in figure 2.10(a), is used for these measurements. It is a dual beam photometer with a deuterium

lamp which produces ultraviolet (UV) light and a halogen lamp which produces visible and near infrared light (Vis-NIR) light beam. A monochromator selects the light component wavelengths and a beam splitter divides the beam into reference beam and sample beam. Using lenses, the beam of light is focussed such that it falls perpendicular on the sample. These measurements use an integrating sphere which is made of a highly reflective and scattering inner surface due to which the light bounces multiple times and stays inside the sphere. A photodetector inside the integrating sphere collects and measures the reflected or transmitted light intensity scattered in all directions. The intensity difference between sample beam and reference beam is detected. The detector transitions from photomultiplier to lead sulphide detector at 870 nm. A schematic representation of spectrophotometer is shown in figure 2.10(b).

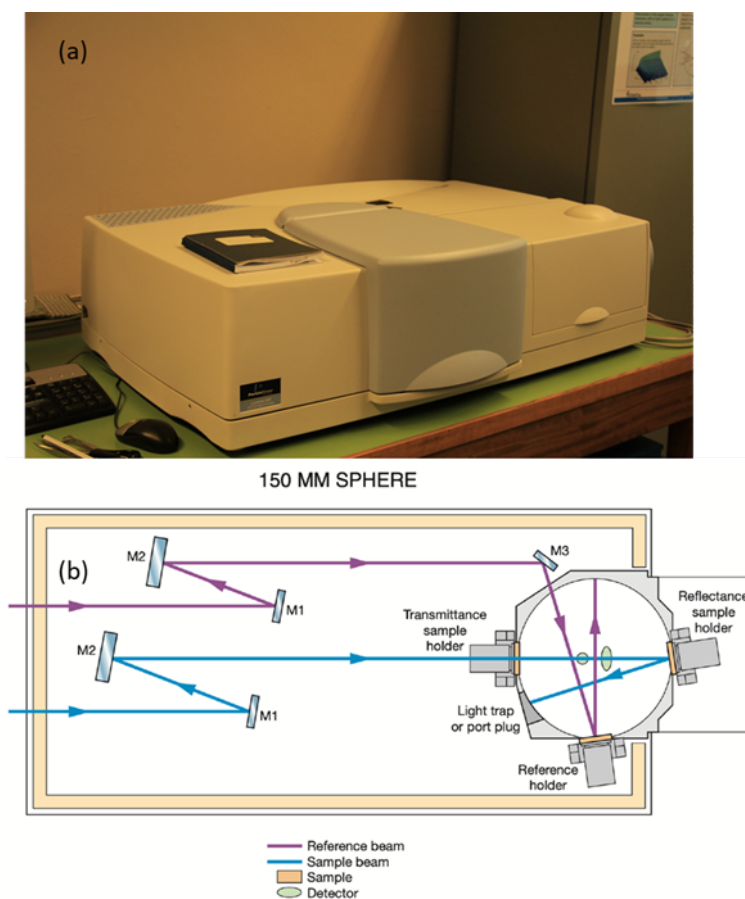


Figure 2.10: (a) PerkinElmer Lambda 950 spectrophotometer (b) Schematic of the spectrophotometer. Taken from [146].

2.5.4. Ellipsometer

Ellipsometer measures the change in polarization of light when it is reflected off the surface of thin film [147]. The two key parameters that are measured are amplitude of ratio of reflected light and the phase shift that occurs between different polarized components of light after reflection. Ellipsometry measurements, are performed in this work using M-2000 ellipsometer by J.A. Woollam (See figure 2.11(a) and (b)). Fitting the obtained data from ellipsometer measurements in CompleteEase software [148, 149], we obtain the thickness, refractive index and extinction coefficient of poly-SiO_x and poly-SiC_x CSPCs (See chapter 3). These values are subsequently used for optical simulations in chapter 4.

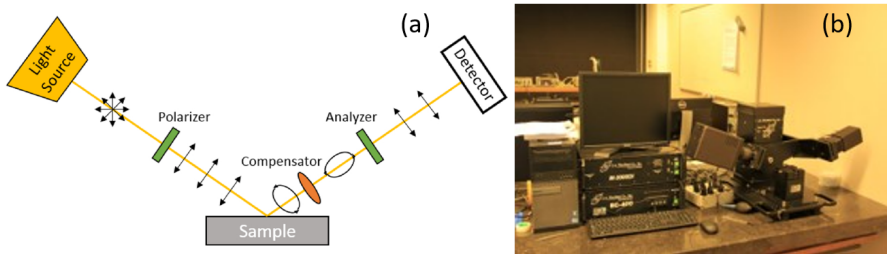


Figure 2.11: (a) schematic of the ellipsometer. Taken from [150] (b) M-2000 ellipsometer by J.A. Woollam used in the experiment.

2.5.5. Electrochemical Capacitance Voltage (ECV) profiling

ECV is used to determine doping concentration and doping profile in semiconductors. The semiconductor is placed in an electrolyte to form an electro-chemical cell. When a bias voltage is applied between electrolyte and semiconductor, a depletion region is formed between semiconductor/electrolyte interface. On measuring the capacitance of this depletion region, its width can be calculated. The width of the depletion region is a function of the applied voltage and is inversely proportional to the doping concentration. On plotting the capacitance (width) Vs voltage, the doping concentration is obtained. In order to get a depth profile of the doping concentration, the semiconductor is etched and at each step, capacitance is measured. ECV profiling is used in chapter 3 to find doping profile of p-type poly-SiO_x on c-Si wafer.

3

Optical characterization of poly-SiO_x and poly-SiC_x carrier-selective passivating contacts

This chapter is based on the following publication :

M. Singh, R. Santbergen, L. Mazzarella, A. Madrampazakis, G. Yang, R. Vis-mara, Z. Remes, A. Weeber, M. Zeman and O. Isabella , "Optical characterization of poly-SiO_x and poly-SiC_x carrier-selective passivating contacts", *Solar Energy Materials and Solar Cells* 210, 110507 (2020). DOI: <https://www.sciencedirect.com.tudelft.idm.oclc.org/science/article/pii/S0927024820301112>

Abstract

The optical modelling for optimizing high-efficiency c-Si solar cells endowed with poly-SiO_x or poly-SiC_x carrier-selective passivating contacts (CSPCs) demands a thorough understanding of their optical properties, especially their absorption coefficient. In this work, the absorption coefficient of doped poly-SiO_x and poly-SiC_x layers as function of oxygen and carbon content, respectively, was obtained for wavelengths (300-2000 nm) by means of two alternative techniques. The first approach, photothermal deflection spectroscopy (PDS), was used for layers grown on quartz substrates and is appealing from the point of view of sample fabrication. The second, a novel inverse modelling (IM) approach based on reflectance and transmittance measurements, was instead used for layers grown on textured c-Si

wafer substrates to mimic symmetrical samples. Although the absorption coefficients obtained from these two techniques slightly differ due to the different used substrates, we could successfully measure weak free carrier absorption (FCA) in our CSPCs layers. Using an in-house developed multi-optical regime simulator and comparing modelled reflectance and transmittance with measured counterparts from symmetrical samples, we confirmed that, as expected, with increasing doping concentration FCA increases; and found that the absorption coefficients obtained from IM can now be used to perform optical simulations of these CSPCs in solar cells.

3.1. Introduction

Polycrystalline silicon (poly-Si) has proven to be a dominating candidate in the field of carrier-selective passivating contacts (CSPCs) [59, 151–153]. However, doped poly-Si suffers from high free carrier absorption (FCA), which has turned the attention of the researchers towards new wide bandgap materials, such as polycrystalline silicon oxide (poly-SiO_x) and polycrystalline silicon carbide (poly-SiC_x). In these materials, the optoelectronic properties depend on oxygen [38] and carbon [63] content. Poly-SiO_x layers are promising candidates as CSPCs for high-efficiency c-Si solar cells [38, 154–156], with implied V_{OC} up to 740 (716) mV for n-type (p-type) doping [38, 157] on flat wafers. Symmetric samples of n-type (p-type) poly-SiC_x layers have shown an implied V_{OC} as high as 746 mV (735 mV) [63, 158] on flat wafers. To increase the efficiency of front/back-contacted (FBC) and interdigitated back-contacted (IBC) c-Si solar cells endowed with poly-SiO_x or poly-SiC_x CSPCs, opto-electrical modelling can provide guidelines. So far, researchers have mostly focused on structural [156, 159] and electrical properties [160, 161] of these layers. However, not much extensive research has been done to optically characterize these poly-SiO_x and poly-SiC_x layers. In this respect, it is instrumental to know — in first place — the absorption coefficient (α), because it is a crucial parameter for understanding the optical properties of these mixed phase materials [38, 156, 161].

The goal of this work is therefore to obtain accurate absorption coefficients of doped poly-SiO_x and poly-SiC_x layers, that can be used for the optical simulations of solar cells with these CSPCs. We first investigate if the substrate affects the absorption coefficients of these CSPCs. Then, we also study the effect of changing the oxygen and carbon concentration on the optical properties of our in-house developed poly-SiO_x and poly-SiC_x layers, respectively.

Owing to their non-trivial structural nature, the approach based on spectroscopic ellipsometry (SE) is prone to under-/over-estimation of the absorption coefficients [38]. Also, weak absorption is difficult to detect using SE [162]. A pos-

sible alternative technique could be photothermal deflection spectroscopy (PDS), which has been previously used to directly measure the absolute absorption in thin films and is sensitive to absorption values lower than 1% [163].

We have therefore deployed the absolute PDS technique to measure the absorption coefficient of doped poly-SiO_x and poly-SiC_x layers. For non-absorptive substrates must be used, layers have been deposited on fused silica quartz substrates. However, in solar cells, these CSPCs layers are deposited on (textured) c-Si wafers, for which the optical properties may be different. Thus, for optical simulations of solar cells with these CSPCs layers, it is necessary to investigate if the absorption coefficients obtained from PDS on a quartz substrate can be used. Hence, absorption coefficients from PDS are used as an input for optical simulations using GenPro4 [114] to generate reflection (R), transmission (T) and absorption (A) spectra of these highly-transparent CSPCs on flat or textured c-Si wafer substrates.

This two-step process – (i) PDS-based absorption coefficients of flat samples (ii) verified on simulated absorption spectra of (textured) c-Si wafers – may not always give an accurate fit. Therefore, we have used also another method, the so-called inverse modelling (IM). This method allows to derive absorption coefficients directly from reflectance/transmittance (RT) measurements of symmetric c-Si samples coated both sides with CSPCs. As RT measurements typically have an accuracy of 1%, this method is usually not sensitive enough for weakly absorbing films, for instance layers that absorb less than 1% of the incident light. Rudiger et al. increase the sensitivity of the RT measurements by utilizing textured c-Si wafers in which weakly-absorbed light can be efficiently trapped. This enhances the path length up to a factor of 50, resulting in a significant absorption enhancement [164]. Therefore, the cumulative multi-pass absorption can be detected using conventional RT measurements, even when the single-pass absorption is much less than 1% [165]. However, Rudiger et al. used a silver (Ag) back reflector, whose optical properties depend on the deposition conditions [166]. The drawback of including an Ag back reflector is that in optical simulations, when Ag has slightly different optical properties compared to the ones used in simulations, it might attribute too little absorptance to Ag and too much to the layer under test, or vice versa. We improve this method by considering symmetrical samples without metal back reflector. This eliminates the need to account for absorption in the metal and the corresponding errors that this might introduce. Rudiger et al. use this method to measure the FCA in doped regions inside the c-Si wafer. In our RT measurements, for photon energies lower than that of c-Si bandgap and knowing wafer's resistivity (i.e. the base doping concentration), we can attribute the absorption mainly to the investigated CSPCs thin film. Then, if the film thickness is known, we hereby show that the corresponding absorption coefficients can be obtained through IM. The

absorption coefficients obtained from PDS measurements have been obviously compared to those obtained from IM and found differences will be discussed here.

3.2. Experiments and methods

3.2.1. Sample preparation

To prepare flat n-type doped poly-SiO_x layers, suitable for certain optical measurements, hydrogenated amorphous silicon oxide (a-SiO_x:H) was deposited using plasma enhanced chemical vapour deposition (PECVD) technique on fused silica substrates. The sample structure is shown in Figure 3.1(a). A combination of gases such as carbon dioxide (CO₂), molecular hydrogen (H₂), silane (SiH₄) was used as basis, while phosphine gas (PH₃) was used as n-type doping source. For p-type doped poly-SiO_x layers, diborane gas (B₂H₆) was used as p-type doping source. For poly-SiO_x layers, we defined volumetric flow rate R_{CO₂} ratio as:

$$R_{CO_2} = \frac{CO_2}{CO_2 + SiH_4} \quad (3.1)$$

to rank our doped poly-SiO_x layers as a function of oxygen content. These layers were annealed at 850 °C for 45 minutes. After high temperature annealing, these amorphous layers became poly-crystalline with phosphorous doping atoms being activated. Similarly (see Figure 3.1a), for n-type doped poly-SiC_x layers, we deposited first hydrogenated amorphous silicon carbide (a-SiC_x:H) from H₂, SiH₄ and methane (CH₄) gases as basis and again PH₃ as n-type doping source. For p-type doped poly-SiC_x layers, B₂H₆ gas was used as p-type doping source. In this case, the volumetric flow rate ratio R_{CH₄} was defined as:

$$R_{CH_4} = \frac{CH_4}{CH_4 + SiH_4} \quad (3.2)$$

and was used to rank doped poly-SiC_x layers as a function of carbon content. These layers were also annealed at 850 °C albeit for a shorter amount of time (5 minutes) with respect to poly-SiO_x counterparts. Other defined ratios are R_{PH₃} = $\frac{PH_3}{PH_3 + SiH_4}$ and R_{B₂H₆} = $\frac{B_2H_6}{B_2H_6 + SiH_4}$ to study the effect of varying doping concentration on the optical properties of our layers. The deposition parameters are given in Table 3.1.

Table 3.1: Deposition parameters of n-type doped poly-SiO_x and poly-SiC_x layers.

Type	T _{substrate} (°C)	P _{deposition} (mbar)	Power density (W/cm ²)
poly-SiO _x	180	1	0.035
poly-SiC _x	180	0.7	0.021

Afterwards, we also prepared n-type and p-type doped poly-SiO_x and poly-SiC_x layers on textured c-Si wafers. Float zone (FZ) double-side polished n-type c-Si wafers (thickness: $280 \pm 20 \mu\text{m}$, orientation: $\langle 100 \rangle$, resistivity: 1-5 $\Omega \text{ cm}$) were chemically textured in a solution containing TMAH, AlkaText^o surfactant and water to obtain pyramids on both sides. Then, a thin layer of tunnelling SiO₂ [151] was wet-chemically grown on both sides by nitric acid oxidation of silicon (NAOS). These substrates were loaded in PECVD equipment to be coated on both sides by n-type or p-type doped a-SiO_x:H or a-SiC_x:H layers. All samples were annealed at 850 °C for 45 minutes in case of poly-SiO_x and 5 minutes in case of poly-SiC_x. The structure of these samples is sketched in Figure 3.1 (b).

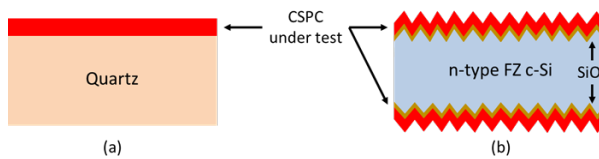


Figure 3.1: Samples (a) are for PDS, Raman and SE measurements; samples (b) are for RT measurements.

3.2.2. Characterization methods

Raman measurements were performed using Renishaw's inVia Raman microscope at an excitation wavelength of 514 nm. The equipment was calibrated by measuring the sharp peak at 520.5 cm^{-1} on a c-Si wafer. SE measurements were performed using a J. A. Woolam ellipsometer to obtain the refractive indices and absorption coefficients of these layers. The absorptance of poly-SiO_x and poly-SiC_x layers were measured using two complementary techniques: PDS and RT. PDS measures the absorption in CSPCs layers on a quartz substrate whereas the RT technique measures the absorption in CSPCs layers on a (textured) c-Si wafer substrates. PDS measures the deflection of a laser beam passing through a cuvette filled with a suitable liquid (FC72 in our case), due to the heat absorbed by the layer under test immersed in the cuvette. The setup used for PDS measurements is shown in Figure 3.2. More details about this technique can be found elsewhere [163]. For these measurements, we used samples as in Figure 3.1 (a), whose quartz substrate does not contribute to absorption.

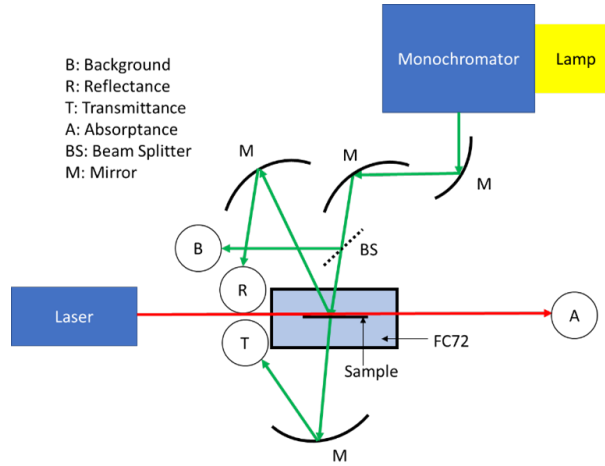


Figure 3.2: Schematic sketch of the absolute PDS setup used in this work.

For obtaining the wavelength-dependent absorption coefficient using the absolute PDS method [163], R_{PDS} , T_{PDS} and A_{PDS} spectra have been simultaneously measured at the same spot in the wavelength range from 300 nm to 2000 nm. R_{PDS} and T_{PDS} were measured with two independent detectors opportunely placed on the optical table and coupled with the PDS setup. In Figure 3.3, these curves have been plotted for n-type doped poly-SiO_x layer. Similar to the finding of Zdenek et al. [163], we find that $1 - R_{PDS} - T_{PDS}$ spectrum aligns well with the measured absorption A_{PDS} . For the RT measurements, total R and T of symmetric samples were measured using a Perkin Elmer Lambda 1050 equipped with an integrating sphere accessory. In the wavelength 300 to 860 nm, the spectral slit width is 2 nm and the integration time of the photomultiplier tube detector was set to 0.4 s. In the wavelength range of 860 to 2000 nm, the spectral slit width varies from 5 to 20 nm and it uses InGaAs detector with integration time set to 1 s. The spectrophotometer was calibrated by measuring the reflectance of a calibrated highly reflective reference sample (Spectralon) and a dark measurement (i.e. with the light beam blocked). We measured the centre spot of the samples in both reflectance and transmittance measurements. Table 3.2 gives an overview of the executed measurements and their related samples.

Table 3.2: Samples for PDS, SE, Raman, and RT measurements.

Experiment	Name	Substrate	Type of layer	d_{layer} [nm]	R_{CO_2} or R_{CH_4} or R_{PH_3} or $R_{\text{B}_2\text{H}_6}$
PDS	R_{CO_2}	quartz	poly-SiO _x (n)	100	[0 - 0.83]
	R_{CH_4}	quartz	poly-SiC _x (n)	100	[0.54 - 0.85]
RT	F0	Flat wafer	-	-	-
	F1	Flat wafer	poly-SiC _x (n)	30	0.69
	X0	Textured wafer	-	-	-
	X1	Textured wafer	poly-SiC _x (n)	30	0.69
	X3	Textured wafer	poly-SiC _x (p)	30	0.69
	X1- R_{PH_3}	Textured wafer	poly-SiC _x (n)	30	[0.13 - 0.33]
	X3- $R_{\text{B}_2\text{H}_6}$	Textured wafer	poly-SiC _x (p)	30	[0.13 - 0.33]
	X2	Textured wafer	poly-SiO _x (n)	60	0.62
	X4	Textured wafer	poly-SiO _x (p)	37	0.20
	X2- R_{PH_3}	Textured wafer	poly-SiO _x (n)	40	[0.33 - 0.83]
X4- $R_{\text{B}_2\text{H}_6}$	Textured wafer	poly-SiO _x (p)	37	[0.11 - 0.65]	

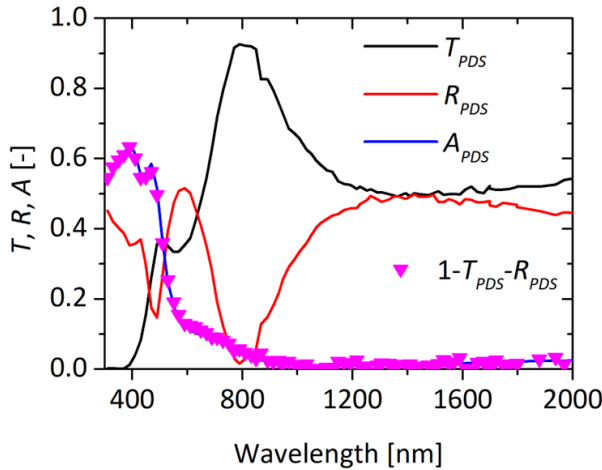


Figure 3.3: R_{PDS} , T_{PDS} , and A_{PDS} spectra measured at the same spot of an n-type doped poly-SiO_x layer on quartz substrate. $1 - T_{\text{PDS}} - R_{\text{PDS}}$ and A_{PDS} spectra coincide, even though they come from different detectors for R_{PDS} and T_{PDS} and CCD camera for A_{PDS} [163].

3.2.3. Optical modelling

The refractive index and absorption coefficients are obtained from ellipsometer using Cody-Lorentz model. As we will show in section 3.3.1, our CSCs are mixed phase materials, and we considered using Effective Medium Approximation (EMA) but this approach did not improve the fit further. It is possible to add a Drude term to represent FCA, as commonly done for metals [167–169]. However, Drude model possesses several deficiencies [170]. In our samples FCA is relatively weak, adding a Drude term did not lead to satisfactory results. Varying input parameters of

Drude model, and therefore varying absorption coefficients at long wavelengths, did not significantly affect the quality of the ellipsometry data fit. This implies that the Drude model, when used for our layers, can give widely different absorption coefficients. As obtained absorption coefficients would not be reliable, the Drude term was not included. GenPro4 is an optical model for simulation of solar cells in which ray optics and wave optics are combined [114]. It is suitable for quickly and accurately simulating c-Si solar cells with multilayer structures [114]. In this study, we have used GenPro4 to simulate the thin films deposited on both sides of textured wafers (see Figure 3.1(b)). The needed absorption coefficients were derived using two methods: the Ritter-Weiser applied on PDS spectra and the IM from RT spectra. To obtain wavelength-dependent α of flat layers on quartz from PDS, the Ritter-Weiser formula [163] was used:

$$2e^{(\alpha d)} = (1 - r) \left(1 + \frac{A_{\text{PDS}}}{T_{\text{PDS}}} \right) + \sqrt{(1 - r)^2 \left(1 + \frac{A_{\text{PDS}}}{T_{\text{PDS}}} \right)^2 + 4r} \quad (3.3)$$

where absorptance, transmittance and thickness are denoted by A, T and d, respectively, and the ratio r is defined as

$$r = \left(\frac{n - m}{n + m} \right)^2 \quad (3.4)$$

In Equation 3.4, n and m are the real parts of the refractive indexes of the layer under test and of the surrounding medium (in our case, FC72), respectively. Wavelength-dependent n and d of the layer were obtained by SE deploying a Cody-Lorentz fitting.

Spitzer et al. provided a detailed physical model for absorption by free charge carriers, taking into account their interaction with the lattice and impurities [171, 172]. The model has been validated for crystalline materials, including c-Si, but it is not directly applicable to the amorphous/crystalline mixed-phase materials like the poly-Si alloys hereby considered [172]. For deriving the absorption coefficient from the absorptance of a layer on textured c-Si substrate, we used the IM approach [165]. This approach is executed using Genpro4 software. For our specific purpose of determining the absorption coefficients of mixed phase materials, the Rudiger model, despite its empirical nature, is an improvement of Schroeder [173] and Green [174] models and therefore is used in this work. Rudiger has given the following equations to calculate the absorption coefficients due to FCA in p-type and n-type highly-doped c-Si, respectively [165]. Here, λ is the wavelength, p and n are the doping concentrations:

$$\alpha_{\text{FC},p} (\text{cm}^{-1}) = 2.6 \times 10^{-18} \times \left(\frac{\lambda}{\mu\text{m}} \right)^{2.4} \times \frac{p}{\text{cm}^{-3}} \quad (3.5)$$

$$\alpha_{FC,n} (\text{cm}^{-1}) = 1.8 \times 10^{-18} \times \left(\frac{\lambda}{\mu\text{m}} \right)^{2.6} \times \frac{n}{\text{cm}^{-3}} \quad (3.6)$$

We assume that in the wavelength range from 800 to 2000 nm, the absorption coefficient is due to the FCA (α_{FC}), and is given by the following equation [165]:

$$\alpha_{FC} (\text{cm}^{-1}) = C \times \left(\frac{\lambda}{\mu\text{m}} \right)^x \quad (3.7)$$

where constant C and exponent x are fitting parameters. At short wavelengths, these CSPCs layers have high absorption coefficient and the free carriers' contribution is almost negligible. On the other hand, at long wavelengths the FCA starts to play a dominating role. SE is expected to accurately detect the absorption at shorter wavelengths but not the weak absorption at longer wavelengths. Hence, we use the absorption coefficients from SE measurements (α_e), combined with those due to FCA accrued from IM approach by choosing accurately C and x in Equation 3.7 ($\alpha = \alpha_e + \alpha_{FC}$). In this way we are able to get the absorption coefficients in entire wavelength range from 300 to 2000 nm. The input thickness of the layer on textured wafer, that is used for these simulations, is calculated by dividing the thickness of layer on flat surface by a factor of 1.7. The contribution of the in-diffused region is relatively small, but the FCA in the in-diffused regions has been incorporated into the model nonetheless. The in-diffused layer has been modelled as a separate layer in the optical model with effective thickness ' d ' and uniform doping concentration C_0 . We choose C_0 as the surface concentration, while the effective thickness follows from the following equation [175]:

$$d = \frac{C_n}{C_0} \quad (3.8)$$

Here C_n is the areal concentration which is calculated by integrating the doping profile in c-Si. The refractive index (' n ') for doped Si varies less than 15% due to FCA within the doping range (10^{15} to 10^{21} cm^{-3}) whereas α_{FCA} varies over several orders of magnitude in the same doping range [176]. Hence, it is safe to assume the refractive index ' n ' of intrinsic silicon for our in-diffused layer too. The absorption coefficients (α) used for our in-diffused layers are calculated from Rudiger's Equation for highly doped silicon (Equation 3.5 and 3.6) [165]. Figure 3.4 shows the measured doping profile of poly-SiO_x layer with in-diffusion in the c-Si bulk. As shown in Figure 3.4, C_0 is in the order 10^{20} cm^{-3} and C_n was derived to be in the order 10^{14} cm^{-2} . This means that we can model the in-diffused layer as a layer of uniform doping concentration C_0 and effective thickness given by Equation 3.8. Using this approach, the effective thickness comes to be around 10 nm. Similarly, for poly-SiC_x layers, C_0 is in the order 10^{17} cm^{-3} [63] and C_n was

derived to be in the order 10¹¹ cm⁻² [63]. Thus the effective thickness comes also to be around 11 nm. The parameters used for modelling the in-diffused region for different CSPCs are given in Table 3.3.

Table 3.3: Parameters used for modelling in-diffused region.

CSPC (source of data)	C ₀ (cm ⁻³)	C _n (cm ⁻²)	d (nm)	$\alpha_{FC}/\text{cm}^{-1} = C \times \left(\frac{\lambda}{\mu\text{m}}\right)^x$
n-type doped poly-SiO _x [156]	3.51×10^{20}	3.63×10^{14}	10.34	$\alpha_{FC}/\text{cm}^{-1} = 631.8 \times \left(\frac{\lambda}{\mu\text{m}}\right)^{2.6}$
p-type doped poly-SiO _x [Fig. 3.4]	2.15×10^{20}	2.07×10^{14}	9.64	$\alpha_{FC}/\text{cm}^{-1} = 559 \times \left(\frac{\lambda}{\mu\text{m}}\right)^{2.4}$
n-type doped poly-SiC _x [63]	7.24×10^{17}	8.50×10^{11}	11.74	$\alpha_{FC}/\text{cm}^{-1} = 1.30 \times \left(\frac{\lambda}{\mu\text{m}}\right)^{2.6}$
p-type doped poly-SiC _x [63]	7.24×10^{17}	8.50×10^{11}	11.74	$\alpha_{FC}/\text{cm}^{-1} = 1.88 \times \left(\frac{\lambda}{\mu\text{m}}\right)^{2.4}$

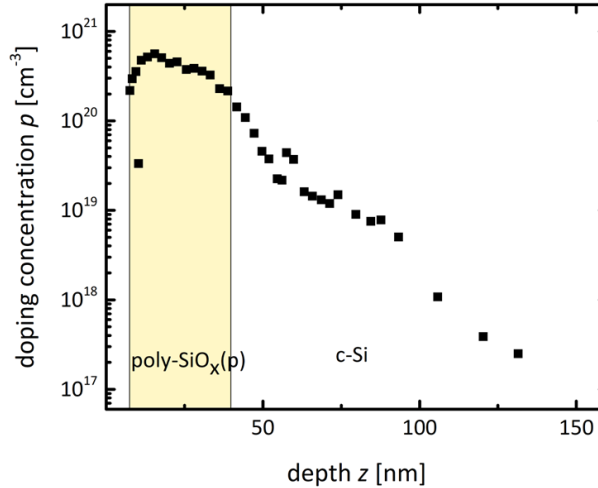


Figure 3.4: Electrochemical Capacitive-Voltage [ECV] profile of a p-type poly-SiO_x layer on c-Si wafer (R_{CO₂} = 0.2 and R_{B₂H₆} = 0.38).

3.2.4. Flowchart for extracting absorption coefficients

In this work, we have used absorption coefficients derived from PDS spectra (flat layers) and verified if they are trustworthy once used to perform optical simulations in GenPro4 software (textured layers). In case the fit was not accurate, we used the IM approach. The followed flowchart is reported in Figure 3.5 and can be applied for the extraction of absorption coefficients of other mixed phase materials as well.

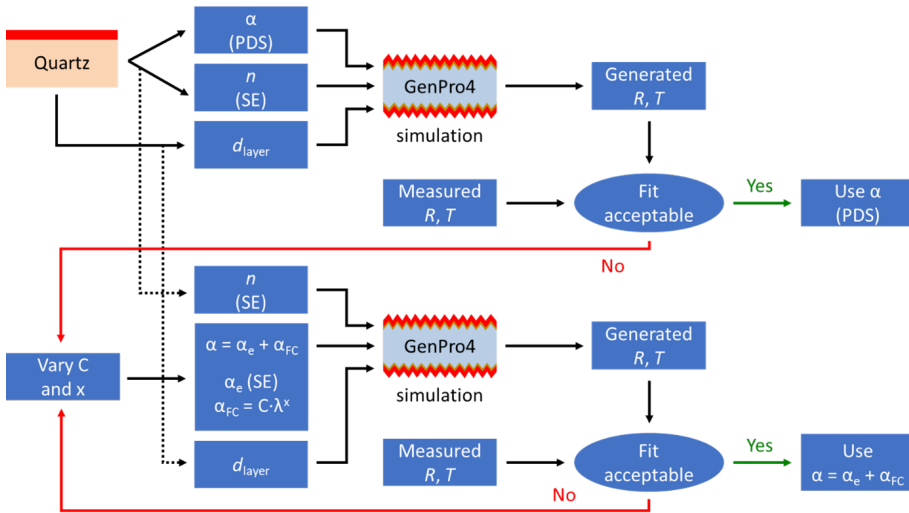


Figure 3.5: Flowchart for deriving the absorption coefficient of mixed phase materials, where n is the real part of the refractive index; α is the absorption coefficient (α_e and α_{FC} are the SE and IM components, respectively); d_{layer} is the thickness of the layer under test on textured c-Si wafer (calculated by dividing the thickness of layer on flat quartz by 1.7).

3.3. Results

3.3.1. Characterization on quartz substrates

Structural characterization

Raman measurements were performed to understand the structure of our poly-SiO_x and poly-SiC_x layers. Figure 3.6(a) shows the Raman measurements of poly-SiO_x layer with varying R_{CO_2} . They all show a peak at 517 cm⁻¹, which is attributed to phosphorus doped c-Si peak [177]. With increasing R_{CO_2} , another broad peak centred at 480 cm⁻¹ becomes evident. This peak is attributed to the transverse optical mode of amorphous Si [178]. Deconvoluting these spectra, as reported in Figure 3.6(b) for $R_{CO_2} = 0.83$ sample, we get also another peak at around 507 cm⁻¹, which is attributed to the grain boundary interface between silicon nanocrystals and the surrounding amorphous silicon-oxide matrix [177, 179, 180]. Our poly-SiO_x layers are therefore mixed phase materials, being formed by a mixture of amorphous and crystalline fractions. As expected, the amorphous silicon-oxide fraction increases with increasing R_{CO_2} .

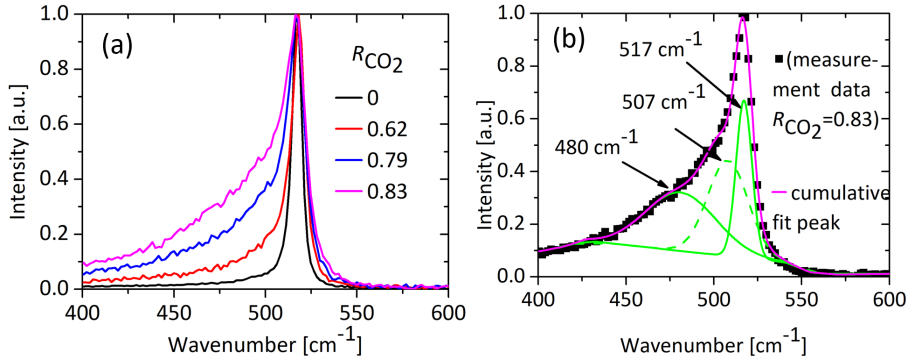


Figure 3.6: (a) Raman spectra of n-type doped poly-SiO_x layers for different R_{CO_2} after annealing; (b) peaks deconvolution reported for the sample with $R_{CO_2} = 0.83$.

Raman measurements performed on the as-deposited and annealed poly-SiC_x layers are included in Figure 3.7. A broad peak at around 480 cm⁻¹ is observed for the as-deposited samples in Figure 3.7(a). This peak is attributed to the transverse optical mode of amorphous Si [178]. After annealing, the obtained spectra shown in Figure 3.7(b) are rather different. Along with the amorphous silicon peak, we observe a peak at around 513 cm⁻¹. This is quite close to 511 cm⁻¹ peak which is attributed to silicon nano-crystals. The downshift of this frequency from 520 cm⁻¹ could be due to the compressive stress and grain size related effects [181, 182]. We observe these two peaks only for $R_{CH_4} = 0.54$ and 0.69. This indicates presence of nc-Si grains and reveals that also these layers have a mixed phase structure. For $R_{CH_4} = 0.85$, we observe only a broad peak at around 480 cm⁻¹ indicating its completely amorphous phase.

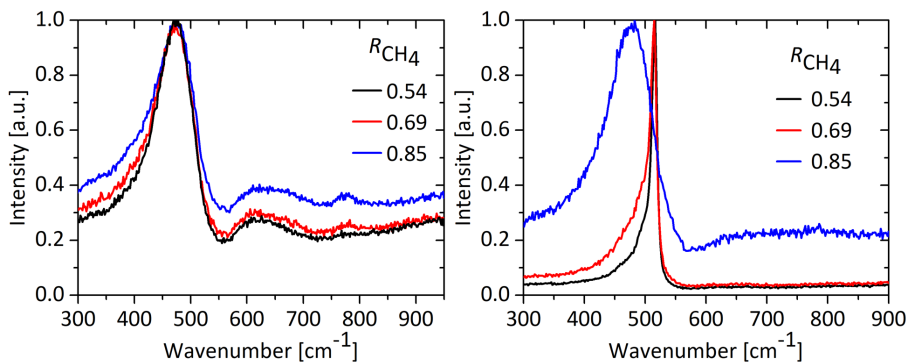


Figure 3.7: Raman measurements of n-type doped poly-SiC_x with varying R_{CH_4} for (a) as deposited layers (b) annealed layers.

Real part of refractive index

SE measurements reported in Figures 3.8(a) and 3.8(b) show the real part of the refractive index of our poly-SiO_x and poly-SiC_x layers, respectively, with intrinsic hydrogenated amorphous silicon (a-Si:H) and n-type c-Si as references. In general, from c-Si reference to poly-SiO_x and poly-SiC_x layers, we see two trends: (i) a decrease of peak value and (ii) a peak shift towards higher wavelengths for increasing R_{CO₂} and R_{CH₄}, respectively. We find that n obtained for poly-SiO_x layers decreases with increasing R_{CO₂} in the entire wavelength range from 300 to 2000 nm. For poly-Si (R_{CO₂} = 0) layer, as expected, n is quite similar to that of n-type c-Si. We also observe that, as the R_{CO₂} increases, the peak value of n decreases down to 3.9, approaching the value of 2.85 for longer wavelengths. The decrease in peak value of n is another indication that our poly-SiO_x becomes more amorphous with increasing R_{CO₂}, as supported by Raman measurements (see Figure 3.6(a)). Similarly, for n-type doped poly-SiC_x layers, the peak value of n decreases with increasing R_{CH₄}, even though already for wavelengths longer than 800 nm all trends are closely bundled (see Figure 3.8(b)).

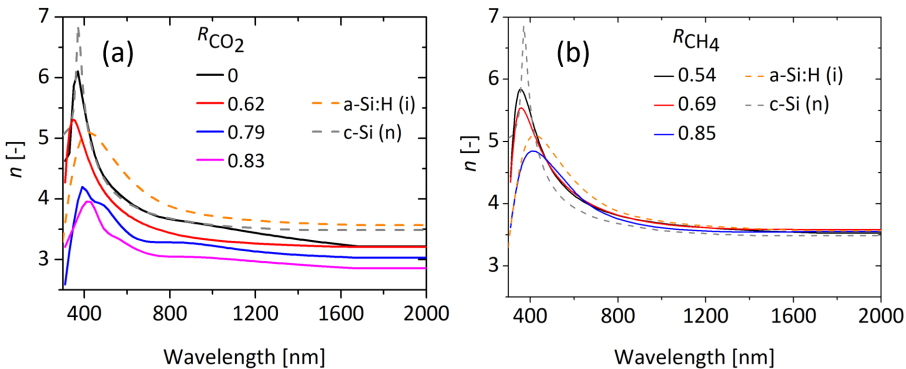


Figure 3.8: Refractive indices of n-type doped (a) poly-SiO_x or (b) poly-SiC_x layers with varying R_{CO₂} or R_{CH₄}, respectively.

Absorption coefficients from PDS

Figures 3.9(a) and 3.9(b) show the absorption coefficients of n-type doped poly-SiO_x and poly-SiC_x layers respectively from PDS measurements. In both cases, we used a-Si and n-type doped c-Si (10²⁰ cm⁻³ and 10²¹ cm⁻³ doping concentrations) as references. The absorption coefficients of n-type doped c-Si with doping concentrations 10²⁰ cm⁻³ and 10²¹ cm⁻³ have been generated using equations 3.5 and 3.6 [165]. Our poly-SiO_x layers, being partly amorphous and partly crystalline as previously shown by Raman measurements, are less absorptive than a-Si and more absorptive than c-Si in the visible region. At longer wavelengths, the absorp-

tion coefficients of poly-SiO_x layers are within the reference lines of doped c-Si. This indicates that our layers have doping concentration in the range between 10²⁰ cm⁻³ and 10²¹ cm⁻³. We observe that by increasing R_{CO₂}, the absorption coefficient increases in the visible region but decreases in the near infrared region. In other words, poly-SiO_x layers absorb more than poly-Si (R_{CO₂} = 0) in the visible region, while they are more transparent in the near infrared region with increasing R_{CO₂}. For poly-SiC_x layers, the absorption coefficients increase for increasing R_{CH₄} in the visible and near infrared region (see Figure 3.9b). In other words, poly-SiC_x layers tend to absorb more in the visible and near infrared region as R_{CH₄} increases. To describe this phenomenon further investigation is needed.

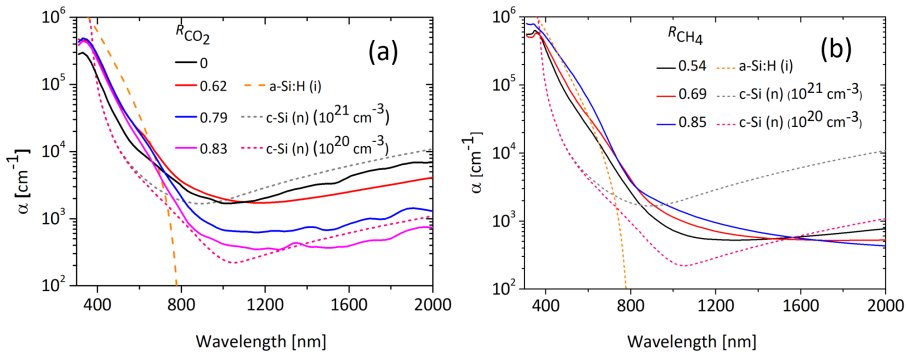


Figure 3.9: Absorption coefficients from PDS measurements of n-type doped (a) poly-SiO_x and (b) poly-SiC_x layers with varying R_{CO₂} and R_{CH₄}, respectively. Intrinsic amorphous silicon and c-Si (characterized by two different doping concentrations) were used as reference.

3.3.2. RT measurements on c-Si substrate

Flat versus textured c-Si wafer substrates

Figure 3.10(a) shows wavelength-dependent R and T spectra of flat samples, a bare c-Si wafer (F0) and a c-Si wafer double-side coated with 30-nm thick layers of poly-SiC_x (F1). Note that in all cases 1-R and T are plotted, so that one can observe the absorbance A directly from the graph in terms of (1 - R) - T. As expected, below 900 nm wavelength the c-Si wafer is opaque (T = 0). Beyond 1200 nm, c-Si is known to have a low absorption coefficient and the flat c-Si wafer hardly absorbs any light (A ≈ 0). Sample F1 also has a low absorbance for wavelengths larger than 1200 nm. If we derive absorption coefficients from this value, the error margin will be large due to the weakness of the absorbance compared to the measurement error. This is the limitation in obtaining the absorption coefficient of weakly absorbing films from RT measurements, at least for flat samples.

Next, referring to Table 3.2, the textured samples X0 to X1 are considered,

whose measured 1-R and T spectra are shown in Figure 3.10(b). The grey symbols show the results of sample X0, the bare double-side textured wafer. Here, we focus on the absorptance for wavelengths longer than 1200 nm. Due to light trapping, texturing has amplified the long-wavelength absorptance in the c-Si wafer, corresponding to an increase in path length of light [183]. The blue symbols show the measured spectra of double-side textured sample X1 symmetrically coated with 30-nm thick poly-SiC_x layers. Compared to sample F1, the absorptance is now increased. This suggests that the texture not only enhances the absorptance in the c-Si wafer, but also that of the thin film deposited on top of the surface textures. Similarly, RT measurements were performed on sample X2 (double-side textured wafer symmetrically coated with 60-nm thick poly-SiO_x layers). The corresponding measurement results are shown in Figure 3.11(a). The results above indicate that using symmetric, double-side textured wafers, the weak absorption of light at wavelength longer than 1200 nm could be successfully amplified and detected with RT measurements.

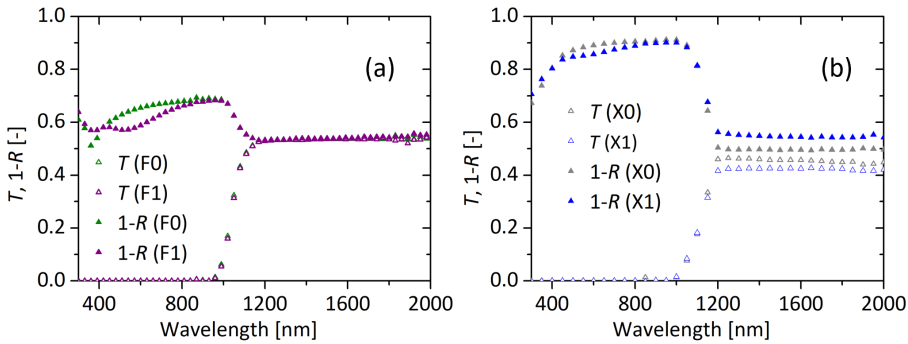


Figure 3.10: Wavelength-dependent spectra from RT measurements (1-R and T) of (a) F0 and F1 samples and (b) X0 and X1 samples. For a description of the samples, refer to Table 3.2.

Verifying PDS absorption coefficients

To verify if the absorption coefficients obtained from PDS of n-type doped poly-SiO_x and poly-SiC_x layers can be used for optical modelling, we have performed simulations using GenPro4. The structure simulated has the thin film layer structure (poly-SiO_x or poly-SiC_x) deposited on both sides of the textured wafer, as shown in Figure 3.1(b). The optical model also incorporates 1.5-nm thick NAOS-based tunnelling SiO₂. These simulations use α obtained from PDS and n from ellipsometry model as input to generate R and T spectra. The input thickness of the layer on textured wafer is calculated by dividing the layer's thickness on flat surface by a factor of 1.7. For thickness values used in optical simulations refer to Table 3.2. Generated R and T spectra have been compared with their

measured counterparts as shown in Figure 3.11a and 3.11b for sample X2 and X1, respectively. The corresponding absorbance and absorption coefficients of poly-SiO_x and poly-SiC_x layers are shown in Figures 3.12a and 3.12b, respectively. A similar analysis has been done for p-type doped poly-SiO_x and poly-SiC_x layers (see Figure 3.13(a) and Figure 3.13(b)).

We observe that the generated curves fit the measured curves quite well from 400 nm to 1200 nm. In the wavelength range between 300 and 400 nm, the curves do not fit for poly-SiO_x and poly-SiC_x layers due to their transmittance being below 1%. This is the case of our CSPCs under test. Also, for wavelengths longer than 1200 nm, we do not observe an accurate fit in case of poly-SiO_x and poly-SiC_x layer. Referring to the flowchart in Figure 3.5, we passed to the IM approach for extracting α directly from RT measurements.

Inverse modelling (IM) approach

Choosing values of C and x in Equation 3.7, FCA coefficients can be derived for the CSPCs under test. The fit of the bare textured sample X0 yields $C = 0.025$ and $x = 2.0$. These values for the c-Si bulk absorption coefficient are then also used in all subsequent IM simulations. In case of sample X2, textured symmetrical 60-nm thick n-type doped poly-SiO_x layer on c-Si wafer, the fit yields $C = 840$ and $x = 1.65$. With respect to the simulated R and T spectra based on α from PDS, there is now a very good agreement measured spectra (see Figure 3.11a). In case of X1 sample, textured symmetrical 30-nm thick n-type doped poly-SiC_x layer on c-Si wafer, the fit yields $C = 650$ and $x = -0.8$, which result in even closer agreement between simulated and measured spectra (see Figure 3.11b). In case of the X4 sample, a textured symmetrical 37-nm thick p-type doped poly-SiO_x layer on c-Si wafer, the fit yields $C = 4200$ and $x = 0.5$ (see Figure 3.13(a)). For X3 sample, a textured symmetrical 30-nm thick p-type doped poly-SiC_x layer on c-Si wafer, $C = 1290$ and $x = -2.5$ give a close agreement between measured and simulated absorbance spectra (see Figure 3.13(b)).

3.4. Discussion

3.4.1. Absorption coefficients

The obtained α from both PDS and IM approaches of some n-type CSPCs layers under test (X2 and X1) are shown in the bottom panels of Figures 3.12(a) and 3.12(b), respectively. In the same Figures, we report also the absorbance spectra, which include both contributions of the bulk c-Si wafer and of the layers sandwiching it. For n-type doped poly-SiO_x layers, we get a fit with an average deviation of 4.3% and 0.7% from PDS and IM approaches, respectively. For n-type doped

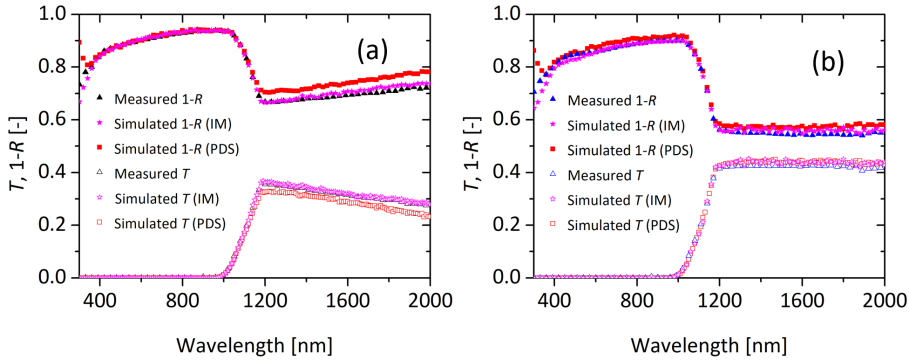


Figure 3.11: GenPro4 simulation results using optical properties from PDS or IM approach compared to measured 1-R and T spectra measurements for (a) X2 and (b) X1 samples. For a description of the samples, ref to Table 3.2.

poly-SiC_x layers, we get a fit with an average deviation of 1.6% and 0.8% from PDS and IM techniques respectively. The obtained α , also from both PDS and IM approaches, of p-type CSPCs layers under test (X4 and X3) are shown in the bottom panels of Figures 3.13a and 3.13b, respectively. In the same Figures, the absorbance spectra are also reported. For p-type doped poly-SiO_x layer, we get an average deviation of 7.6% and 1.1% for PDS and IM approaches, respectively. For p-type doped poly-SiC_x layer, we get an average deviation of 2.9% and 1% for PDS and IM approaches, respectively.

We find that these absorption coefficients successfully estimate FCA in the wavelength range above 800 nm, which ellipsometer is unable to detect. While the PDS approach proves to be straightforward with regards to sample preparation, the IM approach ultimately shows a better fit for optical modelling of CSPCs on c-Si substrate. Thus, α from IM approach can be used as an input for optical modelling of solar cells endowed with poly-SiO_x and poly-SiC_x CSPCs. In this way, parasitic losses will be better quantified and both single- and multi-junction solar cells will be further improved.

We observe that the absorption coefficients obtained from both techniques have differences especially in the UV and IR part of the spectrum. This is ascribed to the likely difference in growth and subsequent crystallization of the layers under test on the different substrates used in these two methods. By obtaining absorption coefficients from PDS and IM techniques independently, we could compare the optical behaviour of the layer on both quartz and c-Si substrates. Using the advantages of both the techniques, accurate absorption coefficients for optical modelling can be obtained in the wavelength range from 300 to 2000 nm for both poly-SiO_x and poly-SiC_x layers either on quartz or on textured c-Si wafer.

PDS can be used to measure absolute absorption directly. Using this technique, the absorption coefficients can be derived as discussed in sections 3.2.3 and 3.2.4. However, its limitation is that it does not predict correct absorption when the transmittance is below 1%. On the other hand, the IM approach helps in getting data at long wavelengths for CSPCs in solar cells. This approach depends on the absorption coefficients from SE in the UV/visible range but adds the FCA component, which starts to play a role for wavelength longer than 800 nm.

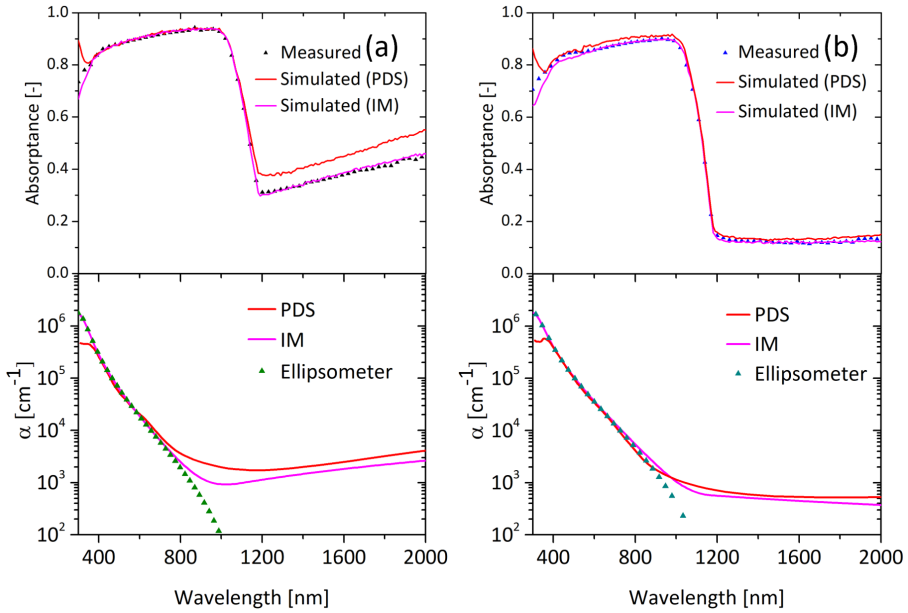


Figure 3.12: Top panels: overall absorbance in n-type doped layer / textured c-Si substrate symmetric samples; bottom panels: absorption coefficient of the CSPC layer under test. (a) poly-SiO_x ($R_{CO_2} = 0.62$); (b) poly-SiC_x ($R_{CH_4} = 0.69$).

3.4.2. Effect of R_{CO_2} , R_{CH_4} , R_{PH_3} , and $R_{B_2H_6}$ on Optical Properties

The poly-SiO_x and poly-SiC_x CSPCs are mixed phase materials and, by varying, respectively, R_{CO_2} and R_{CH_4} , their optical properties can be altered. We observe that their n decreases with increasing R_{CO_2} or R_{CH_4} [63]. Thus, n can be somewhat tuned to minimize front reflection in FBC cells endowed with these CSPCs. We also note that FCA decreases for n-type doped poly-SiO_x layers in the infrared region with respect to the reference poly-Si ($R_{CO_2} = 0$). The reference poly-Si ($R_{CO_2} = 0$) can be found in Ref. [38]. The probable reason could be that, with increasing R_{CO_2} , the a-SiO_x phase in the poly-SiO_x layer is expected to increase, as supported by Raman measurements (see Figure 3.6a). Since the doping efficiency

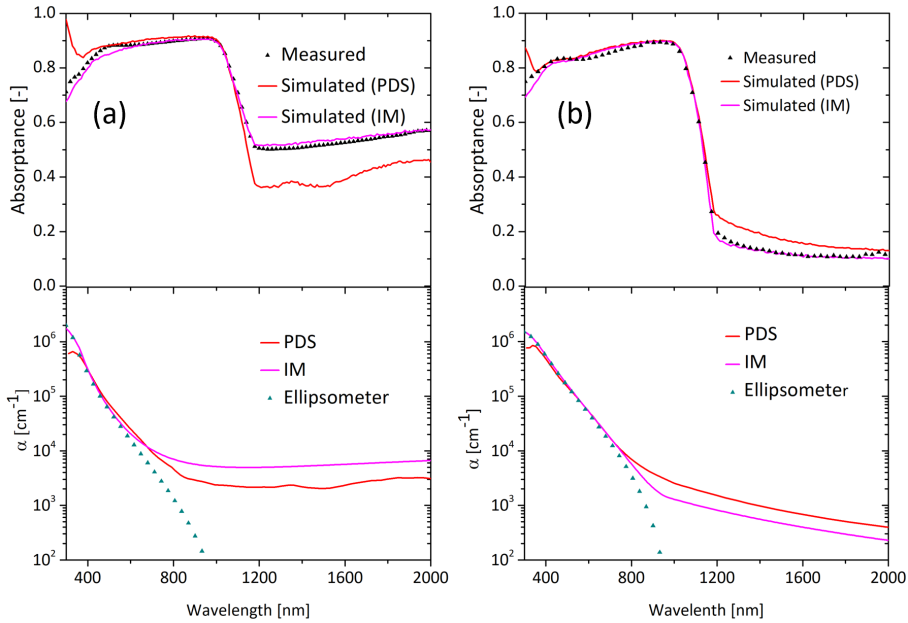


Figure 3.13: Top panels: overall absorbance in p-type doped layer / textured c-Si substrate symmetric samples; bottom panels: absorption coefficient of the CSPC layer under test. (a) poly-SiO_x ($R_{CO_2} = 0.2$); (b) poly-SiC_x ($R_{CH_4} = 0.69$).

of the crystalline phase is higher than that of the amorphous phase [184], the incorporation of the dopants into the a-SiO_x phase is more difficult, thereby decreasing FCA for increasing R_{CO_2} .

Figures 3.14(a) and 3.14(b) show the analysis of additional samples for n-type doped poly-SiO_x and p-type doped poly-SiO_x layers using IM analysis with different R_{PH_3} and $R_{B_2H_6}$, respectively. A similar analysis is shown for n-type and p-type doped poly-SiC_x layers in Figures 3.15(a) and 3.15(b), respectively. Samples with ratio $R_{PH_3} = 0.54$ (Figure 3.14(a)) and $R_{PH_3} = 0.13$ (Figure 3.15(a)) are the reference samples used in Figure 3.12(a) and 3.12(b), respectively. Similarly, samples with ratio $R_{B_2H_6} = 0.38$ (Figure 3.14(b)) and $R_{B_2H_6} = 0.13$ (Figure 3.15(b)) are the reference samples shown in Figure 3.13(a) and 3.13(b), respectively. As expected, we find that with the increase in doping gas flow ratio, the FCA increases. In these cases, our IM approach not only proves to be effective with regards to textured CSPC layers, but also to carry out the expected trend.

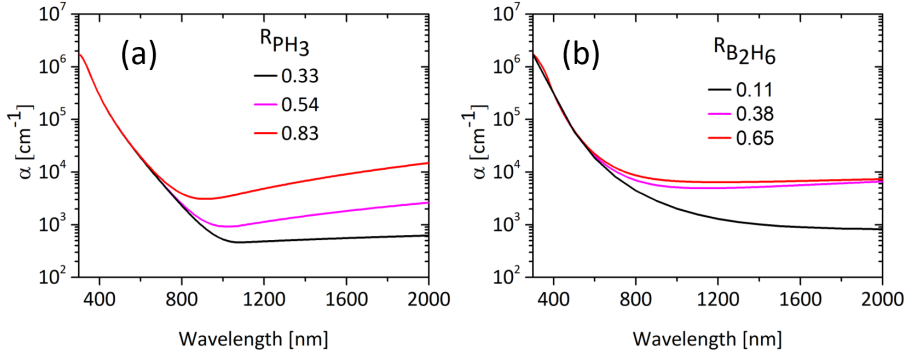


Figure 3.14: Variation of absorption coefficients with changing R_{PH_3} and $R_{\text{B}_2\text{H}_6}$ of (a) n-type doped poly-SiO_x ($R_{\text{CO}_2} = 0.62$); (b) p-type doped poly-SiO_x ($R_{\text{CH}_4} = 0.2$).

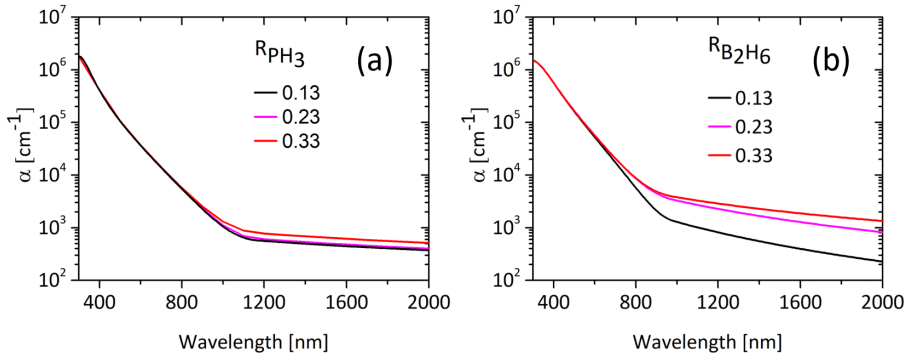


Figure 3.15: Variation of absorption coefficients with changing R_{PH_3} and $R_{\text{B}_2\text{H}_6}$ of (a) n-type doped poly-SiC_x ($R_{\text{CO}_2} = 0.69$); (b) p-type doped poly-SiC_x ($R_{\text{CH}_4} = 0.69$).

3.4.3. Effect of thickness on absorption coefficients extracted by IM

We performed additional experiments, in which we have deposited different thickness of p-type doped poly-SiO_x layer ($R_{\text{CO}_2} = 0.2$ and $R_{\text{B}_2\text{H}_6} = 0.38$). A fixed absorption coefficient obtained from inverse modelling approach (as shown in Figure 3.13(a)) of p-type doped poly-SiO_x layer has been used. The simulated absorbance of this layer deposited on both sides of double side textured wafer for thickness values of 10 nm, 15 nm and 37 nm is shown in Figure 3.16(a) and confirms that the thicker the layer is, the higher the absorbance is. With only one refractive index and absorption coefficient data sets, we managed to get a very good fit with an average deviation of only 1%, 0.8% and 1.2% for samples with thickness of 10 nm, 15 nm and 37 nm, respectively. A similar analysis was done for p-type doped poly-SiC_x layer ($R_{\text{CH}_4} = 0.69$ and $R_{\text{B}_2\text{H}_6} = 0.13$). Using the

absorption coefficient of this p-type doped poly-SiC_x layer (as shown in Figure 3.13(b)), we measured and simulated the total absorbance in layers deposited on both sides of double side textured wafer for different thicknesses. The results are shown in Figure 3.16(b), where we demonstrate an average deviation of 1%, 0.6% and 1.2% for samples with thickness 30 nm, 51 nm and 90 nm, respectively. Again, this shows that the absorption coefficient obtained from IM approach for a single layer thickness can be used to simulate absorbance of layers of different thicknesses.

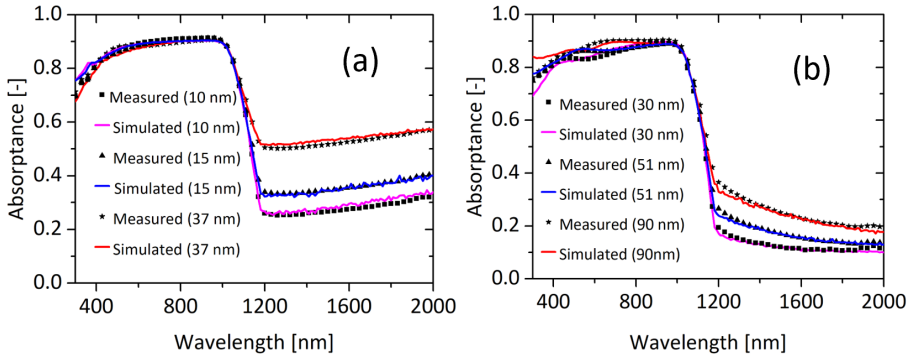


Figure 3.16: Measured and simulated overall absorbance in p-type doped layer / textured c-Si substrate symmetric samples (a) p-type doped poly-SiO_x ($R_{CO_2} = 0.2$ and $R_{B_2H_6} = 0.38$); (b) p-type doped poly-SiC_x ($R_{CH_4} = 0.69$ and $R_{B_2H_6} = 0.13$).

3.5. Conclusions

In this study, we demonstrated that, from PDS or IM approach, we could successfully extract the absorption coefficients of n-type and p-type doped poly-SiO_x and poly-SiC_x layers on fused silica quartz substrate and on textured c-Si wafer substrate, respectively, in the extended wavelength range from 300 to 2000 nm. The absorption coefficients of n-type and p-type doped poly-SiO_x and poly-SiC_x layers obtained from PDS and IM approach have differences. These most likely stem from the different substrates used in these two techniques. By using the RT measurement technique on double-side textured samples, we could successfully measure the weak FCA in our CSPCs layers. Using the absorption coefficients from the IM approach, we got a good fit (around or less than 1% average deviation) between measured and simulated R and T spectra. Obtained α can now be used as an input to study the optical behaviour of single- and multi-junction solar cells endowed with poly-SiO_x and poly-SiC_x CSPCs. We also analysed that by changing the R_{CO_2} and R_{CH_4} , the optical properties of poly-SiO_x and poly-SiC_x layers can be altered. With increase in R_{pH_3} and $R_{B_2H_6}$, FCA increases in our CSPCs.

4

Comparing optical performance of perovskite/silicon tandem architectures under real-world conditions

This chapter is based on the following publication :

M. Singh, R. Santbergen, I. Syifai, A. Weeber, M. Zeman, O. Isabella, "Comparing optical performance of a wide range of perovskite/silicon tandem architectures under real world conditions", *Nanophotonics* 10(8), 2043-2057 (2021). DOI: <https://doi-org.tudelft.idm.oclc.org/10.1515/nanoph-2020-0643>

Abstract

Since single junction c-Si solar cells are reaching their practical efficiency limit. Perovskite/c-Si tandem solar cells hold the promise of achieving greater than 30% efficiencies. In this regard, optical simulations can deliver guidelines for reducing the parasitic absorption losses and increasing the photocurrent density of the tandem solar cells. In this work, an optical study of 2, 3 and 4 terminal perovskite/c-Si tandem solar cells with c-Si solar bottom cells passivated by high thermal-budget poly-Si, poly-SiO_x and poly-SiC_x is performed to evaluate their optical performance with respect to the conventional tandem solar cells employing silicon heterojunction bottom cells. The parasitic absorption in these carrier selective passivating contacts has been quantified. It is shown that they enable greater than 20 mA/cm² matched implied photocurrent density in un-encapsulated 2T tan-

dem architecture along with being compatible with high temperature production processes. For studying the performance of such tandem devices in real world irradiance conditions and for different locations of the world, the effect of solar spectrum and angle of incidence on their optical performance is studied. Passing from mono-facial to bifacial tandem solar cells, the photocurrent density in the bottom cell can be increased, requiring again optical optimization. Here, we analyse the effect of albedo, perovskite thickness and band gap as well as geographical location on the optical performance of these bifacial perovskite/c-Si tandem solar cells. Our optical study shows that bifacial 2T tandems, that also convert light incident from the rear, require radically thicker perovskite layers to match the additional current from the c-Si bottom cell. For typical perovskite bandgap and albedo values, even doubling the perovskite thickness is not sufficient. In this respect, lower bandgap perovskites are very interesting for application not only in bifacial 2T tandems but also in related 3T and 4T tandems.

4.1. Introduction

Crystalline silicon (c-Si) solar cells dominate the photovoltaic market due to their relatively high efficiency, low manufacturing costs and long-term stability. However, single junction c-Si solar cells are reaching their practical efficiency limit of about 27% [95, 153]. One way to improve this efficiency limit is by stacking high bandgap cell on top of low bandgap cell in tandem configuration to reduce thermalization losses. Perovskite/perovskite [185–188] and perovskite/c-Si [47, 88, 91, 101, 110, 189–203] tandem solar cells are gaining lot of attention in this regard. This is because perovskite solar cells have a sharp optical edge, a long diffusion length, a tuneable bandgap range and a good short wavelength response [74, 204–206]. These properties make perovskite-based solar cells ideal top cell in combination with c-Si bottom cell to form tandem solar cells. Several c-Si bottom cell technologies can be considered for this application. So far, most of the high efficiency tandem solar cells have been fabricated using silicon heterojunction (SHJ) bottom cell [88, 91, 189, 197–200, 202], which are processed at temperatures well below 250 °C. On the other hand, widespread industrial c-Si solar cells are compatible with high temperature processes such as impurity gettering, thermal oxidation, dopants diffusion, and firing through metallization. In this respect, perovskite/silicon-homojunction tandem cell has been demonstrated [207]. Carrier-selective passivating contacts (CSPCs) based on poly-Si [59, 151–153, 208–211], poly-SiO_x [38, 156] or poly-SiC_x [63, 158] are typically formed at temperatures higher than 800 °C. Hence, they are excellent candidates for increasing the efficiency of high-thermal budget c-Si solar cells [208, 209, 212]. A potential drawback is their parasitic absorption, especially when they are deployed at the

front side of the c-Si solar cell. These high temperature CSPCs have also been used in fabricating high efficiency perovskite/c-Si tandem solar cells [47, 110]. In view of potential efficiencies well above 30%, perovskite/c-Si tandem solar cells with bottom cells passivated with different CSPCs can significantly reduce the leveled cost of electricity [213]. However, an important step in improving the efficiency of such tandem devices is by design optimization. Such design optimization can be performed by optical and electrical simulations. Researchers in the past have focussed on the optical simulations of perovskite/c-Si tandem solar cells with mostly silicon heterojunction c-Si solar cells [197, 214–216]. However, research regarding the optical simulations of perovskite/c-Si tandem solar cells with high temperature CSPCs is less developed. The abovementioned issue of increased parasitic absorption in high temperature CSPC occurs mostly in the shorter wavelength range ($\lambda < 800$ nm). It is therefore expected to be less severe in perovskite / silicon tandems where these shorter wavelengths are largely absorbed by the perovskite top cell before reaching the CSPCs. The parasitic absorption losses in high temperature CSPC in perovskite / silicon tandems have thus far not been quantified and this will be one of the objectives of this work. In this work, we have optically simulated perovskite/c-Si tandem solar cells with such high temperature CSPCs in GenPro4 software [114] and analysed different architectures, such as monolithically integrated two terminal (2T), three terminal (3T) and mechanically stacked four terminal (4T) perovskite/c-Si tandem solar cells. The performance of tandem solar cells endowed with poly-Si, poly-SiO_x or poly-SiC_x CSPCs are compared with that of tandem solar cells comprising a heterojunction bottom solar cell. Finally, as these tandem solar cells are used in modules, where encapsulation materials such as glass and Ethylene-Vinyl Acetate (EVA) are deployed, we have also studied the optical effect of encapsulation. 2T perovskite/c-Si tandem solar cells require current matching between the top perovskite solar cell and the bottom c-Si solar cell. The advantage of 4T tandem solar cell is that it does not require current matching. However, fabrication of top cell and bottom cell separately requires additional transparent contacts, which adds optical losses and fabrication costs. The pros and cons of mechanically stacked 4T tandem and monolithically integrated 2T are well documented [217, 218]. The advantages of both 2T and 4T configurations are combined in a 3T tandem configuration, which we consider as well. The 3T tandem configuration that we consider has one contact at the front and two contacts interdigitated at the rear [219]. Also, different tunnel recombination junction (TRJ) layers are studied to find the junction material with the most suitable optical properties for perovskite/c-Si tandem solar cells with CSPCs. Here, we have compared a wide range of tandem configurations and optimized the thickness of each layer to achieve maximum photocurrent current density and quantified the parasitic absorption losses in the high temperature

CSPCs. The optical simulations of perovskite/c-Si tandem solar cells are done at Standard Test Conditions (STC) [17]. However, in real-world operating conditions, the solar cell is not (always) illuminated perpendicularly, and the absorption of photons is influenced by the apparent position of the sun and spectral conditions [220, 221]. Here, we simulate and study the effect of different spectra and angles of incidence. In addition, we consider bifacial tandem configurations, which can also convert the light incident on the rear side e.g. after ground reflection. For these solar cells, we study the effect of albedo, perovskite thickness and bandgap on the optical performance of the tandem solar cells for different locations in the world. This contribution is organized as follows. We evaluate the potential of several 2T, 3T and 4T architectures and we study their optical behaviour in real-world conditions. Finally, we discuss the results and draw our conclusions.

4.2. Evaluation of optical potential of device architectures

Cell and module level modelling approaches and the modelling framework have been explained in the supplementary information A. In this section, we use the validated optical model (see supplementary information A) to quantify the implied photocurrent density of the perovskite/c Si tandem solar cells. Our goal is to explain the subtle differences in implied photocurrent between (i) various electrical configurations (2T, 3T and 4T), (ii) various c-Si bottom cell architectures (with poly-Si, poly-SiO_x and poly-SiC_x CSPCs), and (iii) encapsulated and un-encapsulated tandems. An overview of the 2T, 3T and 4T perovskite/c-Si tandem structures simulated in GenPro4 are shown in Fig. 4.1. Aside the case of the top cell in the 4T tandem configuration, for which it is still challenging to demonstrate a perovskite solar cell on a glassy textured substrate, all other configurations under test are endowed with textured surfaces. This choice was made not only to simulate the highest possible J_{ph} in tandem devices, but also to realize a flat broadband reflectance spectrum that allows for high optical performance also in encapsulated devices. Unless explicitly stated, simulated 2T and 3T tandem devices are endowed with a $p^+ - nc - Si : H / n^+ - nc - Si : H$ stack that has the role of a TRJ, as in the validated 2T tandem solar cell reported in Ref. [88]. In this section we consider 'standard' illumination conditions (AM1.5 spectrum and normal incidence). These results will lay the foundation for the analysis of real-world illumination conditions that will be considered in Section 4.3.

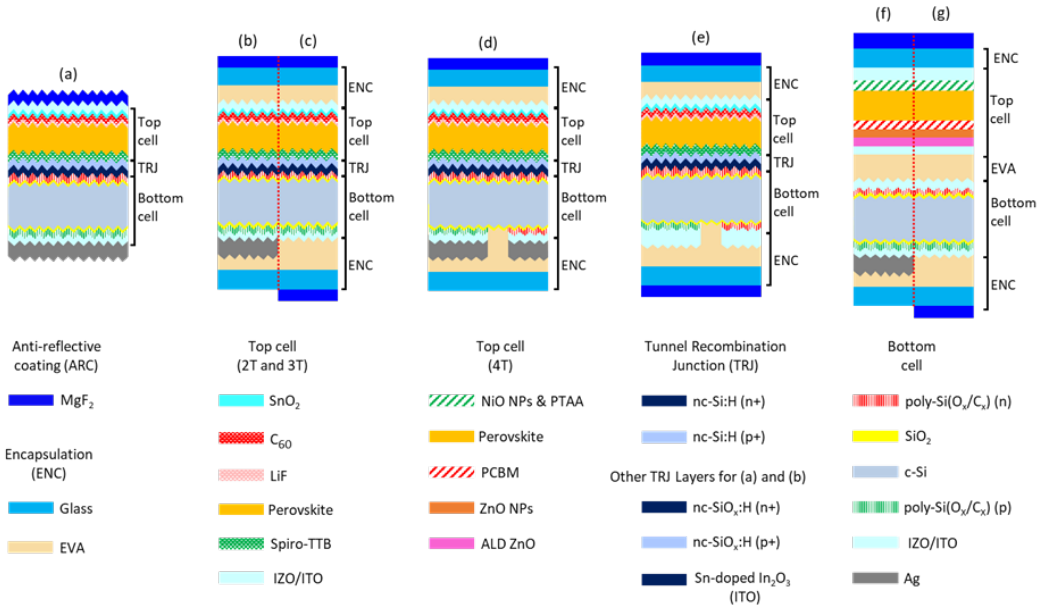


Figure 4.1: Simulated tandem structures: (a) 2T, (b) encapsulated 2T, (c) encapsulated 2T bifacial, (d) encapsulated 3T, (e) encapsulated 3T bifacial, (f) encapsulated 4T, and (g) encapsulated 4T bifacial.

4.2.1. 2T perovskite/c-Si tandem solar cells

Referring to Fig. 4.1(a), we compare here the optical performance of 2T tandem configurations comprising poly-Si, poly-SiO_x or poly-SiC_x CSPCs in the bottom cell and with simulation inputs, such as optical properties and thicknesses of each layer, as explained in supplementary information A. Fig. 4.2(a) shows the wavelength-dependent reflectance and absorptance spectra for the 2T tandem solar cell with poly-SiO_x passivated c-Si solar cell. The useful absorption in perovskite and c-Si solar cells is shown by orange and grey lines, respectively. Integrating these spectra over the AM 1.5 spectrum gives an implied photocurrent density of 20.2 mA/cm², as the top and bottom cell photocurrent densities were perfectly matched by tuning the perovskite thickness to 545 nm. The white area represents the reflection loss, and the remaining coloured areas represent the parasitic absorption losses in supporting layers, such as transparent contacts (light blue) or electron transport layer (light red). The absorption losses in the n- and p-type poly-SiO_x CSPCs, indicated by the red and dark green areas, correspond to 0.32 mA/cm² and 0.63 mA/cm², respectively. As anticipated, because the perovskite layer on top absorbs most shorter wavelength light ($\lambda < 800$ nm), these parasitic absorption losses in the poly-SiO_x CSPC are much lower than in case

of a single junction device, especially for the light-facing n-type poly-SiO_x (see supplementary information A). When used in modules, these solar cells are encapsulated with glass and EVA (see Fig.4.1 (b)). The glass and EVA absorb 0.46 mA/cm² and 0.21 mA/cm², respectively, and cause additional reflection losses from the air/glass interface. As a result, the implied photocurrent density after current matching is 19.49 mA/cm², a reduction of 3.5% compared to the un-encapsulated case. Because the absorption in glass is slightly larger in the infrared compared to the visible part of the spectrum, a slightly lower perovskite thickness of 515 nm is now required to match the top and bottom cell currents. A similar analysis was performed for 2T tandem solar cell with poly-SiC_x and poly-Si CSPCs. Fig. 4.2(b) reports the wavelength-dependent reflectance and absorptance spectra for 2T tandem with poly-SiC_x passivated CSPCs. Again, the perovskite thickness is tuned to achieve a matched implied photocurrent density. The reference tandem with SHJ has the thinnest supporting layers (15-nm thick electron transport and hole transport stacks, see supplementary information A), exhibiting the lowest parasitic absorption losses and thus giving the highest J_{ph} . The poly-SiO_x is more absorbing than poly-SiC_x for wavelengths longer than 1000 nm, but slightly less absorbing for shorter wavelengths (see Fig. 4.2(b) and supplementary information A). These two effects compensate each other and thus numerically similar J_{ph} for poly-SiC_x and poly-SiO_x tandems is obtained. On the other hand, as both n-type and p-type poly-Si materials, used in this work, are less absorptive than their poly-SiO_x and poly-SiC_x counterparts, the performance of the tandem with poly-Si CSPCs is higher than that of the other high-thermal budget CSPCs but is still slightly lower than the SHJ reference. We fixed a priori the thickness of the high-thermal budget CSPCs to comply with the typical architecture of reported devices in literature that do not show fill factor issues. Given the full planar deployment of such layers in tandem devices and their contact with the TRJ on one side and with the transparent conductive oxide (TCO) on the other side, it could be optically beneficial to attempt their thinning. However, we leave this sensitivity study to a more experimental setting for also verifying the electrical behaviour of the resulting devices. Table 4.1 gives an overview of the perovskite thickness with the matched implied photocurrent density achieved in the 2T tandem with different CSPCs in both un-encapsulated and encapsulated cases.

Tunnel recombination junction

The tunnel recombination junction is an important part of the 2T tandem solar cell. From the optical point of view, the tunnel recombination layers should be transparent to the light transmitted by the perovskite absorber so that it can reach the bottom c-Si solar cell. Also, the real part of refractive index should be in between the refractive indices of the layer above and below of the TRJ

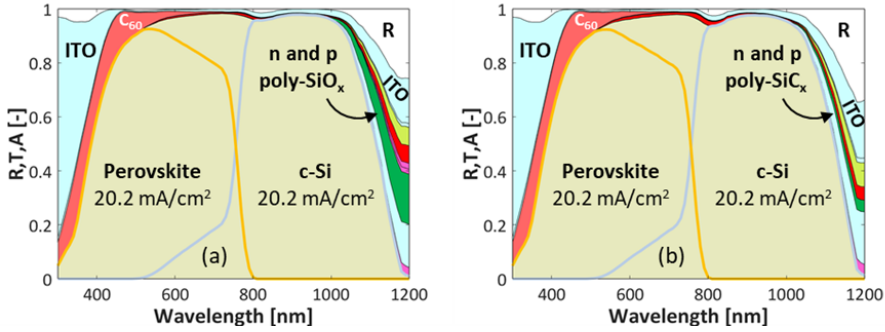


Figure 4.2: Reflectance and absorbance of 2T perovskite/c-Si tandem solar cell (see Fig. 4.1(a)) with top cell as in Ref. [88] and bottom cell as (a) poly-SiO_x passivated c-Si solar cell or (b) poly-SiC_x passivated c-Si solar cell.

(in this case Spiro-TTB and n-type doped poly-Si, poly-SiO_x or poly-SiC_x). The electrical requirements of a tunnel recombination junction are important as well [222], but they are outside the scope of this optical study. Results so far rely on doped nc-Si:H layers [88] used as TRJ. In this section, we explore the possibility of using nc-SiO_x:H [223–225] or Sn-doped In₂O₃ (ITO) TCO as TRJ layers (see Table 4.1). We find that by using nc-SiO_x:H as TRJ, J_{ph} values nearly the same as those computed for tandems with nc-Si:H TRJ are obtained. This is due to two factors cancelling out: (i) the nc-SiO_x:H absorbs less compared to nc-Si:H, while (ii) the nc-SiO_x:H has a refractive index value less ideally situated between Spiro and CSPC, which increases the reflection losses slightly. Note that because of this increased reflectance, perovskite layers have to be used that are 10 to 15 nm thinner. The TCO-based TRJ, on the other hand, parasitically absorbs more than the other two TRJs, so the matched J_{ph} is lower and this trend is observed for all the four CSPCs considered in Table 4.1. It also includes the case of direct contact between Spiro-TTB (Hole transporting material of the perovskite) and CSPCs. We observe that in this case, a slightly higher matched implied photocurrent density can be achieved due to less parasitic absorption in TRJ. However, the electrical performance of such tandems without TRJ would need further electrical investigations.

4.2.2. 3T perovskite/c-Si tandem solar cell

As shown in Fig. 4.1(d), the 3T tandem solar cell is optically very similar to the 2T tandem, but it has a c-Si IBC solar cell as the bottom cell. Thus, at the rear side of the device, there are alternating n-contact, gap, p-contact, gap, etc. These parts have slightly different optical properties. Since GenPro4 is a 1D simulator,

Table 4.1: Implied photocurrent density (J_{ph}) of 2T tandem with different CSPCs. SHJ stands for silicon heterojunction and is intended as reference.

TRJ	Un-encapsulated		Encapsulated	
	$p^+ - nc - Si:H/n^+ - nc - Si:H$			
	J_{ph} matched (mA/cm ²)	Perovskite thickness (nm)	J_{ph} matched (mA/cm ²)	Perovskite thickness (nm)
SHJ (ref.)	20.41	560	19.70	535
Poly-Si	20.34	560	19.64	527
Poly-SiO _x	20.20	545	19.49	515
Poly-SiC _x	20.20	535	19.53	510
TRJ	$p^+ - nc - SiO_x:H/n^+ - nc - SiO_x:H$			
	J_{ph} matched (mA/cm ²)	Perovskite thickness (nm)	J_{ph} matched (mA/cm ²)	Perovskite thickness (nm)
SHJ	20.41	550	19.70	520
Poly-Si	20.34	550	19.65	523
Poly-SiO _x	20.20	533	19.50	505
Poly-SiC _x	20.20	520	19.53	500
TRJ	Sn-doped In ₂ O ₃ (ITO)			
	J_{ph} matched (mA/cm ²)	Perovskite thickness (nm)	J_{ph} matched (mA/cm ²)	Perovskite thickness (nm)
SHJ	20.36	540	19.66	515
Poly-Si	20.28	540	19.61	515
Poly-SiO _x	20.14	520	19.45	497
Poly-SiC _x	20.15	510	19.50	490
No Tunnel Recombination Junction				
	J_{ph} matched (mA/cm ²)	Perovskite thickness (nm)	J_{ph} matched (mA/cm ²)	Perovskite thickness (nm)
SHJ	20.44	568	19.72	537
Poly-Si	20.39	565	19.66	535
Poly-SiO _x	20.22	547	19.51	517
Poly-SiC _x	20.24	541	19.56	514

separate simulations are performed for each of the n-contact, p-contact, and gap regions. The calculated absorptances are then combined into a weighted average, where the relative surface areas of n-contact (20%), p-contact (70%) and gap (10%) are used as the respective weights. Just as for the 2T tandem, the contacts of the 3T tandem can be endowed with poly-Si, poly-SiO_x or poly-SiC_x. In 3T configuration no current matching between top and bottom cell is required. In our simulation campaign, however, we kept the thickness of the perovskite absorber layer fixed at the value found to get current matching in 2T configuration (see Table 4.1). This choice was (i) to prevent the proposal of 3T devices with an overly thick top absorber, which could result in experimental issues, and (ii) to compare the performance of 3T tandems with their 2T configuration counterparts (see Section 4.4.1). Running our optical model, we found that the influence of TRJ layers for all cases of c-Si bottom cells on the optical performance of 3T tandem devices was negligible and due to the decoupling of J_{ph} between top and bottom cells. In this contribution we then report only the results related to the $p^+ - nc - Si : H/n^+ - nc - Si : H$ TRJ as in Ref. [88]. As an example, the wavelength dependent reflectance and absorptance spectra for an encapsulated 3T tandem with poly-SiO_x passivated c-Si bottom solar cell are given in Fig. 4.3. Aside the broadband increase in reflectance due to the presence of glass, we ob-

serve that this 3T tandem device exhibits an optical behaviour very similar to the un-encapsulated 2T tandem device reported in Fig. 4.2(a). Deploying an IBC architecture for the c-Si bottom cell, for which both contacts based on poly-SiO_x are placed at the rear of the tandem, one could expect a lower absorption loss in such layers with respect to the 2T tandem counterpart. However, this is not case because the top perovskite cell behaves optically very similarly as in the 2T tandem, absorbing most of the light before 800 nm and still exposing at longer wavelengths the parasitically absorptive behaviour of the poly-SiO_x layers. Very similar results are obtained in case of poly-Si and poly-SiC_x technologies. An overview of all the results with different CSPCs and for different tandem configurations are given in Table 4.2.

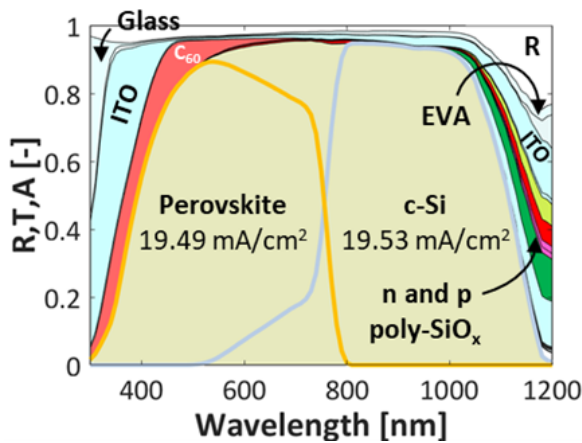


Figure 4.3: Reflectance and absorptance of 3T encapsulated perovskite/c-Si tandem solar cell (see Fig. 4.1(d)) with top cell and TRJ as in Ref. [88] and a c-Si IBC bottom cell passivated with poly-SiO_x CSPCs.

4.2.3. 4T perovskite/c-Si tandem solar cell

In the 4T perovskite/c-Si tandem solar cell, the top and bottom cells are mechanically stacked; thus, they are connected optically but not electrically. Similar to the previous case of 3T tandem configuration, the thickness of the perovskite absorber layer is fixed at 513 nm, which is the value found when validating our modelling platform with the device reported in Ref. [226] (see Fig. 4.1(f)). From an optical point of view, the main difference with 2T and 3T configuration is that in the 4T configuration the perovskite top cell is deposited front-to-back on a flat glass substrate while for the 2T and 3T configurations the perovskite top cell is deposited back-to-front on a textured c-Si bottom cell. From a fabrication point of view, it is so far challenging to fabricate a textured perovskite cell on glass.

Fig. 4.4(a) shows the reflectance and absorptance spectra for an encapsulated 4T tandem with poly-SiO_x passivated c-Si bottom solar cell. This diagram reveals that the flat top cell gives rise to significantly higher reflection losses (white area). Also, next to the n-type and p-type poly-SiO_x layers, which absorb around 0.29 and 0.61 mA/cm², respectively, the additional ITO layer at the rear side of the top cell results in an increase of parasitic absorption losses. The J_{ph} of top and bottom cells are therefore reduced to 19.35 and 18.25 mA/cm², respectively. In case of other CSPCs, a slight increase in bottom cell currents is observed due to lower free carrier absorption in the longer wavelengths (see Table 4.2). Although practically difficult to manufacture, into an attempt to increase the J_{ph} in the top cell, we imagined texturing the top perovskite solar cell. For comparing the 2T, 3T and 4T configurations, we considered the textured perovskite cell from Ref. [88] (see Fig. 4.4(b)). Owing to the texturing, the J_{ph} of the top cell increases, but the J_{ph} of the bottom cell is 18.84 mA/cm², which is lower than that of 2T tandem due to additional losses in ITO layers. Table 4.2 gives an overview of the J_{ph} of the various encapsulated tandem configurations for different CSPCs.

4

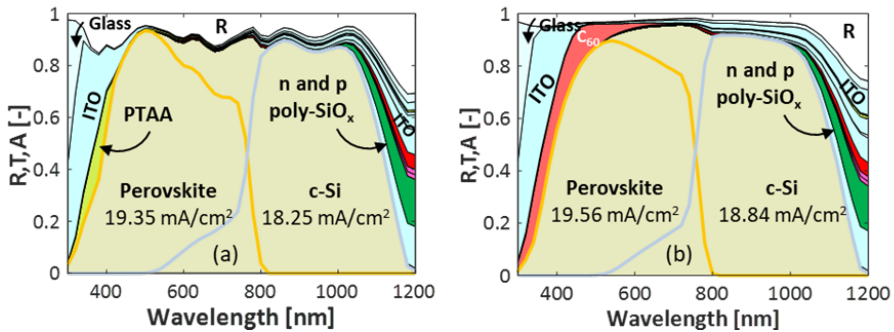


Figure 4.4: Reflectance and absorptance of 4T perovskite/c-Si tandem solar cell with (a) flat top cell as in Ref. [226] (see Fig. 4.1(f)) or (b) textured top cell as in Ref. [88] (Fig. 4.1(f)) but with textured top cell as in Fig. 4.1(b)). The c-Si bottom cell is passivated with poly-SiO_x CSPCs.

4.3. Real world conditions

The results presented thus far assume normal incidence and AM1.5 spectrum for the incident light. However, in real world conditions both the angle of incidence and spectral conditions vary simultaneously as the apparent sun position and cloud coverage vary with the time of day and year. In this section, we first study the individual effects of air mass (AM) and the angle of incidence (AOI) on the implied photocurrent density. To illustrate these effects, we consider the encapsulated 2T perovskite/c-Si tandem with bottom cell passivated with poly-SiO_x CSPC. We choose this CSPC because it is a new material whose optical performance in

tandems has not been reported so far.

4.3.1. Air mass

When the sun's elevation angle above the horizon decreases, the sunlight travels longer distance through the atmosphere, resulting in an increasing AM and corresponding reduction of the spectral irradiance, especially for the shorter wavelengths [17]. The spectra for different air mass are generated using the Simple Model of the Atmospheric Radiative Transfer of Sunshine (SMARTS) v2.9.2 developed by NREL [227]. In Fig. 4.5(a), the effect of AM on the J_{ph} is shown for the encapsulated 2T poly-SiO_x passivated tandem solar cell. Here, we kept the perovskite thickness fixed at the thickness that matches the J_{ph} for the AM 1.5 spectrum. The graph shows that with increasing the AM the implied photocurrent density in both perovskite and c-Si decrease. This is expected as the higher AM spectra have lower irradiance. The implied photocurrents of perovskite top cell and c-Si bottom cell do not decrease at the same rate, causing a current mismatch up to 35% between the top and the bottom cell as the spectrum varies. This effect is especially relevant for 2T tandems, but not for 3T and 4T tandems, which do not require current matching. Note that very similar behaviour was found also in case of tandems with c-Si bottom cells passivated with the other CSPCs considered in this work.

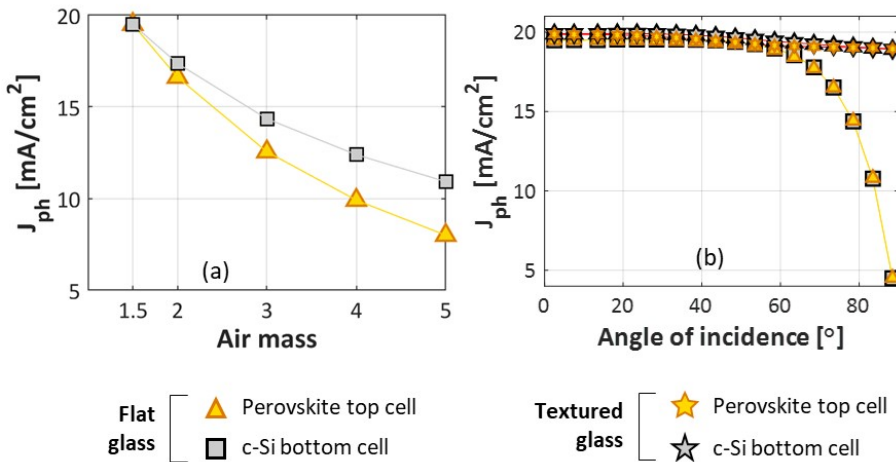


Figure 4.5: : Implied photocurrent density of encapsulated 2T tandem with c-Si bottom cell passivated with poly-SiO_x as function of (a) AM and (b) angle of incidence.

4.3.2. Angle of incidence

Unless the PV module is tracking the sun, the angle of incidence, between the incoming light and the PV module surface normal, also varies with the time of day and year. For increasing angle of incidence, one would expect higher reflection losses, especially at the air/glass interface. At the same time, the un-reflected light enters the solar cell under an oblique angle which might affect the optical path length in perovskite and silicon layers, potentially causing current mismatch. To study this effect on the implied photocurrent density, the angle of incidence is varied from 0° to 90° . The simulation results shown in Fig. 4.5(b) reveal that with increasing the angle of incidence, the absorption in both perovskite and c-Si decreases thereby decreasing the corresponding implied photocurrent densities. Different than in case of the AM variation, the J_{ph} of top and bottom cell for flat glass encapsulation decrease at the same rate, remaining closely matched with changing angle of incidence. The maximum mismatch between the implied photocurrent densities is only 0.88%. Again, a very similar behaviour was found also in case of tandems with c-Si bottom cells passivated with the other CSPCs considered in this work. Light trapping effects due to the c-Si pyramid texture play an important role and are taken into consideration in our GenPro4 [114] model that is used to obtain the presented cell and module simulation results. In addition, textured glass simulations [228, 229] have been considered to study its effect on photocurrent density. Fig. 4.5 (b) reveals the behaviour of perovskite and c-Si solar cells in 2T configuration with textured glass encapsulation. The texture is on the outside of the glass. We observe that texturing increases the photocurrent density significantly especially at larger angles of incidence. The maximum mismatch between top and bottom cell's implied photocurrent densities is below 1.5% in this case.

4.3.3. Effect of location on mono-facial tandem modules

Under real-world conditions the abovementioned variations in AM spectrum and angle of incidence occur simultaneously and vary depending on latitude and cloud coverage. We perform the hourly spectral irradiance analysis, as outlined in supplementary information A, for the cities of Reykjavik (Iceland, $64^\circ 08' N$), Rome (Italy, $41^\circ 53' N$) and Alice Springs (Australia, $23^\circ 42' S$). We consider a module endowed with mono-facial 2T tandem solar cells and decorated with $p^+ - nc - Si : H / n^+ - nc - Si : H$ TRJ. To compare the year-averaged optical performance of different scenarios, we use the concept of the yearly average photocurrent density. For every hour of the year, we calculate the photon absorption rate in the individual perovskite and c-Si absorber layers. We assume that the tandem's current output is limited by the sub-cell with the lowest implied photocurrent

density, which for some hours will be the top cell while at other hours will be the bottom cell. We calculate this limiting implied photocurrent density for every hour of the year and then take its average. As this quantity is related to the annual energy yield, it allows us to optimize the optical design of the 2T tandem solar cell for a particular location without resorting to electrical yield calculations. Figure 4.6(a), (b) and (c) show the variation of the yearly average photocurrent of mono-facial 2T SHJ and poly-SiO_x passivated tandem solar modules with varying perovskite absorber layer thickness for the three abovementioned locations. Under standard test conditions, the optimal perovskite thickness for these tandem solar cells are 535 nm and 515 nm, respectively. However, in real world conditions for which the illumination varies over the year, we define the optimum thickness as the thickness that maximizes the yearly average photocurrent density. We find that for different locations the optimum thickness of the perovskite absorber changes considerably: ~600 nm in case of Reykjavik for both c-Si technologies, 535 nm and 515 nm in case of Rome for SHJ and poly-SiO_x c-Si technologies, respectively, and 500 nm in case of Alice Springs for both c-Si technologies. We explain this by Rome having averaged over the year a similar spectrum as AM 1.5 and that is why the optimum thickness at STC is also the optimum for Rome. For Reykjavik, the spectrum has a higher AM, with relatively less visible light compared to infrared light, which must be compensated with a thicker perovskite. Alice Springs has a lower AM and so a thinner perovskite layer is the optimum. Optically, we observed that the tandem cell endowed with SHJ bottom c-Si cells outperforms that based on c-Si cells passivated with poly-SiO_x CSPCs (see table 4.2). This result translates to module level (see figure 4.6). Note that for perovskite thicknesses thinner than the optimum value, the perovskite current is for most hours of the year lower than that of c-Si and limits the tandem. Conversely, for perovskite thicknesses thicker than the optimum, the c-Si current limits the tandem.

In addition to 2T mono-facial tandem simulations, we also study 3T and 4T mono-facial tandem simulations, both for flat and textured glass encapsulation (as described in section 4.3.2). The location considered here is only Rome. Figure 4.7 (a), (b) and (c) below shows the simulated yearly average photocurrent density of 2T, 3T and 4T mono-facial tandem solar cells. For 2T tandems we find that textured glass simulations give an increase in the yearly average photocurrent of about (3 – 4%) due to reduced reflection loss, especially for larger angles of incidence as shown in Figure 4.5 (b). We also observe that on texturing the glass, the optimum thickness of the perovskite does not change. For 3T tandems, which have a similar structure, glass texture gives a similar (3 – 4%) enhancement for both top and bottom cell currents. In 4T tandems, the glass texture, besides reduced reflection loss, has a secondary effect of making light pass through the flat top cell more obliquely. This further enhances absorption in perovskite and

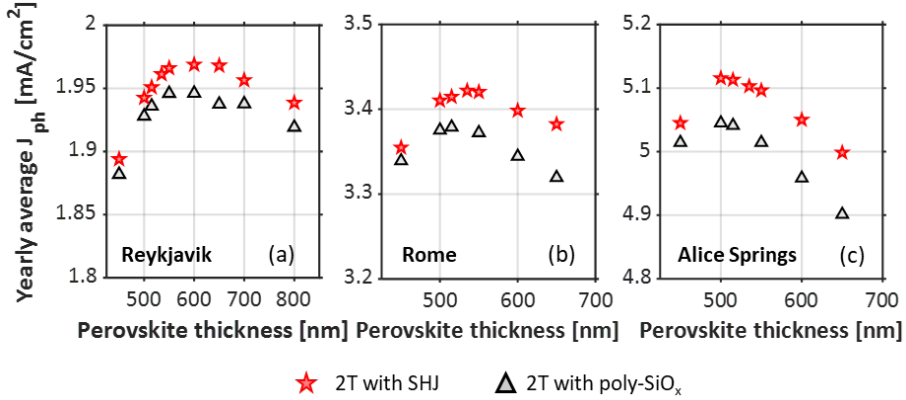


Figure 4.6: Yearly average photocurrent density of mono-facial 2T tandems with SHJ bottom cell (red stars) or c-Si bottom cell passivated with poly- SiO_x (grey triangles) for varying perovskite absorber thickness in (a) Reykjavik (Iceland), (b) Rome (Italy) and (c) Alice Springs (Australia).

increases the gain in top cell current to 6% compared to flat glass. The more oblique path does mean that a lower fraction of incoming photons is transmitted to the bottom cell, limiting the current gain in the bottom cell to 1%. Note that textured glass may increase the module soiling [230], a negative effect not taken into consideration in these simulations.

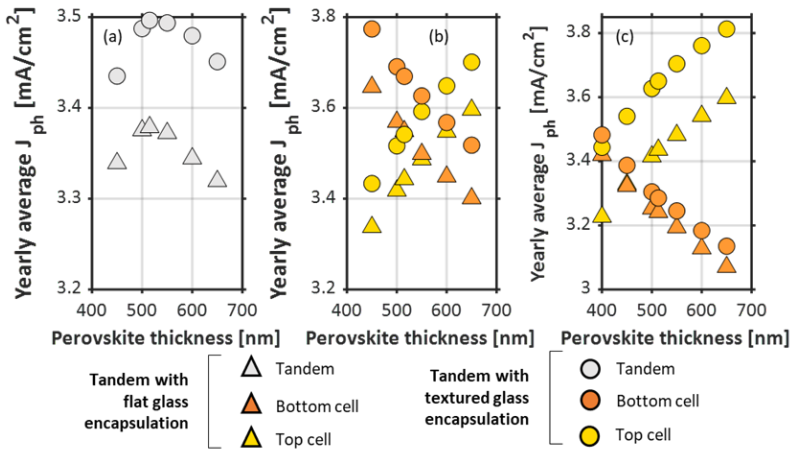


Figure 4.7: Simulated yearly average photocurrent density of mono-facial tandems with poly- SiO_x bottom cell for varying perovskite absorber thickness in Rome. The tandem configurations are (a) 2T, (b) 3T, and (c) 4T,

4.3.4. Effect of albedo and perovskite band gap on bifacial tandem modules

In bifacial 2T tandem solar cells (see Fig. 4.1 (c)), the current in c-Si increases due to the reflection from the ground (albedo). Since the c-Si does not transmit any rear-incident light that can be absorbed by perovskite, the rear side irradiance does not contribute to additional current generation in the perovskite top cell. The effect of albedo on the optical performance of a bifacial 2T tandem module with c-Si bottom cell passivated with poly-SiO_x has been studied. Mean albedo values of 0.09, 0.44, and 0.85 have been taken into consideration for different ground surfaces such as sandstone, dry grass and snow, respectively [122, 231]. Fig. 4.8(a) below shows the yearly average photocurrent in the 2T bifacial tandem for different albedo values as function of perovskite thickness. These values have been calculated for the location of Rome with a module tilt of 27° facing South and compared with the results for the mono-facial module (see grey symbols in 4.8(a)). We observe that for low albedo values of 0.09 (= low impact of rear-incident light on the optical behaviour of the tandem), we get an optimum perovskite thickness between 700 nm and 800 nm. This is much thicker than the optimal 515-nm thick perovskite absorber found for the mono-facial tandem module; but it is still required to match the additional current density from the c-Si due to the rear side irradiance. Beyond 800-nm thick perovskite absorber, the c-Si current limits the tandem. On the other hand, for higher albedo values of 0.44 and 0.85, there is even more additional c-Si current due rear side irradiance, and the perovskite current seems to always limit the tandem, even in case of a 1000-nm thick perovskite layer. To get current matching in case of mid-to-high level of albedo, another option is to reduce the optical bandgap of the perovskite absorber layer so that it can absorb a wider range of the solar spectrum. The optical bandgap of the perovskite has been blue-shifted in steps of 25 nm similar to the approach used in Ref. [232]. To this end, we keep the location of Rome and the abovementioned mounting configuration and we fixed to 700 nm the thickness of the perovskite absorber. We then determine the optimum bandgap corresponding to current matching. As reported in the Fig. 4.8(b), for bifacial tandems with albedo value of 0.09, the optimum bandgap is (1.55 eV) whereas for 0.44 albedo, the optimum bandgap is 1.45 eV. For a very high albedo of 0.85 (snow), the optimum bandgap is less than 1.4 eV. As in Section 4.3.1 and Section 4.3.2, a very similar behaviour was found also in case of tandems with c-Si bottom cells passivated with the other CSPCs considered in this work. However, we assume the ground to have a constant (wavelength independent) albedo. Therefore, the spectral distribution of light incident on the rear side is always the same as on the front side. In reality, the albedo of a material like grass is wavelength dependent [122], which will result in

differences between front and rear spectra. This may introduce a minor deviation in calculated J_{ph} [233].

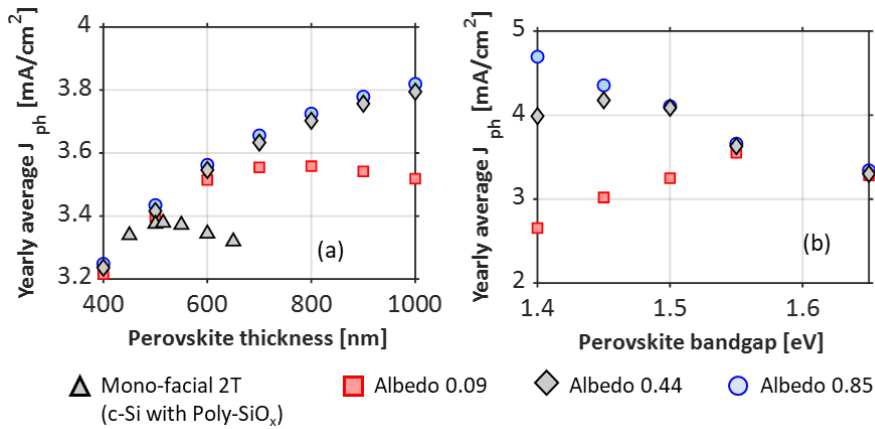


Figure 4.8: Yearly average photocurrent density of bifacial 2T tandem module with c-Si bottom cell passivated with poly-SiO_x computed in Rome (Italy, tilt = 27°, azimuth = South) for different albedo values and as function of (a) perovskite absorber thickness or (b) perovskite absorber band gap (thickness fixed to 700 nm). The black triangles values are the reference from mono-facial 2T tandem cell; instead, red squares values are related to the mean albedo value of sandstone (0.09); the black diamonds to that of dry grass (0.44); and the blue circles to that of snow (0.85).

4.3.5. Effect of location on bi-facial tandem modules

The analysis of perovskite thickness and bandgap in the previous section was presented for only one location and several albedo values. To thoroughly study the effect of location on the 2T bifacial tandem modules, simulations have been performed also for Reykjavik in Iceland and Alice springs in Australia. Fig. 4.9 shows a comparison of the yearly average photocurrent density for perovskite absorber thickness from 400 nm to 700 nm. Going from the least sunny to the sunniest location, the yearly average photocurrent density increases from Reykjavik to Rome to Alice Springs and for perovskite absorber layer thickness from 400 to 700 nm.

4.4. Discussion

4.4.1. Overall comparison between different perovskite/c-Si tandem architectures and CSPCs

The deployment of the poly-SiO_x CSPCs in single junction c-Si solar cells leads to significant additional parasitic absorption losses, which in turn reduces the

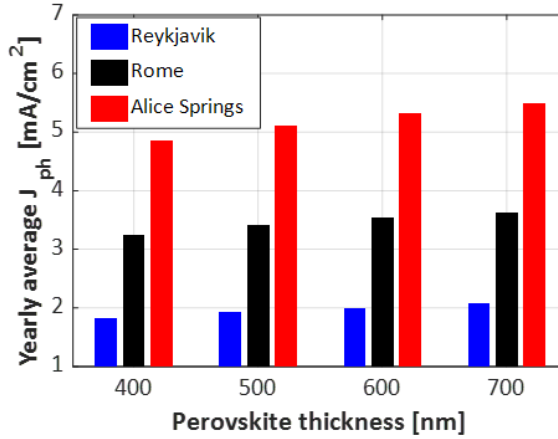


Figure 4.9: Yearly average photocurrent density of bifacial 2T tandem with c-Si bottom cell passivated with poly-SiO_x: comparison between different perovskite absorber thicknesses and different locations. Albedo value considered here is 0.44.

implied photocurrent density (See Fig. A.3 (a) of supplementary information A). However, these optical losses occur largely for shorter wavelengths ($\lambda < 600$ nm) and do not play a critical role in perovskite/c-Si tandem configurations. In the 2T configuration, the implied photocurrent density reduction is limited to at most 0.3% for poly-Si, 0.8% for poly-SiC_x, and 1% for poly-SiO_x CSPCs. The results for 2T, 3T and 4T tandems are summarized in Table 4.2. For 2T, the current matched top and bottom J_{ph} is given with the corresponding perovskite thickness. This shows that careful choice of the perovskite absorber thickness is crucial. For 3T and 4T, separate top and bottom J_{ph} are shown, considering for comparison the same perovskite thickness and texture as in 2T. The 3T and 4T tandem devices exhibit similar trends for the different CSPCs as 2T. Note that for the 3T tandem, the photocurrent density in the bottom cell can be tuned by varying the area of n-type and p-type doped layers at the rear as well as the gap in between them. In this respect, while the difference in absorption coefficient between n-type and p-type doped layers can be optically leveraged, one must take care that emitter-to-pitch ratio of the IBC device does not become too small, giving rise to charge collection issues [234]. For 4T, the bottom cell current is about 3% lower than that in 2T and 3T tandems due to parasitic absorption in additional ITO layers involved. When the perovskite top cell is not textured, the 4T configuration gives rise to additional reflection losses and correspondingly lower J_{ph} in both top and bottom cells.

Compared to tandem solar cells based on SHJ bottom cell, tandem solar cells

based on poly-Si, poly-SiO_x and poly-SiC_x CSPCs have slightly lower photocurrent densities due to the higher parasitic absorption in these high temperature CSPCs. This is because they are thicker and more heavily doped than the low temperature counterparts. Despite this, they can still achieve greater than 20 mA/cm² matched implied photocurrent density in the un-encapsulated architecture along with being compatible with high temperature production processes.

For 2T, it is needed to match the top and bottom J_{ph} . For 3T and 4T, having a thicker perovskite absorber will lead to higher photocurrent in the top cell but lower photocurrent in the bottom cell. In these configurations, a larger perovskite thickness will give voltage output at a potentially higher current which will result in a higher efficiency. However, a very thick perovskite thickness such as around 1000 nm might lead to fabrication issues and to lower electrical properties such as V_{oc} because of a larger recombination triggered by limited diffusion length. For 2T tandem, the optimum perovskite thickness is crucial as by varying the perovskite thickness by 50 nm leads to a significant variation in photocurrent density (see Figure 4.7(a)). Figures 4.7 (b) and (c) show the variation of photocurrent density with perovskite thickness for both top and bottom cell in 3T and 4T configurations. Since current matching is not required in 3T and 4T, even on changing perovskite thickness, the average photocurrent density is almost constant which comes around 3.49 mA/cm² for 3T and 3.33 mA/cm² for 4T (not shown).

Table 4.2: Implied photocurrent density of encapsulated mono-facial tandem devices with c-Si solar cells passivated with poly-Si, or poly-SiO_x, or poly-SiC_x. Tandem devices endowed with SHJ bottom cell are reported as reference. The 4T architecture with textured top cell refers to Figure 4.1(f) but with textured top cell as in Figure 4.1(b); d_{pero} stands for thickness of the perovskite absorber and in case of 2T it is the thickness for which current matching is achieved.

	J_{ph} [mA/cm ²]								
	d_{pero} [nm]	2T	3T		4T Textured top cell		d_{pero} [nm]	4T Flat top cell	
			Top	Bottom	Top	Bottom		Top	Bottom
SHJ (ref.)	535	19.70	19.72	19.63	19.60	19.02	513	19.38	18.58
Poly-Si	527	19.64	19.62	19.62	19.52	18.99	513	19.36	18.53
Poly-SiO_x	515	19.49	19.49	19.53	19.56	18.84	513	19.35	18.25
Poly-SiC_x	510	19.53	19.53	19.51	19.54	18.84	513	19.38	18.23

4.4.2. Comparison of real-world conditions with standard test conditions

In the real-world conditions, the illumination spectrum and the Sun's position change over the entire year. We observe that the optimum thickness of mono-facial 2T tandem with c-Si bottom cell passivated with poly-SiO_x, under standard test conditions, is around 515 nm (see Table 4.2). This thickness is also optimum, averaged over the whole year, for the city of Rome. However, for a location with a somewhat higher AM spectrum such as Reykjavik, the optimum perovskite

thickness is thicker (~ 600 nm). The opposite is also true: for a location with a lower AM spectrum such as Alice Springs, the optimum perovskite thickness is thinner 500 nm (see Fig. 4.6). Hence, the optimum thickness changes for the real-world conditions. So, in general, the spectrum and angle of incidence do influence the absorption in both mono-facial and bifacial perovskite/c-Si tandem solar cell and related modules (see Fig. 4.9). Like 2T tandem solar cells, also the 3T and the 4T tandem solar cells will show a varying yearly average photocurrent density with changing locations.

4.4.3. Comparison of mono-facial and bi-facial tandem solar cells

Compared to mono-facial tandems, a higher yearly averaged photocurrent density can be achieved with bifacial tandems due to the ground reflectance, which contributes to the extra current in the bottom cell. For 2T tandems we observe that by increasing the thickness of perovskite absorber layer, the yearly averaged J_{ph} increases if current generation in perovskite is the limiting factor. This happens even for perovskite thicknesses as high as 1000 nm and for albedo values of 0.44 or 0.85 (see Fig. 4.8(a)). The optimum thickness for 2T tandem is the point where the transition from perovskite to c-Si being the limiting factor in J_{ph} occurs. For a particular bandgap of perovskite absorber, its optimum thickness in bi-facial 2T tandems is higher than that in mono-facial tandems (see Fig. 4.8(a)). Or conversely, for a particular perovskite thickness, the optimum bandgap in bi-facial 2T tandems is lower than that in mono-facial tandems (see Fig. 4.8(b)). These effects are more pronounced the larger the albedo.

To study the effect of tandem architectures, we compared the yearly averaged photocurrent density of mono-facial and bi-facial 2T, 3T and 4T tandem solar modules (see fig. 4.10). We choose the tandems based on poly-SiO_x passivated bottom cell as a comparative example. The mono-facial tandems were simulated for the optimized perovskite thickness of 515 nm in case of 2T and 3T architectures and 513 nm for 4T architecture (see Table 4.2). For bifacial 2T tandems, since the perovskite current is the limiting factor for very thick absorber thickness, an upper value of 700 nm has been chosen (see Fig. 4.8 (a)). On the other hand, 3T and 4T do not have the constraint of current matching. In these architectures, having a thicker perovskite absorber is beneficial because a higher current from the perovskite top cell will lead to higher efficiency. Hence, for bifacial tandems, the perovskite thickness of 700 nm was chosen for comparison. To have a more realistic approach from a fabrication standpoint, flat top cell is chosen for the 4T given in Table 4.2. From mono-facial to bifacial tandems, the thicker perovskite absorber combined with the additional rear side absorption in the c-Si absorber, yield improved performance. Passing from 515-nm to 700-nm thick perovskite ab-

4

sorber (i.e. from mono-facial to bifacial configurations), but still having perovskite as limiting factor, the yearly average photocurrent density of the top cell increases by 7.4%, 5.5%, and 5.5% in case of 2T, 3T and 4T tandem architectures, respectively. At the same time, the yearly average photocurrent density of the bottom cell increases by 46%, 46%, and 50% in case of 2T, 3T, and 4T tandem architectures. This latter gain is due to the rear side absorption in c-Si, minus a small reduction in front-side absorption in c-Si due to the thicker perovskite layer. For bifacial 2T tandem, since the perovskite is limiting the total photocurrent density and thickness of perovskite cannot be increased further, lower bandgap perovskites should be considered to increase the average yearly photocurrent density. Note that changing the bandgap will also affect the electrical parameters of the tandem, such as the open circuit voltage, but this is out of scope for this optical study. For the 3T and 4T tandem configurations, the extra current in the bottom cell due to rear side absorption in c-Si contributes to the total photocurrent independent of the top cell current.

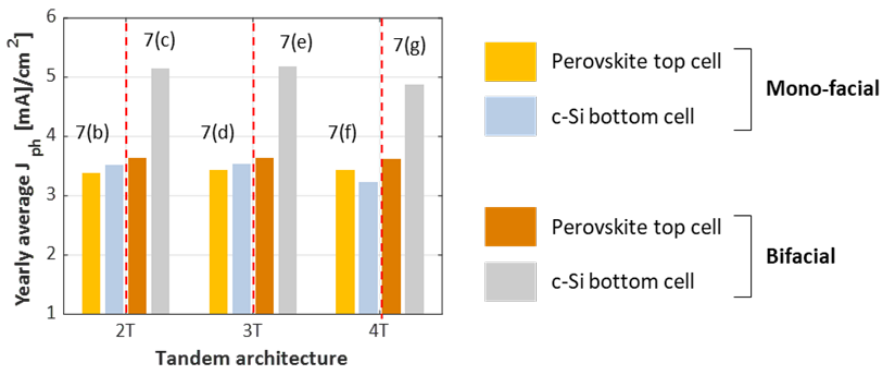


Figure 4.10: Comparison of yearly average photocurrent density of mono-facial and bifacial 2T, 3T, and 4T tandems with c-Si bottom cell passivated with poly-SiO_x. Here bifacial tandems are endowed with 700-nm thick perovskite absorber. Numbers and letters in the diagram refer to sub-figures in Fig. 4.1.

4.5. Conclusions

The goal of our work was to investigate what affects the optimum perovskite thickness for current matching in 2T perovskite / c-Si tandems and how the optical performance of these devices compares with that of related 3T and 4T tandems.

In 2T tandem configuration high temperature CSPCs such as poly-Si, poly-SiO_x and poly-SiC_x can achieve matched photocurrent density greater than 20

mA/cm² and around 19.5 mA/cm² without encapsulation and with encapsulation, respectively. These values are slightly lower than those of a 2T tandem based on SHJ bottom cell because of the high doping-driven free carrier absorption in high-thermal budget CSPCs. However, these CSPCs are compatible with high temperature production processes and are therefore appealing for the mainstream c-Si industry. We observed that when designing a 2T tandem, the effect of encapsulation should be taken into consideration as it reduces the optimum perovskite thickness by about 25 nm. With our modelling approach, we can also optimize the thickness of the perovskite absorber according to the location and angle of incidence, as the optimum thickness of the perovskite absorber under standard test conditions is not the same as in real world conditions.

At module level, we introduced the yearly average photocurrent density as term of comparison among different tandem architectures. Evaluating bifacial tandems, a higher yearly average photocurrent density than that of mono-facial tandems could be obtained due to the ground reflection that contributes extra current to bottom c-Si cell. The optimum thickness of the perovskite absorber for bi-facial tandems is higher than that of the mono-facial tandems. On the other hand, the bandgap of perovskite absorber is another parameter that can be tuned in bifacial 2T, 3T and 4T tandems to harvest more current from the top cell without realizing an overly-thick top cells. For higher albedo values, the optimum bandgap of perovskite is lower as compared to the optimal bandgap found for lower albedo values. Careful optimization of albedo and thickness and bandgap of perovskite absorber is crucial in achieving a high yearly average photocurrent density.

5

Poly-SiO_x passivated c-Si solar cells for perovskite/c-Si tandems

This chapter is based on the following publication :

M. Singh, K. Datta, A. Amarnath, F. Wagner, Y. Zhao, G. Yang, A. Bracesco, N. Phung, D. Zhang, V. Zardetto, M. Najafi, S. C. Veenstra, G. Coletti, L. Mazzarella, M. Creatore, M. M. Wienk, R. A. J. Janssen, A. W. Weeber, M. Zeman, O. Isabella, "Crystalline silicon solar cells with thin poly-SiO_x carrier-selective passivating contacts for perovskite/c-Si tandem applications", *Progress in Photovoltaics: research and applications* 31(9), 877- 887 (2023). DOI: <https://doi.org/10.1002/pip.3693>

Abstract

Single junction crystalline silicon (c-Si) solar cells are reaching their practical efficiency limit while perovskite/c-Si tandem solar cells have achieved efficiencies above the theoretical limit of single junction c-Si solar cells. Next to low-thermal budget silicon heterojunction architecture, high-thermal budget carrier-selective passivating contacts (CSPCs) based on polycrystalline-SiO_x (poly-SiO_x) also constitute a promising architecture for high efficiency perovskite/c-Si tandem solar cells. In this work, we present the development of c-Si bottom cells based on high-temperature poly-SiO_x CSPCs and demonstrate novel high-efficiency four-terminal (4T) and two-terminal (2T) perovskite/c-Si tandem solar cells. First, we tuned the ultra-thin, thermally grown SiO_x. Then we optimized the passivation properties of p-type and n-type doped poly-SiO_x CSPCs. Here, we have optimized the p-type doped poly-SiO_x CSPC on textured interfaces via a two-step annealing process. Finally, we integrated such bottom solar cells in both 4T and 2T tandems,

achieving 28.1% and 23.2% conversion efficiency, respectively.

5.1. Introduction

Single junction c-Si solar cells are reaching their practical efficiency limit [95, 235]. One way to further increase the efficiency of solar cells based on c-Si is to deploy them as bottom device in tandem structures with a wide bandgap top device. Perovskite/c-Si tandem solar cells attract considerable attention in this regard [47, 88, 89, 91, 101, 110, 189–195, 197–202, 236–245] with certified conversion efficiencies so far up to 34.6% [94]. The two common tandem architectures are a monolithically integrated two-terminal (2T) tandem configuration, where the two devices are electrically connected via a tunnel recombination junction (TRJ), and a mechanically stacked four-terminal (4T) tandem configuration where the two devices are optically connected but electrically decoupled. The 2T tandem solar cell design has simple electrical connections but requires current matching between the two devices to reach optimal efficiency. It is thus sensitive to the daily variations of solar spectrum. The 4T tandem configuration does not require current matching between its component devices and so has fewer restrictions on the device optimizations. However, due to the devices being electrically decoupled, each of them has its own transport layers and additional encapsulation layers for optical coupling, which increases the overall parasitic absorption. The advantages and disadvantages of 2T and 4T tandem configurations have been explored before [50, 193, 222, 246]. As bottom device, besides silicon heterojunction (SHJ) cells [88, 91, 193, 197, 236, 238–241] silicon solar cells based on high-thermal budget carrier-selective passivating contacts (CSPCs) have been less developed [47, 111, 112, 242–244]. Such CSPCs are so-called since they require high temperature fabrication steps, which can be up to 1000 °C. Poly-crystalline silicon (poly-Si) is an example of these high-thermal budget CSPCs and has enabled high efficiency single junction c-Si solar cells [59, 152, 208, 247, 248], concurrently yielding high quality surface passivation and charges transport. However, doped poly-Si exhibits a high free carrier absorption, which has turned the attention of researchers towards wide bandgap materials, such as polycrystalline-SiC_x [63, 158] and polycrystalline-SiO_x (poly-SiO_x), which can be more transparent while ensuring similar conductivity with respect to poly-Si [38, 156]. Such CSPCs consist of doped poly-Si, alloyed with carbon or oxygen, which are deposited on an ultra-thin SiO_x layer, prepared by a wet-chemical process (nitric acid oxidation of silicon, NAOS) [38], thermal oxidation [249], UV/O₃ process [250], or low-temperature plasma oxidation [251]. The opto-electronic properties of poly-SiO_x depend on the oxygen content [38, 252]. Poly-SiO_x is a novel material which has been successfully employed in c-Si single junction solar cells [38, 252, 253] and, to the best

of our knowledge, its long-wavelength optical potential in tandems has not been explored so far. As these CSPCs are compatible with high temperature production processes, they are appealing to the mainstream c-Si PV industry. In view of potential tandem efficiencies well above 30%, perovskite/c-Si tandem solar cells with bottom cells fabricated with high-thermal budget CSPCs can significantly reduce the levelized cost of electricity compared to single junction silicon photovoltaics [213].

Solar cells fabricated with poly-SiO_x CSPCs on an ultra-thin tunnelling SiO_x layer grown via NAOS process have exhibited active area efficiency of around 21% in a front/back contacted (FBC) architecture [253]. However, these cells were 2-cm² wide and deployed thermally evaporated metal contacts. In this work, next to adopting screen printing for metallization and developing larger area devices (from 2 cm² to 4 cm²), an ultra-thin SiO_x layer prepared by thermal oxidation of the c-Si surface is used as tunnelling SiO_x. As compared to tunnelling oxide grown via NAOS, thermal oxides are denser and less prone to blistering, have lesser bulk defects, provide better wafer chemical passivation [254] and is more stoichiometric resulting in higher thermal stability [255]. Other advantages of using a thermal oxide are (i) the controllability over the oxide thickness and its microstructures by changing the oxygen flow rate, temperature, and time, and (ii) the industrial applicability in state-of-the-art furnaces.

We optimized the passivation of both n-type and p-type doped poly-SiO_x on the ultra-thin thermally grown SiO_x especially because p-type poly-SiO_x on textured surfaces has been a limiting factor in terms of passivation [158, 254, 256]. To this end, a two-step annealing process was used to improve the passivation quality of p-type poly-SiO_x CSPCs on textured interfaces. Finally, we studied the integration of c-Si solar cells endowed with these optimized high-thermal budget CSPCs in perovskite/c-Si 4T and 2T tandem devices, achieving conversion efficiency of 28.07% and 23.18%, respectively.

5.2. Experimental details

5.2.1. Crystalline silicon (c-Si) solar cells

We used 4-inch n-type float zone (FZ) double-side polished (DSP) Topsil wafers (orientation: <100>, resistivity: 1-5 Ω cm, thickness: 280 ± 20 μm). For double-side textured (DST) solar cells, both sides of the wafers were textured in a tetramethylammonium hydroxide (TMAH) solution containing ALKA-TEX (GP-Solar-GmbH) as additive. For single-side textured (SST) solar cells, the front side was protected by a thick silicon dioxide (SiO₂) layer deposited using plasma-enhanced chemical vapour deposition (PECVD). After partially texturing the wafer, the SiO₂ layer was etched using a Buffered Hydrogen Fluoride (BHF (1:7)) solution. Subsequently,

the samples were cleaned by dipping them in HNO₃ (99%), to remove eventual organic contaminations, and then in HNO₃ (69.5%, at 110 °C) to remove inorganic contaminations. The samples are then dipped in 0.55% HF solution to remove any native oxide layer before thermal oxidation to grow a thin tunnelling oxide layer. Here, after preliminarily investigating an optimal growth temperature (ultimately fixed at 675 °C), the time of the thermal oxidation process is optimized. Then, both the n-type and the p-type poly-SiO_x passivating contacts are deposited on the thermal oxide with a dual-stack layer of 10-nm thick intrinsic a-Si layer using low-pressure chemical vapour deposition (LPCVD) process and 20-nm thick doped a-SiO_x:H layer from PECVD process. Silane (SiH₄), carbon dioxide (CO₂) and hydrogen (H₂) gases are used as the sources to deposit these poly-SiO_x passivating contacts. Phosphine (PH₃) and diborane (B₂H₆) gases are used as doping sources for n-type and p-type poly-SiO_x passivating contacts, respectively [252]. The dopant concentration of such poly-SiO_x CSPCs is in the order of 10²⁰ cm⁻³ [156, 252]. The total thickness of the passivating contact hereby described will not overcome 30 nm. Because of that thickness, an additional TCO layer is needed for lateral transport of carriers. Also here, after an initial study on the optimal annealing temperature seeking for an eventual co-annealing temperature between the n-type and p-type doped layers, these samples were annealed at 950 °C between 5 and 15 minutes to crystallize the abovementioned films into poly-SiO_x layers and drive in the dopants for both DST and SST cells. In this high temperature process, hydrogen effuses from the whole layer stack. Therefore, these cell precursors were hydrogenated by forming gas annealing (FGA) at 400 °C for 1 hour after being preliminarily capped with a 100-nm thick PECVD SiN_x layer [257]. Upon the removal of the SiN_x capping layer, indium tin oxide (ITO) layers were sputtered to ensure efficient (i) lateral carrier transport of charge carriers and (ii) optical performance at the front side as an anti-reflective coating (75 nm) and at the rear side as an optical buffer for the rear reflector (150 nm) [258]. As this step deteriorates the passivation quality [253, 259, 260], an additional annealing was executed in hydrogen for one hour at 400 °C. Finally, screen printing and curing for 30 minutes at 170 °C was used to realize low-temperature front and rear Ag-based metallic contacts. We have also fabricated a front side flat (rear side textured) c-Si solar cell that is deployed in 2T tandem devices (see Figure 5.1). The fabrication of such an architecture is described in more detail in Section 5.2.2. The current-voltage measurements of c-Si solar cells were performed using an AAA class Wacom WXS-90S-L2 solar simulator. The best SST and DST devices were certified at the CalTeC of the Institute for Solar Energy Research Hamelin (ISFH), Germany, which provided also the related external quantum efficiency (EQE) spectra (illumination in-between the front metal fingers). For passivation tests, symmetrical samples were fabricated with n-type or p-type doped poly-

SiO_x CSPCs on flat and textured c-Si wafers. A lifetime tester (Sinton WCT-120) was used to perform passivation measurements, such as implied open-circuit voltage (iV_{oc}), on precursors in quasi-steady-state photoconductance (QSSPC) or transient photoconductance decay (transient PCD) mode [261, 262].

5.2.2. Perovskite/c-Si tandem solar cells

For 2T perovskite/ c-Si tandem solar cells, SST solar cells were fabricated with front side flat n-type poly-SiO_x and rear side textured p-type poly-SiO_x. This configuration of the bottom sub- cell is chosen to meet the requirements for depositing the perovskite top device in a p-i-n configuration. After high temperature annealing (900 °C for 15 minutes) and the abovementioned hydrogenation step, the SiN_x capping layer was removed. This was followed by sputtering 30-nm (150-nm) thick ITO layer on the front (rear) side of the cell. Finally, a 500-nm thick Ag layer was deposited on the rear side of the cell using thermal evaporation. Atomic layer deposition (ALD), in combination with solution-processing, thermal evaporation, and sputtering were used to fabricate the perovskite top device. On the front, flat ITO layer of the bottom device, the perovskite top device comprised in a bottom-up sequence NiO_x / 2-(9H-carbazol-9-yl)ethyl]phosphonic acid (2PACz) / perovskite (1.67 eV) / C₆₀ / SnO_x / ITO / MgF₂. The front electrical contact was made of evaporated silver. The 8-nm thick NiO_x layer was deposited on the ITO layer using thermal ALD [263, 264]. The deposition was done at a base pressure of 5×10^{-6} mbar in a home-built reactor using nickel bis(N,N'-di-tert-butylacetamidinate) (Ni(tBu-MeAMD)₂) as nickel precursor and water as the co-reactant. The precursor bubbler was maintained at 90 °C and an Ar flow was used for bubbling. The substrate temperature approached 150 °C during the deposition. Subsequent solution-processed and evaporated layers were processed in an inert atmosphere. 2PACz (TCI, 98%, dissolved 0.3 mg/ml in ethanol) was deposited by spin-coating at 3000 rpm for 30 s followed by annealing the substrate at 100 °C for 10 minutes [265]. The perovskite precursor solution was prepared by mixing 936 μl PbI₂ (TCI, >99.99%, 691.5 mg/ml in DMF:DMSO 4:1) with formamidinium iodide (FAI, Greatcell Solar Materials) (199.9 mg) and 936 μl PbBr₂ (TCI, > 99%, 550.5 mg/ml in DMF:DMSO 4:1) with methylammonium bromide (MABr, Greatcell Solar Materials) (133.1 mg), followed by mixing the FAPbI₃ and MAPbBr₃ solutions in a 79:21 (v/v) ratio and adding 5 vol.% CsI (Sigma Aldrich, 99.999%, dissolved 389.7 mg/ml in DMSO) and 5 vol.% KI (Alfa Aesar, 99.998%, dissolved 249.0 mg/ml in DMF:DMSO 4:1). The precursor was spin-coated at 4000 rpm (5 s to reach 4000 rpm) for 35 s; at 25 s from the start of spin-coating, 300 μl anisole was cast onto the substrate leading to perovskite crystallization. The substrate was then placed on a hot-plate and the film was annealed at 100 °C

for 30 minutes. Following the substrate cooling down, choline chloride (Sigma Aldrich, >99%, 1 mg/mL in 2-propanol) was dynamically spin-coated at 4000 rpm for 35 s followed by thermal annealing at 100 °C for 30 minutes. Then, C₆₀ (10 nm) was deposited by thermal evaporation at a rate of 0.5 Å/s. Following that, spatial atomic layer deposition (s-ALD) was used to deposit a SnO₂ (20 nm) buffer layer [187]. Tetrakis(dimethylamino)tin(IV) was used as tin precursor and water as the co-reactant. A nitrogen curtain was used to isolate the two half-reaction steps. A 180-nm thick ITO layer was deposited using RF sputtering process at a rate of 0.3 Å/s. Finally, a 100-nm thick Ag perimeter contact, and a 120-nm thick MgF₂ anti-reflective coating were thermally evaporated to complete the tandem device. More information about this solar cell stack can be found in [266]. Schematic sketches of single junction solar cells combined with perovskite solar cells in 4T and 2T tandem devices are reported in Figure 5.1.

Current density – voltage (J–V) scans of the 2T perovskite/c-Si tandem solar cells were done under a tungsten-halogen illumination source filtered by a UV filter (Schott GG385) and a daylight filter (Hoya LB120) with intensity adjusted to 100 mW/cm². A 1 cm² shadow mask was used. The solar cells were operated under reverse or forward sweeps (between + 2.0 V and – 0.5 V for tandem solar cells) at a rate of 0.25 V/s using a Keithley 2400 source meter. The EQE measurements of the 2T perovskite/c-Si tandem solar cells were performed using a modulated monochromatic probe light (Philips focusline, 50 W) through a 1 mm radius aperture. The response was recorded and converted to the EQE using a calibrated silicon reference cell. Light- and voltage-biasing was used to isolate the EQE of the individual devices; 530 nm (perovskite) or 940 nm (silicon) bias light and a forward bias close to the open-circuit voltage of the single-junction solar cell was used. The single junction c-Si solar cells, described in Section 5.2.1, were combined with earlier processed and certified semi-transparent perovskite solar cells [86, 226, 267, 268] to fabricate the 4T tandem devices. The efficiency of 4T tandem cells was determined by following the procedure described by Werner et al. [144]. Next to the conversion efficiency of our 4T tandem devices, another outcome of this procedure was the filtered EQE of the deployed bottom devices.

5.3. Results and discussion

5.3.1. Passivation properties of poly-SiO_x CSPCs

Here, we optimized the passivation quality of n-type and p-type doped poly-SiO_x CSPCs. Since, SST poly-SiO_x passivated c-Si solar cell has n-type doped poly-SiO_x CSPC applied on front textured interface and p-type doped poly-SiO_x applied on rear side flat interface, we optimized n-type doped poly-SiO_x CSPC on DST symmetric samples and p-type doped poly-SiO_x on DSP symmetric samples

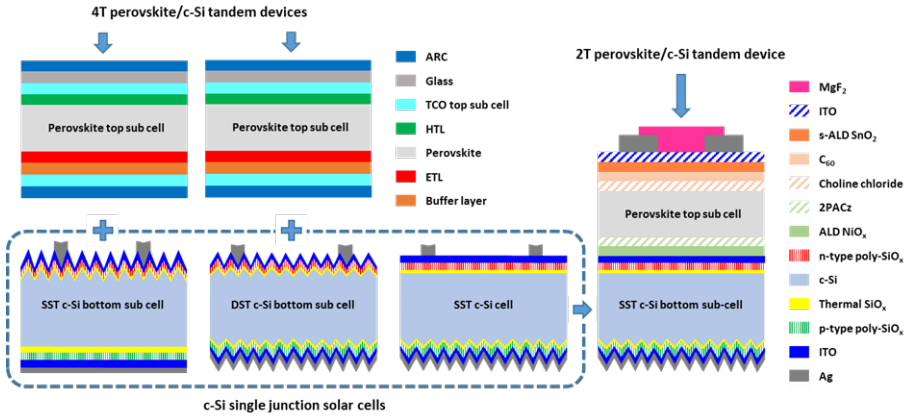


Figure 5.1: Sketches of the various solar cells reported in this work. The c-Si single junction solar cells endowed with p-type and n-type poly-SiO_x CSPCs are shown in the dashed box at the bottom left. The single-side textured (SST) with front textured and the double-side textured (DST) solar cells are then combined with 4T perovskite/c-Si tandem devices. The SST with rear textured solar cell is used for the 2T perovskite/c-Si tandem device. The ITO layers of top and bottom cells in the 2T perovskite/c-Si tandem are prepared in different ways, for which some differences in both optical and electrical properties are expected.

(see Figure 5.2(a)). On the other hand, for DST poly-SiO_x passivated c-Si solar cell, we optimize both n-type and p-type doped poly-SiO_x CSPC applied on DST symmetric samples (see Figure 5.2(b)). As mentioned earlier in Section 2.1, these CSPCs are prepared stacking doped poly-SiO_x layers on a tunnelling oxide grown by thermal oxidation on a c-Si FZ wafer, followed by a high temperature annealing step. The passivation results in Figure 5.3 were obtained after the high temperature annealing step. We use two parameters to optimize the passivation of these CSPCs: (1) the thermal oxidation time for the growth of tunnelling oxide and (2) the annealing time. Figure 5.3(a) and (b) show the passivation (in terms of iV_{oc}) of p-type doped poly-SiO_x CSPC applied on DSP symmetrical sample and n-type doped poly-SiO_x applied on DST symmetrical sample, respectively, for different thermal oxidation time at 675 °C (shown with different colours). Three annealing times (5, 10 and 15 minutes at 950 °C) were considered for each thermal oxidation time. For both p-type doped CSPC on DSP wafers and n-type doped poly-SiO_x CSPC on DST wafers, we found the same optimal thermal conditions for the tunnelling SiO_x and the high temperature annealing: 6 minutes at 675 °C and 10 minutes at 950 °C, respectively (see Figure 5.3(a) for p-type case and Figure 5.3(b) for n-type case).

On the other hand, for the symmetric p-type doped poly-SiO_x on DST wafer, notwithstanding the optimum found again at 10 minutes of thermal annealing in

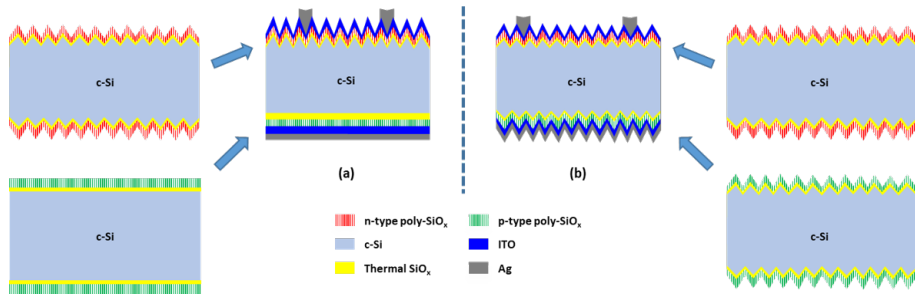


Figure 5.2: (a) SST poly-SiO_x passivated c-Si solar cell with (top) symmetric n-type doped poly-SiO_x on DST substrate and (bottom) symmetric p-type doped poly-SiO_x DSP substrate; (b) DST poly-SiO_x passivated c-Si solar cell with symmetric (top) n-type doped poly-SiO_x and (bottom) p-type doped poly-SiO_x on DST substrates.

5

Figure 5.3(c), thermally grown tunnelling SiO_x prepared at 675 °C for 3 minutes was found to yield better results ($iV_{oc} \sim 640$ mV) than the rest of the samples. The underwhelming passivation performance of these DST samples can be ascribed to a strong Auger recombination due to the excessive diffusion of dopants in the c-Si bulk. To quench such a diffusion, a 2-step annealing was used [269, 270].

The first annealing step, done after the intrinsic a-Si layer deposition, was performed at 950 °C for 1 minute. This was meant to render this intrinsic silicon denser [271] and therefore harder for dopants to be crossed. The second annealing step, done after the deposition of the doped a-SiO_x:H layer, was performed at 950 °C between 5 and 15 minutes like in previous cases so far discussed. For this new series of samples, thermally grown tunnelling SiO_x was prepared at 675 °C for 3 minutes. The passivation results for the symmetric p-type doped poly-SiO_x on DST wafers are reported in Figure 5.3(d), showing more than 20 mV improvement with respect to the best passivation achieved with the single-step annealing.

As described in Section 5.2.1, hydrogenation by FGA after SiN_x layer capping is performed on p-type and n-type doped CSPCs to reintroduce the hydrogen that effused after high temperature annealing. Figure 5.4 shows the comparison in passivation of p-type and n-type doped poly-SiO_x symmetric samples after thermal annealing and after hydrogenation. The optimum thermal oxidation and annealing conditions, as described in Figure 5.3, have been chosen for each type of CSPC. We observe that p-type and n-type doped poly-SiO_x CSPCs applied on DSP and DST symmetric samples, respectively, gave the same iV_{oc} of 690 mV after high-temperature annealing which improved to 710 mV after hydrogenation. The p-type poly-SiO_x symmetric sample without 2-step annealing gave an iV_{oc} of 668 mV after hydrogenation. Using the 2-step annealing technique, the symmetric p-type doped poly-SiO_x applied on DST wafer exhibited an iV_{oc} of 687 mV after

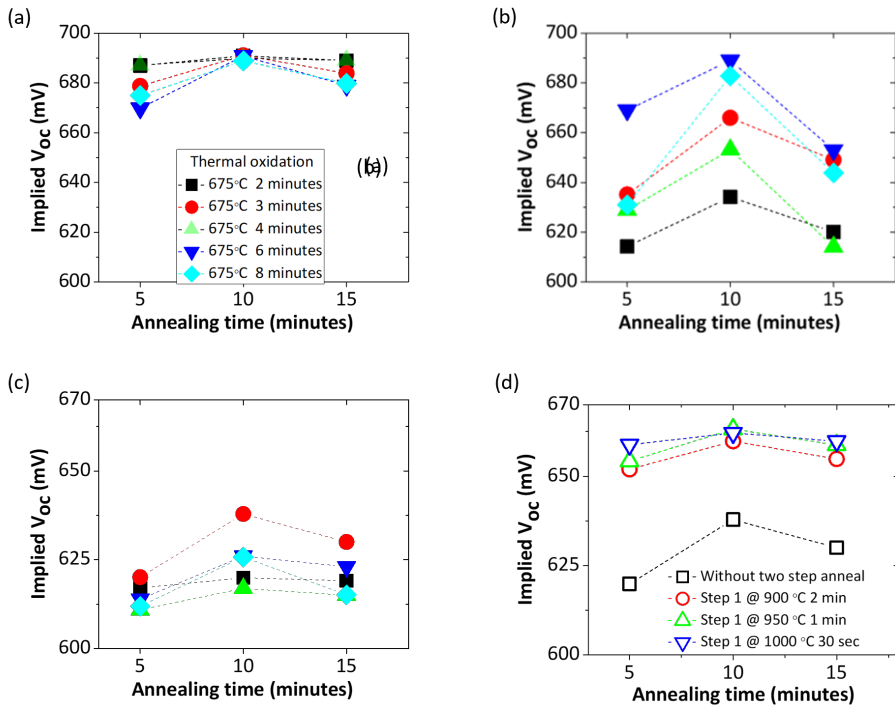


Figure 5.3: Implied V_{oc} of symmetric (a) p-type doped poly-SiO_x on DSP wafer, (b) n-type doped poly-SiO_x on DST wafer, and (c) p-type doped poly-SiO_x on DST wafer for different thermal oxidation time (thermal oxidation temperature is fixed at 675 °C) and three annealing times (annealing temperature is fixed at 950 °C). These three diagrams share the same legend. (d) Implied V_{oc} of symmetric p-type doped poly-SiO_x on DST wafer with two step annealing. In this case, the thermal oxidation temperature and time are fixed at 675 °C for 3 minutes. Here the first step annealing temperature and time have been varied. For each first step annealing condition, a second step annealing time of 5, 10 and 15 minutes is considered, again at fixed annealing temperature (950 °C).

hydrogenation. Applying the same 2-step annealing technique to symmetric n-type doped poly-SiO_x on DST wafer (including the thermally grown tunnelling SiO_x prepared at 675 °C for 3 minutes as in the p-type case), an iV_{oc} of 690 mV was found after hydrogenation, resulting in lower passivation quality than the single step annealing case. Here, as the intrinsic poly-Si layer resulting from the first annealing got denser [271], we speculate that the phosphorus doping atoms do not easily reach the tunnelling SiO_x/c-Si bulk interface to establish an effective electric field. In addition, as shown in Figure 5.3(b), the tunnelling SiO_x prepared at 675 °C for 3 minutes is not the best condition for the n-type doped poly-SiO_x on a textured surface. Still, this case is investigated (and later put forward in solar cell fabrication) to realize a neat flow chart in which both n-type and p-type doped

poly-SiO_x layers essentially undergo the same thermal processes at the same time.

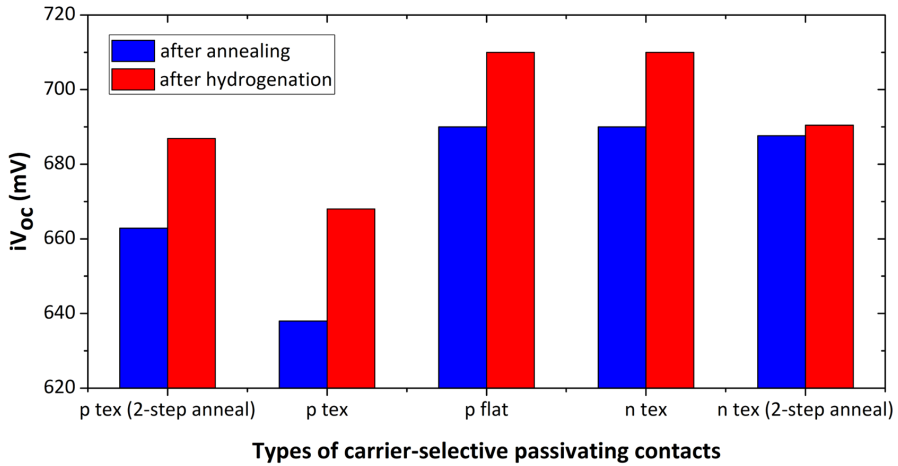


Figure 5.4: Implied V_{oc} for different types of CSPCs after high temperature annealing and after hydrogenation processes. Here, tex is used to denote textured.

5.3.2. Solar cell results

In this Section, we report on the performance of single junction c-Si solar cells based on n-type and p-type poly-SiO_x as CSPCs. The sketches of SST and DST poly-SiO_x passivated c-Si solar cell were shown in Figure 5.2. The evolution of surface passivation quality after annealing, hydrogenation, TCO deposition and hydrogen annealing for SST solar cell precursors is shown in Figure 5.5(a). As expected, the iV_{oc} increases by 20 mV after hydrogenation. Then, the TCO deposition results in a considerable loss in iV_{oc} from 714 mV to 690 mV due to sputtering-related damages [253, 260]. This loss in passivation is recovered by annealing the cell precursor at 400 °C in hydrogen environment for 1 hour [259]. The best SST solar cell exhibited a certified designated area power conversion efficiency (PCE) of 20.47% ($V_{oc} = 695$ mV, $J_{sc} = 36.68$ mA/cm², FF = 80.33%, metallization fraction ~3%, designated area = 3.915 cm², see Figure 5.5(c)). Moving from the previous 2-cm² wide area device, SiO_x layer grown via wet-chemical NAOS and evaporated metallic contacts [253], as well as applying the further optimized doped poly-SiO_x layers, we could keep the V_{oc} relatively high (from 691 mV to 695 mV) and sensibly improve the FF (from 76.4% to 80.3%) of the solar cells based on poly-SiO_x CSPCs.

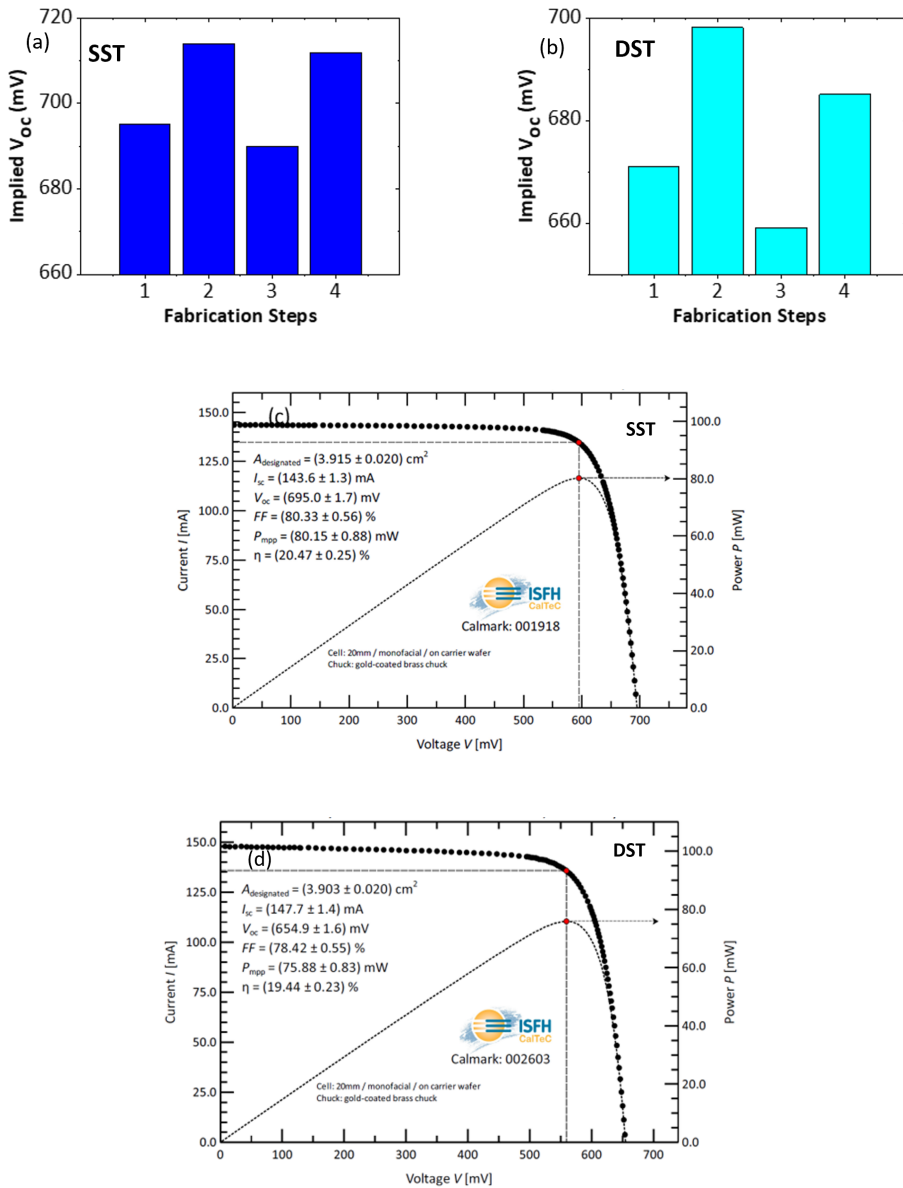


Figure 5.5: (a-b) The evolution in passivation quality (iV_{oc}) after specific steps of single side textured (SST) and double side textured (DST) solar cells fabrication: (1) annealing, (2) hydrogenation, (3) TCO deposition and (4) hydrogen annealing; (c-d) certified current-voltage and power-voltage curves of the best SST and DST poly-SiO_x passivated c-Si solar cell. Sketches of SST and DST solar cells are reported in Figure 5.2. Images of fabricated SST and DST solar cells are given in Appendix B.

As mentioned in Section 5.3.1, the p-type and n-type doped poly-SiO_x CSPCs

with 2-step annealing technique are used as the hole and electron contacts in DST solar cells, respectively. The change in passivation after different fabrication steps for the DST solar cell precursor is shown in Figure 5.5(b). The increase in passivation after hydrogenation and its decrease after ITO deposition are as expected. However, unlike the SST case, the loss in passivation after TCO deposition is not fully recovered after hydrogen annealing at 400 °C for 1 hour. This is because the DST solar cell precursor has p-type doped CSPC applied to the textured side, which is the limiting factor in terms of passivation and does not recover its passivation even after such a hydrogen annealing. The best DST solar cell gave a certified designated area PCE of 19.44% ($V_{oc} = 655$ mV, $J_{sc} = 37.85$ mA/cm², FF = 78.42%, metallization fraction ~3%, designated area = 3.903 cm², see Figure 5.5(d)). Compared to the SST solar cell, despite suffering from poorer surface passivation as witnessed by the lower V_{oc} and FF, the DST cell exhibits higher J_{sc} . This gain can be ascribed to the textured rear side of the DST solar cell which promotes a more efficient light scattering at the rear side and thus higher absorption in the c-Si bulk. Figure 5.6(a) shows the EQE of the SST and DST devices. As expected, the EQE of the DST cell outperforms that of the SST cell at wavelengths above 800 nm.

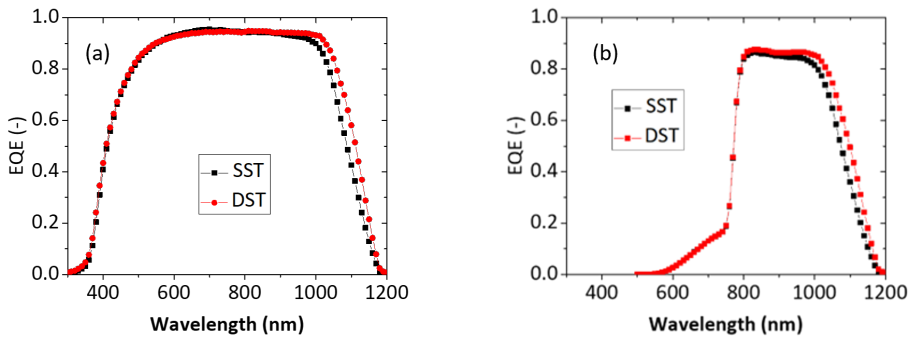


Figure 5.6: (a) EQE spectra of the SST and DST single junction c-Si solar cells endowed with n-type and p-type poly-SiO_x CSPCs. (b) Filtered EQE spectra of the same solar cells deployed as bottom devices in 4T perovskite/c-Si tandem devices.

5.3.3. Application in four terminal (4T) perovskite/c-Si tandem solar cells

The SST and DST poly-SiO_x solar cells were deployed as bottom devices in high efficiency 4T tandem devices together with a previously processed and certified perovskite top device (bandgap 1.60 eV) [86, 226, 267, 268]. The schematic sketches of the two 4T tandem devices alongside their constituting layers are presented in Figure 5.1. Following the method of measurement reported in [144]

and with the certified measurements of both semi-transparent perovskite top and c-Si bottom devices, the combined results are summarized in Table 5.1. The 4T tandem devices based on SST and DST poly-SiO_x bottom devices provide a PCE of 27.97% and 28.07%, respectively. Both SST and DST cells, after being illuminated with the transmitted light through the perovskite top device, experienced similar J_{sc} losses. Looking at the filtered EQE (see Figure 5.6(b)), the DST cell keeps the optical edge over the SST cell for every wavelength above 800 nm. The SST cell loses however more in V_{oc} and FF than the DST cell.

Table 5.1: External parameters of the semi-transparent perovskite top device (certified at ESTI, code XF812), the SST poly-SiO_x bottom cell (certified at ISFH CalTeC, code 0019018), and DST poly-SiO_x bottom cell (certified at ISFH CalTeC, code 002603), and their 4T perovskite/c-Si tandem device combinations.

Solar cell	Description	V_{oc} (mV)	J_{sc} (mA/cm ²)	FF (%)	PCE (%)
Perovskite top device	Single junction	1139	22.00	78.60	19.70
SST poly-SiO _x -based bottom device	Single junction	695	36.68	80.33	20.47
	Filtered	666	16.00	77.60	8.27
	4T Tandem	-	-	-	27.97
DST poly-SiO _x -based bottom device	Single junction	655	37.85	78.42	19.44
	Filtered	637	16.80	78.20	8.37
	4T Tandem	-	-	-	28.07

5.3.4. Application in two terminal (2T) perovskite/c-Si tandem solar cells

As sketched in Figure 5.1, we also fabricated SST solar cells with flat front side coated with n-type poly-SiO_x and textured rear side coated with p-type poly-SiO_x. This solar cell architecture was deployed to form a 2T perovskite/c-Si tandem device with a p-i-n perovskite top device. Due to the textured p-type poly-SiO_x CSPC limiting the passivation quality, these solar cells suffered large passivation loss after the ITO deposition. Again, some of the passivation loss was recovered after annealing in hydrogen at 400 °C for 1 hour. The best single junction solar cell achieved a designated area PCE of 16.67% (V_{oc} = 649 mV, J_{sc} = 34.28 mA/cm², FF = 74.93%, metallization fraction 3.15%, designated area = 3.92 cm²). The current density-voltage characteristic and the EQE spectrum of the single junction solar cell are reported in Figure 5.7(a) and (b), respectively. From the EQE and reflectance spectra in Figure 5.7(b), we note large parasitic absorption at short wavelengths (300 - 400 nm) and at very long wavelengths (1000 - 1200 nm). This light is absorbed in the front/rear ITO and in the front/rear poly-SiO_x CSPCs. Between 600 and 1000 nm, other than the reflection losses, most of the light is absorbed in c-Si solar cell.

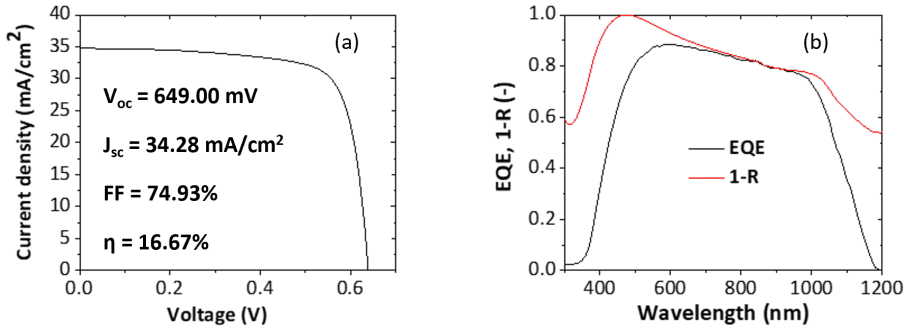


Figure 5.7: (a) Current density-voltage characteristic and (b) EQE and 1-Reflectance (1-R) spectra of the single junction c-Si solar cell with front side flat n-type poly-SiO_x and rear side textured p-type poly-SiO_x. The schematic of the corresponding structure is given in Figure 5.1

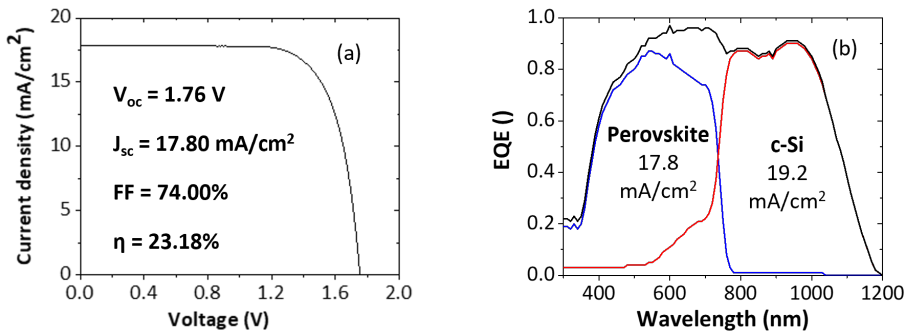


Figure 5.8: (a) JV curve and (b) EQE curve of 2T perovskite/c-Si tandem solar cell with poly-SiO_x passivated c-Si bottom cell. The corresponding device structure is shown in Figure 5.1. The blue, red and black curves represent EQE spectra of perovskite top cell, c-Si bottom cell and tandem cell respectively. The area covered by the blue line indicates the photo-current density generated by the perovskite top cell, while the area covered by the red line indicates the photo-current density generated by c-Si bottom cell.

The abovementioned poly-SiO_x passivated c-Si solar cell was integrated with the perovskite top device into a 2T perovskite/c-Si tandem device yielding an active area PCE of 23.18% ($V_{oc} = 1.76$ V $J_{sc} = 17.8$ mA/cm², FF = 74%, active area: 1 cm², see Figure 5.8(a)). The 2T tandem efficiency is higher than the efficiency of its top device by 5%abs (with respect to an opaque analogous single junction perovskite solar cell efficiency [266, 272]) and the efficiency of its bottom device by 6.5%abs. This efficiency is higher than that of the earlier reported value of 21.3% for a monolithic 2T perovskite/PERC-POLO tandem device [243]. On the other hand, it is lower than that of the earlier reported value of 25.1% for monolithic 2T perovskite/c-Si tandem device where the bottom device is endowed with poly-

SiC_x CSPCs [158]. These three types of high-thermal budget devices exhibit similar V_{oc}s (1.74 to 1.8 V) and FFs (74%) in 2T tandem devices while only the one with poly-SiC_x CSPCs could achieve better current matching between the devices (19.5 mA/cm²). The EQE of the 2T tandem device (Figure 5.8(b)) shows that our bottom device can deliver 19.2 mA/cm², but that the top device limits the short-circuit current density of the stack to 17.8 mA/cm². By further optimizing the layer thickness and perovskite bandgap, the current generation of the two devices can be better matched and consequently the efficiency of the 2T tandem devices can be further increased.

5.4. Conclusions

In this study, we optimized n-type and p-type poly-SiO_x CSPCs on an ultra-thin thermally grown tunnelling SiO_x layer. We incorporated these into single junction c-Si solar cells which were eventually used as bottom devices in 4T and 2T tandem devices. Good passivation quality was achieved for textured n-type poly-SiO_x (iV_{oc} = 710 mV). Using a two-step annealing process, the passivation quality of the textured p-type doped poly-SiO_x could be improved too (iV_{oc} = 687 mV). With the developed n-type and p-type poly-SiO_x CSPCs, we fabricated ~4-cm² wide, screen-printed, a SST single junction c-Si solar cell with certified efficiency of 20.47% and FF > 80%. Likewise, a certified efficiency of 19.44% was obtained for a DST cell endowed poly-SiO_x CSPCs. This DST solar cell architecture is presented here for the first time and exhibits, without any dual anti-reflective coating, an active area J_{sc} = 37.85 mA/cm². This is in line with state-of-the-art FBC silicon heterojunction solar cells and other architectures based on high-thermal budget CSPCs.

We tested our c-Si solar cells in combination with a previously processed and certified semi-transparent 19.70% perovskite solar cell. The internally measured efficiencies of the 4T perovskite/c-Si tandem devices featuring SST and DST poly-SiO_x passivated c-Si bottom devices are 27.97% and 28.07%, respectively. Based on the improved passivation quality of the textured p-type poly-SiO_x, we fabricated SST solar cell with flat n-type poly-SiO_x at the front side and textured p-type poly-SiO_x at the rear side with an efficiency of 16.79%. Integrating such a poly-SiO_x solar cell as bottom device with a p-i-n perovskite solar cell on top, resulted in a 2T tandem device with an efficiency of 23.18%.

6

On the annual energy yield of perovskite/silicon tandem modules with different bottom cell technologies

This chapter is based on the following publication :

M. Singh, J. Finazzo, Y. Blom, M. Jayan, C. R. Tobon, A. Weeber, M. Zeman, R. Santbergen, O. Isabella , "On the annual energy yield of perovskite/silicon tandem modules with different bottom cell technologies and optimized top cell properties for different locations", EPJ Photovoltaics (2025).

DOI: <https://doi.org/10.1051/epjpv/2025009>

Abstract

At standard test conditions (STC), the performance of photovoltaic modules is compared using efficiency. As irradiance and module temperature fluctuate over the year and STC efficiency does not assess the performance of the module accurately in real world conditions, the annual energy yield is used instead as performance metric. Perovskite/silicon tandem solar cells are being massively researched and sought after in PV industry for their efficiency well above 34% with further growth perspective. In this work, to evaluate and compare performance of different perovskite/silicon tandem photovoltaic (PV) modules based on different bottom cell technologies, we use a hybrid modelling approach. Such approach, combining experimentally obtained and simulated current-voltage curves, flexi-

bly predicts the annual energy yield of novel tandem PV modules via our PVMD toolbox and enables their optimization in any location. In particular, considering (i) mono- and bi-facial architectures, (ii) 2-terminal and 4-terminal module configurations, and (iii) silicon heterojunction or novel poly-SiO_x passivated c-Si solar bottom cells, we compare the annual energy yield of different perovskite/silicon tandem modules and we optimize their performance in different locations with respect to different perovskite thickness and bandgaps.

6.1. Introduction

Crystalline silicon solar cells (c-Si) dominate the photovoltaic (PV) market. As single junction crystalline silicon (c-Si) solar cells are approaching their theoretical efficiency limit [80, 235, 273] with record conversion efficiency above 27% [274], perovskite/c-Si tandem solar cells are gaining attention [47, 88, 89, 91, 93, 101, 110, 189–195, 198–202, 236–245, 275, 276]. Perovskite solar cells are being extensively studied in various domains, including simulation and optimization [277–284], fabrication [285–293], and energy yield analysis [86, 190, 220, 294–303]. Perovskite/c-Si tandem solar cells have shown efficiencies of 34.6% [94] and have the potential to go beyond that. 2-terminal (2T) and 4-terminal (4T) configurations are typically considered for tandem solar cells and modules. In 2T configuration, the top and bottom cells are monolithically integrated and the current matching between them is crucial to obtain a high efficiency. In 4T configuration, the top and bottom cells are fabricated separately, and no current matching is required; but optical losses increase. This is due to additional charge transport layers required for top and bottom cells as well as the optical matching layer in between the component cells. More information about the 2T and 4T tandem configurations can be found in [50, 193, 222, 246].

A performance metric more relevant than the efficiency, which is measured at standard test conditions (STC) [17], is the annual energy yield. This performance metric accounts for time-dependent and location-dependent variations in spectral irradiance and cell temperature, to which solar cells, and especially tandem devices, are sensitive. Dedicated software can be used to simulate from certain input data the irradiance-dependent and temperature-dependent current density-voltage (JV) curves and from those predict the energy yield of novel tandem device designs for various climate conditions [115, 301], study their performance losses [304] or evaluate their degradation [296]. In this work, we introduce a hybrid experimental-modelling approach for predicting the energy yield of prospective tandem modules. We use measured IV curves of lab-scale c-Si solar cells based on carrier-selective passivating contacts (CSPCs), taken at different irradiance and temperature levels, and combine those with simulated IV curves of perovskite top

cell endowed with different absorber thickness and band gap. Then, we combine such information in our PVMD toolbox [115] to predict the annual energy yield of perovskite/*c*-Si tandem modules with different bottom cell technologies and in different climatic conditions.

CSPCs passivate the silicon surface along with providing carrier selectivity. One way CSPCs are incorporated in *c*-Si solar cells is by depositing intrinsic and doped amorphous silicon layer on *c*-Si wafers as in silicon heterojunction (SHJ) solar cells [305–307]. Another way is by depositing thin tunnelling silicon di-oxide (SiO_2) on *c*-Si wafers followed by a doped polysilicon (poly-Si) layer as in Tunnel Oxide Passivated Contact (TOPCon) solar cells technology [308]. TOPCon technology has replaced the Passivated Emitter Rear Cell (PERC) and Al-based Back Surface Field (Al-BSF) technologies and is now actually dominating the PV market [71]. The world market share of TOPCon solar cells is anticipated to reach 50% in 2034 [71]. Poly-Si solar cells based on TOPCon technology have shown high efficiency [59, 152, 153, 208, 247, 248, 254, 309, 310], but poly-Si layers exhibit parasitic absorption losses [60]. To reduce the parasitic absorption in these layers, poly-SiO_x [38, 38, 156, 156, 252, 311, 312] and poly-SiC_x [63, 158] are also being explored as CSPCs. Researchers have conducted studies on energy yield of perovskite/*c*-Si tandem solar cells with SHJ bottom solar cell. However not much attention has been devoted to the modelling of energy yield of perovskite/*c*-Si tandem solar cells with high temperature CSPCs bottom solar cells. In our previous work, we have shown the optical optimization and fabrication of perovskite/*c*-Si tandem solar cells where the bottom cell is endowed with novel poly-SiO_x-based CSPCs [252, 311, 312]. In this work, we extend that study to predict the annual energy yield of prospective perovskite/*c*-Si tandem modules with bottom poly-SiO_x CSPCs cells. To this end, (i) we use our physics-based comprehensive modelling framework in real world conditions; (ii) we optimize both the bandgap and thickness of the perovskite top absorber; and (iii) we evaluate, in reference to SHJ, the performance of poly-SiO_x bottom cell in 2T and 4T configurations for both mono- and bi-facial cell architectures.

6.2. Experimental

In this study, we use front/back contacted (FBC) poly-SiO_x based *c*-Si solar cell [312] to study the effect of high temperature CSPCs in tandem applications. JV measurements have been performed for different irradiance and temperature on FBC poly-SiO_x based *c*-Si solar cell using a AAA-class solar simulator which shines artificial light using xenon and halogen lamps with a spectrum close to standard air mass 1.5. The JV measurements at different temperatures are performed by cooling/heating the stage on which measurement sample is kept. Also, the JV

measurements at different irradiance levels are performed by using polka dot beam splitters that scale down the intensity of the incident light without affecting the shape of the spectrum. JV curves at different irradiance and temperature of the FBC poly-SiO_x based c-Si solar cell are shown in Figure 6.1 (a) and (b), respectively. The irradiance ranges between 200 W/m² to 1000 W/m² and the temperature ranges from 15 °C to 55 °C. As expected, the J_{sc} increases with increasing illumination intensity and the V_{oc} decreases with increasing temperature. The fabrication details of FBC poly-SiO_x based c-Si solar cell are given elsewhere [312] and its schematic diagram is shown in Figure 6.3(b).

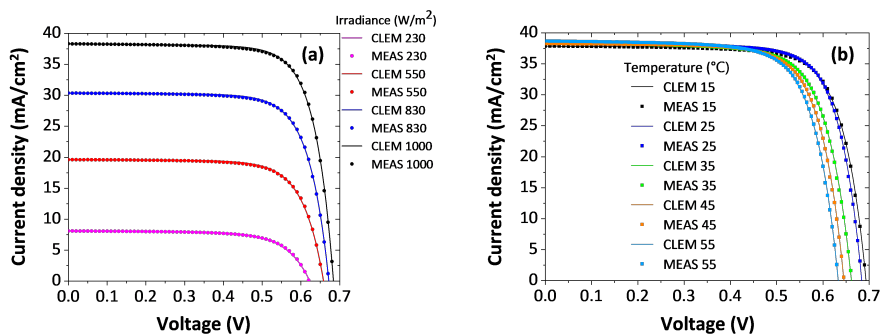


Figure 6.1: Measured JV curves (denoted by Meas) and reconstructed JV curves by Calibrated Lumped Element Model (CLEM) of front side textured c-Si solar cell endowed with poly-SiO_x CSPCs (solar cell structure shown in Figure 6.3 (b)) for varying (a) irradiance for a fixed temperature of 25 °C and (b) temperature for a fixed irradiance of 1000 W/m².

6.3. Simulation approach

The PVMD toolbox has been used to calculate the energy yield of perovskite/c-Si tandem modules with different bottom cell technologies [115]. The PVMD toolbox consists of cell, module, weather, thermal and electrical models which together enable to simulate the energy yield of a solar cell or a PV module [115]. GenPro4 software is used to calculate the optical properties of the solar module [114]. We define the layer stack and give optical constants (refractive index and absorption coefficient) as well as the thickness of each layer as input in GenPro4. GenPro4 calculates the angle- and wavelength-resolved reflectance and absorptance of each layer in the module. The absorption calculated in GenPro4 is also depth resolved. For the bi-facial tandem modules, such calculation is performed for both front and rear irradiance. The absorption in each layer is given as an input to the module part, which uses a ray tracing model [126] to calculate the absorption of the cells in the module. Note that the module comprises 60 series-connected and encapsulated cells. The angle- and wavelength-dependent absorption is

given as an input to the weather model to calculate the photocurrent generated by each cell in the module. We use the Perez model to reconstruct the sky map from Diffused Horizontal Irradiance (DHI) and Direct Normal Irradiance (DNI). This sky map indicates the brightness of each part of the sky. The tilt and other mounting conditions are given as input in module part which calculates the sensitivity map. This sensitivity map is multiplied by the sky map to obtain the global tilted irradiance [127]. The sky map and therefore also the tilted irradiance are spectrally resolved. The spectral distribution is calculated by the SBDART model [131]. The thermal module then calculates the temperature of the cell, and the electrical part uses a calibrated lumped element model (CLEM) to compute the module JV curves and DC energy yield for every hour of the year.

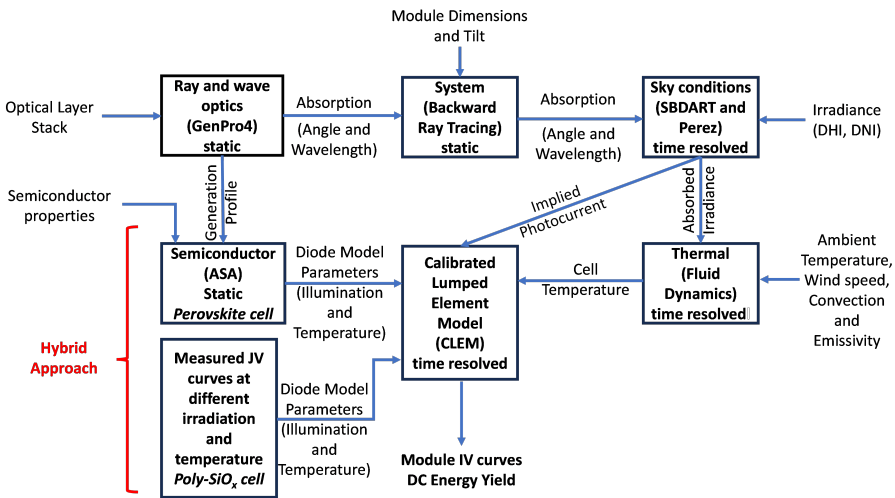


Figure 6.2: Flowchart showing hybrid approach used to calculate the (annual) energy yield of tandem modules with poly-SiO_x bottom cell.

The implied photocurrent density (output of the weather module) and the other electrical parameters (extracted from simulated/measured JV) are given as input in the CLEM model to generate tandem JV curves. Note that this CLEM is based on a five-parameter single diode model in which each of the parameters are temperature and irradiance (corresponding photocurrent density) dependent. These temperature- and irradiance-dependent parameters are obtained by fitting the JV curves at different temperature and irradiance levels. In our hybrid approach, the JV curves can either be obtained from measurements, or from semiconductor device simulations such as those carried out with ASA software [115, 119, 313]. For the perovskite/c-Si tandem device endowed with the reference SHJ bottom cell, the JV curves of both the top and the bottom cell are obtained

from simulations. The schematic process flow of this simulation framework used to compute the energy yield of perovskite/c-Si tandem solar cells is shown in Figure 6.2. Our hybrid approach is an extension of the existing simulation framework [115] whereas the input JV parameters of the top perovskite solar cell have been simulated and the bottom poly-SiO_x c-Si solar cell has been experimentally measured.

6.4. Validation

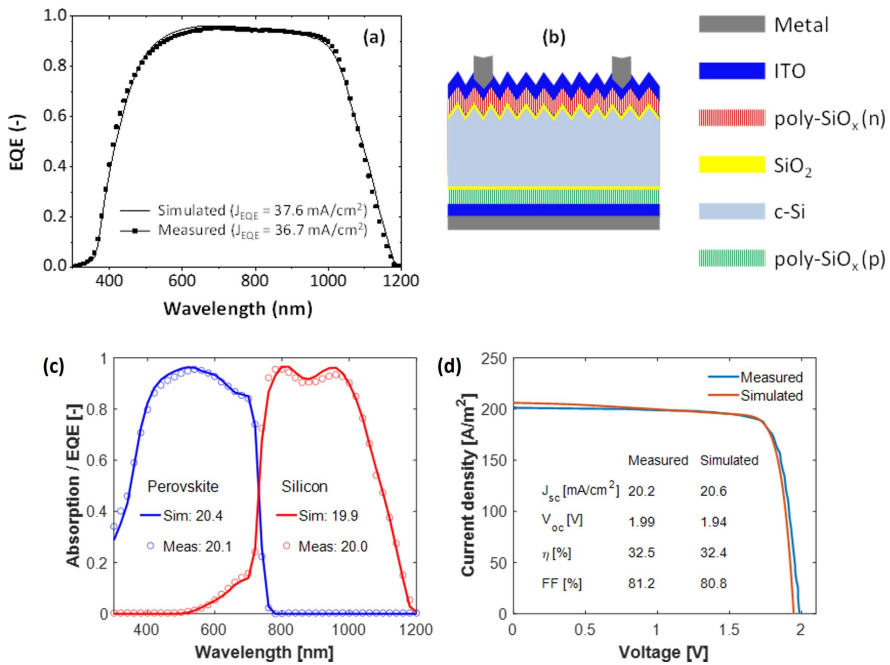


Figure 6.3: (a) Comparison of simulated absorptance (black line) with EQE (black squares) for front back contacted (FBC) single side textured (SST) poly-SiO_x passivated c-Si solar cell (b) solar cell structure used for simulation and measurement of EQE. Comparison of (c) simulated absorptance with EQE (given in Ref. [314]) and (d) simulated JV with measured JV (given in Ref. [314]) for the reference 2T perovskite/c-Si tandem with SHJ bottom cell.

The in-house developed and manufactured FBC poly-SiO_x solar cell [312], with a certified efficiency of 20.47%, has been used for validating the proposed modelling framework. The FBC poly-SiO_x solar cell has a front side texture and rear side flat interface. The refractive index (n), extinction coefficient (k) and thickness of n-type and p-type doped poly-SiO_x CSPCs have been taken from our earlier work [252]. Figure 6.3 (a) shows the simulated absorptance and measured EQE of the

FBC poly-SiO_x cell. The simulated values have an average deviation of 1.6% from the measured values, which shows that the simulated values are a good match with the measured values. The schematic of the simulated structure is shown in Figure 6.3 (b). Validation of EQE and JV of the reference 2T perovskite/c-Si tandem with SHJ bottom cell is shown in Figure 6.3 (c) and (d) respectively.

Measured JV curves at varying irradiance and temperature of the FBC poly-SiO_x solar cell are given as dots in Figure 6.1 (a) and (b) respectively. This shows that, as expected, increasing irradiance increases the current and increasing temperature reduces voltage in these solar cells. These JV curves are used for parameter extraction which are given as an input to the electrical part of the PVMD toolbox. As explained in Section 6.3, the measured curves are fitted using the five-parameter model, and the irradiance and temperature dependence of each of these five parameters is again parameterized. The average deviation between measured JV curves (details in Section 6.2) and reconstructed JV curves (from CLEM parameters) is less than 5%, showing that the fit is a good match. The JV curves of the top perovskite solar cell and the reference SHJ bottom cell [115, 314] have been obtained by ASA simulations and have been shown in Figure 6.4. The main effect of increasing temperature is a decrease in the V_{oc} , which is clearly observed in both the JV-curves from measurement (of the poly-SiO_x cell), and those from ASA simulation (of the perovskite and SHJ cells), and is included in our energy yield model. A secondary effect of increasing temperature, is a slight increase in J_{sc} due to bandgap variations. This is naturally included in the JV-curves obtained from measurement. However, this effect is not included in the JV-curves obtained from ASA simulations. This might lead to an underestimation of energy yield by a few percentage.

While the poly-SiO_x solar cell is fabricated in-house and holds potential for improvement in both passivation quality and optical performance, the SHJ solar cell considered represents an optimized, high-efficiency device as described in Ref. [314]. In terms of parameters relevant to the energy yield model, transitioning from the SHJ to the poly-SiO_x-based solar cell results in a reduction in V_{oc} . This decline is primarily attributed to the poly-SiO_x cell's lower passivation quality, which requires further optimization. Consequently this leads to an increase in recombination current density (J_o). Additionally, the SHJ solar cell demonstrates better carrier collection, as evident by a lower series resistance compared to the poly-SiO_x-based solar cell. Furthermore, differences in the optical constants of the carrier-selective passivation contacts (CSPCs) between the two c-Si technologies contribute to performance variations. The thicker poly-SiO_x layer introduces higher parasitic absorption losses, slightly diminishing the optical performance of the poly-SiO_x based solar cell compared to the SHJ solar cell.

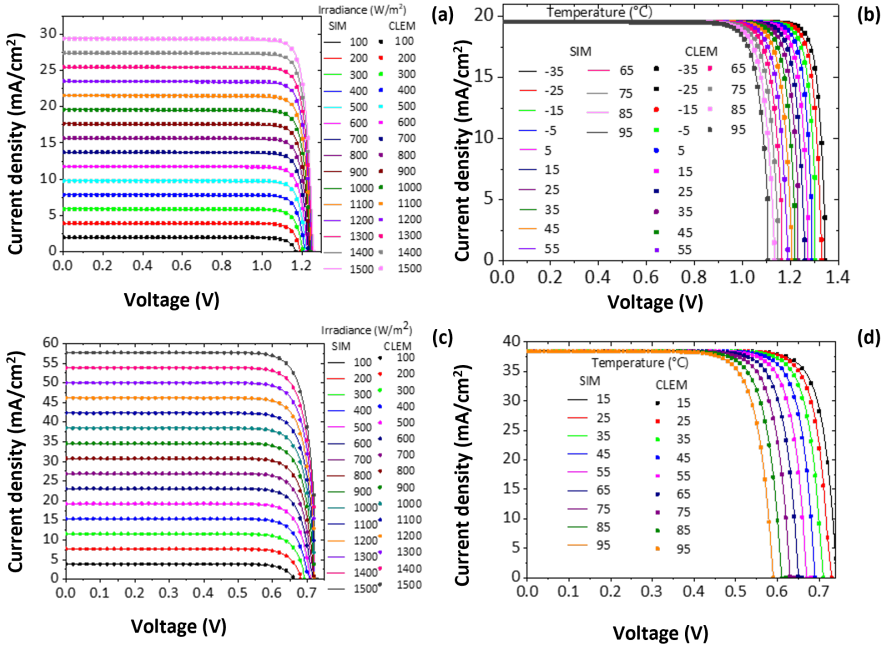


Figure 6.4: Simulated JV curves in ASA and GenPro4 (denoted by SIM) and reconstructed JV curves by Calibrated Lumped Element Model (CLEM) of perovskite solar cell for varying (a) irradiance for a fixed temperature of 25 °C and (b) temperature for a fixed irradiance of 1000 W/m² and SHJ solar cell (c) for varying irradiance for a fixed temperature of 25 °C and (d) temperature for a fixed irradiance of 1000 W/m².

6.5. Input parameters and structures

The FBC poly-SiO_x c-Si solar cell, the 2T tandem based on mono-facial poly-SiO_x cell, the 2T tandem based on bi-facial poly-SiO_x cell, and the 4T tandem based on mono-facial poly-SiO_x cell are shown in Figure 6.5 (a)-(d), respectively. We have considered a front and rear side texturing in the bottom c-Si solar cell to achieve maximum absorption. Perovskite solar cell deposited on top of c-Si solar cell follows the same texturing in 2T. For the 4T tandem, a flat perovskite top cell is considered as the perovskite solar cell in this case is deposited on flat glass. The thickness of the various layers used in simulation is given in Table 6.1. Thickness of c-Si is chosen to be 160 μm to match with industrial standards.

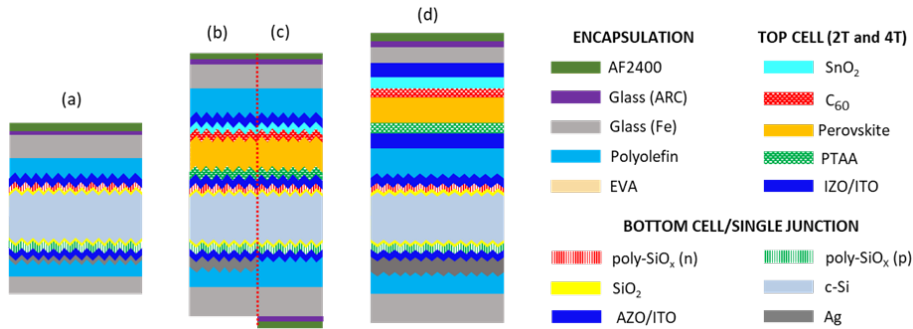


Figure 6.5: Simulated solar modules archetypes: (a) single junction mono-facial encapsulated FBC poly-SiO_x solar cell, (b) 2T mono-facial encapsulated perovskite/c-Si tandem with poly-SiO_x bottom cell, (c) 2T bi-facial encapsulated perovskite/c-Si tandem with poly-SiO_x bottom cell, and (d) 4T mono-facial encapsulated perovskite/c-Si tandem with poly-SiO_x bottom cell. Flat/flat top cell is considered for 4T. In such configuration an ITO layer is added at rear of the top cell for hole collection. Glass (ARC) is used as an anti-reflection coating to reduce reflection losses whereas Glass (Fe) is the soda lime glass typically used as an encapsulant in PV modules [115]

Table 6.1: Input layer thickness of simulated solar cell structures.

2T and 4T tandem			
Perovskite Top cell		c-Si Bottom cell	
Layer	Thickness	Layer	Thickness
TOP ITO / IZO [2T,4T]	40 nm, 175 nm	Top ITO	75 nm
SnO ₂	5 nm	poly-SiO _x (n type)	20 nm
C ₆₀	7 nm	SiO ₂	1.5 nm
Perovskite [2T,4T]	variable	c-Si bulk	160 μm
PTAA	23 nm	poly-SiO _x (p type)	30 nm
Bottom ITO [4T only]	175 nm	Bottom ITO	150 nm
		Ag	300 nm
Encapsulation materials			
AF2400	93 nm	Glass-Fe10ppmM1	3000 μm
Glass ARC	53 nm	Polyolefin-UVT	450 μm

Table 6.2 shows the various module parameters used in simulations. For bi-facial tandems (as shown in Figure 6.5 (c)), no rear metal is considered. Since, the rear TCO will increase the series resistance in bi-facial tandem, we consider twice the value of interconnection losses in the bi-facial case. Cell to module losses such as the parasitic absorption losses due to encapsulation, spacing losses to account for the spacing between the cells and metal contact shading have been included. The location specific input parameters used in simulation, such as

Global Horizontal Irradiance (GHI), optimum tilt, latitude and longitude, average Air Mass (AM) and average Ambient Temperature (T_{avg}) for each location are also included in Table 6.3. The architecture and input parameters of the double side textured reference SHJ tandem has been taken from Ref. [89, 115, 314].

Table 6.2: Module and electrical parameters used in energy yield simulation.

Parameter	Value	Parameter	Value
Number of Cell rows	10	Bypass diodes	3
Number of Cell columns	6	Module thickness	0.5 cm
Cell length	15.675 cm	Module row spacing	800 cm
Cell width	15.675 cm	Module area	1.5749 m ²
Total number of cells	60	Edge spacing	1 cm
Cell spacing	0.3 cm	Module side spacing	2 cm
Metal Resistance	0.0039 Ω [315]	Module azimuth	South-facing 0°, North-facing 180°
Metal coverage	2% [316, 317]	Mounting height	50 cm

Table 6.3: Global Horizontal Irradiance (GHI), optimum tilt, latitude and longitude, average Air Mass (AM_{avg}) and average Ambient Temperature (T_{avg}) of different locations used in simulation. AM_{avg} and T_{avg} are averaged over the entire year.

Location	Annual Global Horizontal Irradiance (GHI) (kWh/m ²)	Optimum Tilt (°) [318]	Latitude and Longitude	Average Air Mass (AM_{avg})	Average Ambient Temperature T_{avg} (°C)
Reykjavik (Iceland)	752	43	64.1470 °N 21.9408 °E	2.61	5.46
Rome (Italy)	1403	27	41.9028 °N 12.4964 °E	2.17	15.80
Alice Springs (Australia)	2203	-27	23.6980 °S 133.8807 °E	1.87	21.63

6.6. Results and Discussion

6.6.1. Energy yield at Standard Test Conditions (STC)

Table 6.4 gives the parameters of SHJ and poly-SiO_x based c-Si solar cells and modules at STC. The 2T tandems have been current-matched for a perovskite bandgap of 1.68 eV. The matched photocurrent density of the 2T mono-facial tandem based on poly-SiO_x bottom cell is 19.5 mA/cm² for a 550-nm thick perovskite absorber. Using the hybrid modelling approach, we can predict various parameters of the module comprising 2T mono-facial tandem devices based on poly-SiO_x bottom cells, such as the power (421 W_p) and the module efficiency (26.7%) at STC. In the case of 4T mono-facial configuration, a thicker perovskite of 700 nm is used for simulations as there are no current matching restrictions and a thicker perovskite is expected to give better performance. The module comprising 4T mono-facial tandem devices based on poly-SiO_x bottom cell delivers STC power output of 382 W and a module efficiency of 24.3%. We note the STC power output of the 2T tandem is 10.3% higher than that of the 4T tandem. The 4T tandem output is lower due to additional optical losses caused by the intermediate optical matching layers [319] and electrical losses due to the additional ITO layer at the rear of the perovskite top cell. SHJ tandem solar cells present higher output power to poly-SiO_x tandem solar cells. This is due to the lower passivation quality and larger parasitic absorption losses of doped poly-SiO_x CSPCs and ITO in the tandem based on poly-SiO_x bottom cell. Unlike the SHJ tandem, wherein the tunnel recombination junction (TRJ) is optimized for highest performance [89, 115, 314], the ITO layer considered in the poly-SiO_x tandem has been taken from the fabricated poly-SiO_x based single junction (SJ) solar cell [312] and has not been optimized for the tandem case. The TRJ of the tandem device based on poly-SiO_x bottom cell could be further optimized to increase the annual energy yield, but it is not the focus of this work. Table 6.5 shows the calculated voltage, current and power temperature coefficients (TCs) for SHJ and poly-SiO_x single junction (SJ) solar modules as well as perovskite SJ solar modules. For poly-SiO_x c-Si solar cell, the TCs are calculated from measured JV curves as given in Figure 6.1(a) and (b). For SHJ solar cell, the TCs are calculated from simulated JV curves obtained from ASA [115, 314] as shown in Figure 6.4. We find the TCs of the SHJ cell are more negative as compared to poly-SiO_x solar cell. The more negative temperature coefficients observed in SHJ cells could be due to a higher sensitivity of V_{oc} to temperature in SHJ solar cells as their passivation layers are deposited at lower temperatures. In contrast, poly-SiO_x-based cells, where passivation layers are deposited at higher temperature, have better thermal stability and experience less temperature-dependent reduction in V_{oc}. This indicates that the poly-SiO_x based solar cells might be more temperature stable as compared to SHJ solar cells.

In this work we use the TCs of bottom cell of tandem to explain the differences in the performance of tandem as the top perovskite solar cell is similar in both cases.

Table 6.4: Cell and module parameters for c-Si solar cell modules based on silicon heterojunction (SHJ) (reference) and poly-SiO_x technologies. Parameters for both single junction (SJ) and tandem structures are given below. Thickness of c-Si is fixed to 160 μm, while the perovskite thickness has been adjusted to obtain photocurrent density (J_{ph}) matching at STC. For 2T, $J_{ph,top} = J_{ph,bottom}$, while the bandgap of perovskite is 1.68 eV.

Cell Type	Perovskite Thickness [nm]	Silicon Thickness [μm]	Photo-current Density $J_{ph,top}, J_{ph,bottom}$ (mA/cm ²)	Rear side photo-current density (mA/cm ²)	STC Power [W _p]	STC Module Efficiency [%]
SHJ SJ	n.a.	160	37.8	-	323	20.5
Poly-SiO _x SJ	n.a.	160	37.4	-	260	16.5
2T SHJ Tandem	700	160	19.9	35.7	455	28.9
2T Poly-SiO _x Tandem	550	160	19.5	34.8	421	26.7
4T SHJ Tandem	700	160	18.4, 17.7	-	416	26.4
4T Poly-SiO _x Tandem	700	160	18.4, 17.4	-	382	24.3

Table 6.5: Temperature coefficients (TCs) of SHJ and poly-SiO_x based c-Si modules. These temperature coefficients have been calculated from simulated and measured JV curves of c-Si solar cells based on SHJ and poly-SiO_x technology.

Cell Type	TC _{Voc} (%/K)	TC _{Jsc} (%/K)	TC _{Pmpp} (%/K)
SHJ SJ	-0.264	-0.001	-0.322
Poly-SiO _x SJ	-0.233	0.039	-0.250
Perovskite SJ	-0.143	0.0009	-0.174

6.6.2. Energy yield in outdoor conditions

In this section, the energy yield of novel 2T and 4T mono-facial tandem modules based on poly-SiO_x bottom cell is optimized with respect to different perovskite thicknesses and bandgaps. The bi-facial case is also considered for the 2T tandem module. Location chosen for this part of the study is Rome (See Table 6.3). The input parameters and structure of the tandem devices are given in Section 6.5. On the other hand, tandem devices based on SHJ bottom cell have already been optimized in earlier studies [115, 294, 320–322].

2T mono-facial tandem module based on poly-SiO_x bottom cell

As we see from Table 6.4, a 550-nm thick perovskite absorber is required to reach photocurrent density matching in 2T tandem device with poly-SiO_x bottom cell. In outdoor conditions, one has to evaluate the opto-electric performance of the tandem as function of perovskite bandgap and thickness, which affect both V_{oc} and J_{sc} . Hence, we have optimized the bandgap and thickness of the perovskite absorber layer to maximize the annual energy yield of the 2T tandem device in Rome at an optimum tilt of 27°. Figure 6.6 shows such optimization wherein annual energy yield of the 2T perovskite / poly-SiO_x tandem module is simulated for a range of perovskite bandgaps (from 1.56 eV to 1.80 eV) and for different perovskite absorber thicknesses (from 300 to 600 nm). From Figure 6.6, we find the optimum perovskite bandgap for 300-nm thick perovskite absorber is 1.64 eV, which gives 602 kWh/y in terms of annual energy yield. This optimum value increases to 1.68 eV for a 600-nm thick perovskite absorber thickness, which gives 623 kWh/y. Since the optimum energy yield is obtained around photocurrent density matched condition, we find that by increasing the perovskite bandgap in 2T perovskite/c-Si tandem cell, the optimum energy yield is obtained for a thicker perovskite absorber.

2T vs 4T mono-facial tandem module based on poly-SiO_x bottom cell

In this section, the simulation results related to 2T and 4T tandem devices both based on poly-SiO_x solar cell are compared, again as function of perovskite absorber thickness and bandgap. The input structure and parameters for the 4T tandem module have been also given in Section 6.5. Figure 6.7 (a) shows annual energy yield for varying perovskite absorber thickness (from 300 to 900 nm) of both 2T and 4T tandem modules based on poly-SiO_x bottom cell. Note that the perovskite bandgap has been fixed to 1.68 eV for these simulations. We observe an increase in the annual energy yield of the 2T tandem module (592 kWh/y to 624 kWh/y) as the perovskite thickness increases from 300 nm to 550 nm. As the perovskite thickness is further increased beyond 550 nm, the annual energy

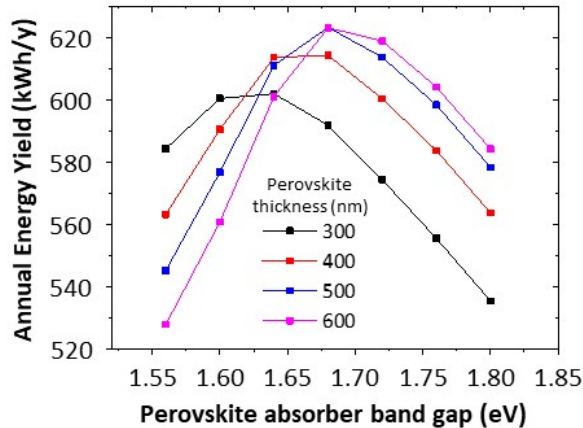


Figure 6.6: Annual energy yield of 2T mono-facial tandem module based on poly-SiO_x bottom cell as function of top cell perovskite absorber bandgap and thickness. Shift in optimum bandgap is seen for increasing thickness of perovskite. The simulations have been carried out in Rome as location at an optimum tilt of 27°.

yield gradually decreases. The annual energy yield for 900-nm thick perovskite thickness is 615 kWh. This shows that at 550 nm, top and bottom sub-cells are current matched and, so, the highest annual energy yield is obtained. In general, we observe the perovskite absorber is limiting the tandem's total current for thinner perovskite absorbers whereas the c-Si bulk is limiting the current for thicker perovskite absorbers. From our previous work, we have seen similar trends for total photocurrent of 2T tandem device [311]. On the other hand, for the 4T tandem module based on poly-SiO_x bottom cell, the current matching is not required. The annual energy yield for 4T tandem increases for increasing perovskite thickness (545 kWh at 300 nm to 569 kWh at 700 nm). On increasing the perovskite thickness after 700 nm, a slight decrease in energy yield is seen (567 kWh at 900nm). Hence, 700 nm is the optimal perovskite thickness for 4T tandem configuration. The annual energy yield of the optimized 2T and 4T tandems modules are 624 kWh/y and 569 kWh/y, respectively. The annual energy yield of the 2T tandem module is higher than the annual energy yield of the 4T tandem module by an average 8.5%. This value is reduced from the 10.3% mark at STC (see Table 6.4) due to varying real world spectral conditions. A lower annual energy yield in 4T tandem module can be attributed to the additional optical and electrical losses in the 4T configuration as compared to the 2T one due to additional charge transport layers in top and bottom cells of 4T tandem.

Figure 6.7 (b) shows again the annual energy yield of 2T and 4T tandem modules based on poly-SiO_x bottom cell but for varying perovskite bandgaps

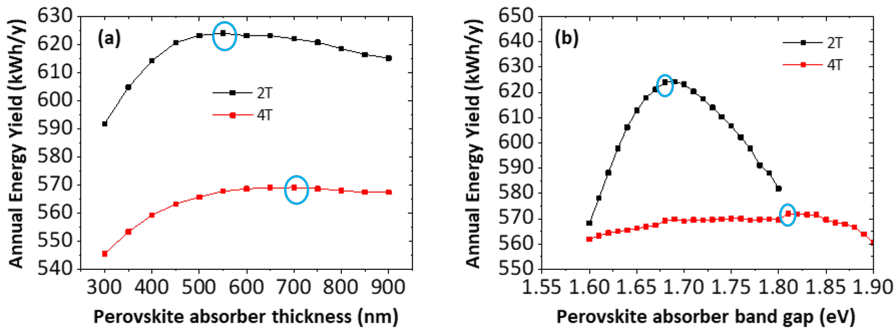


Figure 6.7: Annual energy yield of 2T and 4T perovskite/poly-SiO_x tandem for (a) varying perovskite thickness (perovskite bandgap is fixed to 1.68 eV for 2T and 4T tandem) and (b) varying perovskite bandgap (perovskite thickness is fixed to 550 nm for 2T and 700 nm for 4T). The 4T and 2T poly-SiO_x simulations have been carried out at Rome at an optimum tilt of 27°. The blue circles indicate the optimal perovskite thickness and bandgap respectively.

(from 1.60 to 1.80 eV) and fixed thickness of the perovskite absorber (550 nm and 700 nm for 2T and 4T configurations, respectively). These values are chosen since they realize the highest annual energy yield (see Figure 6.7 (a)). In Figure 6.7 (b) we observe that, as expected, the 2T tandem module based on poly-SiO_x bottom cell is more sensitive than the 4T counterpart to the perovskite absorber bandgap. This is due to the current mismatch conditions that affect the 2T tandem configuration. For the perovskite absorber exhibiting bandgaps lower than 1.68 eV, the c-Si bottom cell is limiting and for perovskite bandgaps above 1.68 eV, the top perovskite cell is limiting. So, in the 2T configuration, the optimum bandgap for 550-nm thick perovskite is 1.68 eV. By increasing the perovskite band-gap from 1.60 eV to 1.68 eV, the annual energy yield increases from 567 kWh/y to 624 kWh/y. Above the 1.68 eV bandgap value, the annual energy yield decreases. However, for the 4T configuration, varying the perovskite bandgap from 1.60 eV to 1.68 eV, the annual energy yield increases from 562 kWh/y to only 569 kWh/y. On further increasing the perovskite bandgap, the energy yield decreases to 560 kWh/y at perovskite bandgap of 1.9 eV. On varying the perovskite bandgap, the energy yield of 4T tandem varies by only 1.78% unlike the 2T case where the energy yield varies by around 10%.

2T mono-facial vs bi-facial tandem module based on poly-SiO_x bottom cell

Bi-facial modules can benefit from the additional irradiation on the rear side of the module. However, in the 2T configuration, this also poses an additional challenge while pursuing the current matching condition as the rear-side irradiance is fully

absorbed by the bottom cell. In this section, annual energy yield of 2T bi-facial perovskite/c-Si tandem modules are simulated with respect to the spectral albedo of several materials, such as dry grass, green grass, white paint and snow. Note an in-house developed ray-tracing model [126, 127, 323] is used to calculate both front and rear side spectrally resolved irradiance for every hour of the year. The wavelength dependent reflectance or spectral albedo of dry grass, green grass, white paint and snow are shown in Figure 6.8 (a). The average reflectance over the wavelength range from 300 nm to 1200 nm is highest for snow (94.3%) followed by white paint (65.1%), green grass (36.5%) and dry grass (25.3%). Snow is close to an ideal reflector and is also considered in this study. Here, we have considered our standard current-matched case of 2T tandem module based on poly-SiO_x bottom cell with 550-nm thick perovskite absorber with 1.68 eV bandgap. Again, the modelling location is Rome for a tilt of 27°. In order for the results to be comparable, for a mono-facial tandem module the ground reflected irradiance has also been taken into account. Spectral albedo of dry grass has been chosen for these simulations.

First, for surfaces with different spectral albedo, the thickness of the perovskite absorber is varied while keeping fixed the bandgap to 1.68 eV. These results are shown in Figure 6.8 (b). As expected, the annual energy yield of the 2T bi-facial tandem module increases on surfaces with higher spectral albedo as the sunlight reflected from the ground is absorbed in c-Si absorber and adds to its current. As expected, the highest annual energy yield is seen for the 2T bi-facial tandem module on snow. For perovskite thicknesses greater than 550 nm, the increased current density from the bottom cell starts limiting the performance. So the annual energy yield can be increased for thicker perovskite absorber. With respect to the 2T mono-facial configuration, the 2T bi-facial configuration on snow shows an increase in annual energy yield of 2.5% (4.5% and 5.3%) for 300-nm (600-nm and 900-nm) thick perovskite absorber. It is evident that a thicker perovskite is needed to current match the extra current generated due to rear absorption in bi-facial case. We observe in Figure 6.8 (b), in case of snow, that the optimum perovskite thickness increases from 550 nm of the mono-facial configuration to 700 nm of the bi-facial configuration. In the former case, the maximum annual energy yield is 624 kWh/y while in the latter the annual energy yield is 652 kWh/y. In Figure 6.8 (c), the perovskite bandgap is varied between 1.56 eV and 1.80 eV while the thickness is set to 550 nm. For perovskite bandgaps below 1.68 eV, the c-Si current is limiting and the additional light absorption from the rear side of the tandem module increases the module's current and, consequently, its annual energy yield as compared to the 2T mono-facial configuration. Hence, the increase in annual energy yield for 2T bi-facial tandem modules with respect to 2T mono-facial tandem modules is higher for perovskite bandgaps lower than 1.68 eV. With

respect to the 2T mono-facial tandem module poly-SiO_x tandem and in case of snow, the 2T bi-facial tandem module shows an increase of 7.5% (4% and 1.9%) for 1.56 eV (1.68 eV and 1.80 eV) perovskite bandgap. We remind the optimum perovskite bandgap and thickness for the 2T mono-facial tandem module being 1.68 eV and 550 nm, respectively. As the spectral albedo increases, we see a slight shift towards lower perovskite bandgaps. To conclude, the optimum perovskite bandgap on snow is 1.67 eV and, for perovskite thickness of 550 nm, the resulting maximum annual energy yield is 650 kWh/y.

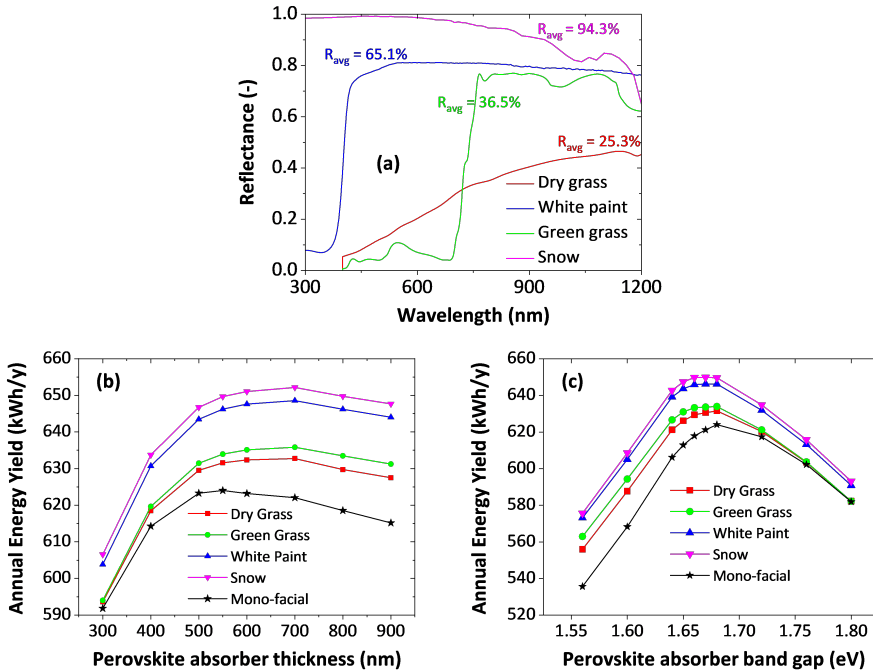


Figure 6.8: (a) Wavelength-dependent reflectance for different surfaces; Annual Energy Yield of 2T bi-facial tandem based on poly-SiO_x bottom cell for (b) varying top cell perovskite thickness on different ground surfaces (perovskite bandgap = 1.68 eV) and (c) varying top cell perovskite bandgap on different ground surfaces (perovskite thickness = 550 nm). The above simulations are carried out in Rome at a tilt of 27°.

Notably, the bi-facial configuration demonstrates flexibility in design, with a broader range of perovskite bandgaps (1.65–1.68 eV) and thicknesses (500–800 nm) resulting in energy yield variations of less than 1%. This indicates the robustness of the bi-facial design to parameter variations. In general, for all surfaces, a perovskite bandgap of 1.68 eV and a thickness of 700 nm yield the best performance for a 2T bi-facial perovskite/c-Si tandem module with a poly-SiO_x bottom

cell. In comparison, for the 2T mono-facial configuration, the optimal perovskite bandgap and thickness are 1.68 eV and 550 nm, respectively.

When fabricating mono-facial and bi-facial modules together, it is feasible to use a common perovskite bandgap of 1.68 eV and a thickness of 550 nm, ensuring efficient performance across both configurations. This approach highlights the potential for standardizing key parameters, simplifying the fabrication process, and maintaining high performance under diverse outdoor conditions.

6.6.3. Comparison of SJ and tandem modules based on poly-SiO_x and SHJ bottom cells

In this section, the annual energy yield of tandem modules with different bottom cell technologies, namely SHJ and poly-SiO_x CSPCs, has been simulated for different locations using the PVMD toolbox. Tilting the photovoltaic module at optimum angle increases the incident irradiance on the plane of the array. The optimum tilt for testing cities, Reykjavik (Iceland), Rome (Italy) and Alice Springs (Australia), are given in Table 6.3. The motivation for choosing these cities is that they cover a wide range of latitudes and an increasing annual global horizontal irradiance (GHI), as shown in Table 6.3. The single junction and tandem module archetypes have been shown in the Figure 6.5, while detailed input parameters are given in Section 6.5.

SJ and 2T tandem modules

Figure 6.9 (a), (b) and (c) show the modelled annual energy yield and specific energy yield of SJ and 2T tandem modules based on SHJ (reference) or poly-SiO_x technologies in Reykjavik, Rome and Alice Springs, respectively. Optimized perovskite thickness of 700 nm and 550 nm are used for simulating 2T tandem modules based on SHJ or poly-SiO_x bottom cells, respectively (See Figure 6.7 (a),(b) and Table 6.4). Results of SJ SHJ and poly-SiO_x modules are also analysed. At STC, we observe the output power of 2T tandem modules based on SHJ (poly-SiO_x) bottom cells is higher than the SJ SHJ (poly-SiO_x) module by ~41% (~62%) (See Table 6.4). Also in outdoor conditions, the 2T modules outperform SJ modules and, with increasing irradiance at different testing cities, the annual energy yield of the various module technologies increases. The annual energy yield of 2T tandem modules based on poly-SiO_x bottom cells is 377 kWh/y, 624 kWh/y and 931 kWh/y in Reykjavik, Rome and Alice Springs, respectively. In contrast, SJ modules based on poly-SiO_x cells realize an annual energy yield of 242 kWh/y, 385 kWh/y and 575 kWh/y in Reykjavik, Rome and Alice Springs, respectively. Therefore, from SJ to 2T tandem modules based on poly-SiO_x, a gain in annual energy yield of 56%, 62% and 62% can be expected in Reykjavik, Rome and Alice Springs respectively.

The slightly lower tandem gain for Reykjavik can be attributed to the incident spectrum in Reykjavik being farthest from the STC spectrum (AM1.5) as compared to Rome and Alice Springs for which the tandem was current matched (See AM_{avg} in Table 6.3).

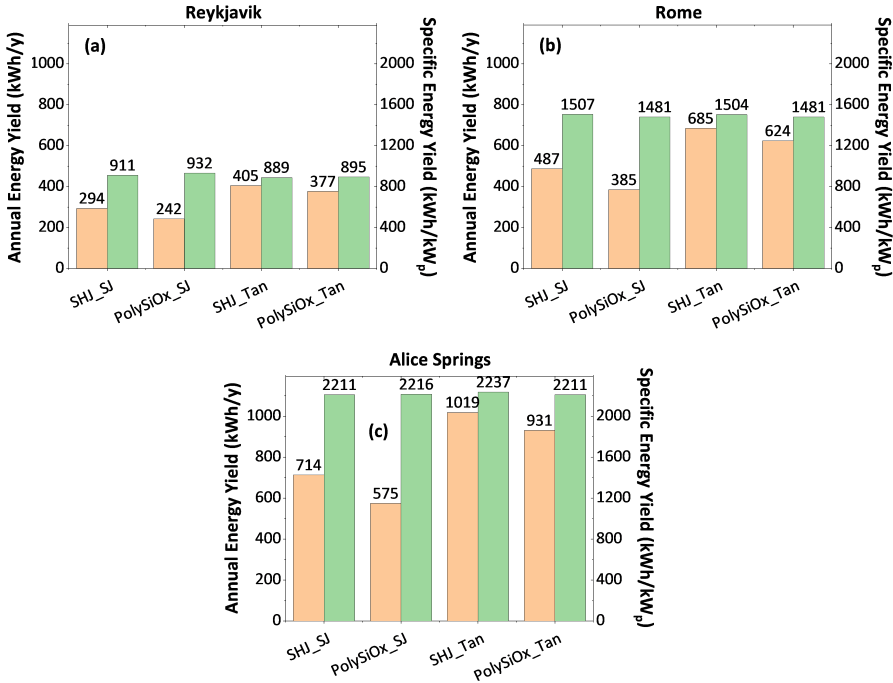


Figure 6.9: Annual energy yield (left axis, orange bars) and specific energy yield (right axis, green bars) of single junction silicon heterojunction (SHJ_SJ) cells module, single junction poly-SiO_x (poly-SiO_x_SJ) cells module, 2T tandem module based on SHJ bottom cell (SHJ_Tan) and 2T tandem module based on poly-SiO_x bottom cell (PolySiOx_Tan) in (a) Reykjavik, (b) Rome and (c) Alice Springs.

Figure 6.9 (a), (b) and (c) show that the annual energy yield of 2T tandem modules based on SHJ bottom cells is higher than that of the 2T tandem module based on poly-SiO_x bottom cells. The specific energy yield, defined as the annual energy yield over the STC power and simply indicated with kWh/kW_p, is an important parameter to compare the performance of different cell technologies relative to their STC performance. The specific energy yield of the 2T tandem module based on poly-SiO_x bottom cells is only ~1.5% (~1.2%) lower than that of the reference 2T tandem module based on SHJ bottom cells tandem in Rome (Alice Springs). Conversely, for locations with lower irradiance such as Reykjavik, the specific energy yield of the 2T tandem module based on poly-SiO_x bottom cells is 0.7% higher than that of the 2T tandem module based on SHJ bottom cells.

We explain this results as follows. At lower irradiance, the voltage and the power output are more sensitive to temperature change [324]. Hence, the 2T tandem module based on SHJ bottom cells suffers from higher power losses in case of temperature changes as compared to the poly-SiO_x-based counterpart due to the more negative temperature coefficient of SHJ bottom cells (see Table 6.5).

4T tandems modules

The series connection of 4T tandem is simulated by simulating the top and bottom cell JV curves separately for every hour of the year. The resistance values of the ITO layers for both top and bottom cell curves are included. Finally, the top and bottom cell's power is added to obtain the total DC power (energy yield) of the 4T tandem. Here we assume to top cells are not connected to the bottom cells, so top and bottom operate independently (each have their own MPPT). Figure 6.10 (a), (b) and (c) show the annual energy yield and the specific energy yield of 4T tandem modules based on SHJ or poly-SiO_x bottom cells in Reykjavik, Rome and Alice Springs, respectively. In these simulations, the perovskite absorber is 700-nm thick and its bandgap is fixed at 1.68 eV (see Figure 6.7 (a) as well as Table 6.4). Although the optimal perovskite bandgap for the 4T configuration is 1.81 eV, we chose a 1.68 eV bandgap for 4T tandem simulations as it closely aligns with the optimal of 2T configuration. Additionally, the differences in energy yield between the two bandgaps are minimal in 4T case (See Figure 6.7(b)).

The annual energy yield of the 4T tandem based on poly-SiO_x bottom cells is 348 kWh/y, 570 kWh/y and 849 kWh/y in Reykjavik, Rome and Alice Springs, respectively. In contrast, the annual energy yield of the 4T tandem module based on SHJ bottom cells is higher than that of the 4T module based on poly-SiO_x bottom cells by 8.7%, 10.8% and 10.4% in Reykjavik, Rome and Alice Springs, respectively. This is due to the additional opto-electrical losses experienced by the 4T tandem module based on poly-SiO_x bottom cells compared to its SHJ-based counterpart, similarly to the loss in performance at STC (See Table 6.4). The specific energy yield of 4T tandem modules based on poly-SiO_x bottom cells decreases with respect to that of the SHJ-based counterpart by 1.7% (1.3%) in Rome (Alice Springs). However, similarly to the 2T tandem modules' results, the specific energy yield of the 4T tandem module based on poly-SiO_x bottom cells is 0.2% higher than that of the SHJ-based counterpart in Reykjavik.

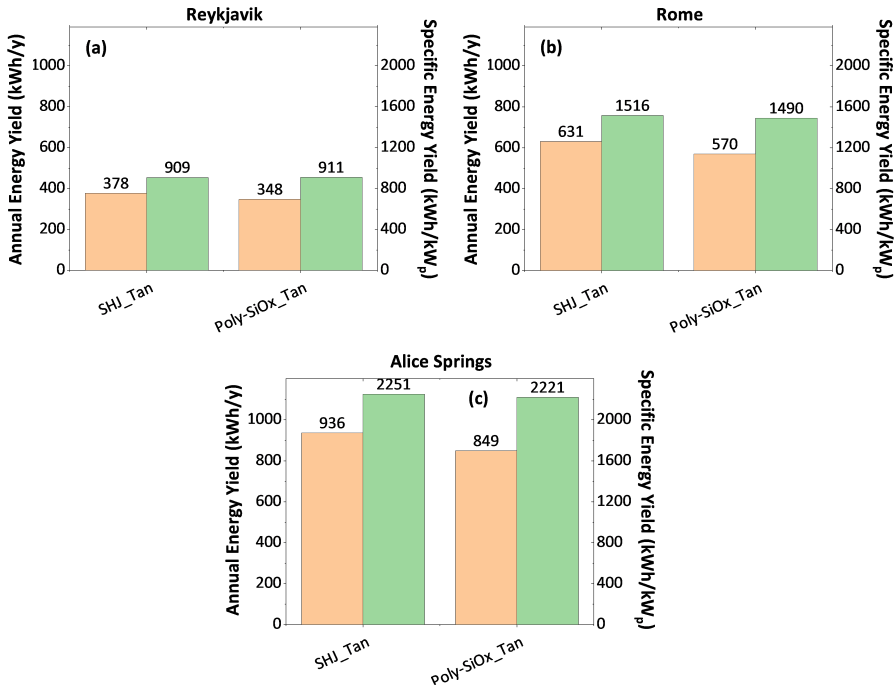


Figure 6.10: Annual energy yield (orange bars) and specific energy yield (green bars) of 4T tandem modules based on SHJ and poly-SiO_x bottom cells in (a) Reykjavik, (b) Rome and (c) Alice Springs. Optimized tilt, given in Table 6.3, are used in the simulations. The perovskite is absorber is 700-nm thick and its bandgap is 1.68 eV.

2T bi-facial and mono-facial tandem modules

Figure 6.11 (a), (b) and (c) show the comparison between 2T bi-facial tandem modules based on SHJ or poly-SiO_x bottom cells for different spectral albedos in Reykjavik, Rome and Alice Springs, respectively. For these bi-facial simulations, we have used the perovskite thickness that gives the current matched condition in 2T mono-facial case, i.e. 700 nm for SHJ-based tandem module and 550 nm for poly-SiO_x-based tandem (see Table 6.4). Also, the optimized perovskite bandgap of 1.68 eV is used in this simulation. The highest annual energy yield values are obtained on snow, which has the largest average spectral albedo of 94.3% (see Figure 6.8 (a)). The annual energy yield of 2T bi-facial tandem modules based on SHJ (poly-SiO_x) bottom cells is 420 kWh/y (397 kWh/y) in Reykjavik, 699 kWh/y (650 kWh/y) in Rome and 1033 kWh/y (964 kWh/y) in Alice Springs. As in the mono-facial configuration case, the difference in annual energy yield between SHJ-based and poly-SiO_x-based tandem modules is higher in places like Rome (+7.5%) and Alice Springs (+7%) and lower in Reykjavik (+5.7%) due to the voltage

of the SHJ-based tandem module being more sensitive to change in temperature in places with lower irradiance like Reykjavik.

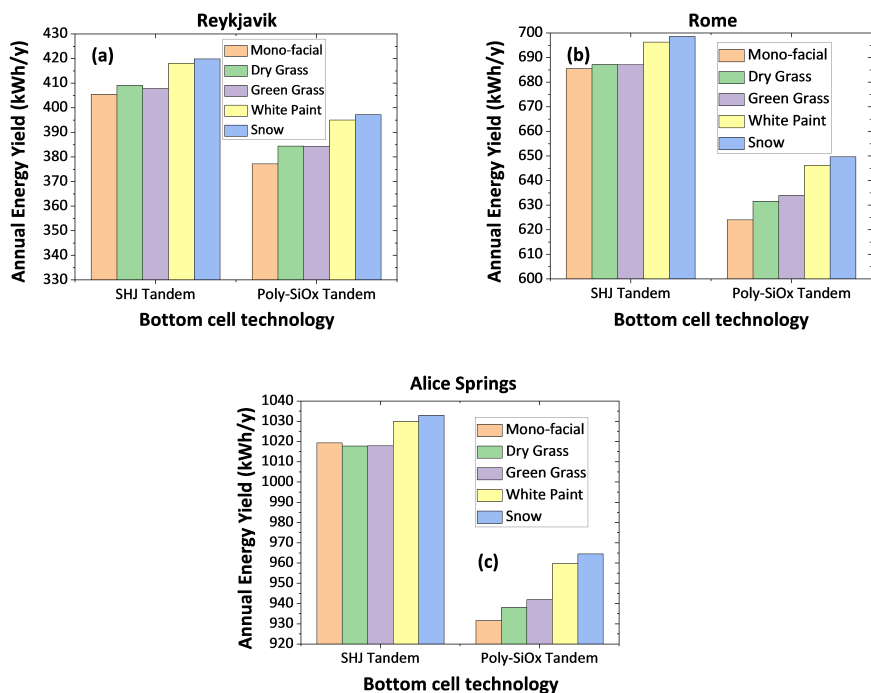


Figure 6.11: Annual energy yield of 2T bi-facial tandem modules based on SHJ or poly-SiO_x bottom cells in (a) Reykjavik, (b) Rome and (c) Alice Springs for different reflecting materials (dry grass, green grass, white paint and snow). Results are compared with mono-facial configuration. The perovskite absorber thickness is set to 700 nm (550 nm) for SHJ-based (poly-SiO_x-based) tandem module. Its bandgap is 1.68 eV. Optimized tilt is considered for each location (Table 6.3).

From Figure 6.11 (a), (b) and (c), we observe that the relative annual energy yield difference between the 2T tandem modules based on SHJ bottom cells with respect to the poly-SiO_x-based counterpart decreases with increasing spectral albedo in all testing cities. For example, in Rome, the annual energy yield of the 2T mono-facial tandem based on SHJ bottom cells is higher than that of the poly-SiO_x-based counterpart by 9.8% but decreases to 7.5% in bi-facial configuration for the case of snow. Since the photo-current density generated from the rear-side irradiance of the SHJ solar cell is higher than that of the poly-SiO_x-based c-Si solar cell in the 2T configuration (See Table 6.4), the reduced difference in energy yield between the SHJ and poly-SiO_x-based cells in the bi-facial case (compared to the mono-facial case) cannot be attributed to optical factors. To explain this, the average operating temperature (T_{avg}), open circuit voltage (V_{oc-avg}), and

short circuit current (I_{sc-avg}) of the 2T tandem modules based on SHJ or poly-SiO_x bottom cells in Rome are given in Table 6.6. The increased irradiance in bi-facial tandem modules increases both the photogenerated current and the voltage. However, the latter increase is curbed by the increase in operating cell temperature due to the increase in absorbed irradiance in the bi-facial tandem modules (see Table 6.6) [297]. Due to the more negative temperature coefficient of the SJ SHJ module (see Table 6.5), the V_{oc-avg} is slightly lower in the 2T tandem modules based on SHJ bottom cells than in the poly-SiO_x-based counterparts. Hence, the voltage gain from mono-facial to bi-facial configuration is smaller in 2T tandem modules based on SHJ bottom cells than in the poly-SiO_x-based counterparts (see Table 6.6). Similarly, the increase in operating temperature due to the additional photogenerated current in bi-facial configuration increases the current more in the 2T tandem module based on poly-SiO_x bottom cells than in the SHJ-based counterpart due to the more positive current temperature coefficient of the SJ poly-SiO_x module (see Table 6.5). Hence, the difference between the 2T bi-facial tandem module based on SHJ bottom cells and the 2T bi-facial tandem module based on poly-SiO_x bottom cells decreases with increasing spectral albedo.

Table 6.6: Average output parameters of 2T tandem modules based on SHJ or poly-SiO_x bottom cells in Rome.

Modules output parameters	SHJ technology			Poly-SiO _x technology		
	2T mono-facial tandem	2T bi-facial tandem on snow	Absolute increase	2T mono-facial tandem	2T bi-facial tandem on snow	Absolute increase
Average operating Temperature T_{avg} (°C)	18.35	18.53	0.18	18.51	18.73	0.22
Average output voltage V_{oc-avg} (V)	55.19	55.54	0.35	53.43	53.93	0.5
Average output current I_{sc-avg} (A)	1.66	1.7	0.04	1.62	1.67	0.05

6.7. Conclusions

In this work, we have used a hybrid approach (combination of simulation and experimental data) in an advanced simulation framework to calculate the annual energy yield and the specific energy yield of novel 2T and 4T tandem modules based on poly-SiO_x bottom cells. This approach makes our device simulations flexible and is especially useful for predicting annual energy yield of tandem modules with novel materials or architectures.

Our results reveal several critical insights into the performance of poly-SiO_x-based tandem modules. Under standard test conditions (STC), we calculated power outputs of 421 Wp and 382 Wp for 2T mono-facial and 4T tandem modules, respectively, based on poly-SiO_x bottom cells. In outdoor realistic conditions, the optimized annual energy yield of a 2T mono-facial and 4T tandem modules based on poly-SiO_x bottom cells is 624 kWh/y and 572 kWh/y, respectively, in the testing city of Rome. By leveraging bi-facial configurations, we further enhanced the annual energy yield of 2T tandem modules to 652 kWh/y on reflective surfaces such as snow, showcasing the potential of poly-SiO_x-based tandems in high-albedo environments.

Using our simulation framework, we have determined the optimum perovskite thickness and bandgap for various tandem configurations. For the mono-facial 2T tandem, the optimal parameters are a bandgap of 1.68 eV and a thickness of 550 nm, while for the 4T perovskite/c-Si tandem, they are 1.81 eV and 700 nm. However, a common perovskite bandgap of 1.68 eV can be effectively utilized for both 2T and 4T configurations, as the 4T tandem demonstrates less than 2% variation in energy yield within the 1.68–1.81 eV bandgap range. In the 2T bi-facial configuration, a bandgap of 1.68 eV and a thickness of 700 nm generally perform best across all surface types. However, we observe that a broader range of perovskite bandgaps (1.65–1.68 eV) and thicknesses (500–800 nm) results in energy yield variations of less than 1% in the bi-facial case. This highlights the flexibility of our modeling framework, which allows for the optimization of a common set of parameters across different conditions.

In this study, we have experimentally shown that the poly-SiO_x passivated c-Si solar cell can be more thermally stable as compared to the modelled SHJ solar cell presented in our previous study [115]. We find that, similarly to the power output under STC, in outdoor realistic conditions the annual energy yield of tandem module based on SHJ bottom cells is higher than that of the poly-SiO_x-based counterpart. However, for locations with lower irradiance such as Reykjavik, the specific energy yield of 2T (4T) tandem module based on poly-SiO_x bottom cells is 0.7% (0.2%) higher than that of SHJ-based counterpart due to the effects of poly-SiO_x solar cells' temperature coefficient on tandem being more significant

at lower irradiance. Using bi-facial tandem modules on snow, the annual energy yield difference between 2T tandem modules based on SHJ and poly-SiO_x bottom cells can be reduced. The increased rear irradiance in bi-facial configuration increases its operating temperature leading to lesser gain in performance of 2T bi-facial tandem based on SHJ bottom cells as compared to the poly-SiO_x-based counterpart due to the difference in their temperature coefficients.

7

Conclusions and Outlook

7.1. Conclusions

In this thesis, high temperature CSPPCs for c-Si solar cells are optimized, evaluated and integrated in perovskite/c-Si tandem solar cells. The main conclusions are summarized below.

Firstly, the absorption coefficients of mixed phase material such as n-type and p-type doped poly-SiO_x and poly-SiC_x are extracted via novel inverse modelling approach based on reflection-transmission measurements in the 300-1200 nm wavelength range. By using this approach, free carrier absorption is accurately modeled in the infrared region. We find that by increasing the doping concentration, the free carrier absorption in n-type and p-type doped poly-SiO_x and poly-SiC_x CSPPCs increases. The obtained absorption coefficients are used in subsequent optical simulations of tandem solar cells with such high temperature CSPPCs. This model could be extended to find absorption coefficients of other silicon based CSPPCs. These results are described in detail in chapter 3.

Secondly, using the absorption coefficients from chapter 3, optical simulations of 2T, 3T and 4T perovskite/c-Si tandem solar cells with high temperature CSPPCs are simulated in real world conditions (See chapter 4 for detailed results). A matched current density of greater than 20 mA/cm² and around 19.5 mA/cm² for un-encapsulated and encapsulated tandem, respectively, with poly-Si, poly-SiO_x and poly-SiC_x CSPPCs is obtained. The performance values are slightly lower than those of a two-terminal (2T) tandem solar cell that uses a silicon heterojunction (SHJ) as the bottom cell. This is due to increased free carrier absorption, which occurs due to the high levels of doping required in poly-Si, poly-SiO_x and poly-SiC_x CSPPCs that undergo high-temperature processing. Despite this, these CSPPCs are well-suited for high-temperature manufacturing methods, which makes them

attractive for the current mainstream crystalline silicon (c-Si) solar cell industry. Their ability to withstand high temperatures means they can be integrated into standard production lines, making them a practical choice even though their efficiency is slightly impacted by doping-related absorption. Using yearly average photocurrent density, tandem architectures are compared at module level. It is shown that a higher yearly average photocurrent density is obtained for bi-facial tandems. The optimum thickness of the perovskite absorber layer in bi-facial tandem solar cells is greater than in mono-facial tandems. Additionally, for higher albedo values, the optimal bandgap of the perovskite absorber is lower compared to the bandgap that is best suited for lower albedo conditions.

Thirdly, an implied V_{oc} of 710 mV was achieved for the textured n-type and flat p-type doped poly-SiO_x CSPCs on thin thermal tunneling oxide after hydrogenation. These CSPCs are incorporated into poly-SiO_x passivated 4 cm² screen-printed single-junction c-Si solar cell with a SST configuration. This cell achieved a certified efficiency of 20.47% and a fill factor above 80%. Using two-step annealing, the passivation of textured p-type doped poly-SiO_x CSPC on thin tunneling thermal oxide was improved to 687 mV. A DST solar cell with poly-SiO_x CSPCs was presented for the first time with a certified efficiency of 19.44%. These results are discussed in detail in chapter 5.

Fourthly, in chapter 5, the fabricated poly-SiO_x passivated SST and DST solar cells are tested as bottom cells in combination with a certified semi-transparent perovskite top cell with a 19.70% efficiency. These novel 4T perovskite/c-Si tandem solar cells give an efficiency of 27.97% and 28.07%, respectively. A 2T tandem with poly-SiO_x passivated bottom cell was fabricated for first time with an efficiency of 23.18%.

Finally, using a hybrid approach, annual energy yield of 2T and 4T perovskite/c-Si tandem with poly-SiO_x passivated bottom cell is estimated for different locations of world in chapter 6. This value comes out around 624 kWh and 569 kWh for 2T and 4T poly-SiO_x tandem, respectively, in Rome. It is shown that using a bi-facial 2T configuration on highly reflecting surface like snow, this annual energy yield can be increased to 652 kWh. In comparison to 4T, the 2T perovskite/c-Si tandem configuration is much more sensitive to perovskite thickness and bandgap variations. We find an optimum bandgap of 1.68 eV and optimum perovskite thickness of 550 nm for our poly-SiO_x tandem. We find that the poly-SiO_x tandem is more thermally stable than the SHJ tandem. Due to the effect of temperature coefficient being more significant in places of lower irradiance, the poly-SiO_x tandem shows a higher specific energy yield than the SHJ tandem in such places. Moreover, the difference between the annual energy yield of bi-facial SHJ tandem and poly-SiO_x tandem is reduced on snow due to the difference in their temperature coefficients.

7.2. Outlook

The following recommendations are offered for future research.

1. Electrical optimization of recombination layer of 2T perovskite/c-Si tandem solar cells with high temperature carrier-selective passivating contacts would help in further improving its efficiency. Role of TCO as a tunnel recombination layer in 2T tandems could be investigated. Doping and thickness of ITO can be optimized to improve the performance of such tandems.
2. In this study, we have not focused on optimizing perovskite solar cells. Optimizing the perovskite top cell is crucial to improve the performance of perovskite/c-Si tandems. Considering different top cell configurations such as nip or pin architecture could lead to interesting observations and improvement in the performance of tandem. Different perovskite composition with varying bandgaps could be investigated. Additionally, dual cation and triple cation perovskite could be compared in terms of its performance in a perovskite/c-Si tandem and the role of additives in perovskite could be further investigated. When we consider perovskite/c-Si tandem modules, fabrication of high efficiency large area perovskite solar cells could be a bottleneck. Fabrication of large area perovskite solar cells need to be investigated and optimized for higher efficiency and energy yield.
3. Stability of perovskite/c-Si tandem solar cells is also crucial considering that perovskite top cell degrades much faster than c-Si solar cells. Tests need be performed to evaluate and improve the stability of perovskite/c-Si tandems with high temperature CSPCs.
4. In this study, optical simulations of 3T poly-SiO_x based tandem solar cells were done. However, an electrical study on 3T poly-SiO_x based tandem solar cells and, subsequently, a fabricated 3T poly-SiO_x tandem could lead to interesting new research areas as 3T tandem does not require current matching.
5. Another potential future research could be the fabrication of perovskite/c-Si tandem modules with high temperature CSPCs. This would give the possibility to measure such modules in real world conditions and compare the experimentally measured value with the estimated value of the model.

A

Comparing optical performance of perovskite/silicon tandem architectures under real-world conditions

This appendix provides supporting information of Chapter 4, which was included in the publication of *Nonanophotonics* *

A.1. Modelling approach

We first explain our cell-level and model-level modelling approaches and we validate our modelling framework

A.1.1. Cell level optical model

Optical software GenPro4 [114], is used to perform optical simulations of perovskite / c-Si tandem solar cells. The generated output is reflectance (R), transmittance (T), absorptance (A) spectra of each layer of a solar cell and their related implied photocurrent densities (J_{ph}). This is calculated by integrating the absorbed photons over the Air mass 1.5 (AM 1.5) [325] spectrum for standard test

*M. Singh, R. Santbergen, I. Syifai, A. Weeber, M. Zeman, O. Isabella, “Comparing optical performance of a wide range of perovskite / silicon tandem architectures under real world conditions,” *Nanophotonics*, 10(8), 2043-2057, 2021.

conditions. The optical model combines wave and ray optics, as illustrated in Fig. A(a) and 1(b) for the perovskite/ c-Si tandem solar cells. This means that it simultaneously takes into consideration the interference in the sub-wavelength layer stack of the perovskite top sub-cell, and the anti-reflective effects of the super-wavelength pyramid texture of the underlying c-Si bottom sub-cell. GenPro4 is a one-dimensional (1D) simulator. It does not take into consideration the width of the device or optical shading by metal contact fingers. When the bottom cell is an interdigitated back contacted (IBC) solar cell, which has two interdigitated rear side contacts, the optical generation profile could vary across the width of the device. To simulate such cells, we have used a weighted averaging technique [216].

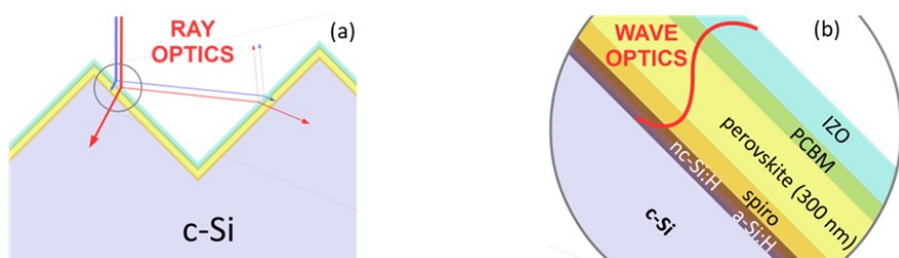


Figure A.1: Working principles of GenPro4 optical model. (a) Ray optics is used to model the anti-reflective and light scattering effect of c-Si pyramid texture; (b) multi-layer wave optics is used to model the interference in the thin films deposited on top of the texture.

A.1.2. Module level optical model

Tandem cells in modules need to be encapsulated. This is reflected in our model by considering both glass and EVA materials. We assume that the simulated modules contain 10 rows of 6 cells. The width of a single cell is 15 cm, even though this dimension could be straightforwardly changed to accommodate larger silicon wafers dimensions. The mounting height is 0.5 m above the ground, tilting 27 degree and azimuth is South (North) for locations in Northern-hemisphere (Southern-hemisphere). Measured hourly global horizontal irradiance and direct normal irradiance data are input for the Perez sky model [128], which - combined with the hourly sun position - is used to recreate the real-world spectral irradiance conditions, considering both the direct and diffuse irradiance contributions. The ray-tracing method outlined in Ref. [127] is then used to calculate the plane of array irradiance. This method was extended for tandem solar cells. The method was made spectrally resolved and layer resolved, such that it can determine the individual photon absorption rate in all layers of the perovskite and silicon sub cells, considering the varying incident angles and illumination spectrum. For

bifacial tandem solar cells, this calculation is performed separately for irradiance incident on front and for irradiance incident on the rear side of the PV module.

A.2. Simulation input and validation

The input of optical simulations in GenPro4 are complex refractive indices ($N = n + ik$), also known as nk data, and the thickness of each layer. For the bottom cell in 2T, 3T and 4T tandem, c-Si solar cells with poly-Si, poly-SiO_x and poly-SiC_x CSPCs have been considered. The refractive indices of poly-Si have been calculated for 10^{20} cm^{-3} doping concentration [58]. For poly-SiO_x and poly-SiC_x carrier-selective passivating contacts, the refractive indices and extinction coefficients are measured using the inverse modelling (IM) technique [252]. The real and imaginary parts of these complex refractive indices are shown in Fig. A.2(a) and (b). In the same diagrams, nk data of Ag and ITO are reported as in-house measured. The corresponding thickness are shown in table A.1. To validate our simulations, we have compared the simulated absorptance with the external quantum efficiency (EQE) of front/back-contacted (FBC) c-Si solar cells with poly-SiO_x CSPCs (see Fig. A.3). The simulated absorptance and the measured EQE are closely matched with an average deviation of less than 2%. These simulations have been performed in the wavelength range between 300 nm and 1200 nm. For single junction poly-SiO_x passivated c-Si solar cells, high parasitic absorption in the front n-doped poly-SiO_x layer is noticeable, which increases further when texturing is considered (not shown here).

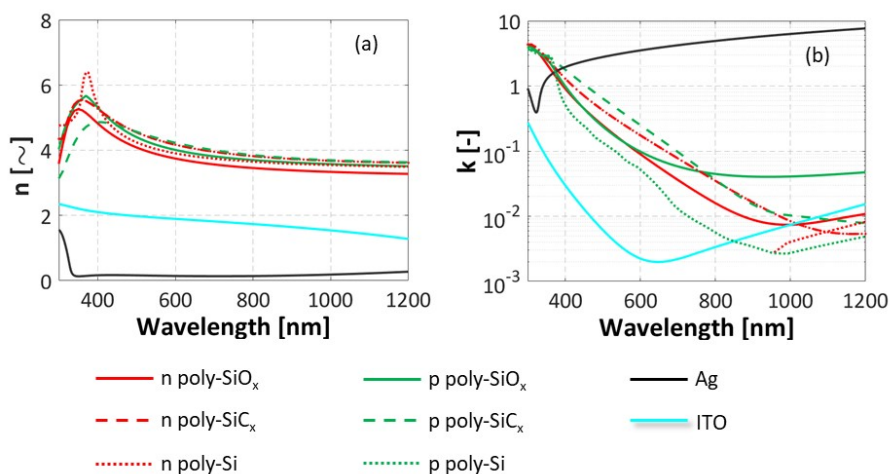


Figure A.2: (a) Refractive index (n) and (b) extinction coefficient (k) of layers used in simulations (poly-Si, poly-SiO_x and poly-SiC_x CSPCs).

A

The tandem structure given in Ref. [88] has been simulated and used as validation platform. The complex refractive indices used for simulations of perovskite /c-Si tandem solar cells are shown in Fig. A.4, the corresponding thicknesses and the source of their nk data are shown in Table A.1. The perovskite considered in our simulations is $(Cs_{0.05}(MA_{0.17}FA_{0.83})_{0.95}Pb(I_{0.9}Br_{0.1})_3)$ absorber layer with a bandgap of 1.55 eV from Ref. [226]. For the perovskite nk data that has been used in 2T simulations has been taken from Ref. [226], blue shifted by 20 nm to account for the slightly higher bandgap in Ref [88] i.e. 1.6 eV. The reflectance of a bare air/glass interface is 4% and most of PV modules installed today employ some form of anti-reflective coating (ARC) to reduce this to less than 1%. In Ref. [88], MgF_2 (magnesium fluoride) has been used as an ARC for 2T un-encapsulated tandem solar cell. To keep similar layer materials, we have used the same ARC (MgF_2) on glass for all encapsulated tandem cases as well. However, MgF_2 coatings are not sufficiently durable for real outdoor use [326]. Other materials such as porous silica [327] are typically used for outdoor applications. Since the typical refractive index of porous silica (1.3 – 1.4 depending on porosity) is in the same range as that of MgF_2 (1.38), the optical effect of MgF_2 coating that we use in our simulations is very similar to that of a porous silica coating (both reduce the air/glass reflectance to <1%). Ethylene Vinyl Acetate (EVA) has been used as an encapsulant in between the glass and the cell. The EVA used is EVAsky S87 from Bridgestone, a UV transmitting EVA. However, EVA does not have high enough barrier properties to protect perovskite against moisture, so real perovskite/silicon tandem modules would rather be encapsulated with polyolefins or ionomers. As these more novel encapsulation materials are still under development, we decided to use the optical constants of the abovementioned EVA instead.

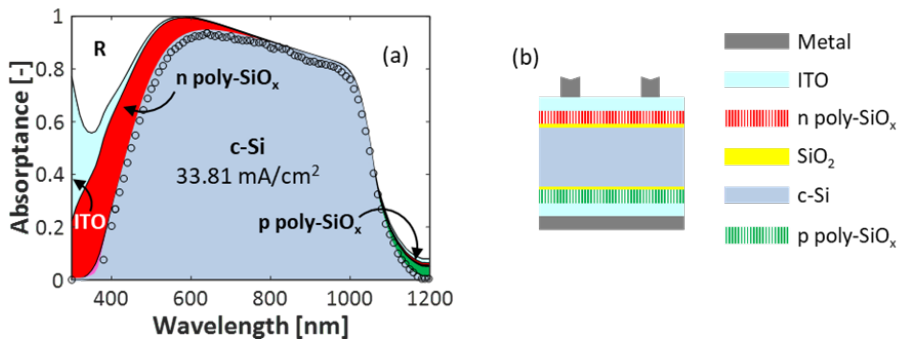


Figure A.3: (a) Comparison of simulated absorbance in c-Si (grey area) with EQE (black circles) for flat/flat poly-SiO_x passivated c-Si solar cell (b) solar cell structure used for simulation and measurement of EQE [38].

For the textured surface, pyramids with a fixed base angle of 52 degrees and

random position are given as input to the simulation. Fig. A.5(a) shows that the simulated reflectance and absorptance spectra in perovskite and silicon absorbers are in excellent agreement with the measured reflectance, top cell EQE and bottom cell EQE, respectively, with average deviation of less than 1%. This shows that the GenPro4 model, combined with the input data, very accurately models this type of tandem device. The nk data and layer thicknesses of the perovskite top cell used in these validation simulations will be used to simulate the top cell optical behaviour in all subsequent 2T and 3T tandem simulations.

Table A.1: Thickness of layers used in tandem simulations. Nps stands for nanoparticles.

2T,3T		4T	
Top cell		Top cell	
Layer	Thickness	Layer	Thickness
MgF ₂ [328]	134 nm	MgF ₂ [328]	161 nm
IZO [329]	110 nm	PTAA and NiO Nps [226]	233 nm
SnO ₂ [216]	10 nm	ALD ZnO [226]	28 nm
C ₆₀ [226]	35 nm	PCBM [226]	44 nm
Perovskite [2T, 3T] [226]	<i>variable</i>	Perovskite [226]	513 nm
Spiro-OMeTAD [215]	12 nm	ITO (front and back) [226]	142 nm and 237 nm
nc-Si (n and p) [measured in house]	10 nm and 10 nm	ZnO Nps [226]	17 nm
Bottom cell			
Layer	Thickness	Layer	Thickness
poly-Si(O _x ,C _x) layers (n) [58],[252]	30 nm	ITO (front and back) [measured in house]	75 nm and 120 nm
c-Si bulk [329]	280 μ m	a-Si (n,p and i) [330]	7,7 and 8 nm
poly-Si(O _x ,C _x) layers (p) [58],[252]	20 nm	c-Si bulk [331]	280 μ m
		Ag [measured in house]	3 μ m
Encapsulation materials			
Glass [332]	3000 μ m	EVA [333]	300 μ m

For the 4T tandem simulations, the semi-transparent top cell structure has been taken from Ref. [226]. The complex refractive indices for the top cell are shown in Fig. A.6. The thicknesses and the source of their nk data are shown in Table A.1. The simulated reflectance, transmittance and absorptance spectra in perovskite absorber are shown in Fig. A.5(b) and compared with the measured reflectance, transmittance and EQE spectra. Again, good agreement between simulation and measurement is obtained with an average deviation of only 1.3%. This shows that also for this architecture the optical model is validated; and the corresponding n and k data are accurate. Textured glass simulations [228, 229] have been considered to study its effect on photocurrent density. We considered 5 μ m size pyramids textures both on the front and rear side of the glass. In reality, rear side texture should be of nano size [334] in order to allow deposition of good quality perovskite layer. However, simulating these rear side nano textures requires rigorous solving of Maxwell's equations, not possible with our simulation approach [335].

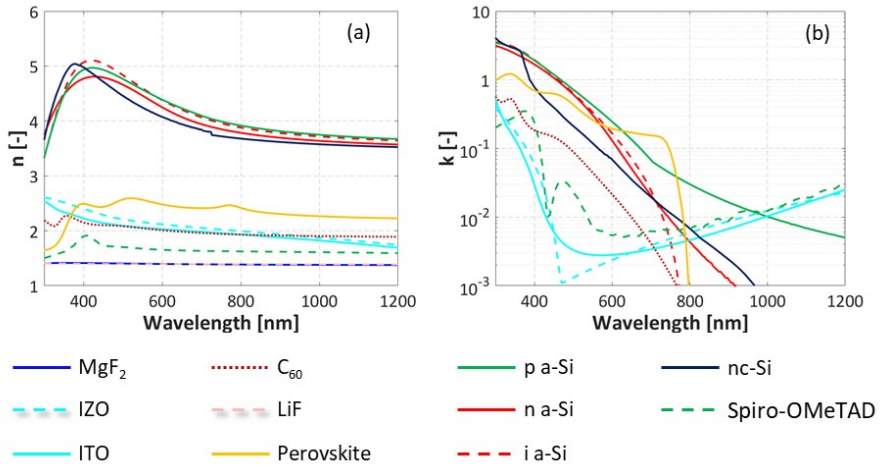


Figure A.4: (a) Refractive index (n) and (b) extinction coefficient (k) of layers used to do simulations of 2T tandem given in Ref. [88]. The top cell data is used for all subsequent 2T and 3T simulations.

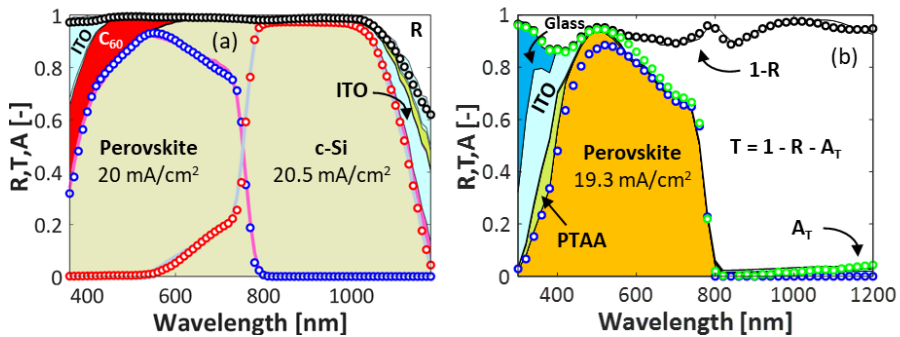


Figure A.5: Comparison of measured EQE (top cell = blue circles, bottom cell = red circles), reflectance (R , black circles) and transmittance (T , between black circles and green circles) spectra with simulated R , T , and absorptance spectra in every layer (perovskite = pink line, c-Si = grey line): (a) 2T tandem from Ref. [88] and (b) transparent perovskite cell from Ref. [226]. A_T in (b) stands for total absorptance.

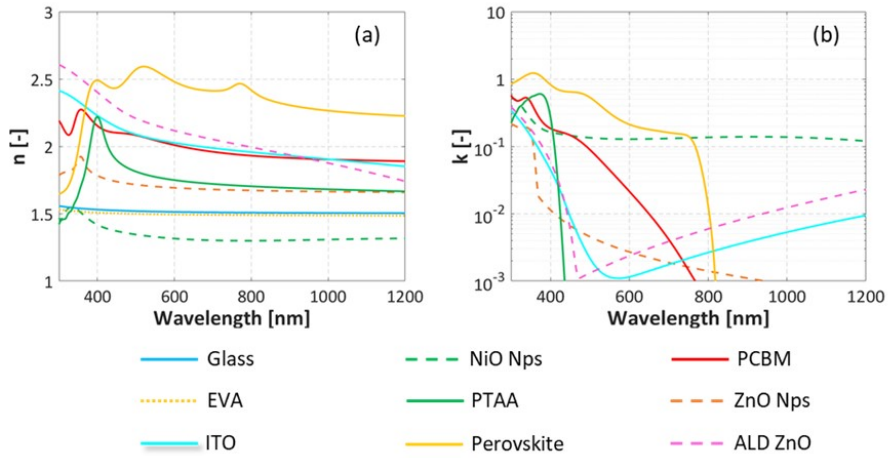


Figure A.6: (a) Refractive index (n) and (b) extinction coefficient (k) of layers used to do simulations of 4T tandem.

B

Poly-SiO_x passivated c-Si solar cells for perovskite/c-Si tandems

This appendix provides supporting information of Chapter 5.

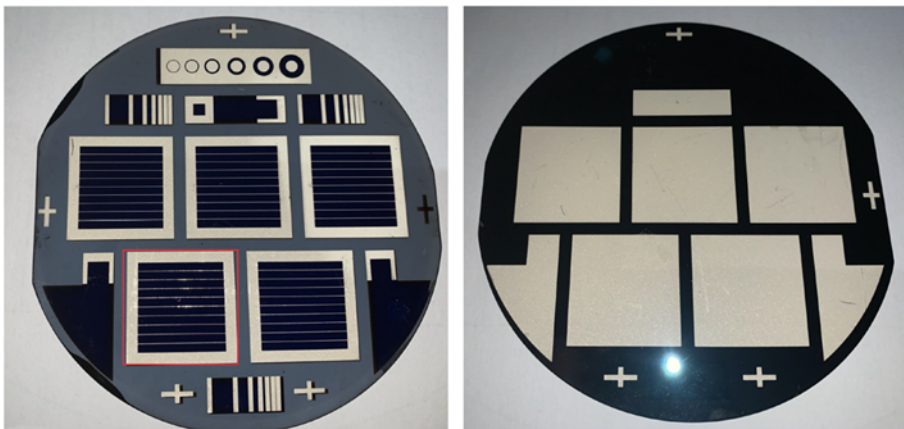
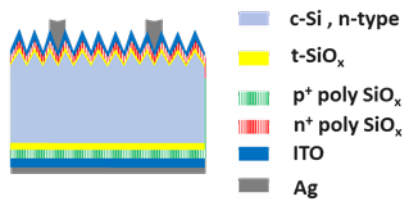


Figure B.1: Front and rear side photos of fabricated wafer-based single side textured (SST) poly-SiO_x passivated c-Si solar cells.

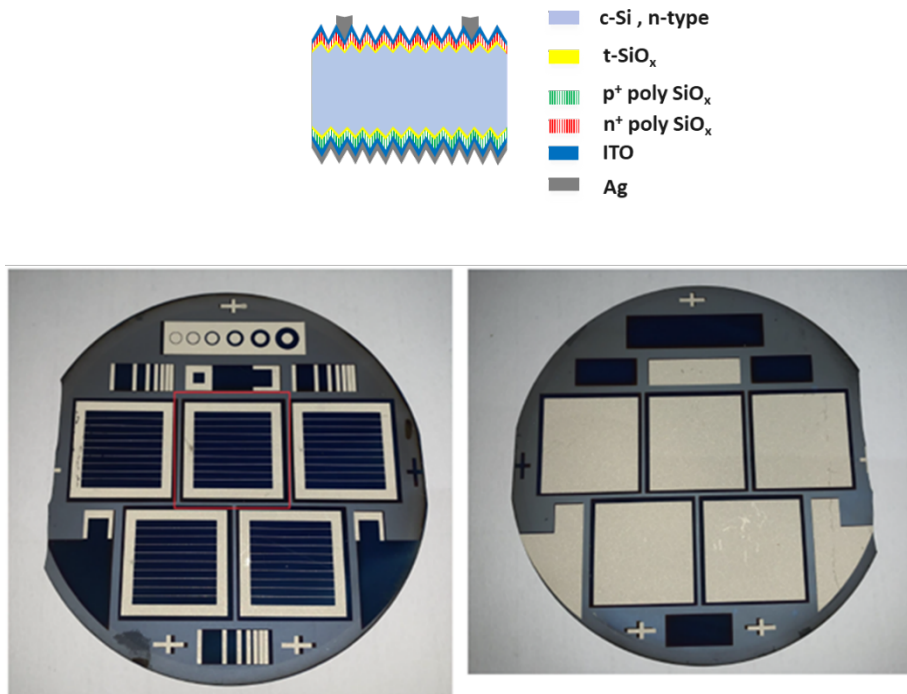


Figure B.2: Front and rear side photos of fabricated wafer-based double side textured (DST) poly-SiO_x passivated c-Si solar cells.

References

- [1] Nadarajah Kannan and Divagar Vakeesan. Solar energy for future world:-a review. *Renewable and sustainable energy reviews*, 62:1092–1105, 2016.
- [2] Shahriar Shafiee and Erkan Topal. When will fossil fuel reserves be diminished? *Energy policy*, 37(1):181–189, 2009.
- [3] N L Panwar, S C Kaushik, and Surendra Kothari. Role of renewable energy sources in environmental protection: A review. *Renewable and sustainable energy reviews*, 15(3):1513–1524, 2011.
- [4] Rajvikram Madurai Elavarasan. The motivation for renewable energy and its comparison with other energy sources: A review. *European Journal of sustainable Development research*, 3(1):em0076, 2019.
- [5] Ibrahim Dincer. Energy and environmental impacts: present and future perspectives. *Energy sources*, 20(4-5):427–453, 1998.
- [6] Martin M Halmann and Meyer Steinberg. *Greenhouse gas carbon dioxide mitigation: science and technology*. CRC press, 1998.
- [7] Hannah Ritchie, Max Roser, and Pablo Rosado. Energy. *Our World in Data*, 2022. <https://ourworldindata.org/energy>.
- [8] Tze-Zhang Ang, Mohamed Salem, Mohamad Kamarol, Himadry Shekhar Das, Mohammad Alhuyi Nazari, and Natarajan Prabakaran. A comprehensive study of renewable energy sources: Classifications, challenges and suggestions. *Energy Strategy Reviews*, 43:100939, 2022.
- [9] Qusay Hassan, Patrik Viktor, Tariq J Al-Musawi, Bashar Mahmood Ali, Sameer Algburi, Haitham M Alzoubi, Ali Khudhair Al-Jiboory, Aws Zuhair Sameen, Hayder M Salman, and Marek Jaszczur. The renewable energy role in the global energy transformations. *Renewable Energy Focus*, 48:100545, 2024.
- [10] Mirunalini Thirugnanasambandam, Selvarasan Iniyan, and Ranko Goic. A review of solar thermal technologies. *Renewable and sustainable energy reviews*, 14(1):312–322, 2010.

- [11] Ehsanul Kabir, Pawan Kumar, Sandeep Kumar, Adedeji A Adelodun, and Ki-Hyun Kim. Solar energy: Potential and future prospects. *Renewable and Sustainable Energy Reviews*, 82:894–900, 2018.
- [12] World energy outlook 2024.
- [13] Net zero roadmap 2023.
- [14] Iea pvps, trends in pv applications 2023, report iea pvps t1-43:2023, october 20.
- [15] Bloomberg new energy finance, report 1 q 2024 global pv market outlook, 19 february 2024.
- [16] Arnulf Jäger-Waldau. Snapshot of photovoltaics- february 2024. *EPJ photovoltaics*, 15:21, 2024.
- [17] Arno Smets, Klaus Jäger, Olindo Isabella, René Van Swaaij, and Miro Zeman. *Solar Energy: The physics and engineering of photovoltaic conversion, technologies and systems*. Bloomsbury Publishing, 2016.
- [18] Uli Würfel, Andres Cuevas, and Peter Würfel. Charge carrier separation in solar cells. *IEEE Journal of Photovoltaics*, 5(1):461–469, 2014.
- [19] Andres Cuevas and Di Yan. Misconceptions and misnomers in solar cells. *IEEE Journal of Photovoltaics*, 3(2):916–923, 2013.
- [20] Jimmy Melskens, Bas WH van de Loo, Bart Macco, Lachlan E Black, Sjoerd Smit, and WMM Kessels. Passivating contacts for crystalline silicon solar cells: From concepts and materials to prospects. *IEEE Journal of Photovoltaics*, 8(2):373–388, 2018.
- [21] Thomas G Allen, James Bullock, Xinbo Yang, Ali Javey, and Stefaan De Wolf. Passivating contacts for crystalline silicon solar cells. *Nature Energy*, 4(11):914–928, 2019.
- [22] Stefan W Glunz and Frank Feldmann. SiO₂ surface passivation layers—a key technology for silicon solar cells. *Solar Energy Materials and Solar Cells*, 185:260–269, 2018.
- [23] Armin G Aberle. Surface passivation of crystalline silicon solar cells: a review. *Progress in Photovoltaics: Research and Applications*, 8(5):473–487, 2000.

- [24] Shuai Nie, Ruy Sebastian Bonilla, and Ziv Hameiri. Unravelling the silicon-silicon dioxide interface under different operating conditions. *Solar Energy Materials and Solar Cells*, 224:111021, 2021.
- [25] MZ Burrows, UK Das, RL Opila, Stefaan De Wolf, and RW Birkmire. Role of hydrogen bonding environment in a-si: H films for c-si surface passivation. *Journal of Vacuum Science & Technology A*, 26(4):683–687, 2008.
- [26] Bart Macco, Jimmy Melskens, Nikolas J Podraza, Karsten Arts, Christopher Pugh, Owain Thomas, and Wilhelmus MM Kessels. Correlating the silicon surface passivation to the nanostructure of low-temperature a-si: H after rapid thermal annealing. *Journal of Applied Physics*, 122(3), 2017.
- [27] Andres Cuevas, Thomas Allen, James Bullock, Yimao Wan, Di Yan, and Xinyu Zhang. Skin care for healthy silicon solar cells. In *2015 IEEE 42nd Photovoltaic Specialist Conference (PVSC)*, pages 1–6. IEEE, 2015.
- [28] R Hezel and R Schörner. Plasma si nitride—a promising dielectric to achieve high-quality silicon mis/il solar cells. *Journal of Applied Physics*, 52(4):3076–3079, 1981.
- [29] Armin G Aberle. Overview on sin surface passivation of crystalline silicon solar cells. *Solar energy materials and solar cells*, 65(1-4):239–248, 2001.
- [30] Gijs Dingemans and WMM Kessels. Status and prospects of al₂o₃-based surface passivation schemes for silicon solar cells. *Journal of Vacuum Science & Technology A*, 30(4), 2012.
- [31] Sakti Prasanna Muduli and Paresh Kale. State-of-the-art passivation strategies of c-si for photovoltaic applications: A review. *Materials Science in Semiconductor Processing*, 154:107202, 2023.
- [32] Utpal Gangopadhyay, Sukhendu Jana, and Sayan Das. State of art of solar photovoltaic technology. In *Conference papers in energy*, volume 2013, pages 1–9. Hindawi Limited, 2013.
- [33] Jingjing Liu, Yao Yao, Shaoqing Xiao, and Xiaofeng Gu. Review of status developments of high-efficiency crystalline silicon solar cells. *Journal of Physics D: Applied Physics*, 51(12):123001, 2018.
- [34] Stefan W Glunz, Martin Bivour, Christoph Messmer, Frank Feldmann, Ralph Müller, Christian Reichel, Armin Richter, Florian Schindler, Jan Benick, and Martin Hermle. Passivating and carrier-selective contacts-basic requirements and implementation. In *2017 IEEE 44th Photovoltaic Specialist Conference (PVSC)*, pages 2064–2069. IEEE, 2017.

- [35] Jimmy Melskens, Bas WH van de Loo, Bart Macco, Martijn FJ Vos, Jurgen Palmans, Sjoerd Smit, and WMM Kessels. Concepts and prospects of passivating contacts for crystalline silicon solar cells. In *2015 IEEE 42nd Photovoltaic Specialist Conference (PVSC)*, pages 1–6. IEEE, 2015.
- [36] Di Yan, Andres Cuevas, Jesus Ibarra Michel, Chun Zhang, Yimao Wan, Xinyu Zhang, and James Bullock. Polysilicon passivated junctions: The next technology for silicon solar cells? *Joule*, 5(4):811–828, 2021.
- [37] Zhaoqing Sun, Xiaoqing Chen, Yongcai He, Jingjie Li, Jianqiang Wang, Hui Yan, and Yongzhe Zhang. Toward efficiency limits of crystalline silicon solar cells: recent progress in high-efficiency silicon heterojunction solar cells. *Advanced Energy Materials*, 12(23):2200015, 2022.
- [38] Guangtao Yang, Peiqing Guo, Paul Procel, Arthur Weeber, Olindo Isabella, and Miro Zeman. Poly-crystalline silicon-oxide films as carrier-selective passivating contacts for c-si solar cells. *Applied Physics Letters*, 112(19), 2018.
- [39] Jan Schmidt, Robby Peibst, and Rolf Brendel. Surface passivation of crystalline silicon solar cells: Present and future. *Solar Energy Materials and Solar Cells*, 187:39–54, 2018.
- [40] Hao Lin, Miao Yang, Xiaoning Ru, Genshun Wang, Shi Yin, Fuguo Peng, Chengjian Hong, Minghao Qu, Junxiong Lu, Liang Fang, et al. Silicon heterojunction solar cells with up to 26.81% efficiency achieved by electrically optimized nanocrystalline-silicon hole contact layers. *Nature Energy*, pages 1–11, 2023.
- [41] Kunta Yoshikawa, Wataru Yoshida, Toru Irie, Hayato Kawasaki, Katsunori Konishi, Hirotaka Ishibashi, Tsuyoshi Asatani, Daisuke Adachi, Masanori Kanematsu, Hisashi Uzu, et al. Exceeding conversion efficiency of 26% by heterojunction interdigitated back contact solar cell with thin film si technology. *Solar Energy Materials and Solar Cells*, 173:37–42, 2017.
- [42] F Haase and R Peibst. 26.1% record efficiency for p-type crystalline si solar cells. *ISFH, Emmerthal/Hannove*, 2018.
- [43] David D Smith, Peter Cousins, Staffan Westerberg, Russelle De Jesus-Tabajonda, Gerly Aniero, and Yu-Chen Shen. Toward the practical limits of silicon solar cells. *IEEE Journal of Photovoltaics*, 4(6):1465–1469, 2014.

- [44] Junichi Nakamura, Naoki Asano, Takeshi Hieda, Chikao Okamoto, Hiroyuki Katayama, and Kyotaro Nakamura. Development of heterojunction back contact si solar cells. *IEEE Journal of Photovoltaics*, 4(6):1491–1495, 2014.
- [45] Martin A Green, Ewan D Dunlop, Masahiro Yoshita, Nikos Kopidakis, Karsten Bothe, Gerald Siefer, and Xiaojing Hao. Solar cell efficiency tables (version 63). *Progress in Photovoltaics: Research and Applications*, 32(1):3–13, 2024.
- [46] Jan Haschke, Olivier Dupré, Mathieu Boccard, and Christophe Ballif. Silicon heterojunction solar cells: Recent technological development and practical aspects—from lab to industry. *Solar Energy Materials and Solar Cells*, 187:140–153, 2018.
- [47] G Nogay, F Sahli, J Werner, R Monnard, M Boccard, M Despeisse, FJ Haug, Q Jeangros, A Ingenito, and C Ballif. 25.1%-efficient monolithic perovskite/silicon tandem solar cell based on ap-type monocrystalline textured silicon wafer and high-temperature passivating contacts. *ACS Energy Letters*, 4(4):844–845, 2019.
- [48] Bisma Bilal and Hakim Najeeb-ud Din. Towards low cost, industrially compatible silicon heterojunction solar cells using hybrid carrier selective passivating contacts. *Optical Materials*, 124:111957, 2022.
- [49] Bishal Kafle, Baljeet Singh Goraya, Sebastian Mack, Frank Feldmann, Sebastian Nold, and Jochen Rentsch. Topcon–technology options for cost efficient industrial manufacturing. *Solar Energy Materials and Solar Cells*, 227:111100, 2021.
- [50] Yohan Ko, HyunJung Park, Chanyong Lee, Yoonmook Kang, and Yongseok Jun. Recent progress in interconnection layer for hybrid photovoltaic tandems. *Advanced Materials*, 32(51):2002196, 2020.
- [51] Yuguo Tao, Vijaykumar Upadhyaya, Keenan Jones, and Ajeet Rohatgi. Tunnel oxide passivated rear contact for large area n-type front junction silicon solar cells providing excellent carrier selectivity. *AIMS Materials Science*, 3(1), 2015.
- [52] Corsin Battaglia, Andres Cuevas, and Stefaan De Wolf. High-efficiency crystalline silicon solar cells: status and perspectives. *Energy & Environmental Science*, 9(5):1552–1576, 2016.
- [53] James Bullock, Danyang Yan, Yufeng Wan, Angel Cuevas, Benedicte Demareux, Aïcha Hessler-Wyser, and Stefaan De Wolf. Amorphous silicon

- passivated contacts for diffused junction silicon solar cells. *Journal of Applied Physics*, 115(16), 2014.
- [54] James Bullock, Andres Cuevas, Christian Samundsett, Di Yan, Josephine McKeon, and Yimao Wan. Simple silicon solar cells featuring an a-si: H enhanced rear mis contact. *Solar Energy Materials and Solar Cells*, 138:22–25, 2015.
- [55] Martin A Green. The path to 25% silicon solar cell efficiency: History of silicon cell evolution. *Progress in photovoltaics: research and applications*, 17(3):183–189, 2009.
- [56] Frank Feldmann, Martin Bivour, Christian Reichel, Heiko Steinkemper, Martin Hermle, and Stefan W Glunz. Tunnel oxide passivated contacts as an alternative to partial rear contacts. *Solar Energy Materials and Solar Cells*, 131:46–50, 2014.
- [57] Sina Reiter, Nico Koper, Rolf Reineke-Koch, Yevgeniya Larionova, Mircea Turcu, Jan Krügener, Dominic Tetzlaff, Tobias Wietler, Uwe Höhne, Jan-Dirk Kähler, et al. Parasitic absorption in polycrystalline si-layers for carrier-selective front junctions. *Energy Procedia*, 92:199–204, 2016.
- [58] Simeon C Baker-Finch, Keith R McIntosh, Di Yan, Kean Chern Fong, and Teng C Kho. Near-infrared free carrier absorption in heavily doped silicon. *Journal of Applied Physics*, 116(6), 2014.
- [59] Frank Feldmann, Christian Reichel, Ralph Müller, and Martin Hermle. The application of poly-si/siox contacts as passivated top/rear contacts in si solar cells. *Solar Energy Materials and Solar Cells*, 159:265–271, 2017.
- [60] Shuo Deng, Yalun Cai, Udo Roemer, Fa-Jun Ma, Fiacre Rougieux, Jialiang Huang, Yuhao Cheng, Martin A Green, and Ning Song. Mitigating parasitic absorption in poly-si contacts for topcon solar cells: A comprehensive review. *Solar Energy Materials and Solar Cells*, 267:112704, 2024.
- [61] Rudi Santbergen, Guangtao Yang, Paul Procel, Gianluca Limodio, Arthur Weeber, Olindo Isabella, and Miro Zeman. Optical analysis of poly-si and poly-siox carrier-selective passivating contacts for c-si solar cells. In *Optical Nanostructures and Advanced Materials for Photovoltaics*, pages PW3A–5. Optica Publishing Group, 2017.
- [62] Maciej K Stodolny, John Anker, Bart LJ Geerligs, Gaby JM Janssen, Bas WH Van De Loo, Jimmy Melskens, Rudi Santbergen, Olindo Isabella, Jurriaan

- Schmitz, Martijn Lenes, et al. Material properties of lpcvd processed n-type polysilicon passivating contacts and its application in perpolly industrial bifacial solar cells. *Energy Procedia*, 124:635–642, 2017.
- [63] Andrea Ingenito, Gizem Nogay, Josua Stuckelberger, Philippe Wyss, Luca Gnocchi, Christophe Allebe, Jörg Horzel, Matthieu Despeisse, Franz-Josef Haug, Philipp Löper, et al. Phosphorous-doped silicon carbide as front-side full-area passivating contact for double-side contacted c-si solar cells. *IEEE Journal of Photovoltaics*, 9(2):346–354, 2018.
- [64] Philippe Wyss, Josua Stuckelberger, Gizem Nogay, Jörg Horzel, Quentin Jeangros, Iris Mack, Mario Lehmann, Xavier Niquille, Christophe Allebé, Matthieu Despeisse, et al. A mixed-phase sio x hole selective junction compatible with high temperatures used in industrial solar cell manufacturing. *IEEE Journal of Photovoltaics*, 10(5):1262–1269, 2020.
- [65] Andrea Ingenito, Christophe Allebé, Sofia Libraro, Christophe Ballif, Bertrand Paviet-Salomon, Sylvain Nicolay, and Juan J Diaz Leon. 22.8% full-area bifacial n-pert solar cells with rear side sputtered poly-si (n) passivating contact. *Solar Energy Materials and Solar Cells*, 249:112043, 2023.
- [66] Ajeet Rohatgi, Brian Rounsaville, Young-Woo Ok, Andrew M Tam, Francesco Zimbardi, Ajay D Upadhyaya, Yuguo Tao, Keeya Madani, Armin Richter, Jan Benick, et al. Fabrication and modeling of high-efficiency front junction n-type silicon solar cells with tunnel oxide passivating back contact. *IEEE Journal of Photovoltaics*, 7(5):1236–1243, 2017.
- [67] Sukhvinder Singh, Patrick Choulat, Jonathan Govaerts, Arvid van der Heide, Valérie Depauw, Filip Duerinckx, Ronald Naber, Martijn Lenes, Marten Renes, Loic Tous, et al. Large area co-plated bifacial n-pert cells with polysilicon passivating contacts on both sides. *Progress in Photovoltaics: Research and Applications*, 30(8):899–909, 2022.
- [68] Xia Yan, Firdaus Bin Suhaimi, Menglei Xu, Jie Yang, Xinyu Zhang, Qi Wang, Hao Jin, and Shubham Duttagupta. Process development and integration of double-side poly-si passivated solar cells with printed contacts via lpcvd and ex-situ tube diffusion. *Solar Energy Materials and Solar Cells*, 230:111249, 2021.
- [69] Dibyendu Kumar Ghosh, Sukanta Bose, Gourab Das, Shiladitya Acharyya, Anupam Nandi, Sumita Mukhopadhyay, and Anindita Sengupta. Fundamentals, present status and future perspective of topcon solar cells: A comprehensive review. *Surfaces and Interfaces*, 30:101917, 2022.

- [70] Daming Chen, Yifeng Chen, Zigang Wang, Jian Gong, Chengfa Liu, Yang Zou, Yu He, Yao Wang, Ling Yuan, Wenjie Lin, et al. 24.58% total area efficiency of screen-printed, large area industrial silicon solar cells with the tunnel oxide passivated contacts (i-topcon) design. *Solar Energy Materials and Solar Cells*, 206:110258, 2020.
- [71] (vdma), v.d.m.u.a, international technology roadmap for photovoltaic, fifteenth edition. 2024.
- [72] Stefaan De Wolf, Jakub Holovsky, Soo-Jin Moon, Philipp Loper, Bjoern Niesen, Martin Ledinsky, Franz-Josef Haug, Jun-Ho Yum, and Christophe Ballif. Organometallic halide perovskites: sharp optical absorption edge and its relation to photovoltaic performance. *The journal of physical chemistry letters*, 5(6):1035–1039, 2014.
- [73] Jun Hong Noh, Sang Hyuk Im, Jin Hyuck Heo, Tarak N Mandal, and Sang Il Seok. Chemical management for colorful, efficient, and stable inorganic–organic hybrid nanostructured solar cells. *Nano letters*, 13(4):1764–1769, 2013.
- [74] Samuel D Stranks, Giles E Eperon, Giulia Grancini, Christopher Menelaou, Marcelo JP Alcocer, Tomas Leijtens, Laura M Herz, Annamaria Petrozza, and Henry J Snaith. Electron-hole diffusion lengths exceeding 1 micrometer in an organometal trihalide perovskite absorber. *Science*, 342(6156):341–344, 2013.
- [75] Priyanka Roy, Numeshwar Kumar Sinha, Sanjay Tiwari, and Ayush Khare. A review on perovskite solar cells: Evolution of architecture, fabrication techniques, commercialization issues and status. *Solar Energy*, 198:665–688, 2020.
- [76] Sisi He, Longbin Qiu, Luis K Ono, and Yabing Qi. How far are we from attaining 10-year lifetime for metal halide perovskite solar cells? *Materials Science and Engineering: R: Reports*, 140:100545, 2020.
- [77] Ritika Sharma, Arushi Sharma, Shikha Agarwal, and MS Dhaka. Stability and efficiency issues, solutions and advancements in perovskite solar cells: A review. *Solar Energy*, 2022.
- [78] National renewable energy laboratory (nrel), best research-cell efficiency chart. <https://www.nrel.gov/pv/cell-efficiency.html>.
- [79] Yaoguang Rong, Yue Hu, Anyi Mei, Hairen Tan, Makhsud I Saidaminov, Sang Il Seok, Michael D McGehee, Edward H Sargent, and Hongwei

- Han. Challenges for commercializing perovskite solar cells. *Science*, 361(6408):eaat8235, 2018.
- [80] Armin Richter, Martin Hermle, and Stefan W Glunz. Reassessment of the limiting efficiency for crystalline silicon solar cells. *IEEE journal of photovoltaics*, 3(4):1184–1191, 2013.
- [81] Steponas Ašmontas and Muhammad Mujahid. Recent progress in perovskite tandem solar cells. *Nanomaterials*, 13(12):1886, 2023.
- [82] Zhihao Zhang, Zicheng Li, Lingyi Meng, Shui-Yang Lien, and Peng Gao. Perovskite-based tandem solar cells: get the most out of the sun. *Advanced Functional Materials*, 30(38):2001904, 2020.
- [83] Ik Jae Park, Hyo Kyung An, Yuna Chang, and Jin Young Kim. Interfacial modification in perovskite-based tandem solar cells. *Nano Convergence*, 10(1):1–13, 2023.
- [84] Nikhil Shrivastav, Jaya Madan, and Rahul Pandey. A short study on recently developed tandem solar cells. *Materials Today: Proceedings*, 2023.
- [85] Michele De Bastiani, Anand S Subbiah, Maxime Babics, Esma Ugur, Lujia Xu, Jiang Liu, Thomas G Allen, Erkan Aydin, and Stefaan De Wolf. Bifacial perovskite/silicon tandem solar cells. *Joule*, 6(7):1431–1445, 2022.
- [86] Gianluca Coletti, Stefan L Luxembourg, LJ Geerligs, V Rosca, AR Burgers, Yu Wu, L Okel, M Kloos, FJK Danzl, M Najafi, et al. Bifacial four-terminal perovskite/silicon tandem solar cells and modules. *ACS energy letters*, 5(5):1676–1680, 2020.
- [87] Rongbo Wang, Meidouxue Han, Ya Wang, Juntao Zhao, Jiawei Zhang, Yi Ding, Ying Zhao, Xiaodan Zhang, and Guofu Hou. Recent progress on efficient perovskite/organic tandem solar cells. *Journal of Energy Chemistry*, 2023.
- [88] Florent Sahli, Jérémie Werner, Brett A Kamino, Matthias Bräuninger, Raphaël Monnard, Bertrand Paviet-Salomon, Loris Barraud, Laura Ding, Juan J Diaz Leon, Davide Sacchetto, et al. Fully textured monolithic perovskite/silicon tandem solar cells with 25.2% power conversion efficiency. *Nature materials*, 17(9):820–826, 2018.
- [89] Amran Al-Ashouri, Eike Köhnen, Bor Li, Artiom Magomedov, Hannes Hempel, Pietro Caprioglio, José A Márquez, Anna Belen Morales Vilches, Ernestas Kasparavicius, Joel A Smith, et al. Monolithic perovskite/silicon

- tandem solar cell with > 29% efficiency by enhanced hole extraction. *Science*, 370(6522):1300–1309, 2020.
- [90] Steve Albrecht, Michael Saliba, Juan Pablo Correa Baena, Felix Lang, Lukas Kegelmann, Mathias Mews, Ludmilla Steier, Antonio Abate, Jörg Rappich, Lars Korte, et al. Monolithic perovskite/silicon-heterojunction tandem solar cells processed at low temperature. *Energy & Environmental Science*, 9(1):81–88, 2016.
- [91] Kevin A Bush, Axel F Palmstrom, Zhengshan J Yu, Mathieu Boccard, Rongrong Cheacharoen, Jonathan P Mailoa, David P McMeekin, Robert LZ Hoyer, Colin D Bailie, Tomas Leijtens, et al. 23.6%-efficient monolithic perovskite/silicon tandem solar cells with improved stability. *Nature Energy*, 2(4):1–7, 2017.
- [92] Jonathan P Mailoa, Colin D Bailie, Eric C Johlin, Eric T Hoke, Austin J Akey, William H Nguyen, Michael D McGehee, and Tonio Buonassisi. A 2-terminal perovskite/silicon multijunction solar cell enabled by a silicon tunnel junction. *Applied Physics Letters*, 106(12), 2015.
- [93] Longi sets a new world record of 33.9% for the efficiency of crystalline silicon-perovskite tandem solar cells, <https://www.prnewswire.com/news-releases/longi-sets-a-new-world-record-of-33-9-for-the-efficiency-of-crystalline-silicon-perovskite-tandem-solar-cells-301978002.html>.
- [94] pv magazine International. Longi claims 34.6 *pv magazine*, 2024.
- [95] William Shockley and Hans Queisser. Detailed balance limit of efficiency of p–n junction solar cells. In *Renewable Energy*, pages Vol2_35–Vol2_54. Routledge, 2018.
- [96] Philipp Tockhorn, Johannes Sutter, Alexandros Cruz, Philipp Wagner, Klaus Jäger, Danbi Yoo, Felix Lang, Max Grischek, Bor Li, Jinzhao Li, et al. Nano-optical designs for high-efficiency monolithic perovskite–silicon tandem solar cells. *Nature Nanotechnology*, 17(11):1214–1221, 2022.
- [97] Heping Shen, Stefan T Omelchenko, Daniel A Jacobs, Sisir Yalamanchili, Yimao Wan, Di Yan, Pheng Phang, The Duong, Yiliang Wu, Yanting Yin, et al. In situ recombination junction between p-si and tio2 enables high-efficiency monolithic perovskite/si tandem cells. *Science advances*, 4(12):eaau9711, 2018.
- [98] Jianghui Zheng, Cho Fai Jonathan Lau, Hamid Mehrvarz, Fa-Jun Ma, Yajie Jiang, Xiaofan Deng, Anastasia Soeriyadi, Jincheol Kim, Meng Zhang,

- Long Hu, et al. Large area efficient interface layer free monolithic perovskite/homo-junction-silicon tandem solar cell with over 20% efficiency. *Energy & Environmental Science*, 11(9):2432–2443, 2018.
- [99] Yi Hou, Erkan Aydin, Michele De Bastiani, Chuanxiao Xiao, Furkan H Isikgor, Ding-Jiang Xue, Bin Chen, Hao Chen, Behzad Bahrami, Ashraful H Chowdhury, et al. Efficient tandem solar cells with solution-processed perovskite on textured crystalline silicon. *Science*, 367(6482):1135–1140, 2020.
- [100] Daehan Kim, Hee Joon Jung, Ik Jae Park, Bryon W Larson, Sean P Dunfield, Chuanxiao Xiao, Jekyung Kim, Jinhui Tong, Passarut Boonmongkolras, Su Geun Ji, et al. Efficient, stable silicon tandem cells enabled by anion-engineered wide-bandgap perovskites. *Science*, 368(6487):155–160, 2020.
- [101] Jixian Xu, Caleb C Boyd, Zhengshan J Yu, Axel F Palmstrom, Daniel J Witter, Bryon W Larson, Ryan M France, Jérémie Werner, Steven P Harvey, Eli J Wolf, et al. Triple-halide wide-band gap perovskites with suppressed phase segregation for efficient tandems. *Science*, 367(6482):1097–1104, 2020.
- [102] Erkan Aydin, Jiang Liu, Esma Ugur, Randi Azmi, George T Harrison, Yi Hou, Bin Chen, Shynggys Zhumagali, Michele De Bastiani, Mingcong Wang, et al. Ligand-bridged charge extraction and enhanced quantum efficiency enable efficient n-i-p perovskite/silicon tandem solar cells. *Energy & Environmental Science*, 14(8):4377–4390, 2021.
- [103] Dong Zhang, Wiljan Verhees, Maarten Dörenkämper, Weiming Qiu, Klaas Bakker, Astrid Gutjahr, Sjoerd Veenstra, Robert Gehlhaar, Ulrich W Paetzold, Wim Soppe, et al. Combination of advanced optical modelling with electrical simulation for performance evaluation of practical 4-terminal perovskite/c-si tandem modules. *Energy Procedia*, 92:669–677, 2016.
- [104] Xiaoqing Yang, Wei Wang, Ran Ran, Wei Zhou, and Zongping Shao. Recent advances in cs₂agbibr₆-based halide double perovskites as lead-free and inorganic light absorbers for perovskite solar cells. *Energy & Fuels*, 34(9):10513–10528, 2020.
- [105] Christoph Luderer, Michaela Penn, Christian Reichel, Frank Feldmann, Jan Christoph Goldschmidt, Susanne Richter, Angelika Hähnel, Volker Naumann, Martin Bivour, and Martin Hermle. Controlling diffusion in poly-si tunneling junctions for monolithic perovskite/silicon tandem solar cells. *IEEE Journal of Photovoltaics*, 11(6):1395–1402, 2021.

- [106] Robby Peibst, Michael Rienäcker, Byungsul Min, Christina Klamt, Raphael Niepelt, Tobias F Wietler, Thorsten Dullweber, Eduard Sauter, Jens Hübner, Michael Oestreich, et al. From perc to tandem: Polo-and p+/n+ poly-si tunneling junction as interface between bottom and top cell. *IEEE Journal of Photovoltaics*, 9(1):49–54, 2018.
- [107] C Luderer, C Reichel, F Feldmann, M Bivour, and M Hermle. Passivating and low-resistive poly-si tunneling junction enabling high-efficiency monolithic perovskite/silicon tandem solar cells. *Applied Physics Letters*, 115(18), 2019.
- [108] Jingming Zheng, Zhiqin Ying, Zhenhai Yang, Zedong Lin, He Wei, Li Chen, Xi Yang, Yuheng Zeng, Xiaofeng Li, and Jichun Ye. Polycrystalline silicon tunnelling recombination layers for high-efficiency perovskite/tunnel oxide passivating contact tandem solar cells. *Nature Energy*, 8(11):1250–1261, 2023.
- [109] Rahul Pandey, Apurva Jain, and Rishu Chaujar. Novel 4-terminal perovskite/sic-based rear contact silicon tandem solar cell with 27.6% pce. In *2016 IEEE 43rd Photovoltaic Specialists Conference (PVSC)*, pages 0812–0815. IEEE, 2016.
- [110] Ajeet Rohatgi, Kai Zhu, Jinhui Tong, Dong Hoe Kim, Elsa Reichmanis, Brian Rounsaville, Vivek Prakash, and Young-Woo Ok. 26.7% efficient 4-terminal perovskite–silicon tandem solar cell composed of a high-performance semi-transparent perovskite cell and a doped poly-si/sio_x passivating contact silicon cell. *IEEE Journal of Photovoltaics*, 10(2):417–422, 2020.
- [111] Jinkosolar’s perovskite tandem solar cell based on n-type topcon sets new record with conversion efficiency of 33.24%, 2024. available <https://jinkosolar.eu/news/jinkosolars-perovskite-tandem-solar-cell-based-on-n-type-topcon-sets-new-record-with-conversion-efficiency-of-33-24/>. 2024.
- [112] Jinkosolar’s perovskite tandem solar cell based on n-type topcon sets new record with conversion efficiency of 33.84%, 2025. available <https://www.pv-magazine.com/2025/01/06/jinkosolar-claims-33-84-efficiency-for-perovskite-silicon-tandem-solar-cell/>.
- [113] Yuguo Tao. *Screen-printed front junction n-type silicon solar cells*. IntechOpen, 2016.
- [114] Rudi Santbergen, Tomomi Meguro, Takashi Suezaki, Gensuke Koizumi, Kenji Yamamoto, and Miro Zeman. Genpro4 optical model for solar cell

- simulation and its application to multijunction solar cells. *IEEE journal of photovoltaics*, 7(3):919–926, 2017.
- [115] MR Vogt, C Ruiz Tobon, A Alcaniz, P Procel, Y Blom, A Nour El Din, T Stark, Z Wang, E Garcia Goma, JG Etxebarria, et al. Introducing a comprehensive physics-based modelling framework for tandem and other pv systems. *Solar Energy Materials and Solar Cells*, 247:111944, 2022.
- [116] Robert Siegel. Net radiation method for transmission through partially transparent plates. *Solar Energy*, 15, 1973.
- [117] K Jäger, M Fischer, RACMM Van Swaaij, and M Zeman. A scattering model for nano-textured interfaces and its application in opto-electrical simulations of thin-film silicon solar cells. *Journal of Applied Physics*, 111(8), 2012.
- [118] K. jäger, “on the scalar scattering theory for thin-film solar cells,” ph.d. dissertation, delft univ. technol., delft, the netherlands, 2012. doi: 10.4233/uuid:4220e3ee-bdcb-4a46-ade1-470d3c2ad6da.
- [119] M Zeman, O Isabella, S Solntsev, and K Jäger. Modelling of thin-film silicon solar cells. *Solar Energy Materials and Solar Cells*, 119:94–111, 2013.
- [120] Asa web simulator [online]. <https://asa.ewi.tudelft.nl/>.
- [121] Haohui Liu, Carlos D Rodríguez-Gallegos, Zhe Liu, Tonio Buonassisi, Thomas Reindl, and Ian Marius Peters. A worldwide theoretical comparison of outdoor potential for various silicon-based tandem module architecture. *Cell Reports Physical Science*, 1(4), 2020.
- [122] Jonathan Lehr, Malte Langenhorst, Raphael Schmagel, Fabrizio Gota, Simon Kirner, Uli Lemmer, Bryce S Richards, Chris Case, and Ulrich W Paetzold. Energy yield of bifacial textured perovskite/silicon tandem photovoltaic modules. *Solar Energy Materials and Solar Cells*, 208:110367, 2020.
- [123] Daxue Du, Chao Gao, Haiyan Wang, and Wenzhong Shen. Photovoltaic performance of bifacial perovskite/c-si tandem solar cells. *Journal of Power Sources*, 540:231622, 2022.
- [124] Nico Tucher, Oliver Höhn, JN Murthy, JC Martinez, Marc Steiner, Alfons Armbruster, Elke Lorenz, Benedikt Bläsi, and Jan Christoph Goldschmidt. Energy yield analysis of textured perovskite silicon tandem solar cells and modules. *Optics Express*, 27(20):A1419–A1430, 2019.

- [125] Lixiang Ba, Tun Wang, Jiayuan Wang, and Wenzhong Shen. Perovskite/c-si monolithic tandem solar cells under real solar spectra: improving energy yield by oblique incident optimization. *The Journal of Physical Chemistry C*, 123(47):28659–28667, 2019.
- [126] Andres Calcabrini, Hesam Ziar, Olindo Isabella, and Miro Zeman. A simplified skyline-based method for estimating the annual solar energy potential in urban environments. *Nature Energy*, 4(3):206–215, 2019.
- [127] R Santbergen, VA Muthukumar, RME Valckenborg, WJA van de Wall, AHM Smets, and M Zeman. Calculation of irradiance distribution on pv modules by combining sky and sensitivity maps. *Solar Energy*, 150:49–54, 2017.
- [128] Richard Perez, Robert Seals, and Joseph Michalsky. All-weather model for sky luminance distribution—preliminary configuration and validation. *Solar energy*, 50(3):235–245, 1993.
- [129] Christian Gueymard. Simple model of the atmospheric radiative transfer of sunshine (smarts2): algorithms and performance assessment. *Florida: Solar Energy Center*, 1995.
- [130] Christian A Gueymard. Parameterized transmittance model for direct beam and circumsolar spectral irradiance. *Solar Energy*, 71(5):325–346, 2001.
- [131] Paul Ricchiazzi, Shiren Yang, Catherine Gautier, and David Sowle. Sbdart: A research and teaching software tool for plane-parallel radiative transfer in the earth's atmosphere. *Bulletin of the American Meteorological Society*, 79(10):2101–2114, 1998.
- [132] Martin K Fuentes. A simplified thermal model for flat-plate photovoltaic arrays. Technical report, Sandia National Labs., Albuquerque, NM (USA), 1987.
- [133] Amit Jain and Avinashi Kapoor. Exact analytical solutions of the parameters of real solar cells using lambert w-function. *Solar Energy Materials and Solar Cells*, 81(2):269–277, 2004.
- [134] Abdallah Nour El Din. Improved electrical model and experimental validation of the pvmd toolbox: Extending the energy yield prediction model to tandem pv modules. 2020.
- [135] Bandana Singha and Chetan S Solanki. N-type solar cells: advantages, issues, and current scenarios. *Materials Research Express*, 4(7):072001, 2017.

- [136] JE Cotter, JH Guo, PJ Cousins, MD Abbott, FW Chen, and KC Fisher. P-type versus n-type silicon wafers: prospects for high-efficiency commercial silicon solar cells. *IEEE Transactions on Electron Devices*, 53(8):1893–1901, 2006.
- [137] Karsten Bothe, Ron Sinton, and Jan Schmidt. Fundamental boron–oxygen-related carrier lifetime limit in mono- and multicrystalline silicon. *Progress in photovoltaics: Research and Applications*, 13(4):287–296, 2005.
- [138] J Melskens. Optimisation of a protocrystalline hydrogenated amorphous silicon top solar cell for highest stabilised efficiency. 2007.
- [139] R Street, D Biegelsen, and J Stuke. Defects in bombarded amorphous silicon. *Philosophical Magazine B*, 40(6):451–464, 1979.
- [140] Bénédicte Demaurex, Stefaan De Wolf, Antoine Descoeurdes, Zachary Charles Holman, and Christophe Ballif. Damage at hydrogenated amorphous/crystalline silicon interfaces by indium tin oxide overlayer sputtering. *Applied Physics Letters*, 101(17), 2012.
- [141] Ke Tao, Shuai Jiang, Rui Jia, Ying Zhou, Pengfei Zhang, Xiaowan Dai, Hengchao Sun, Zhi Jin, and Xinyu Liu. The impact of indium tin oxide deposition and post annealing on the passivation property of topcon solar cells. *Solar Energy*, 176:241–247, 2018.
- [142] Leonard Tutsch, Frank Feldmann, Jana Polzin, Christoph Luderer, Martin Bivour, Anamaria Moldovan, Jochen Rentsch, and Martin Hermle. Implementing transparent conducting oxides by dc sputtering on ultrathin siox/poly-si passivating contacts. *Solar Energy Materials and Solar Cells*, 200:109960, 2019.
- [143] Woojun Yoon, David Scheiman, Young-Woo Ok, Zhaoning Song, Cong Chen, Glenn Jernigan, Ajeet Rohatgi, Yanfa Yan, and Phillip Jenkins. Sputtered indium tin oxide as a recombination layer formed on the tunnel oxide/poly-si passivating contact enabling the potential of efficient monolithic perovskite/si tandem solar cells. *Solar Energy Materials and Solar Cells*, 210:110482, 2020.
- [144] Jérémie Werner, Loris Barraud, Arnaud Walter, Matthias Brauning, Florent Sahli, Davide Sacchetto, Nicolas Tétreault, Bertrand Paviet-Salomon, Soo-Jin Moon, Christophe Allebé, et al. Efficient near-infrared-transparent perovskite solar cells enabling direct comparison of 4-terminal and monolithic perovskite/silicon tandem cells. *ACS Energy Letters*, 1(2):474–480, 2016.

- [145] Sinton instruments, boulder, co, usa. available: <https://www.sintoninstruments.com>.
- [146] Perkin Elmer Inc. Applications and use of integrating spheres with the la 650 and 850 uv/vis and lambda 950 uv/vis/nir spectrophotometers. Technical report, Perkin Elmer Inc., 2004.
- [147] Hiroyuki Fujiwara and Robert W Collins. *Spectroscopic ellipsometry for photovoltaics*, volume 1. Springer, 2018.
- [148] Joseph Kreb. Spectroscopic ellipsometry on thin films of tio₂: Comparing cauchy and cody-lorentz models in completeease. 2020.
- [149] Tahereh G Avval, Brian I Johnson, James N Hilfiker, and Matthew R Linford. A tutorial on spectroscopic ellipsometry (se), 1.
- [150] Dawei Hu, Aaron J Rosenberg, Houssam Chouaib, Natalia Malkova, and Zhengquan Tan. Tracking the defects of ultra-thin hfo₂ using a cody-lorentz multiple oscillator model. In *Metrology, Inspection, and Process Control for Microlithography XXXII*, volume 10585, pages 683–689. SPIE, 2018.
- [151] Guangtao Yang, Andrea Ingenito, Nienke van Hameren, Olindo Isabella, and Miro Zeman. Design and application of ion-implanted polysi passivating contacts for interdigitated back contact c-si solar cells. *Applied Physics Letters*, 108(3), 2016.
- [152] Guangtao Yang, Andrea Ingenito, Olindo Isabella, and Miro Zeman. Ibc c-si solar cells based on ion-implanted poly-silicon passivating contacts. *Solar Energy Materials and Solar Cells*, 158:84–90, 2016.
- [153] Armin Richter, Jan Benick, Frank Feldmann, Andreas Fell, Martin Hermle, and Stefan W Glunz. n-type si solar cells with passivating electron contact: Identifying sources for efficiency limitations by wafer thickness and resistivity variation. *Solar Energy Materials and Solar Cells*, 173:96–105, 2017.
- [154] Guangtao Yang, Yue Zhang, Paul Procel, Arthur Weeber, Olindo Isabella, and Miro Zeman. Poly-si (o) x passivating contacts for high-efficiency c-si ibc solar cells. *Energy Procedia*, 124:392–399, 2017.
- [155] Josua Stuckelberger, Gizem Nogay, Philippe Wyss, Andrea Ingenito, Christophe Allebé, Jörg Horzel, Brett A Kamino, Matthieu Despeisse, Franz-Josef Haug, Philipp Löper, et al. Recombination analysis of phosphorus-doped nanostructured silicon oxide passivating electron contacts for silicon solar cells. *IEEE Journal of Photovoltaics*, 8(2):389–396, 2018.

- [156] Josua Stuckelberger, Gizem Nogay, Philippe Wyss, Quentin Jeangros, Christophe Allebé, Fabien Debrot, Xavier Niquille, Martin Ledinsky, Antonin Fejfar, Matthieu Despeisse, et al. Passivating electron contact based on highly crystalline nanostructured silicon oxide layers for silicon solar cells. *Solar Energy Materials and Solar Cells*, 158:2–10, 2016.
- [157] O. Isabella, G. Yang, G. Limodio, P. Procel, M. Singh, Y. Zhao, A. Weeber, and M. Zeman. Fully-passivated, black, high-efficiency c-si solar cells featuring passivating contacts. In *Silicon PV*, Leuven, Belgium, 2019.
- [158] Gizem Nogay, Andrea Ingenito, Esteban Rucavado, Quentin Jeangros, Josua Stuckelberger, Philippe Wyss, Monica Morales-Masis, Franz-Josef Haug, Philipp Löper, and Christophe Ballif. Crystalline silicon solar cells with coannealed electron-and hole-selective sic x passivating contacts. *IEEE Journal of Photovoltaics*, 8(6):1478–1485, 2018.
- [159] Fabio Iacona, Corrado Bongiorno, Corrado Spinella, Simona Boninelli, and Francesco Priolo. Formation and evolution of luminescent si nanoclusters produced by thermal annealing of sio x films. *Journal of Applied Physics*, 95(7):3723–3732, 2004.
- [160] I Mack, J Stuckelberger, P Wyss, G Nogay, Q Jeangros, J Horzel, C Allebé, M Despeisse, F-J Haug, A Ingenito, et al. Properties of mixed phase silicon-oxide-based passivating contacts for silicon solar cells. *Solar Energy Materials and Solar Cells*, 181:9–14, 2018.
- [161] Gizem Nogay, Josua Stuckelberger, Philippe Wyss, Quentin Jeangros, Christophe Allebé, Xavier Niquille, Fabien Debrot, Matthieu Despeisse, Franz-Josef Haug, Philipp Loper, et al. Silicon-rich silicon carbide hole-selective rear contacts for crystalline-silicon-based solar cells. *ACS applied materials & interfaces*, 8(51):35660–35667, 2016.
- [162] H Fujiwara. *Spectroscopic Ellipsometry: Principles and Applications*. John Wiley & Sons, 2007.
- [163] Zdenek Remes, Ravi Vasudevan, Karol Jarolimek, Arno HM Smets, and Miro Zeman. The optical spectra of a-si: H and a-sic: H thin films measured by the absolute photothermal deflection spectroscopy (pds). *Solid State Phenomena*, 213:19–28, 2014.
- [164] Eli Yablonovitch. Statistical ray optics. *JOSA*, 72(7):899–907, 1982.

- [165] Marc Rüdiger, Johannes Greulich, Armin Richter, and Martin Hermle. Parameterization of free carrier absorption in highly doped silicon for solar cells. *IEEE Transactions on Electron Devices*, 60(7):2156–2163, 2013.
- [166] Celine Pahud, Olindo Isabella, Ali Naqavi, Franz-Josef Haug, Miro Zeman, Hans Peter Herzig, and Christophe Ballif. Plasmonic silicon solar cells: impact of material quality and geometry. *Optics express*, 21(105):A786–A797, 2013.
- [167] Martin Dressel and Marc Scheffler. Verifying the drude response. *Annalen der Physik*, 518(7-8):535–544, 2006.
- [168] S Roberts. Optical properties of nickel and tungsten and their interpretation according to drude's formula. *Physical Review*, 114(1):104, 1959.
- [169] So Roberts. Interpretation of the optical properties of metal surfaces. *Physical Review*, 100(6):1667, 1955.
- [170] AF Gibson. Infra-red and microwave modulation using free carriers in semiconductors. *Journal of Scientific Instruments*, 35(8):273, 1958.
- [171] HY Fan, W Spitzer, and RJ Collins. Infrared absorption in n-type germanium. *Physical Review*, 101(2):566, 1956.
- [172] W Spitzer and HY Fan. Infrared absorption in n-type silicon. *Physical Review*, 108(2):268, 1957.
- [173] Dieter K Schroder, R Noel Thomas, and John C Swartz. Free carrier absorption in silicon. *IEEE Journal of solid-state circuits*, 13(1):180–187, 1978.
- [174] Martin A Green. Silicon solar cells: Advanced principles and practice. 1995. Sydney, NSW: Bridge printery.
- [175] Rudi Santbergen and RJ Ch van Zolingen. The absorption factor of crystalline silicon pv cells: A numerical and experimental study. *Solar energy materials and solar cells*, 92(4):432–444, 2008.
- [176] Joerg Isenberg and Wilhelm Warta. Free carrier absorption in heavily doped silicon layers. *Applied physics letters*, 84(13):2265–2267, 2004.
- [177] Terry Chien-Jen Yang, Keita Nomoto, Binesh Puthen-Veetil, Ziyun Lin, Lingfeng Wu, Tian Zhang, Xuguang Jia, Gavin Conibeer, and Ivan Perez-Wurfl. Properties of silicon nanocrystals with boron and phosphorus doping fabricated via silicon rich oxide and silicon dioxide bilayers. *Materials Research Express*, 4(7):075004, 2017.

- [178] M Marinov and N Zotov. Model investigation of the raman spectra of amorphous silicon. *Physical review B*, 55(5):2938, 1997.
- [179] Junwei Wei, Adrian Wirth, Michael C Downer, and Bernardo S Mendoza. Second-harmonic and linear optical spectroscopic study of silicon nanocrystals embedded in sio 2. *Physical Review B—Condensed Matter and Materials Physics*, 84(16):165316, 2011.
- [180] Qijin Cheng, Shuyan Xu, and Kostya Ken Ostrikov. Single-step, rapid low-temperature synthesis of si quantum dots embedded in an amorphous sic matrix in high-density reactive plasmas. *Acta Materialia*, 58(2):560–569, 2010.
- [181] S Veprek, F-A Sarott, and Z Iqbal. Effect of grain boundaries on the raman spectra, optical absorption, and elastic light scattering in nanometer-sized crystalline silicon. *Physical Review B*, 36(6):3344, 1987.
- [182] Ch Ossadnik, S Vepřek, and I Gregora. Applicability of raman scattering for the characterization of nanocrystalline silicon. *Thin solid films*, 337(1-2):148–151, 1999.
- [183] TOM Tiedje, ELI Yablonovitch, George D Cody, and Bonnie G Brooks. Limiting efficiency of silicon solar cells. *IEEE Transactions on electron devices*, 31(5):711–716, 1984.
- [184] A Lambertz, T Grundler, and F Finger. Hydrogenated amorphous silicon oxide containing a microcrystalline silicon phase and usage as an intermediate reflector in thin-film silicon solar cells. *Journal of applied physics*, 109(11), 2011.
- [185] Ke Xiao, Renxing Lin, Qiaolei Han, Yi Hou, Zhenyuan Qin, Hieu T Nguyen, Jin Wen, Mingyang Wei, Vishal Yeddu, Makhsud I Saidaminov, et al. All-perovskite tandem solar cells with 24.2% certified efficiency and area over 1 cm² using surface-anchoring zwitterionic antioxidant. *Nature Energy*, 5(11):870–880, 2020.
- [186] Ke Xiao, Jin Wen, Qiaolei Han, Renxing Lin, Yuan Gao, Shuai Gu, Yipeng Zang, Yuefeng Nie, Jia Zhu, Jun Xu, et al. Solution-processed monolithic all-perovskite triple-junction solar cells with efficiency exceeding 20%. *ACS Energy Letters*, 5(9):2819–2826, 2020.
- [187] Junke Wang, Valerio Zardetto, Kunal Datta, Dong Zhang, Martijn M Wienk, and René AJ Janssen. 16.8% monolithic all-perovskite triple-junction solar

- cells via a universal two-step solution process. *Nature Communications*, 11(1):5254, 2020.
- [188] Zhimin Fang, Qiang Zeng, Chuantian Zuo, Lixiu Zhang, Hanrui Xiao, Ming Cheng, Feng Hao, Qinye Bao, Lixue Zhang, Yongbo Yuan, et al. Perovskite-based tandem solar cells. *Science Bulletin*, 66(6):621–636, 2021.
- [189] Yuqiang Liu, Yajuan Li, Yiliang Wu, Guangtao Yang, Luana Mazzarella, Paul Procel-Moya, Adele C Tamboli, Klaus Weber, Mathieu Boccard, Olindo Isabella, et al. High-efficiency silicon heterojunction solar cells: materials, devices and applications. *Materials Science and Engineering: R: Reports*, 142:100579, 2020.
- [190] Fabrizio Gota, Malte Langenhorst, Raphael Schmager, Jonathan Lehr, and Ulrich W Paetzold. Energy yield advantages of three-terminal perovskite-silicon tandem photovoltaics. *Joule*, 4(11):2387–2403, 2020.
- [191] Saba Gharibzadeh, Ihteaz M Hossain, Paul Fassel, Bahram Abdollahi Nejand, Tobias Abzieher, Moritz Schultes, Erik Ahlswede, Philip Jackson, Michael Powalla, Sören Schäfer, et al. 2d/3d heterostructure for semitransparent perovskite solar cells with engineered bandgap enables efficiencies exceeding 25% in four-terminal tandems with silicon and cigs. *Advanced Functional Materials*, 30(19):1909919, 2020.
- [192] Raphael Schmager, Malte Langenhorst, Jonathan Lehr, Uli Lemmer, Bryce S Richards, and Ulrich W Paetzold. Methodology of energy yield modelling of perovskite-based multi-junction photovoltaics. *Optics express*, 27(8):A507–A523, 2019.
- [193] Niraj N Lal, Yasmina Dkhissi, Wei Li, Qicheng Hou, Yi-Bing Cheng, and Udo Bach. Perovskite tandem solar cells. *Advanced Energy Materials*, 7(18):1602761, 2017.
- [194] Helen Hejin Park, Jincheol Kim, Geunjin Kim, Hyunmin Jung, Songhee Kim, Chan Su Moon, Seon Joo Lee, Seong Sik Shin, Xiaojing Hao, Jae Sung Yun, et al. Transparent electrodes consisting of a surface-treated buffer layer based on tungsten oxide for semitransparent perovskite solar cells and four-terminal tandem applications. *Small Methods*, 4(5):2000074, 2020.
- [195] Bin Chen, Se-Woong Baek, Yi Hou, Erkan Aydin, Michele De Bastiani, Benjamin Scheffel, Andrew Proppe, Ziru Huang, Mingyang Wei, Ya-Kun Wang, et al. Enhanced optical path and electron diffusion length enable high-efficiency perovskite tandems. *Nature communications*, 11(1):1257, 2020.

- [196] Helmholtz-Zentrum Berlin. Record: efficiency of perovskite tandem solar cells jumps to 29.15 percent. https://www.helmholtz-berlin.de/pubbin/news_seite?nid=21020;sprache=en, 2020.
- [197] Luana Mazzarella, Yen-Hung Lin, Simon Kirner, Anna B Morales-Vilches, Lars Korte, Steve Albrecht, Ed Crossland, Bernd Stannowski, Chris Case, Henry J Snaith, et al. Infrared light management using a nanocrystalline silicon oxide interlayer in monolithic perovskite/silicon heterojunction tandem solar cells with efficiency above 25%. *Advanced Energy Materials*, 9(14):1803241, 2019.
- [198] Ziyu Wang, Xuejie Zhu, Shengnan Zuo, Ming Chen, Cong Zhang, Chenyu Wang, Xiaodong Ren, Zhou Yang, Zhike Liu, Xixiang Xu, et al. 27%-efficiency four-terminal perovskite/silicon tandem solar cells by sandwiched gold nanomesh. *Advanced Functional Materials*, 30(4):1908298, 2020.
- [199] Eike Köhnen, Marko Jošt, Anna Belen Morales-Vilches, Philipp Tockhorn, Amran Al-Ashouri, Bart Macco, Lukas Kegelmann, Lars Korte, Bernd Rech, Rutger Schlatmann, et al. Highly efficient monolithic perovskite silicon tandem solar cells: analyzing the influence of current mismatch on device performance. *Sustainable Energy & Fuels*, 3(8):1995–2005, 2019.
- [200] Patricia SC Schulze, Alexander J Bett, Martin Bivour, Pietro Caprioglio, Fabian M Gerspacher, Özde Ş Kabaklı, Armin Richter, Martin Stolterfoht, Qinxin Zhang, Dieter Neher, et al. 25.1% high-efficiency monolithic perovskite silicon tandem solar cell with a high bandgap perovskite absorber. *Solar RRL*, 4(7):2000152, 2020.
- [201] Jianghui Zheng, Hamid Mehrvarz, Chwenhaw Liao, Jueming Bing, Xin Cui, Yang Li, Vinicius R Gonçales, Cho Fai Jonathan Lau, Da Seul Lee, Yong Li, et al. Large-area 23%-efficient monolithic perovskite/homojunction-silicon tandem solar cell with enhanced uv stability using down-shifting material. *ACS Energy Letters*, 4(11):2623–2631, 2019.
- [202] Anand S Subbiah, Furkan H Isikgor, Calvyn T Howells, Michele De Bastiani, Jiang Liu, Erkan Aydin, Francesco Furlan, Thomas G Allen, Fuzong Xu, Shynggys Zhumagali, et al. High-performance perovskite single-junction and textured perovskite/silicon tandem solar cells via slot-die-coating. *ACS Energy Letters*, 5(9):3034–3040, 2020.
- [203] Oxford PV. Oxford pv perovskite solar cell achieves 28% efficiency. <https://www.oxfordpv.com/news/>

- oxford-pv-perovskite-solar-cell-achieves-28-efficiency, 2020.
- [204] Stefaan De Wolf, Jakub Holovsky, Soo-Jin Moon, Philipp Loper, Bjoern Niesen, Martin Ledinsky, Franz-Josef Haug, Jun-Ho Yum, and Christophe Ballif. Organometallic halide perovskites: sharp optical absorption edge and its relation to photovoltaic performance. *The journal of physical chemistry letters*, 5(6):1035–1039, 2014.
- [205] EL Unger, Lukas Kegelmann, K Suchan, D Sörell, Lars Korte, and Susanne Albrecht. Roadmap and roadblocks for the band gap tunability of metal halide perovskites. *Journal of Materials Chemistry A*, 5(23):11401–11409, 2017.
- [206] Henry J Snaith. Present status and future prospects of perovskite photovoltaics. *Nature materials*, 17(5):372–376, 2018.
- [207] YiLiang Wu, Di Yan, Jun Peng, Yimao Wan, Sieu Pheng Phang, Heping Shen, Nandi Wu, Chog Barugkin, Xiao Fu, Sachin Surve, et al. Monolithic perovskite/silicon-homojunction tandem solar cell with over 22% efficiency. *Energy & Environmental Science*, 10(11):2472–2479, 2017.
- [208] Felix Haase, Christina Hollemann, Sören Schäfer, Agnes Merkle, Michael Rienäcker, Jan Krügener, Rolf Brendel, and Robby Peibst. Laser contact openings for local poly-si-metal contacts enabling 26.1%-efficient polo-ibc solar cells. *Solar Energy Materials and Solar Cells*, 186:184–193, 2018.
- [209] C Hollemann, F Haase, M Rienäcker, V Barnscheidt, J Krügener, N Folchert, R Brendel, S Richter, S Großer, E Sauter, et al. Separating the two polarities of the polo contacts of an 26.1%-efficient ibc solar cell. *Scientific reports*, 10(1):658, 2020.
- [210] Andrea Ingenito, Gizem Nogay, Quentin Jeangros, Esteban Rucavado, Christophe Allebé, Santhana Eswara, Nathalie Valle, Tom Wirtz, Jörg Horzel, Takashi Koida, et al. A passivating contact for silicon solar cells formed during a single firing thermal annealing. *Nature Energy*, 3(9):800–808, 2018.
- [211] Manuel Schnabel, William M Nemeth, San Theingi, Abhijit Kale, Talysa R Klein, Benjamin G Lee, Marinus F Van Hest, Sumit Agarwal, David L Young, and Pauls Stradins. Approaches to metallization for poly-si/siox passivated contacts. Technical report, National Renewable Energy Lab.(NREL), Golden, CO (United States), 2019.

- [212] Armin Richter, Jan Benick, Ralph Müller, Frank Feldmann, Christian Reichel, Martin Hermle, and Stefan W Glunz. Tunnel oxide passivating electron contacts as full-area rear emitter of high-efficiency p-type silicon solar cells. *Progress in Photovoltaics: Research and Applications*, 26(8):579–586, 2018.
- [213] Christoph Messmer, Baljeet S Goraya, Sebastian Nold, Patricia SC Schulze, Volker Sittinger, Jonas Schön, Jan Christoph Goldschmidt, Martin Bivour, Stefan W Glunz, and Martin Hermle. The race for the best silicon bottom cell: Efficiency and cost evaluation of perovskite–silicon tandem solar cells. *Progress in Photovoltaics: Research and Applications*, 29(7):744–759, 2021.
- [214] Rudi Santbergen, Ryota Mishima, Tomomi Meguro, Masashi Hino, Hisashi Uzu, Johan Blanker, Kenji Yamamoto, and Miro Zeman. Minimizing optical losses in monolithic perovskite/c-si tandem solar cells with a flat top cell. *Optics express*, 24(18):A1288–A1299, 2016.
- [215] Miha Filipič, Philipp Löper, Bjoern Niesen, Stefaan De Wolf, Janez Krč, Christophe Ballif, and Marko Topič. Ch 3 nh 3 pbi 3 perovskite/silicon tandem solar cells: characterization based optical simulations. *Optics express*, 23(7):A263–A278, 2015.
- [216] Rudi Santbergen, Hisashi Uzu, Kenji Yamamoto, and Miro Zeman. Optimization of three-terminal perovskite/silicon tandem solar cells. *IEEE Journal of Photovoltaics*, 9(2):446–451, 2019.
- [217] Jérémie Werner, Bjoern Niesen, and Christophe Ballif. Perovskite/silicon tandem solar cells: marriage of convenience or true love story?—an overview. *Advanced Materials Interfaces*, 5(1):1700731, 2018.
- [218] Tomas Leijtens, Kevin A Bush, Rohit Prasanna, and Michael D McGehee. Opportunities and challenges for tandem solar cells using metal halide perovskite semiconductors. *Nature Energy*, 3(10):828–838, 2018.
- [219] Emily L Warren, William E McMahon, Michael Rienacker, Kaitlyn T VanSant, Riley C Whitehead, Robby Peibst, and Adele C Tamboli. A taxonomy for three-terminal tandem solar cells. *ACS Energy Letters*, 5(4):1233–1242, 2020.
- [220] Marko Jošt, Eike Köhnen, Anna Belen Morales-Vilches, Benjamin Lipovšek, Klaus Jäger, Bart Macco, Amran Al-Ashouri, Janez Krč, Lars Korte, Bernd Rech, et al. Textured interfaces in monolithic perovskite/silicon tandem solar cells: advanced light management for improved efficiency and energy yield. *Energy & Environmental Science*, 11(12):3511–3523, 2018.

- [221] Moritz H Futscher and Bruno Ehrler. Modeling the performance limitations and prospects of perovskite/si tandem solar cells under realistic operating conditions. *ACS Energy Letters*, 2(9):2089–2095, 2017.
- [222] Marko Jošt, Lukas Kegelmann, Lars Korte, and Steve Albrecht. Monolithic perovskite tandem solar cells: a review of the present status and advanced characterization methods toward 30% efficiency. *Advanced Energy Materials*, 10(26):1904102, 2020.
- [223] Luana Mazzarella, Ana Belen Morales-Vilches, Max Hendrichs, Simon Kirner, Lars Korte, Rutger Schlatmann, and Bernd Stannowski. Nanocrystalline n-type silicon oxide front contacts for silicon heterojunction solar cells: photocurrent enhancement on planar and textured substrates. *IEEE Journal of Photovoltaics*, 8(1):70–78, 2017.
- [224] Yifeng Zhao, Luana Mazzarella, Paul Procel, Can Han, Guangtao Yang, Arthur Weeber, Miro Zeman, and Olindo Isabella. Doped hydrogenated nanocrystalline silicon oxide layers for high-efficiency c-si heterojunction solar cells. *Progress in Photovoltaics: research and applications*, 28(5):425–435, 2020.
- [225] Yifeng Zhao, Paul Procel, Can Han, Luana Mazzarella, Guangtao Yang, Arthur Weeber, Miro Zeman, and Olindo Isabella. Design and optimization of hole collectors based on nc-siox: H for high-efficiency silicon heterojunction solar cells. *Solar Energy Materials and Solar Cells*, 219:110779, 2021.
- [226] Dong Zhang, Mehrdad Najafi, Valerio Zardetto, Maarten Dörenkämper, Xuedong Zhou, Sjoerd Veenstra, LJ Geerligs, Tom Aernouts, and Ronn Andriessen. High efficiency 4-terminal perovskite/c-si tandem cells. *Solar Energy Materials and Solar Cells*, 188:1–5, 2018.
- [227] NREL. Smarts: Simple model of the atmospheric radiative transfer of sunshine. <https://www.nrel.gov/grid/solar-resource/smarts.html>.
- [228] Jordi Escarré, Karin Söderström, Matthieu Despeisse, Sylvain Nicolay, Corsin Battaglia, Gregory Bugnon, Laura Ding, Fanny Meillaud, Franz-Josef Haug, and Christophe Ballif. Geometric light trapping for high efficiency thin film silicon solar cells. *Solar Energy Materials and Solar Cells*, 98:185–190, 2012.
- [229] Fuhua Hou, Can Han, Olindo Isabella, Lingling Yan, Biao Shi, Junfan Chen, Shichong An, Zhongxin Zhou, Wei Huang, Huizhi Ren, et al. Inverted

- pyramidally-textured pdms antireflective foils for perovskite/silicon tandem solar cells with flat top cell. *Nano energy*, 56:234–240, 2019.
- [230] Juan Lopez-Garcia, Alberto Pozza, and Tony Sample. Long-term soiling of silicon pv modules in a moderate subtropical climate. *Solar Energy*, 130:174–183, 2016.
- [231] MP Brennan, AL Abramase, Rob W Andrews, and Joshua M Pearce. Effects of spectral albedo on solar photovoltaic devices. *Solar Energy Materials and Solar Cells*, 124:111–116, 2014.
- [232] Steve Albrecht, Michael Saliba, Juan-Pablo Correa-Baena, Klaus Jäger, Lars Korte, Anders Hagfeldt, Michael Grätzel, and Bernd Rech. Towards optical optimization of planar monolithic perovskite/silicon-heterojunction tandem solar cells. *Journal of Optics*, 18(6):064012, 2016.
- [233] MR Vogt, T Gewohn, K Bothe, C Schinke, and R Brendel. Impact of using spectrally resolved ground albedo data for performance simulations of bifacial modules. In *Proceedings of the 35th Eur. Photovolt. Sol. Energy Conference Exhibition, Brussels*, pages 1011–1016, 2018.
- [234] Paul Procel, Guangtao Yang, Olindo Isabella, and Miro Zeman. Numerical simulations of ibc solar cells based on poly-si carrier-selective passivating contacts. *IEEE Journal of Photovoltaics*, 9(2):374–384, 2019.
- [235] Lucio Claudio Andreani, Angelo Bozzola, Piotr Kowalczewski, Marco Liscidini, and Lisa Redorici. Silicon solar cells: toward the efficiency limits. *Advances in Physics: X*, 4(1):1548305, 2019.
- [236] Oxford pv perovskite solar cell achieves 28% efficiency, 2018. Press Release by Oxford PV.
- [237] Oxford pv hits new world record for solar cell, 2020. Press Release by Oxford PV.
- [238] World record: Efficiency of perovskite silicon tandem solar cell jumps to 29.15 per cent, 2020. Press release by HZB.
- [239] World record again at hzb: Almost 30% efficiency for next-generation tandem solar cells, 2021. Press release by HZB.
- [240] Jiang Liu, Erkan Aydin, Jun Yin, Michele De Bastiani, Furkan H Isikgor, Atteq Ur Rehman, Emre Yengel, Esmâ Ugur, George T Harrison, Mingcong Wang, et al. 28.2%-efficient, outdoor-stable perovskite/silicon tandem solar cell. *Joule*, 5(12):3169–3186, 2021.

- [241] 2 new world records: perovskite-on-silicon-tandem solar cells, 2022. Press release by CSEM, EPFL.
- [242] Yiliang Wu, Peiting Zheng, Jun Peng, Menglei Xu, Yihua Chen, Sachin Surve, Teng Lu, Anh Dinh Bui, Nengxu Li, Wensheng Liang, et al. 27.6% perovskite/c-si tandem solar cells using industrial fabricated topcon device. *Advanced Energy Materials*, 12(27):2200821, 2022.
- [243] Silvia Mariotti, Klaus Jäger, Marvin Diederich, Marlene S Härtel, Bor Li, Kári Sveinbjörnsson, Sarah Kajari-Schröder, Robby Peibst, Steve Albrecht, Lars Korte, et al. Monolithic perovskite/silicon tandem solar cells fabricated using industrial p-type polycrystalline silicon on oxide/passivated emitter and rear cell silicon bottom cell technology. *Solar RRL*, 6(4):2101066, 2022.
- [244] Zhiqin Ying, Zhenhai Yang, Jingming Zheng, He Wei, Li Chen, Chuanxiao Xiao, Jingsong Sun, Chunhui Shou, Ganghua Qin, Jiang Sheng, et al. Monolithic perovskite/black-silicon tandems based on tunnel oxide passivated contacts. *Joule*, 6(11):2644–2661, 2022.
- [245] Yuxin Yao, Pengjie Hang, Biao Li, Zechen Hu, Chenxia Kan, Jiangsheng Xie, Ying Wang, Yiqiang Zhang, Deren Yang, and Xuegong Yu. Phase-stable wide-bandgap perovskites for four-terminal perovskite/silicon tandem solar cells with over 30% efficiency. *Small*, 18(38):2203319, 2022.
- [246] Hui Li and Wei Zhang. Perovskite tandem solar cells: from fundamentals to commercial deployment. *Chemical Reviews*, 120(18):9835–9950, 2020.
- [247] Armin Richter, Ralph Müller, Jan Benick, Frank Feldmann, Bernd Steinhäuser, Christian Reichel, Andreas Fell, Martin Bivour, Martin Hermle, and Stefan W Glunz. Design rules for high-efficiency both-sides-contacted silicon solar cells with balanced charge carrier transport and recombination losses. *Nature Energy*, 6(4):429–438, 2021.
- [248] Jinkosolar's high-efficiency n-type monocrystalline silicon solar cell sets our new record with maximum conversion efficiency of 26.4 Press release by Jinko Solar.
- [249] Agnes Mewe, Maciej Stodolny, John Anker, Martijn Lenes, Yu Wu, Kees Tool, Bart Geerligs, Ingrid Romijn, et al. Full wafer size ibc cell with polysilicon passivating contacts. In *AIP Conference Proceedings*, volume 1999. AIP Publishing, 2018.

- [250] Rik van der Vossen, Frank Feldmann, Anamaria Moldovan, and Martin Hermle. Comparative study of differently grown tunnel oxides for p-type passivating contacts. *Energy Procedia*, 124:448–454, 2017.
- [251] W Lerch, W Kegel, J Niess, A Gschwandtner, J Gelpey, and Fuccio Cristiano. Scaling requires continuous innovation in thermal processing: low-temperature plasma oxidation. *ECS Transactions*, 45(6):151, 2012.
- [252] M Singh, R Santbergen, L Mazzarella, A Madrampazakis, G Yang, R Vismara, Z Remes, A Weeber, M Zeman, and O Isabella. Optical characterization of poly-siox and poly-sicx carrier-selective passivating contacts. *Solar Energy Materials and Solar Cells*, 210:110507, 2020.
- [253] Guangtao Yang, Can Han, Paul Procel, Yifeng Zhao, Manvika Singh, Luana Mazzarella, Miro Zeman, and Olindo Isabella. Oxygen-alloyed poly-si passivating contacts for high-thermal budget c-si heterojunction solar cells. *Progress in Photovoltaics: research and applications*, 30(2):141–151, 2022.
- [254] Bill Nemeth, David L Young, Matthew R Page, Vincenzo LaSalvia, Steve Johnston, Robert Reedy, and Paul Stradins. Polycrystalline silicon passivated tunneling contacts for high efficiency silicon solar cells. *Journal of Materials Research*, 31(6):671–681, 2016.
- [255] Jana-Isabelle Polzin, Stefan Lange, Susanne Richter, Anamaria Moldovan, Martin Bivour, Christian Hagendorf, Martin Hermle, Stefan W Glunz, and Frank Feldmann. Temperature-induced stoichiometric changes in thermally grown interfacial oxide in tunnel-oxide passivating contacts. *Solar Energy Materials and Solar Cells*, 218:110713, 2020.
- [256] Zhe Rui, Yuheng Zeng, Xueqi Guo, Qing Yang, Zhixue Wang, Chunhui Shou, Waner Ding, Jie Yang, Xinyu Zhang, Qi Wang, et al. On the passivation mechanism of poly-silicon and thin silicon oxide on crystal silicon wafers. *Solar Energy*, 194:18–26, 2019.
- [257] Jan Temmler, Jana-Isabelle Polzin, Frank Feldmann, Leonard Kraus, Bishal Kafle, Sebastian Mack, Anamaria Moldovan, Martin Hermle, and Jochen Rentsch. Inline pecvd deposition of poly-si-based tunnel oxide passivating contacts. *physica status solidi (a)*, 215(23):1800449, 2018.
- [258] Zachary C Holman, Miha Filipič, Antoine Descoeur, Stefaan De Wolf, Franc Smole, Marko Topič, and Christophe Ballif. Infrared light management in high-efficiency silicon heterojunction and rear-passivated solar cells. *Journal of Applied Physics*, 113(1), 2013.

- [259] Can Han, Guangtao Yang, Ana Montes, Paul Procel, Luana Mazzarella, Yifeng Zhao, Stephan Eijt, Henk Schut, Xiaodan Zhang, Miro Zeman, et al. Realizing the potential of rf-sputtered hydrogenated fluorine-doped indium oxide as an electrode material for ultrathin $\text{SiO}_x/\text{poly-Si}$ passivating contacts. *ACS Applied Energy Materials*, 3(9):8606–8618, 2020.
- [260] Depeng Qiu, Weiyuan Duan, Andreas Lambertz, Karsten Bittkau, Kaifu Qiu, Uwe Rau, and Kaining Ding. Effect of oxygen and hydrogen flow ratio on indium tin oxide films in rear-junction silicon heterojunction solar cells. *Solar Energy*, 231:578–585, 2022.
- [261] Ronald A Sinton and Andres Cuevas. Contactless determination of current-voltage characteristics and minority-carrier lifetimes in semiconductors from quasi-steady-state photoconductance data. *Applied Physics Letters*, 69(17):2510–2512, 1996.
- [262] Mark J Kerr, Andres Cuevas, and Ronald A Sinton. Generalized analysis of quasi-steady-state and transient decay open circuit voltage measurements. *Journal of applied physics*, 91(1):399–404, 2002.
- [263] Nga Phung, Marcel Verheijen, Anna Todinova, Kunal Datta, Michael Verhage, Amran Al-Ashouri, Hans Kobler, Xin Li, Antonio Abate, Steve Albrecht, et al. Enhanced self-assembled monolayer surface coverage by Al_2O_3 in pin perovskite solar cells. *ACS Applied Materials & Interfaces*, 14(1):2166–2176, 2021.
- [264] Nga Phung, Cristian van Helvoirt, Wolfhard Beyer, John Anker, Ronald CG Naber, Marten Renes, Wilhelmus MM Kessels, LJ Geerligs, Mariadriana Creatore, and Bart Macco. Effective hydrogenation of poly-Si passivating contacts by atomic-layer-deposited nickel oxide. *IEEE Journal of Photovoltaics*, 12(6):1377–1385, 2022.
- [265] Amran Al-Ashouri, Artiom Magomedov, Marcel Roß, Marko Jošt, Martynas Talaikis, Ganna Chistiakova, Tobias Bertram, José A Márquez, Eike Köhnen, Ernestas Kasparavičius, et al. Conformal monolayer contacts with lossless interfaces for perovskite single junction and monolithic tandem solar cells. *Energy & Environmental Science*, 12(11):3356–3369, 2019.
- [266] Kunal Datta. *PhD Research Thesis*. PhD thesis, Eindhoven University of Technology, 2022.
- [267] 30% yield achieved with four terminal perovskite silicon pv tandem cells, 2022. Press Release by TNO.

- [268] Mehrdad Najafi, Valerio Zardetto, Dong Zhang, Dibyashree Koushik, Maarten S Dörenkämper, Mariadriana Creatore, Ronn Andriessen, Paul Poodt, and Sjoerd Veenstra. Highly efficient and stable semi-transparent p-i-n planar perovskite solar cells by atmospheric pressure spatial atomic layer deposited zno. *Solar RRL*, 2(10):1800147, 2018.
- [269] Guangtao Yang, Remon Gram, Paul Procel, Can Han, Zhirong Yao, Manvika Singh, Yifeng Zhao, Luana Mazzarella, Miro Zeman, and Olindo Isabella. Will siox-pinholes for siox/poly-si passivating contact enhance the passivation quality? *Solar Energy Materials and Solar Cells*, 252:112200, 2023.
- [270] Josua Stuckelberger, Di Yan, Sieu Pheng Phang, Chris Samundsett, Jiali Wang, Luca Antognini, Franz-Josef Haug, Zhao Wang, Jie Yang, Peiting Zheng, et al. Pre-annealing for improved lpcvd deposited boron-doped poly-si hole-selective contacts. *Solar Energy Materials and Solar Cells*, 251:112123, 2023.
- [271] J S Custer, Michael O Thompson, DC Jacobson, JM Poate, S Roorda, WC Sinke, and F Spaepen. Density of amorphous si. *Applied physics letters*, 64(4):437–439, 1994.
- [272] Kunal Datta, Bruno Branco, Yifeng Zhao, Valerio Zardetto, Nga Phung, Andrea Brancesco, Luana Mazzarella, Martijn M Wienk, Mariadriana Creatore, Olindo Isabella, et al. Efficient continuous light-driven electrochemical water splitting enabled by monolithic perovskite-silicon tandem photovoltaics. *Advanced Materials Technologies*, 8(2):2201131, 2023.
- [273] William Shockley. The shockley-queisser limit. *J. Appl. Phys*, 32(3):510–519, 1961.
- [274] LONGi. Longi sets a new world record of 27.09 <https://www.longi.com/en/news/post-2024-09-28/>, 2024.
- [275] World record back at hzb: Tandem solar cell achieves 32.5 percent efficiency, 2022. Press release by HZB.
- [276] Kaust team sets world record for tandem solar cell efficiency, <https://www.pv-magazine.com/2024/08/10/kaust-claims-33-7-efficiency-for-perovskite-silicon-tandem-solar-cell>.
- [277] Antonio J Riquelme, Karen Valadez-Villalobos, Pablo P Boix, Gerko Oskam, Iván Mora-Seró, and Juan A Anta. Understanding equivalent circuits in perovskite solar cells. insights from drift-diffusion simulation. *Physical Chemistry Chemical Physics*, 24(26):15657–15671, 2022.

- [278] Taylor Moot, Jay B Patel, Gabriel McAndrews, Eli J Wolf, Daniel Morales, Isaac E Gould, Bryan A Rosales, Caleb C Boyd, Lance M Wheeler, Philip A Parilla, et al. Temperature coefficients of perovskite photovoltaics for energy yield calculations. *ACS Energy Letters*, 6(5):2038–2047, 2021.
- [279] Faiza Azri, Afak Meftah, Nouredine Sengouga, and Amjad Meftah. Electron and hole transport layers optimization by numerical simulation of a perovskite solar cell. *Solar energy*, 181:372–378, 2019.
- [280] Lingyan Lin, Linqin Jiang, Ping Li, Hao Xiong, Zhenjing Kang, Baodian Fan, and Yu Qiu. Simulated development and optimized performance of cspb₃ based all-inorganic perovskite solar cells. *Solar Energy*, 198:454–460, 2020.
- [281] Varkey Sebastian, Joji Kurian, et al. Simulation and optimization studies on cspb₃ based inorganic perovskite solar cells. *Solar Energy*, 221:99–108, 2021.
- [282] Hossein Abedini-Ahangarkola, Samaneh Soleimani-Amiri, and Somayeh Gholami Rudi. Modeling and numerical simulation of high efficiency perovskite solar cell with three active layers. *Solar Energy*, 236:724–732, 2022.
- [283] Numeshwar Kumar Sinha, Dhriti Sundar Ghosh, and Ayush Khare. A comprehensive guide to bifacial perovskite solar cells: simulation and optimization. *Advanced Theory and Simulations*, 7(1):2300633, 2024.
- [284] Rohan Ghosh, Anterdipan Singh, and Pratima Agarwal. Study on effect of different htl and etl materials on the perovskite solar cell performance with tcad simulator. *Materials Today: Proceedings*, 2023.
- [285] Jin Young Kim, Jin-Wook Lee, Hyun Suk Jung, Hyunjung Shin, and Nam-Gyu Park. High-efficiency perovskite solar cells. *Chemical reviews*, 120(15):7867–7918, 2020.
- [286] Furkan H Isikgor, Shynggys Zhumagali, Luis V T. Merino, Michele De Bastiani, Iain McCulloch, and Stefaan De Wolf. Molecular engineering of contact interfaces for high-performance perovskite solar cells. *Nature Reviews Materials*, 8(2):89–108, 2023.
- [287] Zhihao Zhang, Lu Qiao, Ke Meng, Run Long, Gang Chen, and Peng Gao. Rationalization of passivation strategies toward high-performance perovskite solar cells. *Chemical Society Reviews*, 52(1):163–195, 2023.

- [288] Feng Qin, Jing Chen, Jiangwei Liu, Li Liu, Chaojun Tang, Bin Tang, Gongfa Li, Liangcai Zeng, Hailiang Li, and Zao Yi. Design of high efficiency perovskite solar cells based on inorganic and organic undoped double hole layer. *Solar Energy*, 262:111796, 2023.
- [289] Alexander D Taylor, Qing Sun, Katelyn P Goetz, Qingzhi An, Tim Schramm, Yvonne Hofstetter, Maximillian Litterst, Fabian Paulus, and Yana Vaynzof. A general approach to high-efficiency perovskite solar cells by any antisolvent. *Nature communications*, 12(1):1878, 2021.
- [290] Guixiang Li, Zhenhuang Su, Laura Canil, Declan Hughes, Mahmoud H Aldamasy, Janardan Dagar, Sergei Trofimov, Luyao Wang, Weiwei Zuo, José J Jerónimo-Rendon, et al. Highly efficient pin perovskite solar cells that endure temperature variations. *Science*, 379(6630):399–403, 2023.
- [291] Do-Kyoung Lee and Nam-Gyu Park. Materials and methods for high-efficiency perovskite solar modules. *Solar RRL*, 6(3):2100455, 2022.
- [292] Sanwan Liu, Vasudevan P Biju, Yabing Qi, Wei Chen, and Zonghao Liu. Recent progress in the development of high-efficiency inverted perovskite solar cells. *NPG Asia Materials*, 15(1):27, 2023.
- [293] Yue Yu, Fu Zhang, Tian Hou, Xiaoran Sun, Hua Yu, and Meng Zhang. A review on gas-quenching technique for efficient perovskite solar cells. *Solar Rrl*, 5(10):2100386, 2021.
- [294] Maximilian T Hörantner and Henry J Snaith. Predicting and optimising the energy yield of perovskite-on-silicon tandem solar cells under real world conditions. *Energy & Environmental Science*, 10(9):1983–1993, 2017.
- [295] Jonathan Lehr, Malte Langenhorst, Raphael Schmager, Simon Kirner, Uli Lemmer, Bryce S Richards, Chris Case, and Ulrich W Paetzold. Energy yield modelling of perovskite/silicon two-terminal tandem pv modules with flat and textured interfaces. *Sustainable energy & fuels*, 2(12):2754–2761, 2018.
- [296] Seyedamir Orooji and Ulrich W Paetzold. Energy yield modeling of perovskite–silicon tandem photovoltaics: Degradation and total lifetime energy yield. *Energy Technology*, page 2400998, 2024.
- [297] Michele De Bastiani, Alessandro J Mirabelli, Yi Hou, Fabrizio Gota, Erkan Aydin, Thomas G Allen, Joel Troughton, Anand S Subbiah, Furkan H Isikgor, Jiang Liu, et al. Efficient bifacial monolithic perovskite/silicon tandem solar cells via bandgap engineering. *Nature Energy*, 6(2):167–175, 2021.

- [298] Benjamin Lipovšek, Marko Jošt, Špela Tomšič, and Marko Topič. Energy yield of perovskite solar cells: Influence of location, orientation, and external light management. *Solar Energy Materials and Solar Cells*, 234:111421, 2022.
- [299] Pilar Lopez-Varo, Mohamed Amara, Stefania Cacovich, Arthur Julien, Armelle Yaiche, Mohamed Jouhari, Jean Rousset, Philip Schulz, Jean-Francois Guillemoles, and Jean-Baptiste Puel. Dynamic temperature effects in perovskite solar cells and energy yield. *Sustainable Energy & Fuels*, 5(21):5523–5534, 2021.
- [300] Marko Remec, Špela Tomšič, Mark Khenkin, Quiterie Emery, Jinzhao Li, Florian Scheler, Boštjan Glažar, Marko Jankovec, Marko Jošt, Eva Unger, et al. From sunrise to sunset: Unraveling metastability in perovskite solar cells by coupled outdoor testing and energy yield modelling. *Advanced Energy Materials*, 14(29):2304452, 2024.
- [301] Špela Tomšič, Marko Jošt, Kristijan Brecl, Marko Topič, and Benjamin Lipovšek. Energy yield modeling for optimization and analysis of perovskite-silicon tandem solar cells under realistic outdoor conditions. *Advanced Theory and Simulations*, 6(4):2200931, 2023.
- [302] Marko Jošt, Benjamin Lipovšek, Boštjan Glažar, Amran Al-Ashouri, Kristijan Brecl, Gašper Matič, Artiom Magomedov, Vytautas Getautis, Marko Topič, and Steve Albrecht. Perovskite solar cells go outdoors: field testing and temperature effects on energy yield. *Advanced energy materials*, 10(25):2000454, 2020.
- [303] Ramez Hosseinian Ahangharnejhad, Willis Becker, Jayson Jones, Annick Anctil, Zhaoning Song, Adam Phillips, Michael J Heben, and Ilke Celik. Environmental impact per energy yield for bifacial perovskite solar cells outperforms crystalline silicon solar cells. *Cell Reports Physical Science*, 1(10), 2020.
- [304] Youri Blom, Malte Ruben Vogt, Carlos M Ruiz Tobon, Rudi Santbergen, Miro Zeman, and Olindo Isabella. Energy loss analysis of two-terminal tandem pv systems under realistic operating conditions—revealing the importance of fill factor gains. *Solar RRL*, 7(8):2200579, 2023.
- [305] Mikio Taguchi, Akira Terakawa, Eiji Maruyama, and Makoto Tanaka. Obtaining a higher voc in hit cells. *Progress in photovoltaics: research and applications*, 13(6):481–488, 2005.

- [306] Mikio Taguchi, Ayumu Yano, Satoshi Tohoda, Kenta Matsuyama, Yuya Nakamura, Takeshi Nishiwaki, Kazunori Fujita, and Eiji Maruyama. 24.7% record efficiency hit solar cell on thin silicon wafer. *IEEE Journal of photovoltaics*, 4(1):96–99, 2013.
- [307] Keiichiro Masuko, Masato Shigematsu, Taiki Hashiguchi, Daisuke Fujishima, Motohide Kai, Naoki Yoshimura, Tsutomu Yamaguchi, Yoshinari Ichihashi, Takahiro Mishima, Naoteru Matsubara, et al. Achievement of more than 25% conversion efficiency with crystalline silicon heterojunction solar cell. *IEEE Journal of Photovoltaics*, 4(6):1433–1435, 2014.
- [308] Frank Feldmann, Martin Bivour, Christian Reichel, Martin Hermle, and Stefan W Glunz. Passivated rear contacts for high-efficiency n-type si solar cells providing high interface passivation quality and excellent transport characteristics. *Solar energy materials and solar cells*, 120:270–274, 2014.
- [309] Di Yan, Andres Cuevas, James Bullock, Yimao Wan, and Christian Samundsett. Phosphorus-diffused polysilicon contacts for solar cells. *Solar Energy Materials and Solar Cells*, 142:75–82, 2015.
- [310] R Peibst, U Römer, Y Larionova, M Rienäcker, A Merkle, N Folchert, S Reiter, M Turcu, B Min, J Krügener, et al. Working principle of carrier selective poly-si/c-si junctions: Is tunnelling the whole story? *Solar Energy Materials and Solar Cells*, 158:60–67, 2016.
- [311] Manvika Singh, Rudi Santbergen, Indra Syifai, Arthur Weeber, Miro Zeman, and Olindo Isabella. Comparing optical performance of a wide range of perovskite/silicon tandem architectures under real-world conditions. *Nanophotonics*, 10(8):2043–2057, 2021.
- [312] Manvika Singh, Kunal Datta, Aswathy Amarnath, Fabian Wagner, Yifeng Zhao, Guangtao Yang, Andrea Bracesco, Nga Phung, Dong Zhang, Valerio Zardetto, et al. Crystalline silicon solar cells with thin poly-siox carrier-selective passivating contacts for perovskite/c-si tandem applications. *Progress in Photovoltaics: research and applications*, 31(9):877–887, 2023.
- [313] Andrea Ingenito, Olindo Isabella, Serge Solntsev, and Miro Zeman. Accurate opto-electrical modeling of multi-crystalline silicon wafer-based solar cells. *Solar energy materials and solar cells*, 123:17–29, 2014.
- [314] Silvia Mariotti, Eike Köhnen, Florian Scheler, Kári Sveinbjörnsson, Lea Zimmermann, Manuel Piot, Fengjiu Yang, Bor Li, Jonathan Warby, Artem

- Musiienko, et al. Interface engineering for high-performance, triple-halide perovskite–silicon tandem solar cells. *Science*, 381(6653):63–69, 2023.
- [315] Tae-hee Jung, Hee-eun Song, Hyung-keun Ahn, and Gi-hwan Kang. A mathematical model for cell-to-module conversion considering mismatching solar cells and the resistance of the interconnection ribbon. *Solar Energy*, 103:253–262, 2014.
- [316] Atteq Ur Rehman, Emmanuel P Van Kerschaver, Erkan Aydin, Waseem Raja, Thomas G Allen, and Stefaan De Wolf. Electrode metallization for scaled perovskite/silicon tandem solar cells: Challenges and opportunities. *Progress in Photovoltaics: Research and Applications*, 31(4):429–442, 2023.
- [317] Robert Witteck, Henning Schulte-Huxel, Hendrik Holst, David Hinken, Malte Vogt, Susanne Blankemeyer, Marc Köntges, Karsten Bothe, and Rolf Brendel. Optimizing the solar cell front side metallization and the cell interconnection for high module power output. *Energy procedia*, 92:531–539, 2016.
- [318] Mark Z Jacobson and Vijaysinh Jadhav. World estimates of pv optimal tilt angles and ratios of sunlight incident upon tilted and tracked pv panels relative to horizontal panels. *Solar energy*, 169:55–66, 2018.
- [319] Y Zhao. Hydrogenated nanocrystalline silicon-based layers for silicon heterojunction and perovskite/c-si tandem solar cells. 2023.
- [320] Chan Ul Kim, Jae Choul Yu, Eui Dae Jung, In Young Choi, Wonjin Park, Hyungmin Lee, Inho Kim, Dok-Kwon Lee, Kuen Kee Hong, Myoung Hoon Song, et al. Optimization of device design for low cost and high efficiency planar monolithic perovskite/silicon tandem solar cells. *Nano Energy*, 60:213–221, 2019.
- [321] Aimal Daud Khan, Fazal E Subhan, Adnan Daud Khan, Sultan Daud Khan, Muhammad Shakeel Ahmad, Muhammad Saad Rehan, Muhammad Norman, et al. Optimization of efficient monolithic perovskite/silicon tandem solar cell. *Optik*, 208:164573, 2020.
- [322] YiLiang Wu, Andreas Fell, and Klaus J Weber. A step-by-step optimization of the c-si bottom cell in monolithic perovskite/c-si tandem devices. *Solar RRL*, 2(11):1800193, 2018.
- [323] GJ Faturrochman, MM De Jong, R Santbergen, W Folkerts, M Zeman, and AHM Smets. Maximizing annual yield of bifacial photovoltaic noise barriers. *Solar Energy*, 162:300–305, 2018.

- [324] Fabiano Perin Gasparin, Felipe Detzel Kipper, Fernando Schuck de Oliveira, and Arno Krenzinger. Assessment on the variation of temperature coefficients of photovoltaic modules with solar irradiance. *Solar Energy*, 244:126–133, 2022.
- [325] Nrel solar spectra. <https://www.nrel.gov/grid/solar-resource/spectra.html>, 2020. Accessed: December 3, 2020.
- [326] Lianghong Yan, Nan Liu, Songnan Zhao, Hongwei Yan, Haibing Lü, and Xiaodong Yuan. Effect of hydrophobic modification on the durability and environmental properties of porous mgf 2 antireflective films. *Acta Metallurgica Sinica (English Letters)*, 27:649–655, 2014.
- [327] Cecilia Agustín-Sáenz, Maider Machado, Jiri Nohava, Naiara Yurrita, Asier Sanz, Marta Brizuela, Oihana Zubillaga, and Agnieszka Tercjak. Mechanical properties and field performance of hydrophobic antireflective sol-gel coatings on the cover glass of photovoltaic modules. *Solar Energy Materials and Solar Cells*, 216:110694, 2020.
- [328] Marilyn J Dodge. Refractive properties of magnesium fluoride. *Applied optics*, 23(12):1980–1985, 1984.
- [329] Jérémie Werner, Guy Dubuis, Arnaud Walter, Philipp Löper, Soo-Jin Moon, Sylvain Nicolay, Monica Morales-Masis, Stefaan De Wolf, Bjoern Niesen, and Christophe Ballif. Sputtered rear electrode with broadband transparency for perovskite solar cells. *Solar Energy Materials and Solar Cells*, 141:407–413, 2015.
- [330] D Zhang, IA Digdaya, R Santbergen, RACMM Van Swaaij, P Bronsveld, M Zeman, JAM Van Roosmalen, and AW Weeber. Design and fabrication of a siox/ito double-layer anti-reflective coating for heterojunction silicon solar cells. *Solar Energy Materials and Solar Cells*, 117:132–138, 2013.
- [331] Martin A Green and Mark J Keevers. Optical properties of intrinsic silicon at 300 k. *Progress in Photovoltaics: Research and applications*, 3(3):189–192, 1995.
- [332] Malte Ruben Vogt, Harald Hahn, Hendrik Holst, Matthias Winter, Carsten Schinke, Marc Köntges, Rolf Brendel, and Pietro P Altermatt. Measurement of the optical constants of soda-lime glasses in dependence of iron content and modeling of iron-related power losses in crystalline si solar cell modules. *IEEE Journal of Photovoltaics*, 6(1):111–118, 2015.

-
- [333] Malte R Vogt, Hendrik Holst, Henning Schulte-Huxel, Susanne Blankemeyer, Robert Witteck, David Hinken, Matthias Winter, Byungsul Min, Carsten Schinke, Ingo Ahrens, et al. Optical constants of uv transparent eva and the impact on the pv module output power under realistic irradiation. *Energy Procedia*, 92:523–530, 2016.
- [334] Honglei Wang, Ross Haroldson, Balasubramaniam Balachandran, Alex Zakhidov, Sandeep Sohal, Julia Y Chan, Anvar Zakhidov, and Walter Hu. Nanoimprinted perovskite nanograting photodetector with improved efficiency. *ACS nano*, 10(12):10921–10928, 2016.
- [335] Philipp Tockhorn, Johannes Sutter, Rémi Colom, Lukas Kegelmann, Amran Al-Ashouri, Marcel Roß, Klaus Jager, Thomas Unold, Sven Burger, Steve Albrecht, et al. Improved quantum efficiency by advanced light management in nanotextured solution-processed perovskite solar cells. *ACS photonics*, 7(9):2589–2600, 2020.

Acknowledgements

"Life is a blend of challenges and joys – and so is the journey through a PhD."

First, I would like to thank my father for his unconditional support, guidance and advice throughout my PhD journey. I never sought a formal mentor during my PhD because I consider my father to be my greatest mentor. My strength, motivation, and encouragement have all come from him. He has been my pillar of support during my challenges, showing incredible patience with me along the way and his advice has often helped me navigate difficult situations. It is because of him that I have reached this point in my life. His decision to send me to Delft for my master's and then PhD was a turning point in my life and I am deeply grateful to him for shaping my path.

I am thankful to Prof. Olindo Isabella, my PhD promoter, for his supervision and guidance during my work. I would also like to thank him for the opportunities he provided to attend various conferences, which were valuable experiences for my academic growth. I would like to thank Prof. Miro Zeman, my PhD promoter, for welcoming me into the JSP III program, which has been instrumental in shaping my PhD journey.

I would also like to extend my thanks to my PhD co-promoter, Dr. Rudi Santbergen, for his insightful discussions on GenPro4 and optical modeling, which were valuable to my research. Additionally, I am grateful to Prof. Arthur Weeber for his positive outlook towards me, as well as for the helpful feedback and constructive comments he provided throughout my work.

I would like to thank the members of my jury, Prof. Pere Roca i Cabarrocas, Prof. Bernd Stannowski, Prof. Arthur Weeber and Prof. Ivan Gordan, who accepted our invitations and devoted time to read this thesis and provide insightful comments. Besides, my acknowledgements also go to Prof. Arno Smets and Dr. Rene van Swaaij for raising thought-provoking questions during the group meetings. I fondly remember Dr. Ivan Gordon as the editor of SOLMAT during the release of my first publication.

The best things often happen when you least expect them. The final six

months of my thesis were the most enjoyable, thanks to my colleagues, Youri, David, Arturo, Alba, Yilong, Katarina, and Afshin. I cherish the great moments shared with them. I would like to thank my colleagues, Yilei, Carlos, Juan Camillo, Robin, Can, Guangato, Andres, Rita, Nasim, Malte, Liqi, Zhirong, Mirco, Daniele, Yudai, Maarten, Thierry, Federica, Patrizio and Hesam for their pleasant interactions. I also fondly remember the late evening conversations I had with Carlos and Hesam while leaving the office. I would like to extend my heartfelt thanks to Yilei for his kindness. On one occasion, when I was feeling down and alone in the office, he went out of his way to check on me, even though we hadn't known each other before then. It means a lot.

I would like to thank my students, Indra, Aswathy, Fabian, Mahesh and Jacopo for their contribution to my thesis. I enjoyed the process of supervising them. I thank Martijn Tijssen for his support in the lab. I am also thankful to the secretaries, Mark and Sharmila, for their support in administrative affairs. I would also like to thank Zdenek Remes and Martin Ledinsky in Prague for their assistance with the PDS experiments during my first year of PhD. I would like to thank Dong Zhang and Kunal Datta for their contribution to the perovskite top cell in my publications. My thanks also goes to the entire perovskite group at TNO, where I have been working for the past two years.

Life is truly magical, and you never know what surprises it holds. I am humbled to have received three awards during my PhD journey. A special moment for me was receiving the Poster Award at the World Conference in Milan in 2022, for which I am deeply thankful to the almighty. In that moment, I truly felt the grace of the universe.

I would like to sincerely thank my mother for her many sacrifices, one of which was choosing not to go abroad, despite receiving several offers for office training when I was young. Just like her, I have tried to incorporate hard work, perseverance, and perfection into my own work. However, I know that I have only achieved a small fraction of what she exemplifies. I would like to thank my sister, Anulika, for offering valuable advice on my PhD when I needed it. A special thank goes to my friend, Kruti (Kitty), for always being there to listen to me through the ups and downs of my PhD journey.

In 2025, I have completed ten years in the Netherlands, with *Delft* holding a special place in my heart—a true fairytale town. Here, I have memories both good and challenging, and I feel as though I have truly grown in this place. As one chapter ends, another begins, with many more memories waiting to be made.....

List of Publications, Conference Contributions and Awards

This chapter lists the publications, conference contributions and awards received during my PhD period.

Peer-reviewed journal articles

First-authored peer-reviewed journal articles

1. **M. Singh**, R. Santbergen, L. Mazzarella, A. Madrampazakis, G. Yang, R. Vismara, Z. Remes, A. Weeber, M. Zeman and O. Isabella, *Optical characterization of poly-SiO_x and poly-SiC_x carrier-selective passivating contacts*, Solar Energy Materials and Solar Cells, 210, 110507 (2020).
2. **M. Singh**, R. Santbergen, I. Syifai, A. Weeber, M. Zeman, O. Isabella, *Comparing optical performance of a wide range of perovskite/silicon tandem architectures under real world conditions*, Nanophotonics 10(8), 2043-2057 (2021).
3. **M. Singh**, K. Datta, A. Amarnath, F. Wagner, Y. Zhao, G. Yang, A. Bracesco, N. Phung, D. Zhang, V. Zardetto, M. Najafi, S. C. Veenstra, G. Coletti, L. Mazzarella, M. Creatore, M. M. Wienk, R. A. J. Janssen, A. W. Weeber, M. Zeman, O. Isabella, *Crystalline silicon solar cells with thin poly-SiO_x carrier-selective passivating contacts for perovskite/c-Si tandem applications*, Progress in Photovoltaics: research and applications 31(9), 877-887 (2023). *
4. **M. Singh**, J. Finazzo, Y. Blom, M. Jayan, C. R. Tobon, A. Weeber, M. Zeman, R. Santbergen, O. Isabella, *On the annual energy yield of perovskite/silicon tandem modules with different bottom cell technologies and optimized top cell properties for different locations*, EPJ Photovoltaics (2025).

Co-authored peer-reviewed journal articles

1. G. Yang, C. Han, P. Procel, Y. Zhao, **M. Singh**, L. Mazzarella, M. Zeman, and O. Isabella, *Oxygen-alloyed poly-Si passivating contacts for high-thermal budget c-Si heterojunction solar cells*, Progress in Photovoltaics: research and applications, 30, 141-151, (2022).

*This work is among top 10 most-cited papers published by Progress in Photovoltaics in 2023

2. G. Yang, R. Gram, P. Procel, C. Han, Z. Yao, **M. Singh**, Y. Zhao, L. Mazzarella, M. Zeman and O. Isabella, *Will SiO_x-pinholes for SiO_x/poly-Si passivating contact enhance the passivation quality?*, Solar Energy Materials and Solar Cells, 252, 112200 (2023).

First-authored conference contributions

1. Poster presentation @ SiliconPV 2019: **M. Singh**, G. Yang, L. Mazzarella, R. Santbergen, R. Vismara, Z. Remes, L. Vančo, M. Lendinsky, A. Fejfar, A. Weeber, O. Isabella and M. Zeman, *Optical Properties of Poly-SiO_x Carrier-Selective Passivating Contacts*, Leuven, Belgium, 2019.
2. Oral presentation @ MRS Fall Meeting and Exhibit 2019: **M. Singh**, R. Santbergen, L. Mazzarella, G. Yang, Z. Remes, A. Weeber, O. Isabella and M. Zeman, *Optical characterization of poly-SiO_x and poly-SiC_x carrier selective passivating contacts*, Boston, USA 2019.
3. Poster presentation @ EUPVSEC 2020: **M. Singh**, R. Santbergen, Z. Wang, A. Nour El Din, C. Ruiz Tobon, P. Procel, M. Zeman and O. Isabella, *Combined PV Device, Module and System Modelling for Predicting the Annual Energy Yield of Perovskite / Silicon Tandem Based PV Systems*, Online, 2020.
4. Poster presentation @ Silicon PV 2021: **M. Singh**, P. Procel, I. Syifai, R. V. Heerden, A. Weeber, M. Zeman, R. Santbergen and O. Isabella, *Combination of advanced optical and electrical modelling for simulations of high efficiency perovskite/c-Si tandem solar cells*, Online, 2021.
5. Poster presentation @ Tandem PV workshop 2021: **M. Singh**, P. Procel, I. Syifai, R. van Heerden, A. Weeber, M. Zeman, R. Santbergen and O. Isabella, *On carriers' collection in perovskite/c-Si tandem solar cells*, Online, 2021.
6. Poster presentation @ Tandem PV workshop 2021: **M. Singh**, R. Santbergen, I. Syifai, A. Weeber, M. Zeman, O. Isabella, *Comparing optical performance of a wide range of perovskite/c-Si tandem architectures under real world conditions*, Online, 2021.
7. Poster presentation @ IEEE PVSEC 2021: **M. Singh**, R. Santbergen, I. Syifai, A. Weeber, M. Zeman and O. Isabella, *Comparing optical performance of a wide range of perovskite/c-Si tandem architectures under real world conditions*, Online, 2021.
8. Oral presentation @ IEEE PVSEC 2021: **M. Singh**, P. Procel, I. Syifai, R. van Heerden, A. Weeber, M. Zeman, R. Santbergen and O. Isabella, *On carriers'*

- collection in perovskite/c-Si tandem solar cells*, Online, 2021.
9. Poster presentation @ EUPVSEC 2021: **M. Singh**, R. Santbergen, I. Syifai, A. Weeber, M. Zeman and O. Isabella, *Comparing optical performance of a wide range of perovskite/c-Si tandem architectures under real world conditions*, Online, 2021.
 10. Poster presentation @ EUPVSEC 2021: **M. Singh**, P. Procel, I. Syifai, R. van Heerden, A. Weeber, M. Zeman, R. Santbergen and O. Isabella, *On carriers' collection in perovskite/c-Si tandem solar cells*, Online, 2021.
 11. Oral presentation @ MRS 2021: **M. Singh**, A. Amarnath, G. Yang, A. Weeber, M. Zeman and O. Isabella, *Fabrication of solar cells with poly-SiO_x carrier-selective passivating contacts on ultra-thin thermal tunnelling oxide*, Online, 2021.
 12. Invited talk @ Optica Advanced Photonics Congress 2022: **M. Singh**, R. Santbergen, A. Weeber, M. Zeman and O. Isabella, *Perovskite/c-Si tandem solar cells with poly-SiO_x carrier-selective passivating contacts*, Maastricht, Netherlands, 2022.
 13. Poster presentation @ WCPEC-8: **M. Singh**, M. Singh, K. Dutta, A. Amarnath, F. Wagner, Y. Zhao, G. Yang, A. Bracesco, D. Zhang, V. Zardetto, M. Najafi, S. Veenstra, G. Coletti, L. Mazzarella, A. Creatore, R. Janssen, A. W. Weeber, M. Zeman and O. Isabella, *Screen-printed c-Si solar cells with poly-SiO_x carrier selective passivating contacts on ultra-thin thermal tunnelling oxide*, Milan, Italy, 2022.

Awards

1. **Poster Award** at European Photovoltaic Solar Energy Conference and Exhibition (EUPVSEC), 2021
M. Singh et al., Comparing optical performance of a wide range of perovskite/c-Si tandem architectures under real world conditions, Online, 2021.
2. **Best Presentation Award** at Materials Research Society (MRS), 2021
M. Singh et al., Fabrication of solar cells with poly-SiO_x carrier-selective passivating contacts on ultra-thin thermal tunnelling oxide, Online, 2021.
3. **Poster Award** at 8th World Conference on Photovoltaic Energy Conversion (WCPEC-8), 2022
M. Singh et al., Screen-printed c-Si solar cells with poly-SiO_x carrier selective passivating contacts on ultra-thin thermal tunnelling oxide, Milan, Italy, 2022.

Curriculum Vitae

Manvika Singh was born on 15 February 1993 in Jabalpur, Madhya Pradesh, India. In 2015, she earned a **Bachelor of Engineering (B.E.)** in Electrical and Electronics Engineering from BITS Pilani, Dubai Campus. During her studies, she gained industry experience through internships at companies such as Siemens and Petrofac.

In 2017, she completed her **Master of Science (MSc)** in Electrical Engineering (Microelectronics Track) at Delft University of Technology (TU Delft), Netherlands, where she conducted her master's thesis on "Suspended Graphene Membranes for Electrostatically Actuated Resonators" under the supervision of Prof. Dr. Lina Sarro.

In August 2018, she began her **PhD** in the Photovoltaic Materials and Devices (PVMD) group at TU Delft under the guidance of Prof. Dr. Miro Zeman and Prof. Dr. Olindo Isabella. Her thesis focuses on the modelling and experimental optimization of perovskite/c-Si tandem solar cells with high temperature carrier-selective passivating contacts.

Since February 2023, she has been working as a **Research Scientist** in the Perovskite Group at the Netherlands Organisation for Applied Scientific Research (TNO) where her work focuses on the fabrication and upscaling of perovskite solar cell technology.

Contact:

Email: manvikasingh15@gmail.com

LinkedIn: <https://www.linkedin.com/in/manvika-singh>

ResearchGate: https://www.researchgate.net/profile/Manvika_Singh

Google Scholar:





Manvika Singh received her Bachelor of Engineering (B.E.) degree in Electrical and Electronics Engineering in 2015. In 2017, she completed her Master of Science (MSc) in Electrical Engineering (Microelectronics Track) at TU Delft, Netherlands. In August 2018, she started her PhD in the Photovoltaic Materials and Devices (PVMD) group at Delft University of Technology (TU Delft). Her thesis focuses on the modelling and experimental optimization of perovskite/c-Si tandem solar cells with high temperature carrier-selective passivating contacts. In February 2023, she joined the Perovskite Group at the Netherlands Organisation for Applied Scientific Research (TNO) as a Research Scientist. Her work focuses on the fabrication and upscaling of perovskite solar cell technology.